CANADIAN THESES ON MICROFICHE

THÈSES CANADIENNES SUR MICROFICHE

National Library of Canada
Collections Development Branch

Canadian Theses on
Microfiche Service

Ottawa, Canada
K1A 0N4

Bibliothèque nationale du Canada
Direction du développement des collections

Service des thèses canadiennes
sur microfiche

NOTICE

The quality of this microfiche is heavily dependent upon the quality of the original thesis submitted for microfilming. Every effort has been made to ensure the highest quality of reproduction possible.

If pages are missing, contact the university which granted the degree.

Some pages may have indistinct print especially if the original pages were typed with a poor typewriter ribbon or if the university sent us an inferior photocopy.

Previously copyrighted materials (journal articles, published tests, etc.) are not filmed.

Reproduction in full or in part of this film is governed by the Canadian Copyright Act, R.S.C. 1970, c. C-30. Please read the authorization forms which accompany this thesis.

AVIS

La qualité de cette microfiche dépend grandement de la qualité de la thèse soumise au microfilmage. Nous avons tout fait pour assurer une qualité supérieure de reproduction.

S'il manque des pages, veuillez communiquer avec l'université qui a conféré le grade.

La qualité d'impression de certaines pages peut laisser à désirer, surtout si les pages originales ont été dactylographiées à l'aide d'un ruban usé ou si l'université nous a fait parvenir une photocopie de qualité inférieure.

Les documents qui font déjà l'objet d'un droit d'auteur (articles de revue, examens publiés, etc.) ne sont pas microfilmés.

La reproduction, même partielle, de ce microfilm est soumise à la Loi canadienne sur le droit d'auteur, SRC 1970, c. C-30. Veuillez prendre connaissance des formules d'autorisation qui accompagnent cette thèse.

THIS DISSERTATION
HAS BEEN MICROFILMED
EXACTLY AS RECEIVED

LA THÈSE A ÉTÉ
MICROFILMÉE TELLE QUE
NOUS L'AVONS REÇUE

Canada

NL 339 (r. 85/09)

CRYSTALLOGRAPHIC AND BAND STRUCTURE PROPERTIES

OF SOME I-III-VI_2 CHALCOPYRITE COMPOUNDS AND ALLOYS

by

Kajornyod YOODEE

Submitted to the School of Graduate Studies

in partial fulfillment of the requirements

for the degree of Ph. D. in Physics

University of Ottawa

Department of Physics

Ottawa, Canada

1985

UNIVERSITÉ D'OTTAWA
UNIVERSITY OF OTTAWA

ACKNOWLEDGMENTS

The author would like to express his sincere gratitude to his supervisor, Professor John C. Woolley for his invaluable guidance and inspiration during the course of his study in the department. He would also like to thank Professor Woolley for the opportunity to work with him and for his guidance, always available, in the preparation of this thesis.

The author wishes to express his sincere gratitude to his supervisor, Professor Virulh Sa-yakanit of Chulalongkorn University for suggesting and making possible graduate work at the University of Ottawa and for his invaluable assistance guidance and inspiration during the theoretical work.

He would like to acknowledge the helpful discussion received from Professor Augustin K. S. Song and Professor Béla Joos during this work.

He wishes to thank his colleagues, Ass. Professor Somphong Chatraphorn for suggestions for the optical work and Dr. Wichit Sritrakool for helping with the use of the computing facility at this university at the beginning of his study.

He also wishes to express his sincere thanks to Dr. Miguel Quintero, who is a friend and a class mate, for his friendship and valuable discussions, Mr. Steve Hernadi for his friendship and his invaluable help with the use of computing facilities at Carleton University and Miss Julie E. Avon for her friendship and discussions. The help received from Mr. D.J. Singh on the use of the computing facility at University of Ottawa is highly appreciated.

The technical assistance from the workshop staff of the Physics Department is deeply appreciated.

He wishes to thank all friends, and all colleagues at Chulalongkorn University for their encouragement. Chulalongkorn University is acknowledged for allowing him a leave of absence for his study.

The Canadian International Development Agency is gratefully acknowledged for providing him full financial support under the Institutional Link in Semiconductors between Physics Departments of Chulalongkorn University in Thailand and of University of Ottawa in Canada.

Special thanks go to Professor Henry R. Glyde and Professor Virulh Sa-yakanit who found him the financial support mentioned above and to Professor John C. Woolley for the financial support from his NSERC grant during the last part of the program.

He wishes to pay special tribute to his parents and his sister who supported him in his early education.

His gratitude goes to a very special person, his wife Shirley, for her patience and understanding. He wishes to say, he would not have made it without her loving support. To her he dedicates this work.

Finally, he wishes to thank Miss Sunee Lertsukitwatana, who really did an excellent job in preparing this manuscript by using the TEXsystem at Carleton University.

ABSTRACT

The thesis gives details of part of a joint general program of research to determine equilibrium conditions in and to investigate the properties of the alloy system $(Cu_{1-x}Ag_x)(Ga_{1-y}In_y)(Se_{1-z}Te_z)_2$. Polycrystalline samples were prepared, Debye-Scherrer x-ray powder photographs were used to investigate the equilibrium conditions and miscibility gaps were determined. Values of lattice parameters a and c were determined for all samples showing single phase condition and for each of the above sections, the variations of a and c with composition were fitted to appropriate power series and contours of constant a and constant c were determined.

The theory of the conservation of tetrahedral bonds (CTB) [84J1] was used to predict the lattice parameter a and the tetragonal deformation η (=c/2a) and then to compare these with the experimental values. The observed values of tetragonal distortion τ (=2-c/a) were also fitted to the parabolic equation in the electronegativity values defined in terms of the hybridized atomic orbital (HAO) radii of the elemental atoms using the nonempirical density functional orbital radii of Zunger [80Z1]

Optical energy gap values (E_g) were determined for the alloys of the Cu- and In-sections by optical absorption measurements. Photoacoustic (PA) measurements also were used to give approximate values of energy gap of powdered samples. E_g were fitted to appropriate power series and contours of constant E_g determined.

A model was developed for I-III-VI_2 chalcopyrite materials by adding the effects of $p-d$ hybridization and the crystal field to the Kane model. Two important parameters are the energy separation E between p and d levels and the interaction matrix element, M, between these levels. It was shown that three previous models are special cases of the present model. The model was used to analyze the available

band-gap data on some 13 I-III-VI_2 compounds. It was found that the dimensionless parameters M/E and $\Delta E_g/E$, where ΔE_g is the band gap anomaly, show a smooth variation with the appropriate fractional d character of the valence-band and appear to be characteristic of the structure. Values of the deformation potentials b_p and b_d of $p-$ and $d-$bands, respectively, averaged over all the compounds were determined and found to be $b_p = (-0.8 \pm 0.2)$ eV and $b_d = (-3.9 \pm 1.5)$ eV.

These values of b_p and b_d were used in the analysis of the data for the temperature variation of the valence-bands splittings of the $CuGa(S_{1-x}Se_x)_2$ system and of some chalcopyrite compounds. These data were explained in terms of temperature dependence of the $p-d$ hybridization effect and of the crystal-field interaction, the latter being due to the temperature variation of the tetragonal distortion. The results obtained were consistent with those from x-ray measurements of tetragonal distortion as a function of temperature. The variation of M/E and fractional d character with both temperature and composition were considered in some detail.

STATEMENT OF ORIGINALITY

The author is responsible for the following work which, to the best of the author's knowledge, has not previously been carried out :

1) Measurements of lattice parameters **a** and **c** for the copper section (x=0).

2) Analysis of lattice parameter data of the Cu-section from 1) and the data of the other sections determined by J.E. Avon [84A1] in terms of power series containing 9 parameters.

3) Contours of constant **a** and **c** for the alloys of the faces determined from 2)

4) General expression of **a** and **c** in terms of power series containing 26 parameters for the general alloy system.

5) Predicting the values of the lattice parameter **a** and the tetragonal deformation η for all of the alloys using the CTB theory [84J1].

6) Correlating the observed values of tetragonal distortion r for all of the alloys with the differences in bond electronegativities (ΔX_{CH}) using the method proposed by Shaukat and Hussian [85S1].

7) Optical absorption measurements made on the alloys of the Cu-section.

8) Analysis of the energy gaps values E_g in terms of power series containing 9 parameters for the alloys of the Cu-section from 7) and of the In-section from Ref. [84A1].

9) Contours of constants E_g for the alloys of the Cu-section and In-section.

10) Photoacoustic measurements made on some of the alloys of the faces.

11) Developing the theoretical model of the effects of $p-d$ hybridization on the uppermost valence bands of the I-III-VI_2 chalcopyrite semiconductors and applying the model to the available data of some 13 chalcopyrite compounds.

12) Analysis of the data of the temperature dependence of the valence-band splittings for the system $CuGa(S_{1-z}Se_z)_2$, obtained by M. Quintero [85Q1], and the compound for $AgGaSe_2$ and $AgGaTe_2$ from Ref. [75S1] and $CuGaSnSe_4$ from Ref. [82L1].

TABLE OF CONTENTS

LIST OF TABLES

LIST OF FIGURES

Chapter 1

Introduction

1.1 General Introduction

The I-III-VI_2 and II-IV-V_2 compounds are ternary semiconductors which normally crystallize in a chalcopyrite (CH) structure. It is a superlattice of the cubic zincblende (ZB) structure. The CH structure may be obtained from the ZB structure by ordering the two cations on the cation sublattice. As a result, the symmetry of the structure is lowered and it is no longer cubic but tetragonal with the lattice parameters ratio c/a equal to, or for most cases, slightly less than 2. Thus the I-III-VI_2 and II-IV-V_2 compounds are ternary analogs of the well-understood ZB II-VI and III-V binary compounds, respectively.

The work on ternary CH compounds was earlier directed towards the production of thermoelectric devices. Presently, these compounds are of technological interest because they show promise for application in the areas of light emitting diodes, optical detectors, photovoltaic solar cell, etc. Because of the noncubic crystal structure, these compound are optically birefringent, and therefore they are applicable for nonlinear optical devices.

Since the CH compound is the simplest ternary analog of the ZB binary compound, their energy band structures are similar but that of the ternary compound differs from that of the binary compound in several nontrivial ways because of the noncubic structure of the former. The uppermost valence bands

are split and forbidden electronic transitions become allowed, etc. The method of folding the energy band of the binary analog into a zone center in order to allow for the reduced size of the Brillouin zone has proved successful in identifying the main features of the energy band of the ternary CH compound. In addition however, whereas the uppermost valence bands of most ZB compounds are composed of s- and p- orbitals only, the noble-metal d levels in the I-III-VI_2 compounds hybridize with these s- and p- orbitals, and lead to several anomalous effects in the energy band structure.

It is found that the 36 known ternary compounds exhibit diverse physical and chemical properties. These have been discussed in a number of review articles [75S2, 79P1, 81M1] and conference proceedings [75C1, 77H1, 80C1, 82C1, 84C1]. The compounds offer a wide range of the energy gap values throughout the infrared and visible spectrum . However in device application, e.g., heterojunction photovoltaic solar cell [74W1, 80T1] specific energy gap values are required with a good lattice and crystallographic match between any epilayer and a substrate. These are often unobtainable from the compounds. In the case of work with III-V compounds, a similar problem was overcome by producing alloy systems such as $(In_{1-x}Ga_x)(P_{1-y}As_y)$ (e.g., [74M1], [76C1], [78N1]), i.e., alloy systems in which there is more than one composition variable.

The problem of achieving a lattice parameter match at the same time as allowing a tailoring of the band gap to a required value indicates the need for studies of alloy systems of these ternary compounds involving at least two composition variables. Previously information regarding the phase relationship in several mixed I-III-VI_2 with one composition variable had been reported by Robbins et al [73R1, 73R2]. Single phase solid solution was found throughout the composition range in the $Cu_{1-x}Ag_xInS_2$ and $Cu_{1-x}Ag_xInSe_2$ systems and in the $AB(S_{1-x}Se_x)_2$ systems, where A=Cu or Ag, and B=Al, Ga or

In. However, only limited solid solubility was found for the $Cu_{1-x}Ag_xBC_2$ systems, where B=Al or Ga, and C=S or Se, with miscibility gaps occuring at interior compositions. Yamamoto and Miyauchi [72Y1] also showed that single phase solid solution exists in the $CuGa_{1-y}In_yS_2$ system. Until recently very little work has been carried out on alloys with two composition variables for these compounds. Chapman et al [79C1] have studied in some detail the crystallographic properties and energy gap values of the $(Cu_{1-x}Ag_x)In(S_{1-z}Se_z)_2$ alloys. Investigations in this area were made as an initial part of the present program for $(Cu_{1-x}Ag_x)(Ga_{1-y}In_y)Te_2$ alloys [81A1] and just recently by Quintero and Woolley [84Q1] for $CuIn(S_xSe_yTe_z)_2$ alloys, where $x + y + z = 1$.

1.2 System Investigated in this Program

The work described here is part a group program and it is necessary at times to describe the results of other members of the group to give a proper picture of the work. At each point in the thesis where this is done, reference will be made to the other workers.

The general alloy system $(Cu_{1-x}Ag_x)(Ga_{1-y}In_y)(Se_{1-z}Te_z)_2$ was studied in collaboration with Julie E. Avon at the University of Ottawa. Polycrystalline alloys were used to investigated the range of solid solution and to determine lattice parameter values for the alloys. Room temperature energy gap value (E_g) for all single phase samples of the Cu-section (x=0) and of the In-section (y=1) were measured using the optical absorption and photoacoustic methods. The author obtained the experimental data for the alloys of the Cu-section (x=0), the photoacoustic energy gaps for the alloys of the faces, and carried out all of the fitting analysis to the lattice parameter and energy gap data.

A more detailed investigation of the valence band structure of the pseudobinary section

$CuGa(S_{1-z}Se_z)_2$ and of other CH compounds by members of the Ottawa research group and other workers showed that a theoretical study of the effects of p-d hybridization on the uppermost valence bands of I-III-VI_2 compounds was needed. A model was proposed and developed and was used by the author to analyse the available data for some 13 ternary CH compounds.

The work on the alloys of the system $CuGa(S_{1-z}Se_z)_2$ was carried out in collaboration with Miguel Quintero. Single crystals of these alloys were grown by Miguel Quintero and Jesus Gonzales. Measurements of the three energy gaps (E_A,E_B,E_C) as a function of alloy composition and temperature were performed by Miguel Quintero. The analysis of these data using the p-d hybridization model was then made by the author.

This thesis can be divided into two parts : (1) experimental part, (2) theoretical development and analysis. An introduction with review of relevant work, a description of the present work and a summary are given in each chapter.

The first part is dealt with in Chapter 2 and 3 which present the preparation of the samples, determination of their lattice parameters, and measurements of their energy gaps. Contours of constant lattice parameter and energygap are also given. Chapter 4 and 5 form the second part of the thesis. The model giving the effects of p-d hybridization on the valence bands of I-III-VI_2 compounds is proposed and developed and is then used to analyse the available data for some 13 compounds in Chapter 4. The analysis of the three transition energies between the valence bands and conduction band as a function of temperature and composition for the $CuGa(S_{1-z}Se_z)_2$ alloy system is made in the last chapter.

The model gives a clear picture of how the p-d hybridization affects the uppermost valence bands of I-III-VI_2 compounds. It has two important parameters, the energy separation E between the p- and

d- levels and the interaction M between these levels. The analysis also enables the mean values of the deformation potentails b_p and b_d of the p- and d- bands, respectively, to be determined over the range of the compounds considered. The values of b_p and b_d so obtained are very useful and are needed in the analysis of the variation of energy gap with both composition and temperature for $CuGa(S_{1-x}Se_x)_2$.

Chapter 2

Sample Preparation and Crystallographic Work

2.1 Overview

In this chapter, the crystallographic properties of alloys of the system $(Cu_{1-x}Ag_x)(Ga_{1-y}In_y)(Se_{1-z}Te_z)_2$ are discussed. The CH structure will be described and compared with the isoelectronic ZB structure, in terms of the CH crystal structure parameters, i.e., lattice parameters a and c, tetragonal distortion $\tau = 2 - c/a$ or tetragonal deformation $\eta = c/2a$, and anion position parameter u. The study of these parameters also will be briefly reviewed in the next section.

The melt and anneal techniques which were used to prepare the alloy samples will be presented in Section 2.3. The Debye - Scherrer x-ray powder method was used to determine the equilibrium condition of the alloys and provided x-ray photographs allowing the lattice parameter a and c to be determined in Section 2.4. In Section 2.5 results and analysis will be given and contours of constant a and c obtained from the power series equations in Section 2.6. A general series expression for a and c will be discussed in Section 2.6.

The last two sections will consider the predictions of a and η using the conservation of tetrahedral bonds (CTB) theory proposed by Jaffe and Zunger [84 J1] and the correlation between τ and the difference in electronegativity between the $A - C$ and $B - C$ bonds in a CH crystal (ΔX_{CH}). The latter is similar to that of the ternary compound study proposed by Shaukat and Hussain [85S1].

2.2 Crystal Structure of $A^{I}\ B^{III}\ C_2^{VI}$ Chalcopyrite Semiconductors

The I-III-VI_2 ternary compounds are tetrahedrally coordinated semiconductors which crystallize in the uniaxial CH structure. They are the simplest structural analogs of II-VI ZB compound. Therefore the crystal structure of these two types of materials can be expected to be very similar.

The ZB structure, which has the space group symmetry T_d^2 (or $F\bar{4}3m$) containing 24 symmetry operations, consists of two interpenetrating face centered cubic lattices. The two sublattices are displaced by one quarter of a body diagonal and each consists entirely of one type of atom and these may be considered as a cation and an anion sublattice. Hence, each atom is tetrahedrally surrounded by four atoms of the other type (see Fig. 2.1(a)).

In each I-III-VI_2 compound, the anion sublattice is occupied by the VI-atoms, while the cation sublattice is shared by the I- and III-atoms. If the I- and III-atoms are randomly distributed in the sublattice, the structure of the compound remains ZB. However, if they are ordered as shown in Fig. 2.1(b), the structure of the compound is CH. It shows the space group symmetry D_{2d}^{12} (or $I\bar{4}2d$) containing 8 symmetry operations. The symmetry is decreased from T_d^2 to D_{2d}^{12}, D_{2d}^{12} being a subgroup of T_d^2.

Hence each cation I and III in the I-III-VI_2 compound has four VI anions as nearest neighbours, and each anion has two I and two III cations as nearest neighbours. It is also apparent [75S2] that although the atomic site positions are virtually the same as for the ZB structure, there are three additional noncubic aspects of CH structure, i.e.,

1) a doubling of the unit cell in the z-direction resulting from an ordering of the two cations (a cationic asymmetry),

2) a compression of the crystal lattice along the z-axis which is indicated by a tetragonal distortion

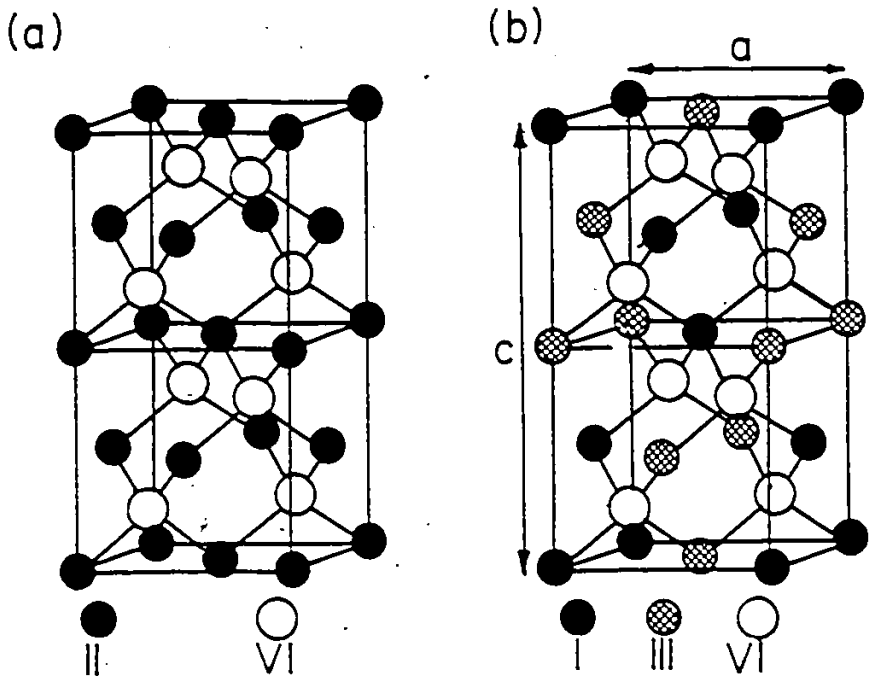

Fig. 2.1 Crystal structure of (a) zincblende and (b) chalcopyrite lattices [S4J1].

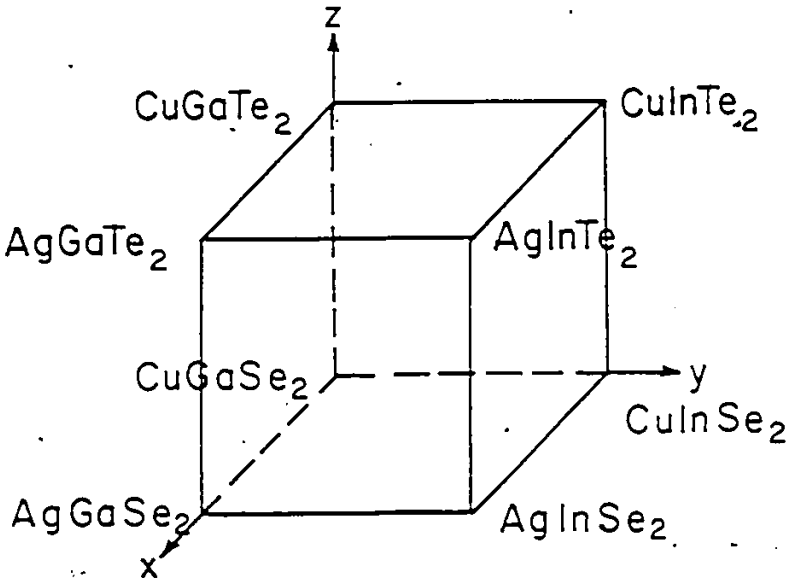

Fig. 2.2 The representation cube for the $(Cu_{1-x}Ag_x)(Ga_{1-y}In_y)(Se_{1-z}Te_z)_2$ system.

$\tau = 2 - c/a$ or a tetragonal deformation $\eta = c/2a$ (a tetragonal compression),

3) distortion of the anion sites away from the cubic $(\frac{1}{4}, \frac{1}{4}, \frac{1}{4})$ to the tetragonal $(u, \frac{1}{4}, \frac{1}{8})$ position and symmetrically related positions (an anionic displacement) which is caused by the unequal bond lengths R_{I-VI} and R_{III-VI} between I & VI and III & VI ions, respectively.

These nearest-neigbour anion-cation bond lengths are related to the other parameters by [S4J1]

$$R_{I-VI} = \left[u^2 + \frac{(1+\eta^2)}{16}\right]^{\frac{1}{2}} a \quad , \qquad (2-1)$$

and

$$R_{III-VI} = \left[(u-\frac{1}{2})^2 + \frac{(1+\eta^2)}{16}\right]^{\frac{1}{2}} a \quad . \qquad (2-2)$$

The tetragonal distortion parameters seem to have been the interesting subject over the past ten years for CH compounds. There have been many attemps to relate the observed tetragonal distortion to parameters characteristic of the constituent elements or bonds, such as covalent radii and electronegativity values. The tetragonal distortions have also been analysed in terms of the interactions present in the crystal lattice.

Phillips [74P1] has shown that the tetragonal distortion of II-IV-V_2 compounds is determined by charge redistribution and it can be linearly expressed in terms of the electronegativities X_{II}, X_{IV}, and X_V as

$$\tau = -0.60X_{II} + 0.25X_{IV} + 0.15X_V + 0.01 \quad . \qquad (2-3)$$

This equation gives good qualitative agreement between the observed values of $\tau \lesssim 0.05$, but for larger values of τ it under-estimates the observed distortions.

Noolandi [74N1] developed the valence-force-field model for the tetragonal distortion of both

I-III-VI_2 and II-IV-V_2 compounds (ABC_2). It has been found that for a given A atom, the tetragonal distortion obeys the relation

$$\tau \propto (X_A - X_B)^2 \quad , \qquad (2-4)$$

rather accurately [75W1]. To produce a good fit to observed values of tetragonal distortion Noolandi's formula is expressed as

$$\tau = \alpha R_A^{\beta} R_C^{\gamma} (X_A - X_B)^2 \quad , \qquad (2-5)$$

where R_A and R_C are tetrahedral radii. The different values of β and γ obtained for the I-III-VI_2 and II-IV-V_2 families suggested that this part of the formula may not be meaningful.

Chelikowsky and Phillips [78C1] later developed the correlation between the observed values of τ and a suitable function of the bond orbital radii of the constituent atoms. The orbital radii were defined as the crossing point of the Pauli-force model potential by St. John and Bloch [74S1]. A good fit could be established for all of the II-IV-V_2 compounds (except Cd Sn P_2 and Cd Sn As_2) but not for the I-III-VI_2 compounds.

A similar approach was made by Shaukat and Singh [78S1] in the case of I-III-VI_2 compounds. They, however, had to define a different set of orbital radii using the same model potential as developed by Simon and Bloch [73S1]. They separately expressed τ for Cu- compounds and Ag- compounds as parabolic function of the difference in bond electronegativities (ΔX_{CH}) defined through these bond orbital radii. Jaffe and Zunger [84J1], however, suggested that these correlations, both for I-III-VI_2 and II-IV-V_2 compounds, can be improved using instead nonempirical density functional orbital radii [80Z1]. They were defined as the crossing points of the ground-state screened atomic pseudopotentials, i.e., $V_{eff}^{(l)}(r) = 0$.

Recently, using the same method as Shaukat and Singh [78S1] and the density functional orbital

radii. Shaukat and Hussian [85S1] showed that the observed values of r could be well expressed in a parabolic function of ΔX_{CH} separately for Cu- compounds, Ag- compounds and II-IV-V_2 compounds.

However, there has been much less study of the anion position parameters u and the lattice parameter a. The first investigation of the anion parameter was made by Abrahams and Berstein [71A1]. They discovered from x-ray analysis that despite the nonzero value of η for the II-IV-V_2 compounds, the C atoms form a nearly tetrahedron around each B atom in these chalcopyrites. Under this condition, u and η are related by

$$u = \frac{1}{2} - \frac{1}{4}[2\eta^2 - 1]^{\frac{1}{2}} \quad . \qquad (2-6)$$

They then used the experimental values of η to predict u. It was found that the equation gave good agreement for the II-IV-V_2 compounds, except for cases of II-Sn-V_2, but not for most of the I-III-VI_2 compounds [73 A1]. The relation was improved by fitting the deviation from the experimental values to a linear combination of eletronegativities of the constituent atoms similar to those of Eq.(2-3). The fitted numerical coefficients obtained were different for the I-III-VI_2 and for the II-IV-V_2 compounds [73A1, 74A1].

De Gil [82D1] derived an interrelation between all of the structural parameters of the ABC_2 semiconductors with CH structure. On the basis of this, the existence of the CH structure was predicted and the limits of existence related to the values of R_{BC} / R_{AC} and c/a.

Bhar and Samanta [82B1] analyzed the temperature variation of the tetragonal distortion r which had been proposed by Weaire and Noolandi [75W1] and by Brühl et al [80B1]. They suggested the relation

$$\frac{dr}{dT} = Ar \quad . \qquad (2-7)$$

where A is a constant. They also showed that the temperature coefficients of the two noncubic parameters τ and u of the CH compounds were linearly related.

More recently, Jaffe and Zunger [84J1] applied the ideas of the semiclassical model of conservation of tetrahedral bonds (CTB) [20B1] to derive the equations for determining the values of lattice parameter a, tetragonal deformation η and anion position parameter u in ternary ABC_2 CH semiconductors. These parameters can be predicted solely from elemental tetrahedral radii without the use of the data from the ternaries by assuming that the cation-anion distance R_{ij} is equal to the sum of elemental radii $r_i + r_j$. Thus the structural parameters a, η and u will freely adjust their values so as to minimize simultaneously for each of the $A-C$ and $B-C$ bonds, the difference between the actual anion-cation bond length (R_{AC} or R_{BC}) and the sum of the elemental radii ($r_A + r_C$ or $r_B + r_C$), i.e.,

$$\begin{aligned} R_{AC}(a,\eta,u) - (r_A + r_C) &= 0 \quad , \\ R_{BC}(a,\eta,u) - (r_B + r_C) &= 0 \quad . \end{aligned} \tag{2-8}$$

Using Eqs.(2-1) and (2-2) for R_{AC} and R_{BC} and Eq.(2-6) for u, the solutions of Eq.(2-8) will provide expressions for a,η, and u in terms of the elemental radii r_A, r_B and r_C only. The resulting correlation between the observed and calculated values of a and u is very good. However, the expression for η is not well suited for predicting experimental values, which are probably determined by longer-range electrostatic forces. The correlation between the observed and calculated values for η would be improved by using the effective electronegativity scales of Shaukat and Hussian [85S1] discussed above.

The CTB theory has also been used by Jaffe and Zunger [83J1] in an attempt to correlate the calculated and experimental values of the lattice parameters a of the $CuIn(S_{1-x}Se_x)_2$ alloys [79C1] and by Chatraphorn et al [85C1] to compare the theoretical prediction with the observed values a,η and u

of the $AgGa(Se_{1-x}Te_x)_2$ alloys. In these applications the effective radii of the anions were taken as the weighted mean of the elemental values. It was found that in the former case the variation in $a_{cal}(Z)$ was within $\leq 0.1\%$ of the observed variation. For the latter case, the values predicted for a and u using the Phillips radii were in good agreement with the observed values but for η the correlation was not as good as those for a and u.

The same method will be applied to the alloy system $(Cu_{1-x}Ag_x)(Ga_{1-y}In_y)(Se_{1-z}Te_z)_2$ in Section 2.7. The method proposed by Binsma et al will be also used to correlate the observed values of r with the differences in bond electronegativities (ΔX_{CH}) in Section 2.8.

2.3 Sample Preparation

All of the alloys used were prepared from the elements by the standard melt and anneal technique. Appropriate amounts of the elements were weighted out and sealed in an evacuated quartz ampoule at a pressure of approximate 10^{-5} torr. All the elements used were at least 99.99% pure. The components of each 1-gram sample were slowly heated (30 – 50° c per hour) up to 1100 °c and left at that temperature for 4-6 hours. They were then slowly cooled (10 – 20°c per hour) down to approximately 600 – 800°c and annealed at these temperatures. The choice of annealing temperature was guided by the melting point values of ternary compounds [75S2]. X-ray powder photographs were used to determine whether equilibrium had been obtained and to indicate the equilibrium condition of the alloys, the criterion being resolution of the $K\alpha_1, K\alpha_2$ doublet. If the x-ray diffraction patterns revealed the presence of nonequilibrium state, the samples were annealed further. It was found that for most alloys, annealing times of 2-3 months were necessary for reasonable equilibrium conditions to be obtained.

2.4 X-ray Diffraction Determination of Lattice Parameters

When the samples were in equilibrium, a final powder photograph was taken using the Debye-Scherrer method. The 114.6 mm diameter cameras were used with $Cu - K\alpha$ radiation. Each specimen to be measured was ground into fine powder and applied on a glas fibre sample holder using, as an adhesive, a grease known to give little absorption. The internal calibration method for correcting the effect of x-rays absorption was used by intimately mixing with the sample a fine powder of silicon for which the lattice parameter is accurately known. After the exposure, the position of the diffracted lines on the film were measured using a travelling microscope which has an accuracy of 0.01 mm and the corresponding Bragg angles, θ, were determined. They were corrected using the values of $\Delta sin^2\,\theta$ from the graph plotted between the values of $\Delta sin^2\theta_{Si}$ against the measured values of $sin^2\theta_{Si}$, $\Delta sin^2\theta_{Si}$ being the difference between the calculated and measured values of $sin^2\theta_{Si}$ of the silicon lines.

The Bragg angles of the diffracted lines of the samples having been corrected, the Miller indices involved for each line had to be determined . The indexing of the lines was clear for low angle reflections. The data of these lines only were used to determined lattice parameters a and c by a least squares fitting to the Bragg equation for CH structure,

$$sin^2\theta = \frac{\lambda^2}{4}\left(\frac{h^2+k^2}{a^2} + \frac{l_{CH}^2}{c^2}\right) \quad . \qquad (2-9)$$

where λ being the x-rays wavelength, h, k and l_{CH} Miller indices. The values of a and c determined in this manner were then used to establish the indices of the higher angle of reflections which are more sensitive to the values of a and c. Once all diffraction lines were indexed, a and c in Eq.(2-9) were recalculated using all of the diffraction lines.

This analysis of the x-ray photographs was approached by directly relating the CH structure of the

alloys to the well understood, cubic ZB structure. As can be seen from Figs. 2.1(a) and 2.1(b), the same atomic sites are occupied in both structures, but due to ordering of the cations along the z-axis, the lattice parameter c is doubled in the CH case. This in turn doubles the Miller index l_{ZB} and the Bragg equation is no longer given by

$$sin^2\theta = \frac{\lambda^2}{4}\left(\frac{h^2+k^2+l_{ZB}^2}{a^2}\right) \qquad (2-10)$$

as in the ZB case, but by Eq.(2-9) for the tetragonal lattice. In addition, it is known from the structure factor equation for the ZB case that only reflections satisfying the conditions $h+k+l_{ZB} = 4n, 4n+2, 2n+1, n$ being integers, will occur. These conditions give strong lines for $N = h^2+k^2+l_{ZB}^2 = 3, 8, 11, 16, 19, 24$,etc and weak lines for $N = 4, 12, 20$,etc. Thus, these reflections will also occur in the CH case, with $l_{CH} = 2l_{ZB}$. Possible combinations of the values of h, k, l are listed in Table 2.1 for the ZB and CH structures. Consider now, for example, reflections for which N=8. If c=2a, the CH 220 and 204 diffraction lines will occur at exactly the same angle, θ. However, if there is compression of the lattice, i.e. $c < 2a$, the 220 and 204 lines will split showing two diffraction lines rather than only one as in the case $c = 2a$.

It would be possible with care to determine the position of the center of a diffracted line to 0.1 mm (accuracy of a travelling microscope = 0.01mm). This corresponds to an angular accuracy of 0.1° or a fractional change in d-spacing of 0.0002 at Bragg angle $\theta = 85°$. The good resolution obtained in the high-angle region of a powder photograph enables very accurate values of lattice parameters to be obtained. When the alloy sample reached a condition very close to equilibrium the diffracted lines on the film were so clear and sharp that the $K\alpha_1$ $K\alpha_2$ doublet could be easily seen. The observed distances between the lines of the doublet, which has the difference in wavelength of about 0.0038 A°, are

Table 2.1 Possible combination of h,k,l for zinc blende and chalcopyrite structures.

N	hkl	
	zinc blende	chalcopyrite
3	111	112
4	200	200
		004
8	220	220
		204
11	311	312
		116
12	222	224
16	400	400
		008
19	331	332
		316
20	420	420
		404
		208
24	422	424
		228
27	511	512
	333	336
		1110
32	440	440
		408
35	531	532
		516
		3110
36	600	600
		0012
40	620	620
		604
		2012
43	533	536
		3310
		101
		103
		105
		130
		202
		211
		213
		301
		323
		325
		402
		413

approximately 1 mm at $\theta \approx 70°$. Preliminary photographs indicated that annealing time of 2-3 months were necessary for reasonable equilibrium conditions to be obtained. In some cases, however, annealing time of up to 5 months were required before equilibrium condition were attained.

2.5 Results and Discussion

The alloy system $(Cu_{1-x}Ag_x)(Ga_{1-y}In_y)(Se_{1-z}Te_z)_2$ can be conveniently represented by a representation cube as shown in Fig. 2.2 (see page 8) with a ternary compound at each corner of the representation cube. The crystallographic properties of the alloys of the $(Cu_{1-x}Ag_x)(Ga_{1-y}In_y)Te_2$ section or z=1 face, were studied previously and the contours of constant lattice parameter a and c as a function of composition obtained [SLA1]. The five other faces of the cube represent convenient sections for investigation and these can be labelled the copper face (x=0), the indium face (y=1), etc. This work was a group project and the author had the responsibility for the experimental data for the Cu face. The other experimental results quoted here was obtained by other members of the group, e.g., Julie Avon, etc. However, the majority of the analysis of the data was carried out by the author. Samples were prepared with values of x,y and z of 0, 0.25, 0.50, 0.75 and 1.0 giving a total of 125 different alloy compositions with 98 of these being on the surface of the cube. In all cases, chalcopyrite structure was obtained and lattice parameters determined. The values of a and c for each composition are summarized in Table 2.2 - 2.6. Each composition is conveniently identified by a six-digit number, the first two digits represent x, the next two y, and the last two z, as an atomic percentage. For the case of 100%, the digit 10 are used since no composition involving 10% was investigated in the present work.

In order to present the data graphically, various section of the cube need to be considered and it is

Table 2.2 $(Cu_{1-x}Ag_x)(Ga_{1-y}In_y)(Se_{1-z}Te_z)_2$ Lattice parameter values for alloys with $x = 0$.

Sample	a(nm)	c(nm)
000000	0.5619	1.1026
000025	0.5715	1.1232
000050	0.5813	1.1483
000075	0.5923	1.1709
000010	0.6025	1.1935
002500	0.5657	1.1181
002525	0.5759	1.1395
002550	0.5862	1.1626
002575	0.5957	1.1842
002510	0.6058	1.2068
005000	0.5697	1.1354
005025	0.5790	1.1595
005050	0.5900	1.1806
005075	0.5999	1.1984
005010	0.6098	1.2196
007500	0.5741	1.1483
007525	0.5841	1.1680
007550	0.5947	1.1893
007575	0.6052	1.2110
007510	0.6147	1.2295
001000	0.5794	1.1572
001025	0.5886	1.1767
001050	0.5964	1.1936
001075	0.6095	1.2186
001010	0.6201	1.2379

Table 2.3 $(Cu_{1-x}Ag_x)(Ga_{1-y}In_y)(Se_{1-z}Te_z)_2$ Lattice parameter values and multiphase samples (m) for alloys with $x = 0.25$ lying on the face of the representaiton cube.

Sample	a(nm)	c(nm)
250000	0.5695	1.1039
250025	0.5770	1.1218
250050	0.5865	1.1470
250075	0.5955	1.1705
250010	0.6081	1.1977
252500	0.5719	1.1187
252510	0.6119	1.2078
255000	m	m
255010	0.6169	1.2252
257500	m	m
257510	0.6196	1.2392
251000	0.5844	1.1690
251025	0.5918	1.1848
251050	0.6040	1.2082
251075	0.6145	1.2292
251010	0.6241	1.2468

Table 2.4 $(Cu_{1-x}Ag_x)(Ga_{1-y}In_y)(Se_{1-z}Te_z)_2$ Lattice parameter values and multiphase samples (m) for alloys with $x = 0.50$ lying on the face of the representation cube.

Sample	a(nm)	c(nm)
500000	m	m
500025	m	m
500050	m	m
500075	0.5955	1.1667
500010	0.6143	1.1996
502500	m	m
502510	0.6177	1.2129
505000	m	m
505010	0.6223	1.2309
507500	m	m
507510	0.6268	1.2440
501000	0.5919	1.1740
501025	0.6025	1.1935
501050	0.6087	1.2143
501075	0.6202	1.2402
501010	0.6309	1.2576

Table 2.5 $(Cu_{1-x}Ag_x)(Ga_{1-y}In_y)(Se_{1-z}Te_z)_2$ Lattice parameter values and multiphase samples (m) for alloys with $x = 0.75$ lying on the face of the representation cube.

Sample	a(nm)	c(nm)
750000	0.5880	1.0970
750025	m	m
750050	0.6021	1.1470
750075	0.6127	1.1726
750010	0.6218	1.1995
752500	0.5902	1.1143
752510	0.6265	1.2160
755000	0.5935	1.1356
755010	0.6296	1.2336
757500	0.5973	1.1545
757510	0.6335	1.2497
751000	0.6000	1.1745
751025	0.6100	1.1961
751050	0.6152	1.2124
751075	0.6259	1.2392
751010	0.6369	1.2641

Table 2.6 $(Cu_{1-x}Ag_x)(Ga_{1-y}In_y)(Se_{1-z}Te_z)_2$ Lattice parameter values and multiphase samples (m) for alloys with $x = 1.0$

Sample	a(nm)	c(nm)
100000	0.5971	1.0952
100025	0.6054	1.1083
100050	0.6135	1.1400
100075	0.6221	1.1685
100010	0.6325	1.1991
102500	0.6017	1.1091
102525	m	m
102550	m	m
102575	0.6241	1.1829
102510	0.6349	1.2157
105000	0.6042	1.1284
105025	m	m
105050	0.6186	1.1734
105075	0.6255	1.1990
105010	0.6388	1.2338
107500	0.6072	1.1500
107525	0.6145	1.1667
107550	0.6220	1.1974
107575	0.6288	1.2185
107510	0.6415	1.2477
101000	0.6103	1.1713
101025	0.6161	1.1878
101050	0.6220	1.2111
101075	0.6388	1.2339
101010	0.6452	1.2639

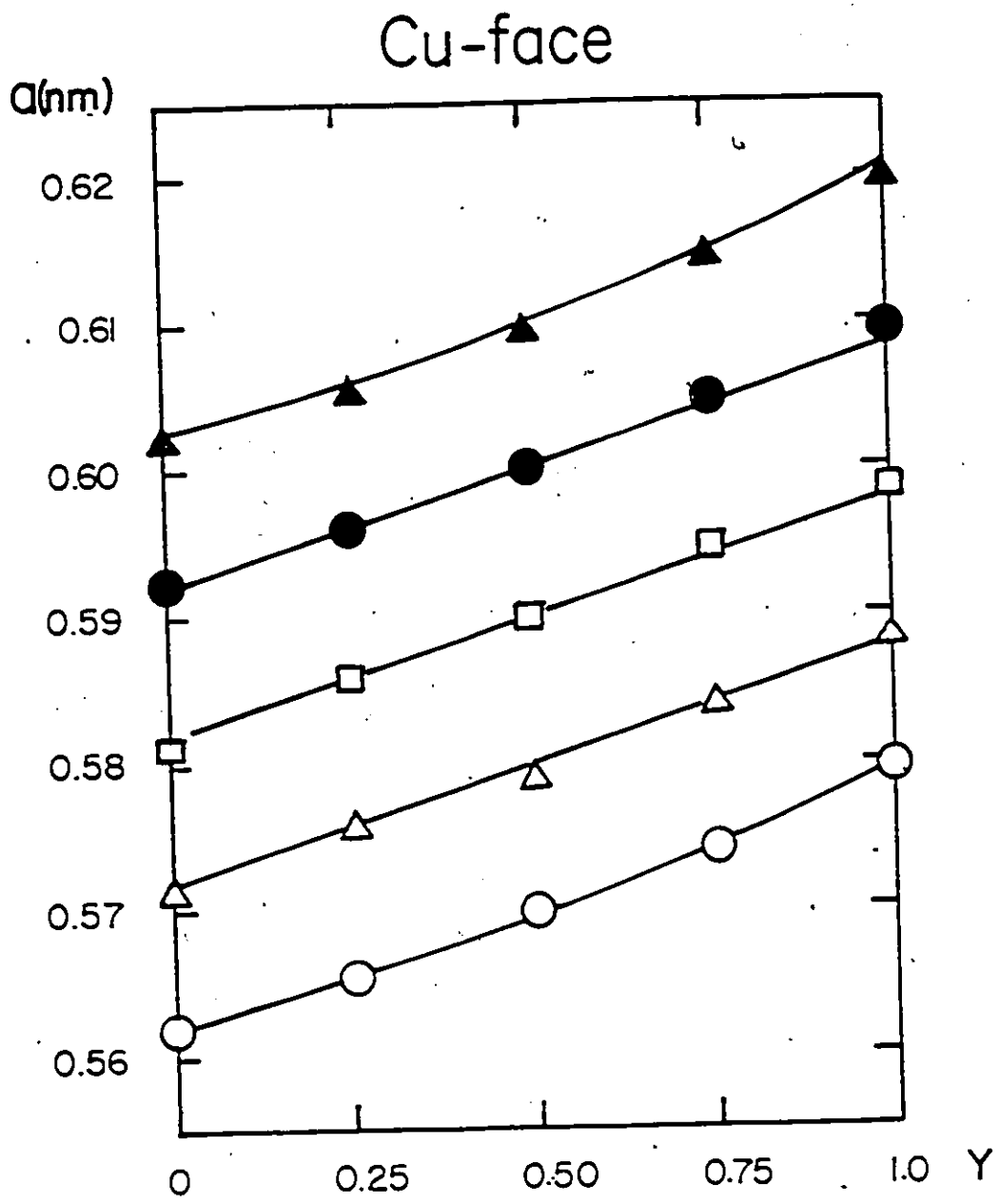

Fig. 2.3 $Cu(Ga_{1-y}In_y)(Se_{1-z}Te_z)_2$ section. Variation of lattice parameter a with y for lines of constant z.

○ : $z = 0$ △ : $z = 0.25$ □ : $z = 0.50$ ● : $z = 0.75$ ▲ : $z = 1.0$

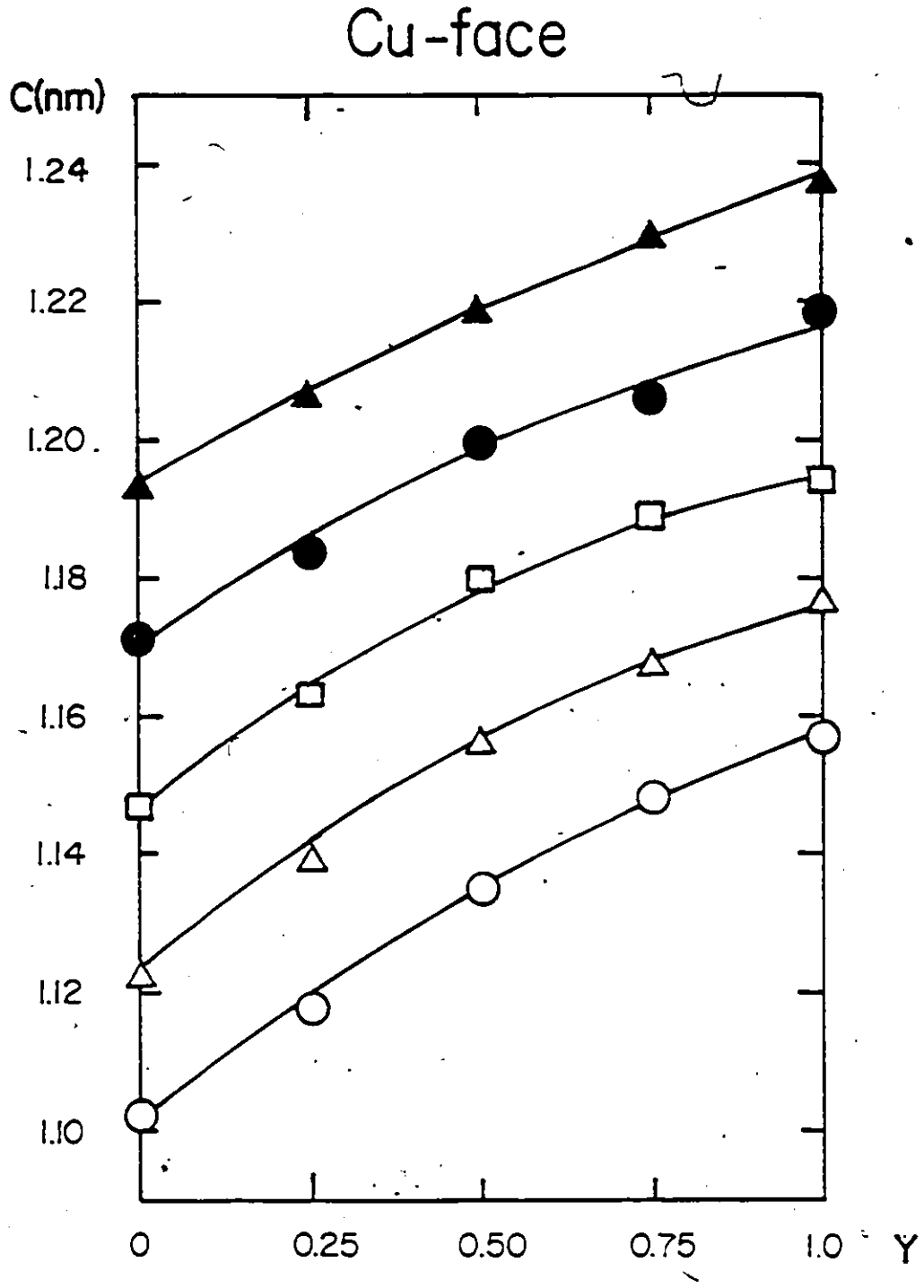

Fig. 2.4 $Cu(Ga_{1-y}In_y)(Se_{1-z}Te_z)_2$ section. Variation of lattice parameter c with y for lines of constant z.

○ : $z = 0$ △ : $z = 0.25$ □ : $z = 0.50$ ● : $z = 0.75$ ▲ : $z = 1.0$

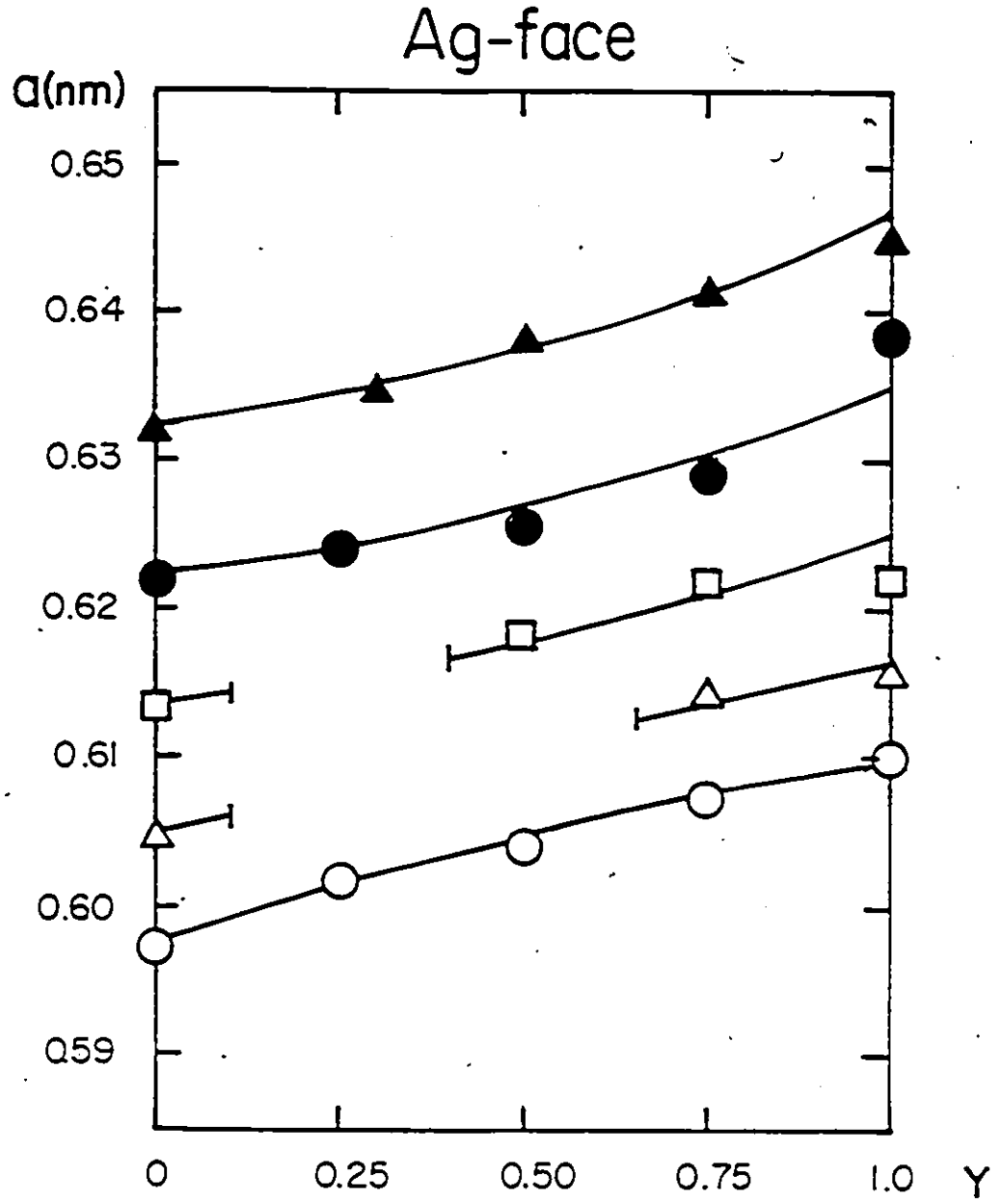

Fig. 2.5 $Ag(Ga_{1-y}In_y)(Se_{1-z}Te_z)_2$ section. Variation of lattice parameter a with y for lines of constant z.

○ : $z = 0$ △ : $z = 0.25$ □ : $z = 0.50$ ● : $z = 0.75$ ▲ : $z = 1.0$

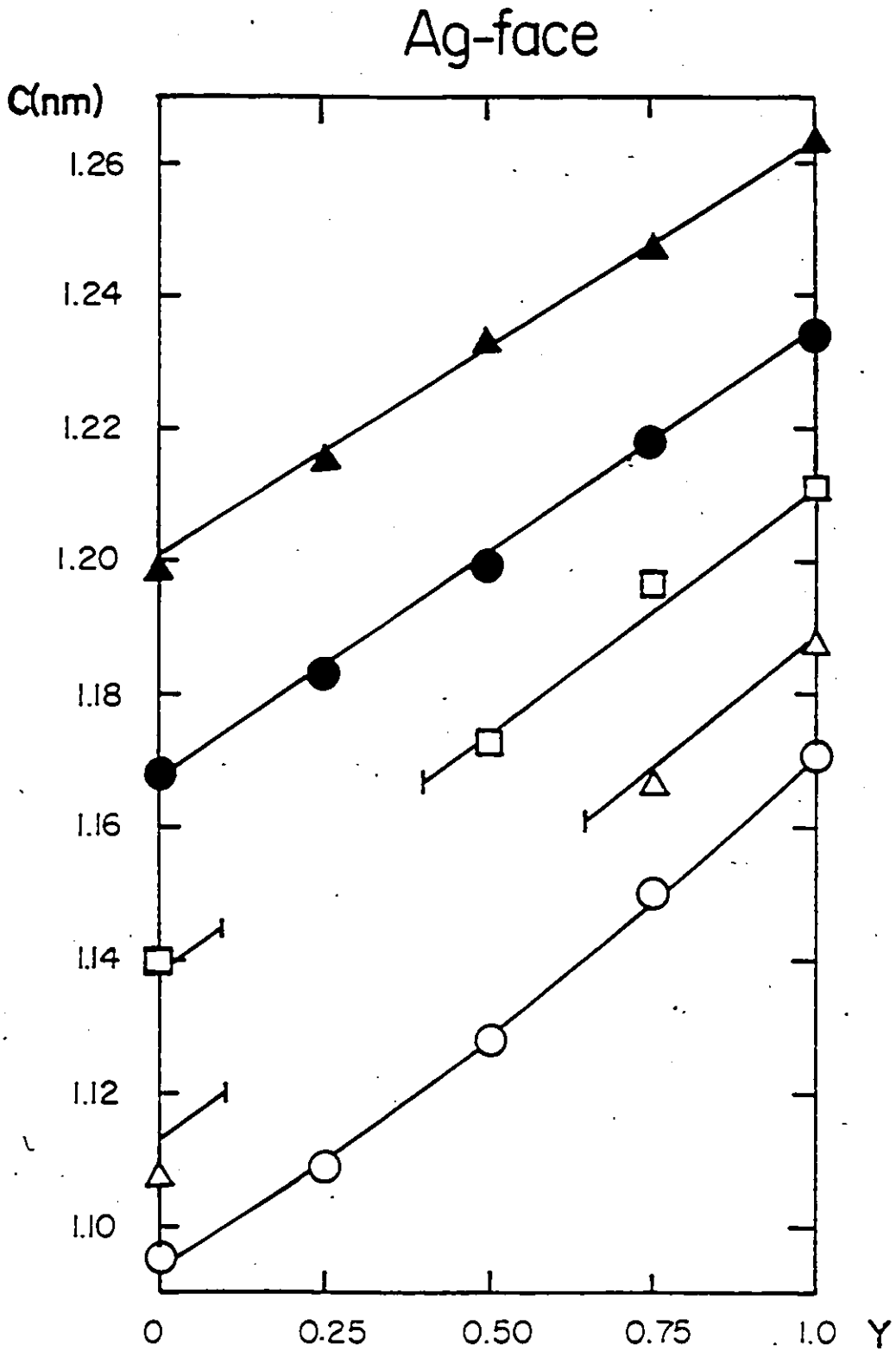

Fig. 2.6 $Ag(Ga_{1-y}In_y)(Se_{1-z}Te_z)_2$ section. Variation of lattice parameter c with y for lines of constant z.

○ : $z = 0$ △ : $z = 0.25$ □ : $z = 0.50$ ● : $z = 0.75$ ▲ : $z = 1.0$

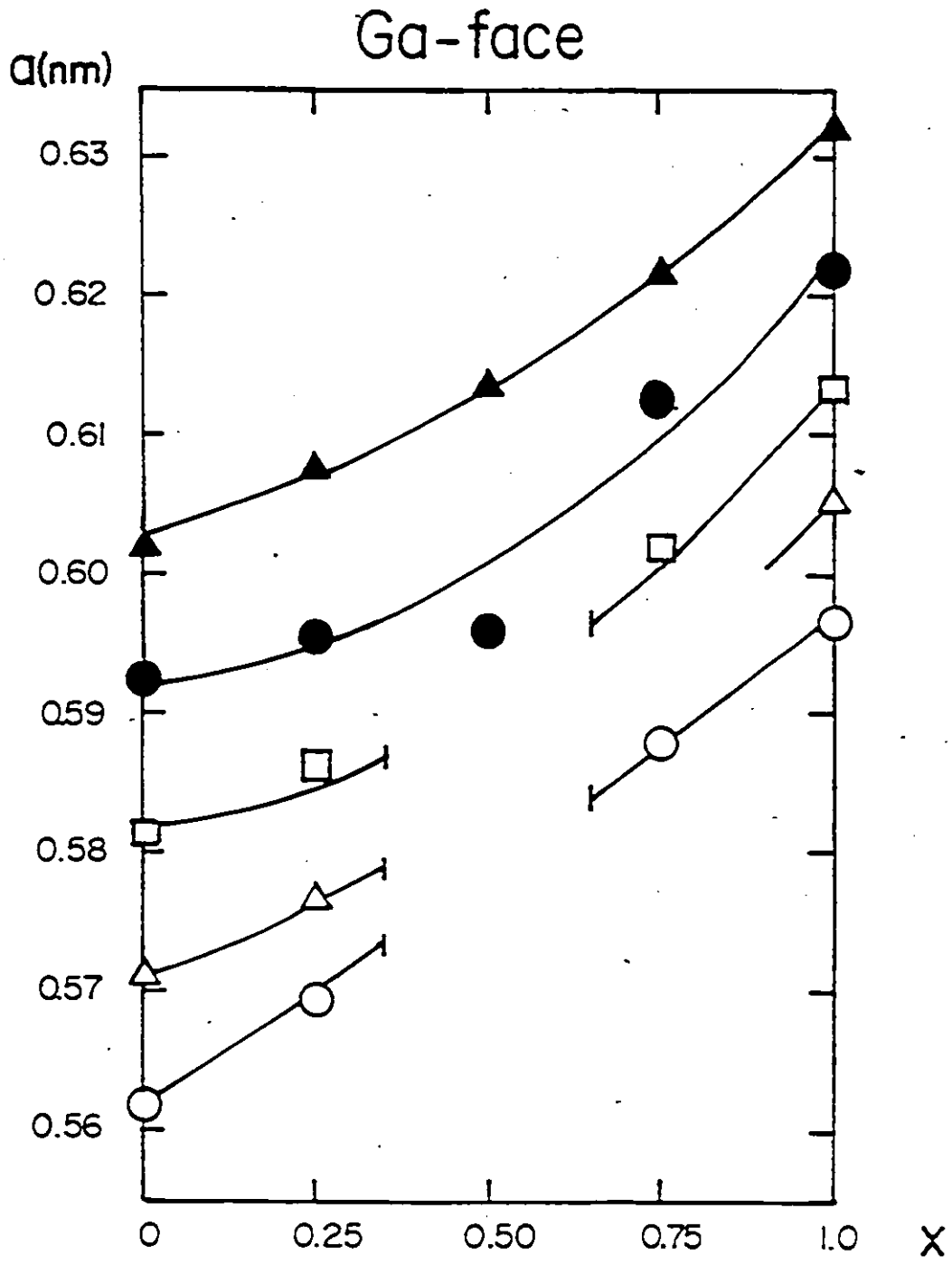

Fig. 2.7 $(Cu_{1-z}Ag_z)Ga(Se_{1-z}Te_z)_2$ section. Variation of lattice parameter a with x for lines of constant z.

○ : $z = 0$ △ : $z = 0.25$ □ : $z = 0.50$ ● : $z = 0.75$ ▲ : $z = 1.0$

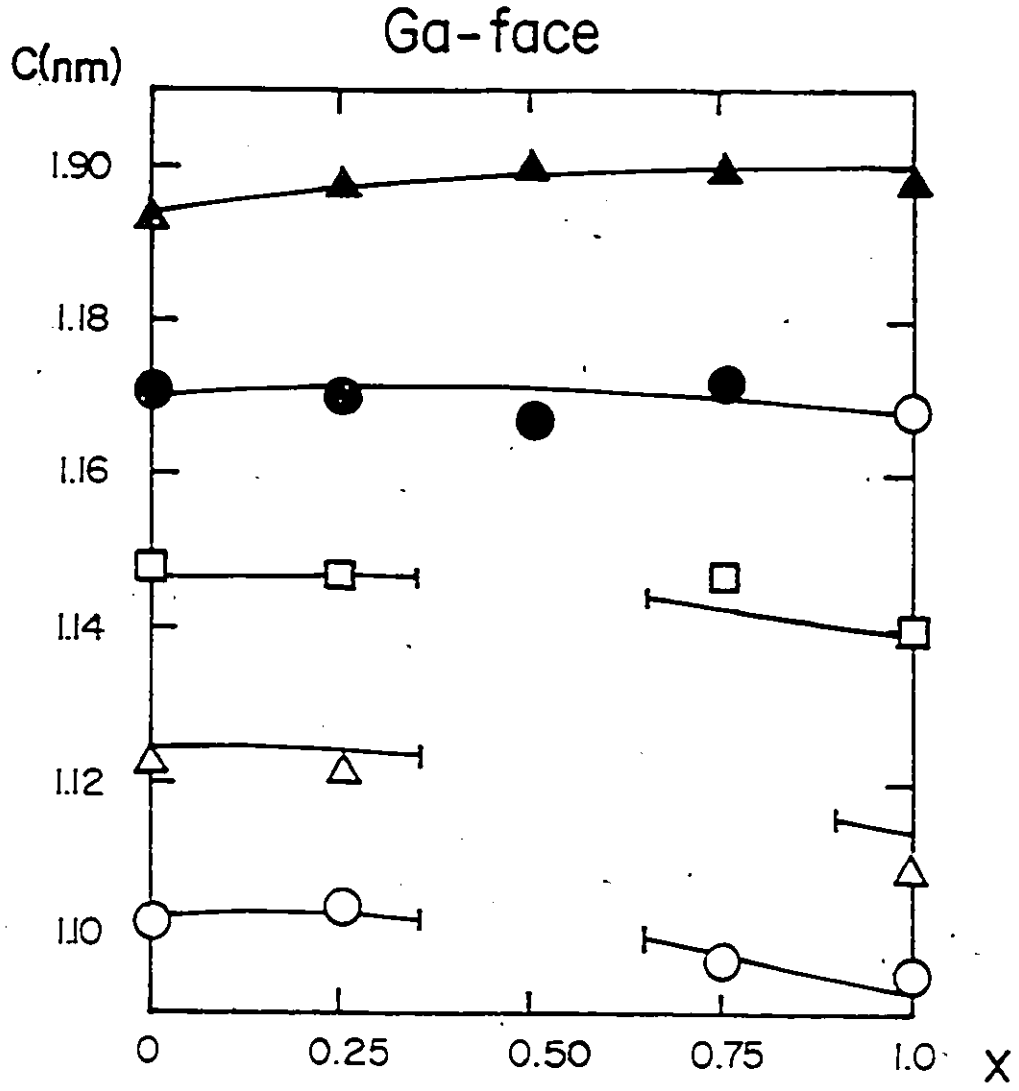

Fig. 2.8 $(Cu_{1-z}Ag_z)Ga(Se_{1-z}Te_z)_2$ section. Variation of lattice parameter c with x for lines of constant z.

○ : $z = 0$ 、△ : $z = 0.25$ □ : $z = 0.50$ ● : $z = 0.75$ ▲ : $z = 1.0$

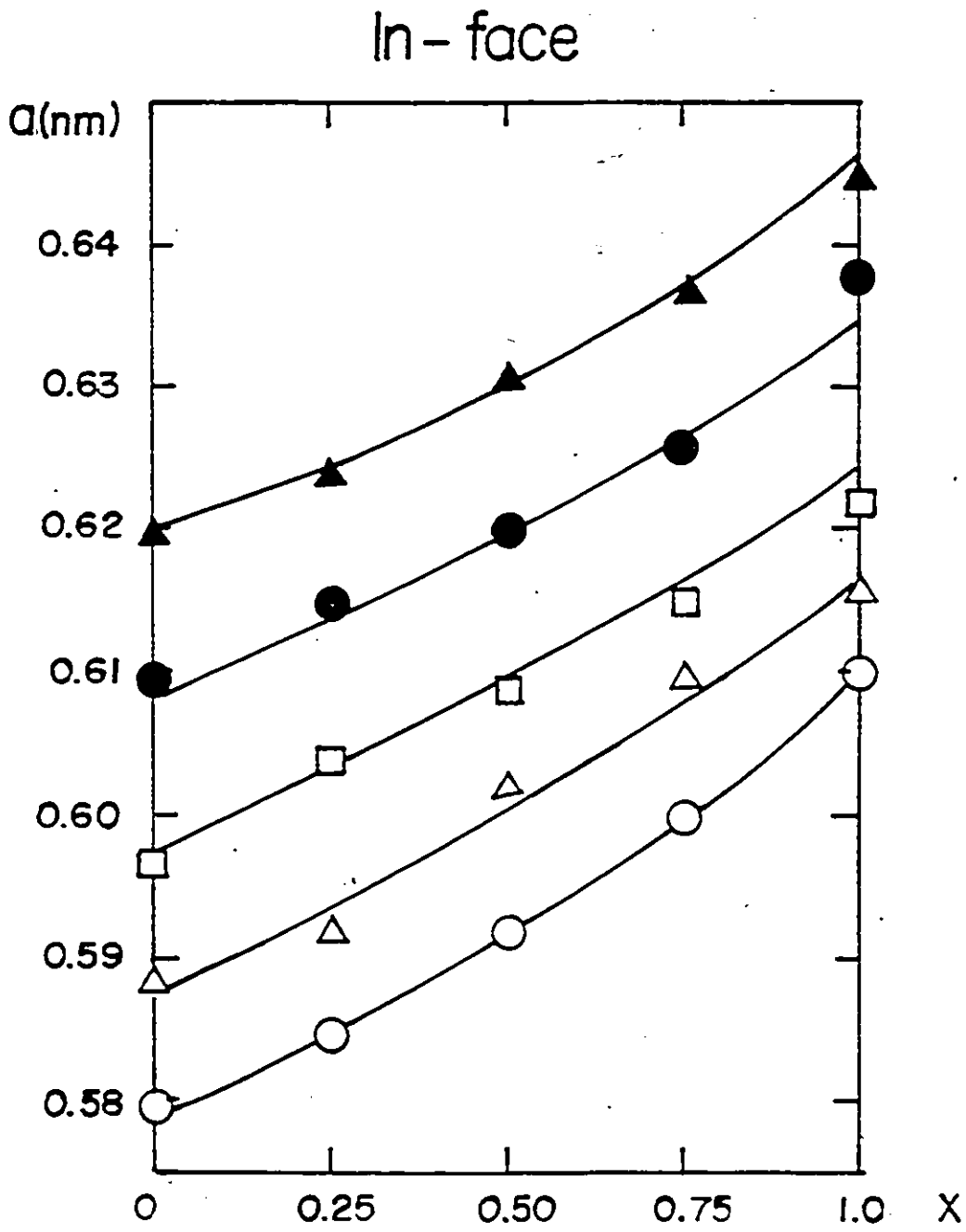

Fig. 2.9 $(Cu_{1-z}Ag_z)In(Se_{1-z}Te_z)_2$ section.. Variation of lattice parameter a with x for lines of constant z.

○ : $z = 0$ △ : $z = 0.25$ □ : $z = 0.50$ ● : $z = 0.75$ ▲ : $z = 1.0$

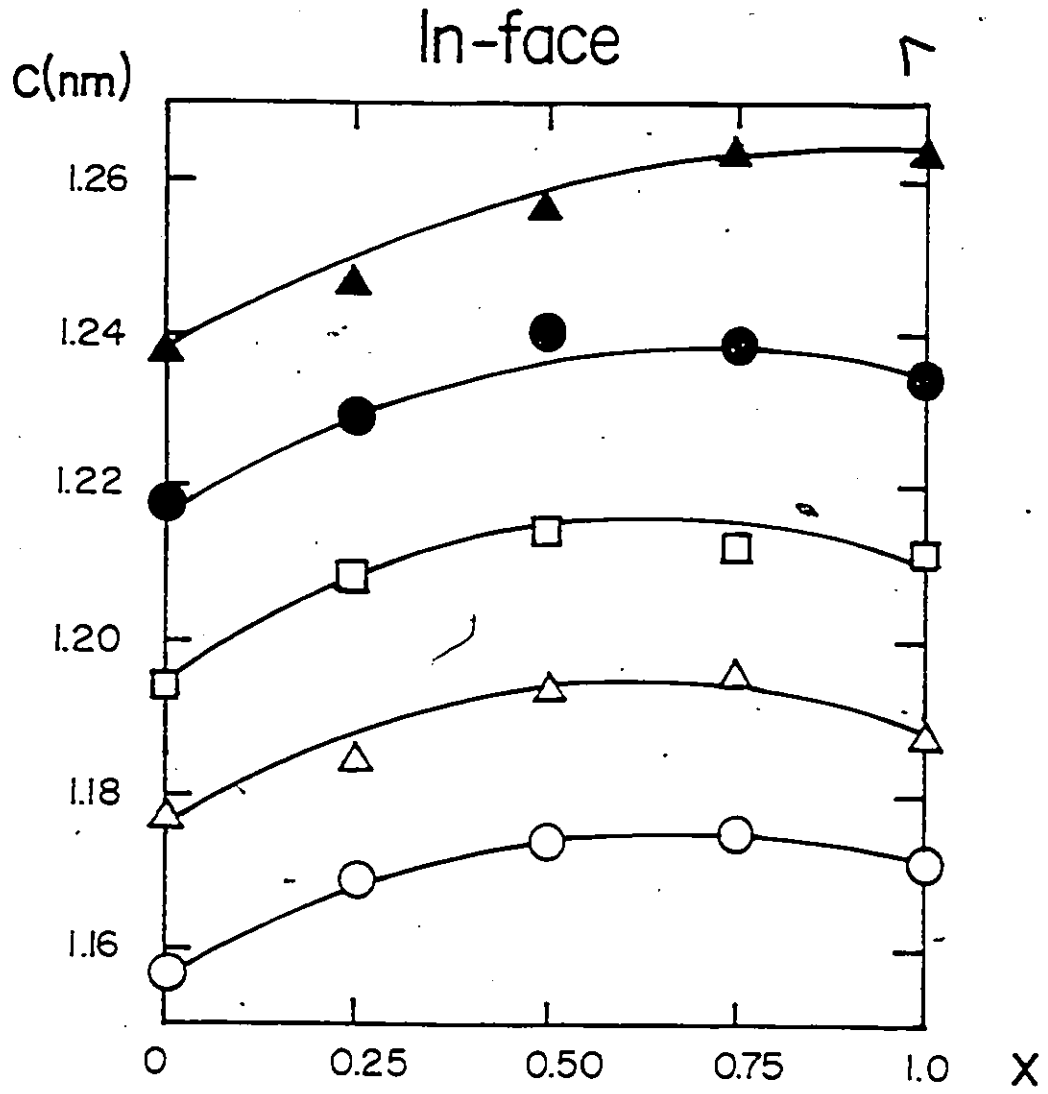

Fig. 2.10 $(Cu_{1-z}Ag_z)In(Se_{1-z}Te_z)_2$ section. Variation of lattice parameter c with x for lines of constant z.

○ : $z = 0$ △ : $z = 0.25$ □ : $z = 0.50$ ● : $z = 0.75$ ▲ : $z = 1.0$

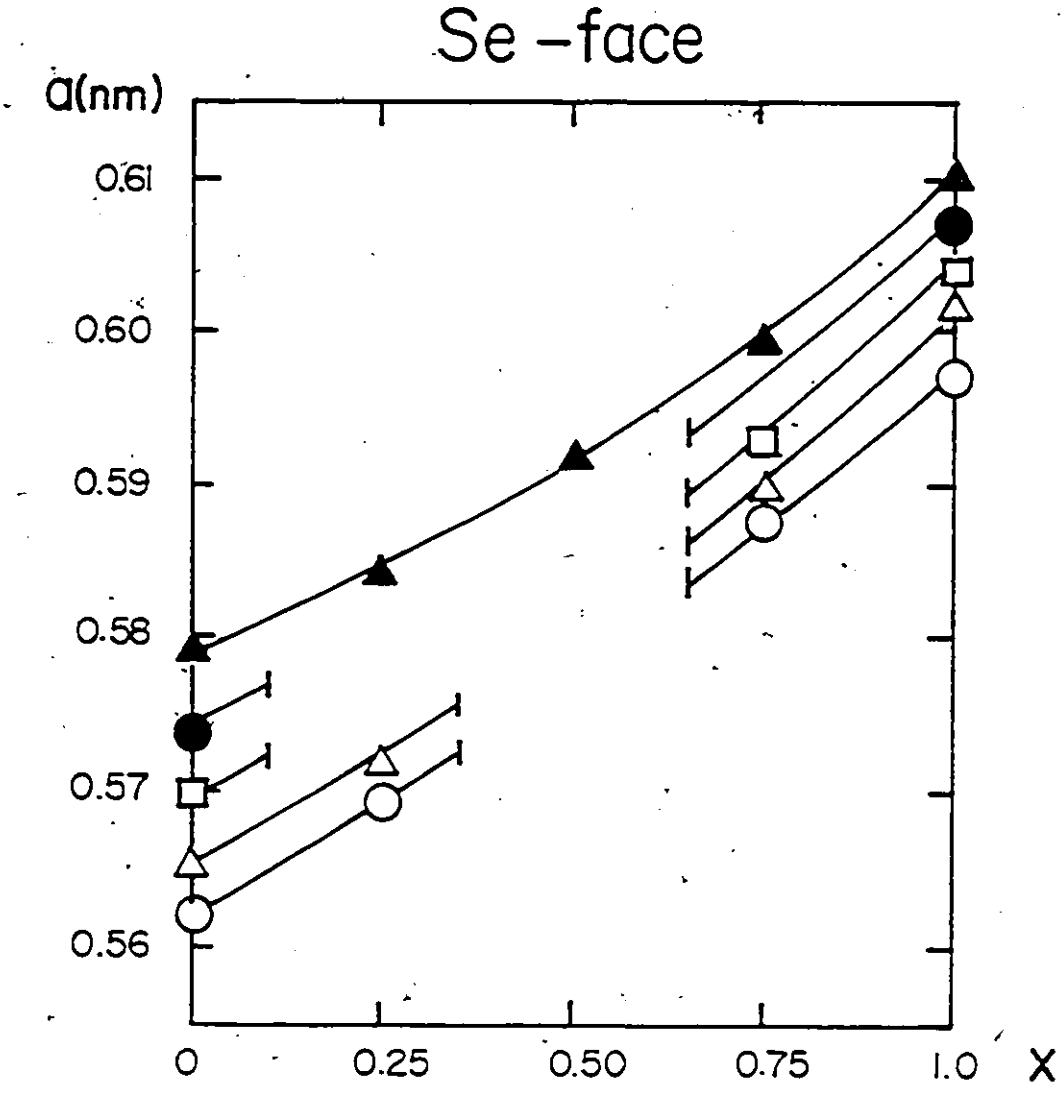

Fig. 2.11 $(Cu_{1-x}Ag_x)(Ga_{1-y}In_y)Se_2$ section. Variation of lattice parameter a with x for lines of constant y.

○ : $y = 0$ △ : $y = 0.25$ □ : $y = 0.50$ ● : $y = 0.75$ ▲ : $y = 1.0$

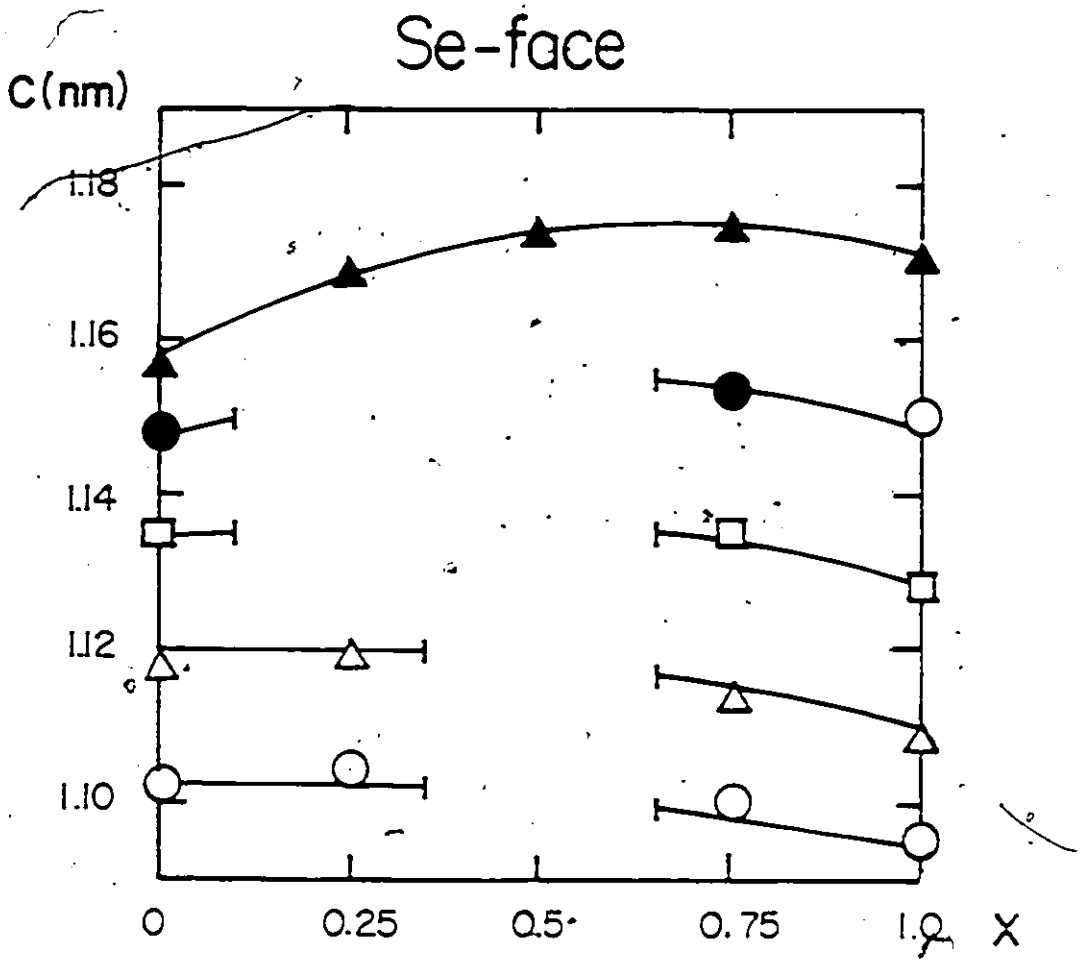

Fig. 2.12 $(Cu_{1-x}Ag_x)(Ga_{1-y}In_y)Se_2$ section. Variation of lattice parameter c with x for lines of constant y.

○ : $y = 0$ △ : $y = 0.25$ □ : $y = 0.50$ ● : $y = 0.75$ ▲ : $y = 1.0$

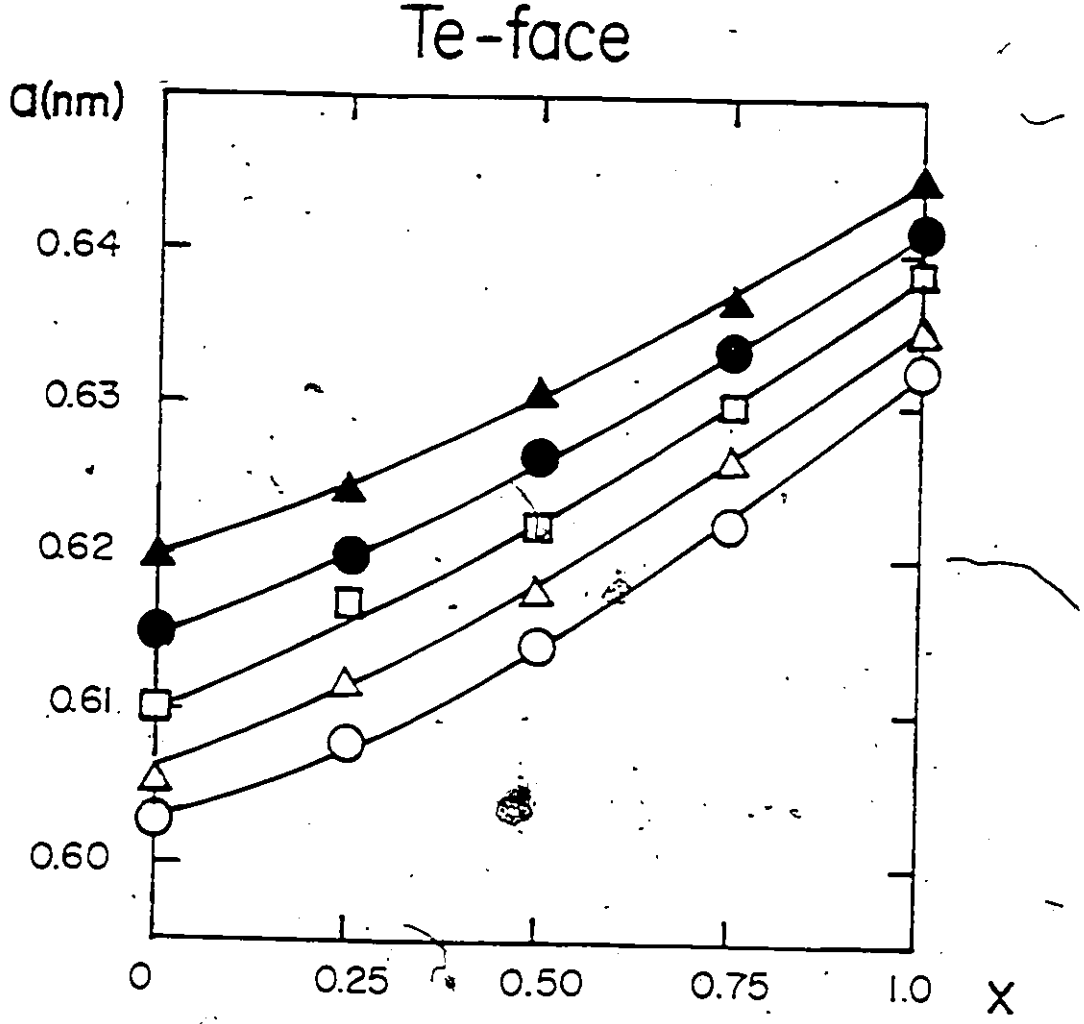

Fig. 2.13 $(Cu_{1-x}Ag_x)(Ga_{1-y}In_y)Te_2$ section. Variation of lattice parameter a with x for lines of constant y.

○ : $y = 0$ △ : $y = 0.25$ □ : $y = 0.50$ ● : $y = 0.75$ ▲ : $y = 1.0$

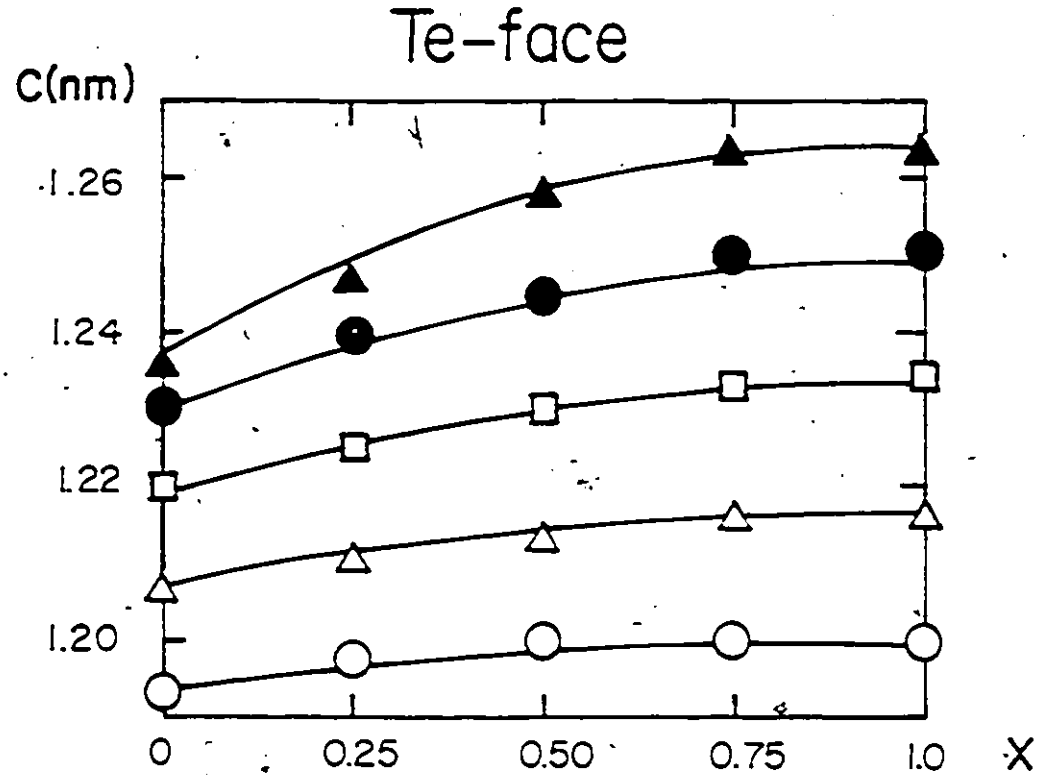

Fig. 2.14 $(Cu_{1-x}Ag_x)(Ga_{1-y}In_y)Te_2$ section. Variation of lattice parameter c with x for lines of constant y.

○ : $y = 0$ △ : $y = 0.25$ □ : $z = 0.50$ ● : $y = 0.75$ ▲ : $y = 1.0$

convenient to deal firstly with the faces of the cube. Fig. 2.3 - 2.14 show the variation of a and c as a function of composition for each of the six faces. For each face, it is possible to plot the lattice parameters as a function of either of two compositions and so in each case the variable giving the clearer set of curves has been used. In general, it can be seen that the variation of a and c with either composition variable is appreciably different from linear but can be resonably fitted within the expected limits of experimental error to a parabolic form. Such a variation was obtained for the $(Cu_{1-x}Ag_x)In(S_{1-z}Se_z)_2$ alloys by Chapman et al [79C1,79S1] and has already been shown for the alloys of the tellurium face [80A1]. It is apparent from the graphs that there is some scatter of the experimental points in certain composition ranges. This is attributed mainly to the fact that for some samples complete equilibrium was not attained even after annealing for periods of up to 5 months, and that for those cases the high angle lines in the photograph were blurred sufficiently that the $K\alpha_1$ $K\alpha_2$ doublet was barely resolved.

However, on the silver, gallium, and selenium faces, it was found that some photographs showing sharp high angle lines gave values of a and c very different from those expected from the curves shown in Fig. 2.3 - 2.14. These results were taken to be indicative of two phase behavior and study of the appropriate photographs showed the presence of another weaker, chalcopyrite phase. The observation of these extra phases was complicated by various factors. Firstly, all of the CH structures show weak ordering lines and since these were not needed in the determination of a and c, they were not measured and identified in that analysis. Thus, lines due to weak second phase could be confused with ordering lines. Secondly, in these multicomponent alloys, multiphase rather than two phase behavior could occur. Thus the initial criterion for determining two phase or multiphase behavior was the observation of systematic large deviations in lattice parameters from the expected values. The compositions for which two-phase

or multiphase behavior is considered to occur are shown in the Tables indicated by a letter m.

It is not possible with the present number of alloy samples to give any more accurate estimate of the limits of the miscibility gap on the faces mentioned above since with a multicomponent system no simple tieline extrapolation can be used as would be the case in a binary system. Only estimates can be made at this stage of the boundaries of the miscibility gap and these are shown in Fig. 2.5 - 2.8 and Fig. 2.11 - 2.12. The results on the gallium and selenium faces are consistent with those of Robbins et al [73R1] for the $(Cu_{1-x}Ag_x)GaSe_2$ line, indicating a miscibility gap in the range $0.45 < x < 0.65$.

From a study of various $(Cu_{1-x}Ag_x)III\ VI_2$ alloy systems [73R1] where III=Al, Ga, or In, and VI=S or Se, it was shown that for a pseudobinary alloy formed from a Cu and the equivalent Ag ternary compound, a miscibility gap occurs if the difference in r between the two compounds is larger than or approximately equal to 0.13, i.e. $\Delta r \gtrsim 0.13$. In the present work it is found that the faces which show the miscibility gap have greater values of r and also a greater range of r values. Also, similar analysis can be made for alloys of each face by considering a difference between the maximum and minimum values of r for the compounds at the corners of that face: the miscibility gap occurs when $\Delta r \gtrsim 0.11$.

Turning to the alloys in the interior of the cube, the results can be presented in terms of sections with x, y, or z equal to 0.25, 0.50, and 0.75. Again a number of alloy samples appeared to be multiphase, indicating that the miscibility gap extends over a considerable range of composition. These values are given in Table 2.7. Because of this range of miscibility gap, graphs of lattice parameter versus composition are shown for only two planes, i.e., y=0.75 and z=0.75 in Fig. 2.15 - 2.18. The curves are obtained from the average values of the coefficient in Tables 2.8 and 2.9 determined in the next section. The estimated region of the miscibility gap of the cube is also shown in Fig. 2.20.

Table 2.7 Values of a and c from experiment and values predicted from Eq.(2-13) using the averaged parameters in Table 2.10 for some alloys lying inside the represention cube. Multiphase samples are also indicated.

Sample	Experiment Values		Predicted Values	
	a(nm)	c(nm)	a(nm)	c(nm)
252525	m	m	m	m
252550	m	m	m	m
252575	0.5973	1.1784	0.6011	1.1889
255025	m	m	m	m
255050	0.5938	1.1780	0.5957	1.1825
255075	0.6084	1.2144	0.6056	1.2044
257525	0.5829	1.1716	0.5901	1.1748
257550	0.6002	1.1965	0.5999	1.1966
257575	0.6139	1.2146	0.6099	1.2178
502525	m	m	m	m
502550	m	m	m	m
502575	0.6055	1.1857	0.6074	1.1897
505025	m	m	m	m
505050	m	m	m	m
505075	0.6112	1.2040	0.6119	1.2068
507525	0.5941	1.1760	0.5971	1.1771
507550	0.6054	1.1960	0.6064	1.1999
507575	0.6157	1.2191	0.6161	1.2224
752525	m	m	m	m
752550	m	m	m	m
752575	0.6153	1.1820	0.6154	1.1886
755025	m	m	m	m
755050	0.6019	1.1674	0.6099	1.1811
755075	0.6189	1.2036	0.6192	1.2065
757525	m	m	m	m
757550	0.6089	1.1909	0.6135	1.1989
757575	0.6224	1.2202	0.6230	1.2231

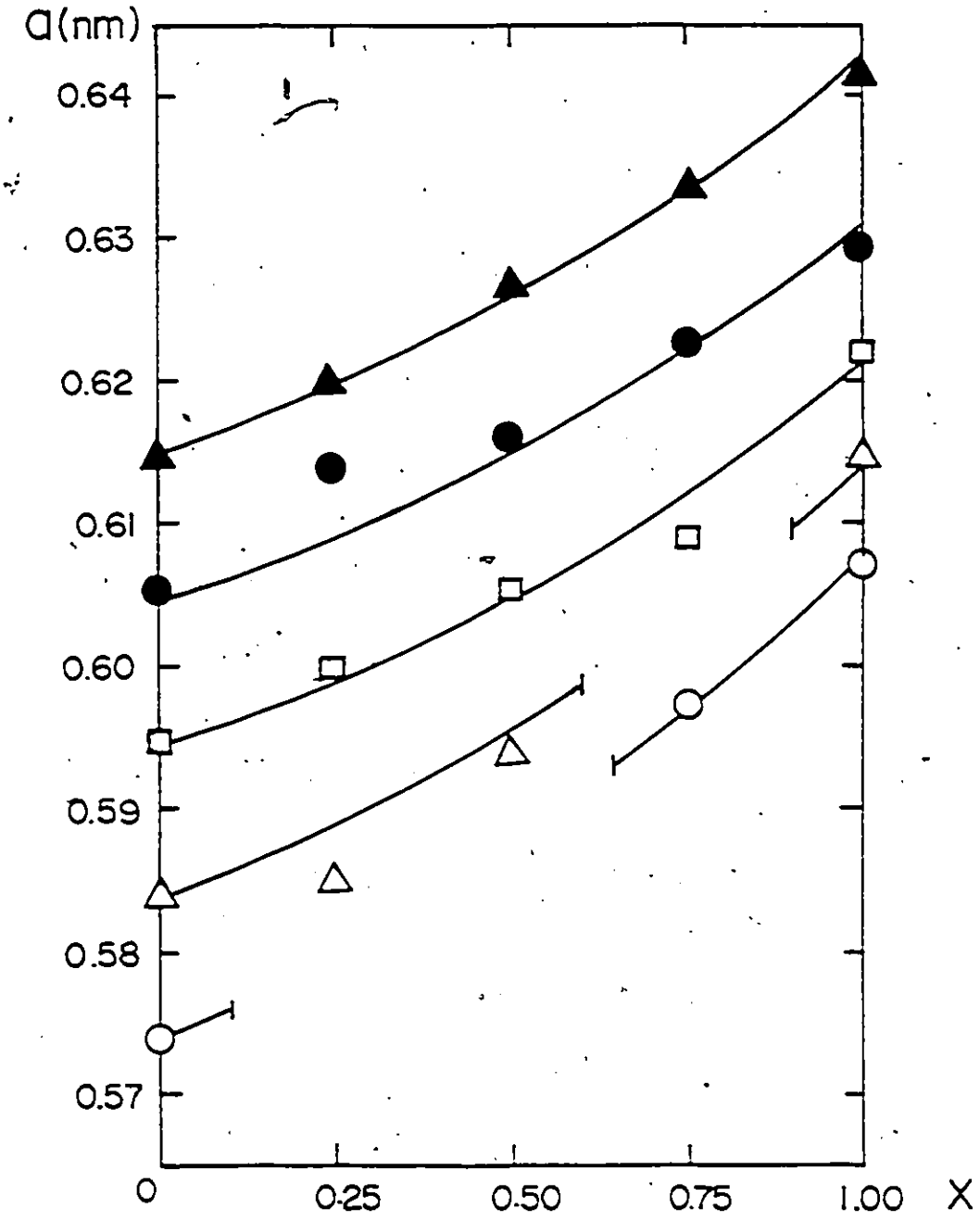

Fig. 2.15 $(Cu_{1-x}Ag_x)(Ga_{0.25}In_{0.75})(Se_{1-z}Te_z)_2$ section. Variation of lattice parameter a with x for lines of constant z. ○ : $z = 0$ △ : $z = 0.25$ □ : $z = 0.50$ ● : $z = 0.75$ ▲ : $z = 1.0$

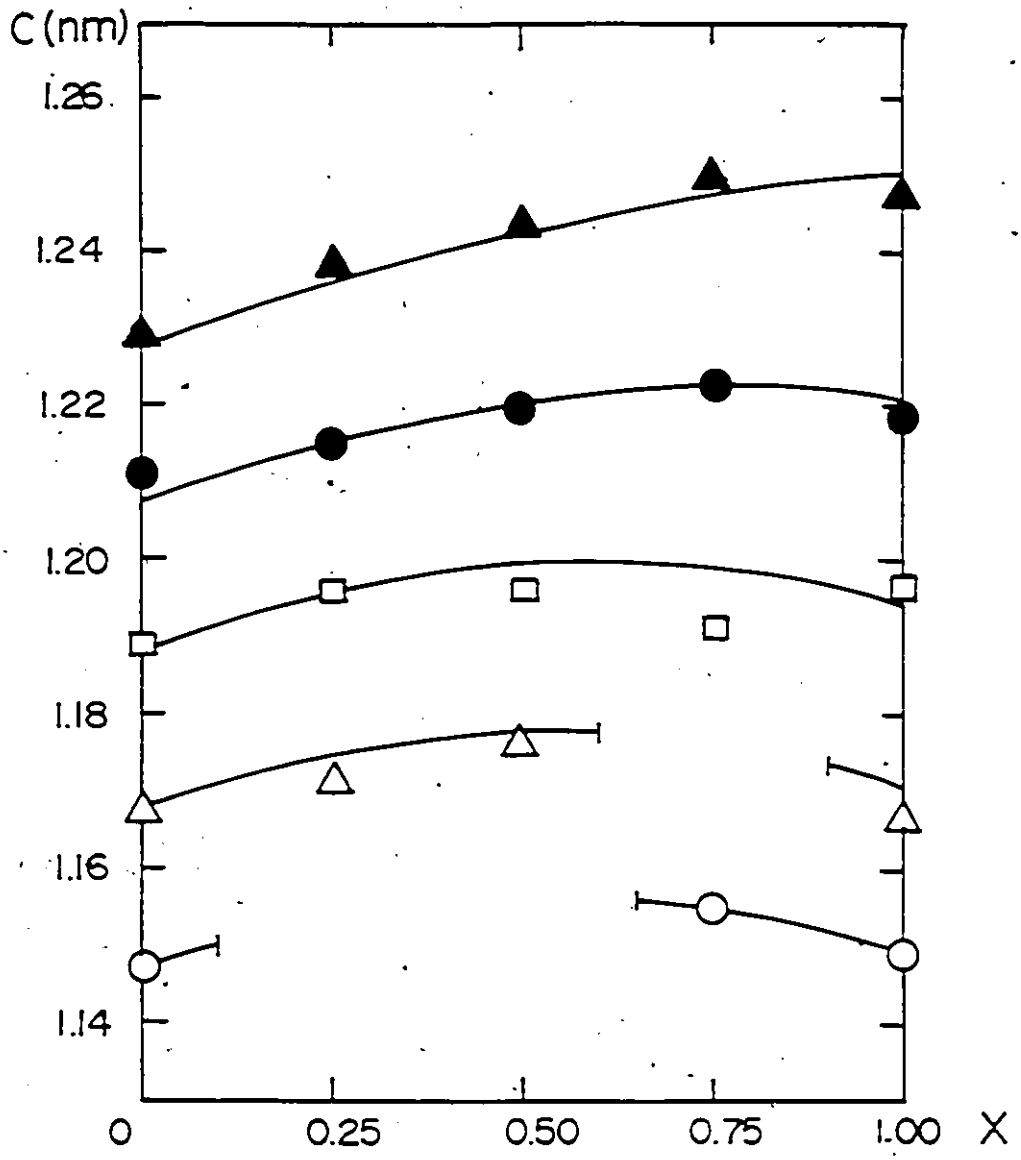

Fig. 2.16 $(Cu_{1-z}Ag_z)(Ga_{0.25}In_{0.75})(Se_{1-z}Te_z)_2$ section. Variation of lattice parameter c with x for lines of constant z. ○ : $z = 0$ △ : $z = 0.25$ □ : $z = 0.50$ ● : $z = 0.75$ ▲ : $y = 1.0$

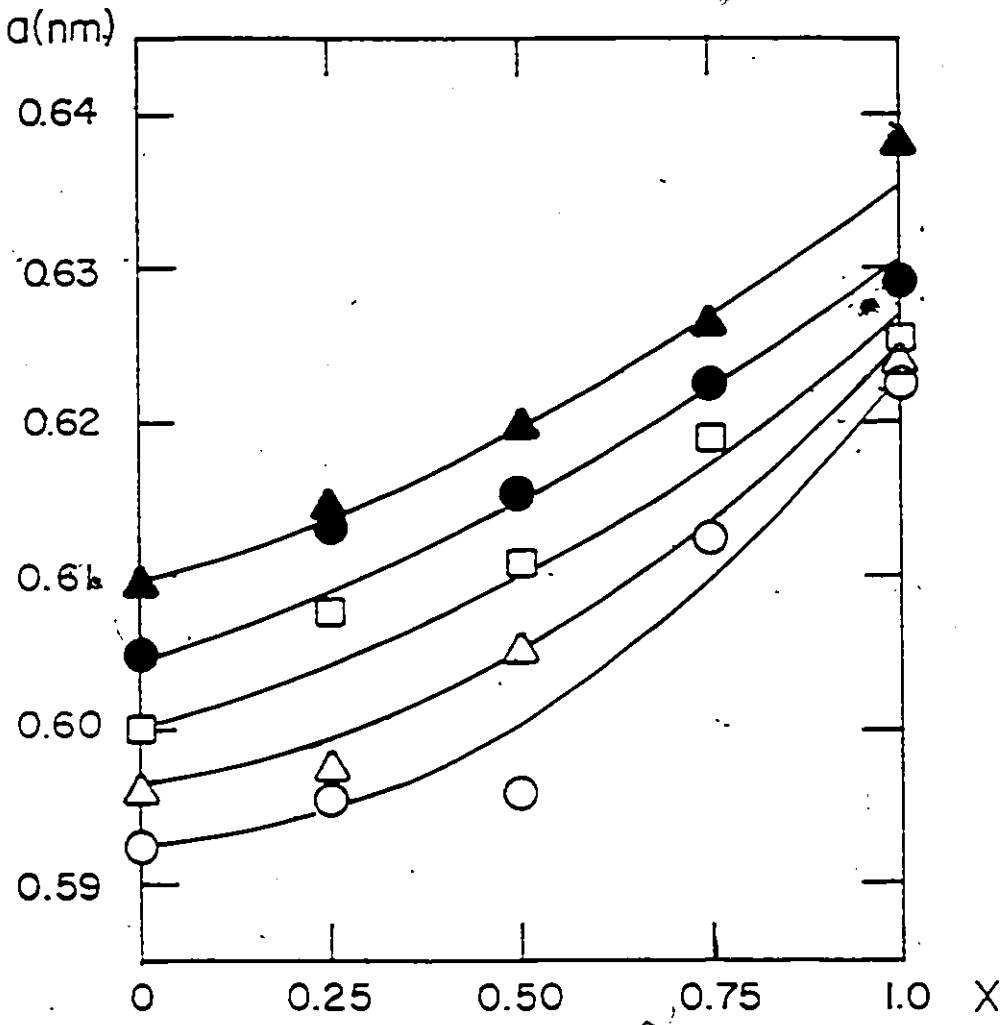

Fig. 2.17 $(Cu_{1-x}Ag_x)(Ga_{1-y}In_y)(Se_{0.25}Te_{0.75})_2$ section. Variation of lattice parameter a with x for lines of constant y. ○ : $y = 0$ △ : $y = 0.25$ □ : $y = 0.50$ ● : $y = 0.75$ ▲ : $y = 1.0$

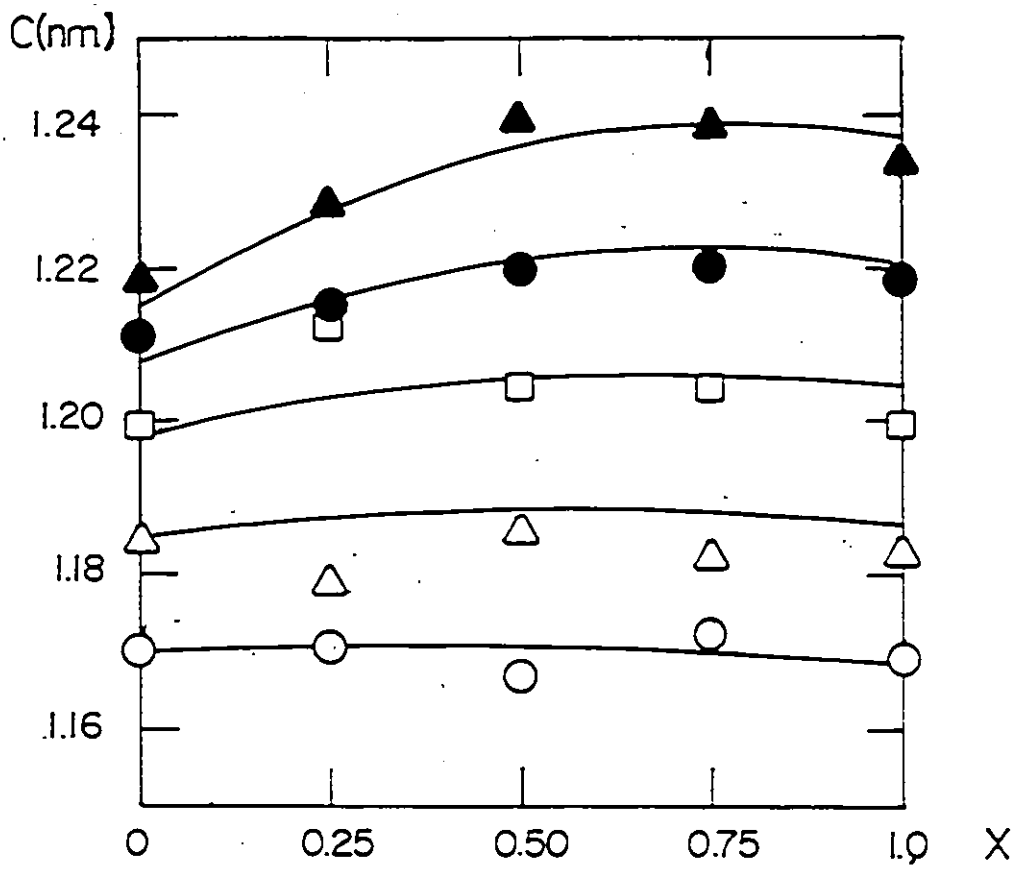

Fig. 2.18 $(Cu_{1-x}Ag_x)(Ga_{1-y}In_y)(Se_{0.25}Te_{0.75})_2$ section. Variation of lattice parameter c with x for lines of constant y. ○ : $y = 0$ △ : $y = 0.25$ □ : $y = 0.50$ ● : $y = 0.75$ ▲ : $y = 1.0$

2.6 Lattice Constant Contour Maps

In order to carry out further analysis of the data, it is convenient to express **a** and **c** as a function of the composition parameters. In previous studies, linear interpolation along the four edges has been used to estimate the contour map of each face and the lattice constant behavior has been described by

$$\mathbf{a}(x,y) = a_0 + a_1 x + a_2 y + a_3 xy \qquad (2-11)$$

as used by Moon et al [74M1] and Nahory et al [78N1].

However, this analysis is not sufficient for the present data, since the variation along each edge of a face may be parabolic. As was shown previously [79S1, 79C1, 80A1], it is possible to express parameters **a** and **c** as a two dimensional Taylor's series expansion or as a power series in the two composition variables appropriate to the face concerned. It has been assumed that neither variable will occur at a greater power than 2 because of a parabolic variation of the lattice parameter along each edge. Then the values of **a** and **c** are expressed as

$$\mathbf{p}(u,v) = \alpha + \beta u + \gamma v + \delta u^2 + \varepsilon v^2 + \rho uv + \eta u^2 v + \theta uv^2 + \lambda u^2 v^2 \qquad (2-12)$$

where **p** is the lattice parameter concerned and u and v are the composition variables appropriate to the particular face. The nine coefficients will be treated as adjustable parameters when a fit is made to the data for **a** and **c**. It is seen that the fitted equations will give convenient mathematical forms for representing experimental data and the coefficients involved in these equation do not necessarily have any physical significance. In each case, a least squares fitting method was used to give values of the nine coefficients in Eq.(2-12). The values obtained, the number of points used in each case, and the standard deviation σ of the experimental points from the fitted curves are shown in Table 2.8-2.9. The standard

Table 2.8 Coefficients corresponding to Eq. (2-12) for each of the six faces. The number of points used in the least squares fit and the standard deviation, σ, is also listed in each case.

	face	Cu	Ag	Ga
	number of points	25	22	21
	variable composition parameters (u,v)	(y,z)	(y,z)	(x,z)
a(nm)	α_o	0.5620	0.5974	0.5617
	β_o	0.0128	0.0173	0.0339
	γ_o	0.0375	0.0288	0.0394
	δ_o	0.0047	-0.0050	0.0016
	ε_o	0.0031	0.0062	0.0018
	ζ_o	0.0223	-0.0336	-0.0046
	η_o	-0.0280	0.0288	0.0806
	θ_o	-0.0247	0.0235	0.0740
	λ_o	0.0299	-0.0171	-0.0720
	σ	0.0005	0.0013	0.0015
c(nm)	α'_o	1.1013	1.0930	1.1024
	β'_o	0.0787	0.0637	0.0050
	γ'_o	0.0895	0.0704	0.0855
	δ'_o	-0.0223	0.0144	-0.0149
	ε'_o	0.0030	0.0367	0.0062
	ζ'_o	0.0159	0.0340	-0.0174
	η'_o	-0.0346	-0.0394	0.0009
	θ'_o	-0.0396	-0.0328	0.0254
	λ'_o	0.0464	0.0236	-0.0020
	σ	0.0015	0.0020	0.0022

Table 2.9 Coefficients corresponding to Eq. (2-12) for each of the six faces. The number of points used in the least squares fit and the standard deviation, σ, is also listed in each case.

	face	In	Se	Te
	number of points	25	19	25
	variable composition parameters (u,v)	(x,z)	(x,y)	(x,y)
a(nm)	α_o	0.5790	0.5618	0.6027
	β_o	0.0207	0.0299	0.0164
	γ_o	0.0331	0.0137	0.0120
	δ_o	0.0103	0.0058	0.0131
	ε_o	0.0084	0.0037	0.0052
	ζ_o	0.0112	-0.0201	0.0209
	η_o	-0.0222	0.0219	-0.0214
	θ_o	-0.0192	0.0092	-0.0209
	λ_o	0.0251	-0.0158	0.0171
	σ	0.0014	0.0003	0.0004
c(nm)	α'_o	1.1572	1.1026	1.1933
	β'_o	0.0516	0.0005	0.0156
	γ'_o	0.0726	0.0723	0.0585
	δ'_o	-0.0375	-0.0091	-0.0099
	ε'_o	0.0079	-0.0168	-0.0145
	ζ'_o	0.0424	-0.0093	0.0150
	η'_o	-0.0544	-0.0204	-0.0019
	θ'_o	-0.0356	0.0413	0.0249
	λ'_o	0.0631	-0.0081	-0.0166
	σ	0.0016	0.0010	0.0012

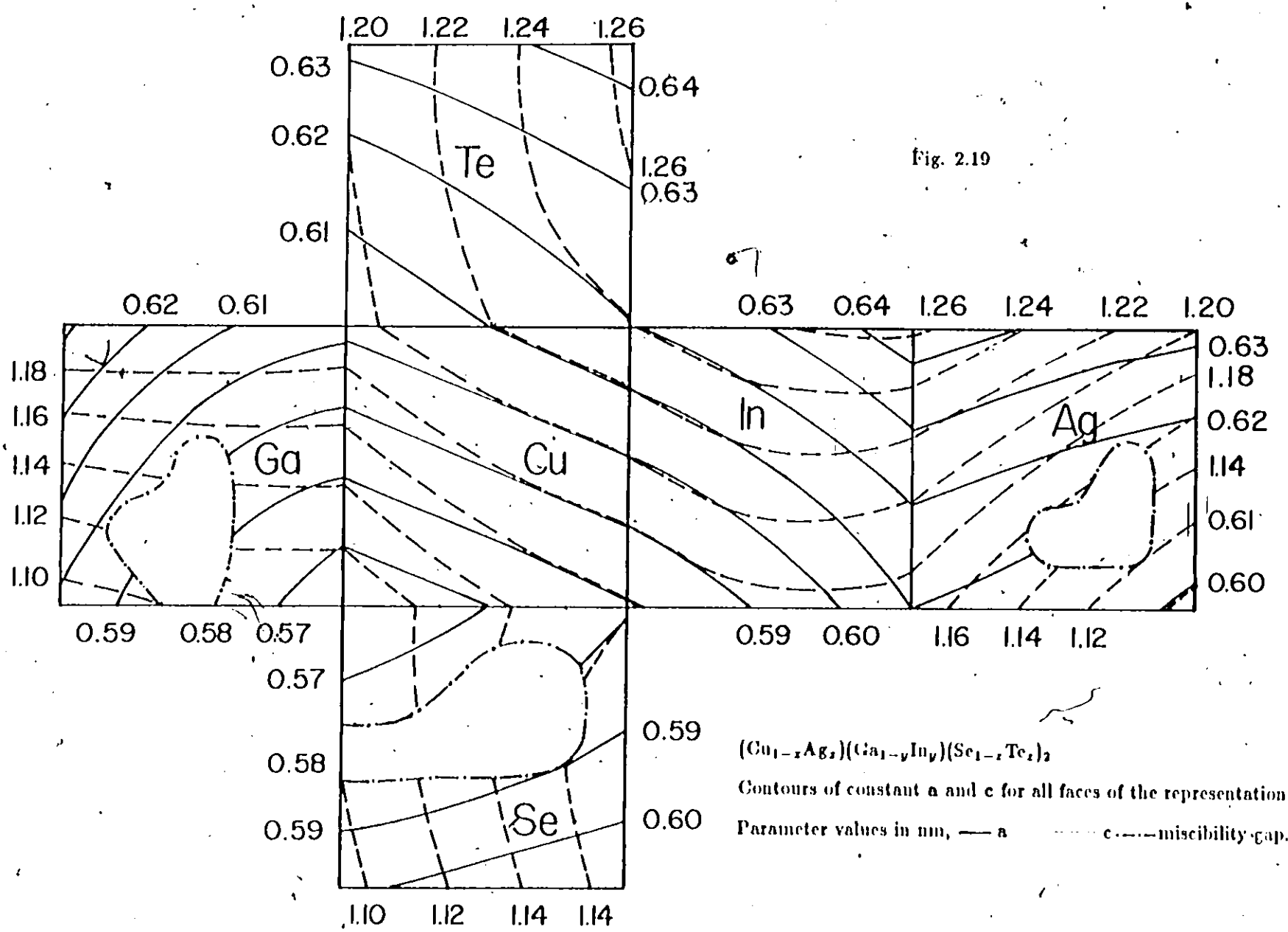

Fig. 2.19

$(Cu_{1-x}Ag_x)(Ga_{1-y}In_y)(Se_{1-z}Te_z)_2$

Contours of constant a and c for all faces of the representation cube.

Parameter values in nm, —— a ------ c -·-·- miscibility gap.

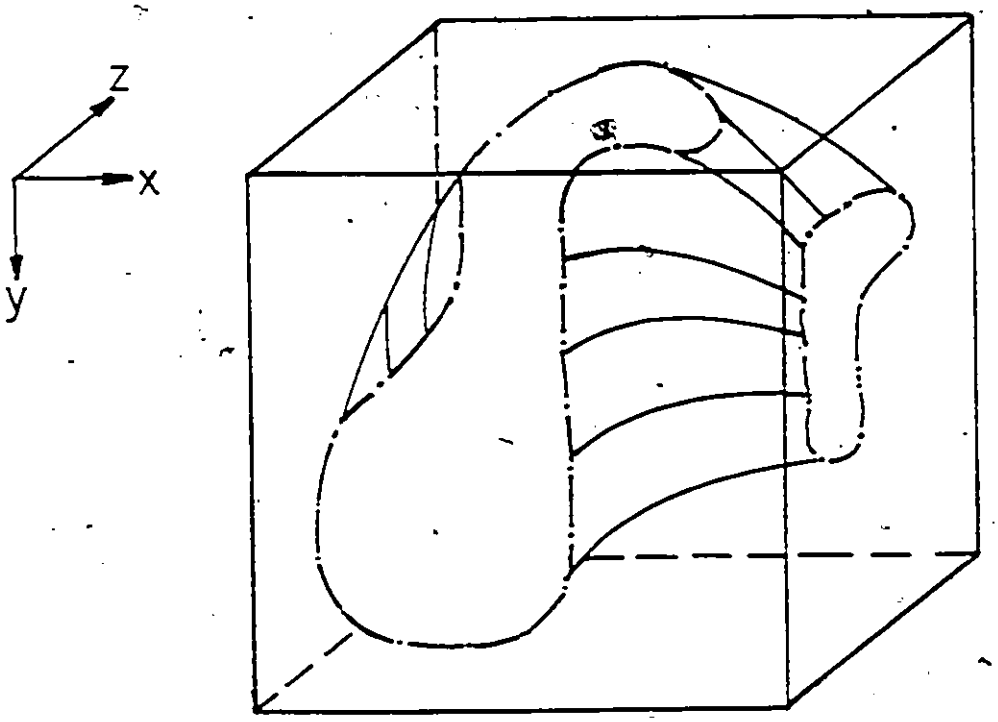

Fig. 2.20 Estimated region of the representation cube showing multiphase behavior.

deviations obtained is about what would expected from the error limits of the lattice measurements. The resulting fitted curves are also shown in Figs. 2.3 - 2.14.

From these coefficients, contours of constant a and c can be produced for each face and these including the estimated miscibility gaps are shown in Fig. 2.19. Since these faces form a cube, each edge is common to two faces. It is seen that the agreement between the fits to the various faces is reasonably good. However, the coefficients listed in Table 2.8-2.9 do not constitute a unique set, for it is found that the coefficients of the higher-order terms (i.e., η, θ, λ) can vary to some extent, with a variation in one coefficient compensating for the variation in another. This occurs without any significant change in the value of the standard deviation from the fitted curves and makes no significant difference in the constant a and c contours.

If a single fit is to be made to all of the data to give a single set of coefficients, a similar equation of 20 terms is required if terms containing cubed or higher order are neglected. No attempt has been made at this stage to use this form, but it is possible to use it to relate the various coefficients of the fitted equations for the faces and hence to obtain averaged values. The equation considered is of the form

$$\begin{aligned} p(x,y,z) = {} & A + Dx + Cy + Dz + Ex^2 + Fy^2 + Gz^2 + Hxy + Iyz + Jzx \\ & Kx^2y + Lxy^2 + Myz^2 + Nyz^2 + Ox^2z + Pxz^2 + Qxyz \\ & Rx^2y^2 + Sy^2z^2 + Tx^2z^2 + Ux^2yz + Vxy^2z + Wxyz^2 \\ & Xx^2y^2z + Yxy^2z^2 + Zx^2yz^2 \end{aligned} \qquad (2-13)$$

In this analysis, because the multiphase results in the silver, gallium and selenium faces used only when possible, only the data from the copper, indium, and tellurium faces were used and the coefficients

Table 2.10 Values of coefficients in Eq.(2-13)

Coefficient	a(nm)	c(nm)
A	0.502	1.102
B	0.032	0.003
C	0.013	0.077
D	0.038	0.058
E	0.004	-0.012
F	0.004	-0.021
G	0.003	0.004
H	-0.020	0.009
I	0.023	0.016
J	-0.005	-0.017
K	0.022	-0.020
L	0.009	0.041
M	-0.028	-0.035
N	-0.025	-0.040
O	0.087	0.010
P	0.074	0.025
Q	0.060	0.059
R	-0.016	-0.008
S	0.020	0.046
T	-0.072	-0.002
U	-0.143	-0.041
V	0.020	0.001
W	-0.045	-0.054
X	0.035	-0.012
Y	-0.048	-0.017
Z	0.097	0.064

of the silver, gallium and selenium faces used only when necessary. The resulting average values of all of the coefficients obtained are shown in Table 2.10. It was found that use of these average values made only small difference to the fitted curves, the overall standard deviation for all of the experimental data being 0.002 nm for a and 0.007 nm for c. This equation has been used to predict the values of a and c for alloys of compositions inside the cube shown in Fig. 2.15 - 2.18. For these interior points (16 data) the standard deviation from the predicted values are 0.003 nm for a and 0.016 nm for c. These values are significantly higher than the values for the points on the faces of the representation cube. This is partially due to the experimental scatter on the points as indicated above, but it can be seen also that there is some degree of systematic variation, with the experimental points in some cases falling systematically below or above the predicted values.

2.7 Predictions of the Lattice Parameter a and Tetragonal Deformation η

Using the CTB Theory

As was shown in Section 2.2, the CTB theory [84J1] can be used to predict the lattice parameter a, tetragonal deformation η, and anion position parameter u of ternary CH compounds and some of CH alloy systems.

In this alloy system, the radii of the anions and cations were taken as the weighted mean of the appropriate elemental radii, i.e.,

$$r_A = (1-x)r_{Cd} + xr_{Ag} \quad .$$

$$r_B = (1-y)r_{Cd} + yr_{In} \quad . \qquad (2-14)$$

$$r_C = (1-z)r_{Se} + zr_{Te} \quad .$$

Three different sets of elemental radii, viz. those of Pauling [67P1], Phillips [70P1], and Shannon-Prewitt [81S1], were used in the analysis to predict values of the structural parameters and the resulting values compared. The CTB theory gives the expressions for a, η and u as [84J1]

$$a^2 = \frac{12\alpha^2}{(2\beta+\alpha) - [(2\beta+\alpha)^2 - 18\alpha^2]^{\frac{1}{2}}}$$

$$\eta^2 = \frac{8(\beta-\alpha)}{3a^2} \qquad (2-15)$$

$$u = \frac{1}{2} - \frac{1}{4}(2\eta^2 - 1)^{\frac{1}{2}}$$

where the bond mismatch parameters α and β are defined as

$$\alpha = R_{AC}^2 - R_{BC}^2 = (r_A + r_C)^2 - (r_B + r_C)^2 \quad .$$

and (2-16)

$$\beta = R_{AC}^2 + R_{BC}^2 = (r_A + r_C)^2 + (r_B + r_C)^2 \quad .$$

Eq.(2-15) then gives values of a, η and u without the use of any experimental data. It was found that the Phillips radii gave the best predicted lattice parameter a with standard deviation 0.005 nm (102 data) but that the best predicted tetragonal deformation η was obtained using Pauling radii with a standard deviation 0.013. The predicted values for u have not been reported since no experimental data

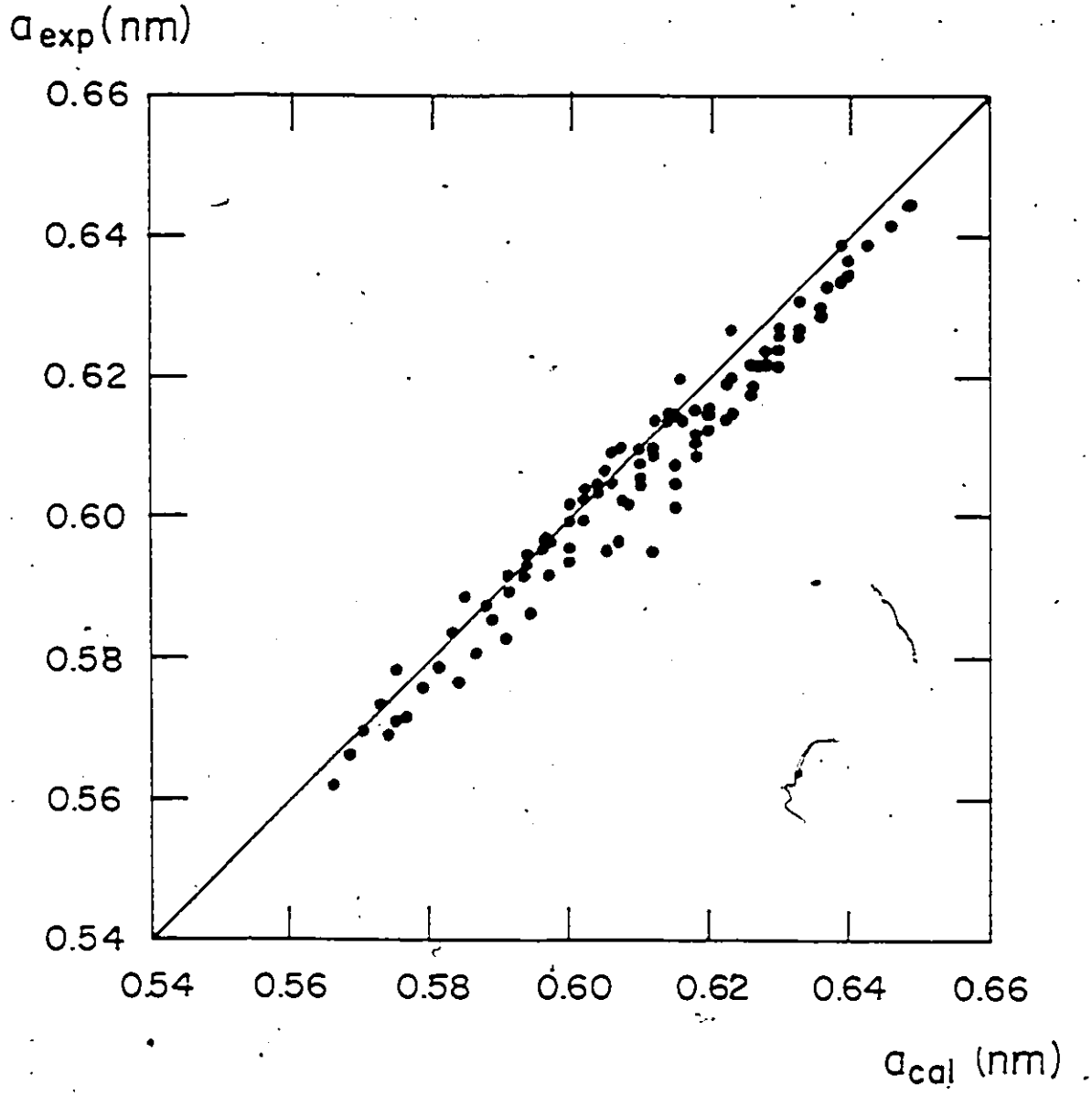

Fig. 2.21 $(Cu_{1-x}Ag_x)(Ga_{1-y}In_y)(Se_{1-z}Te_z)_2$ Plot of the measured lattice parameter a_{exp} against the value a_{cal} calculated from the CTB theory using the Phillips radii.

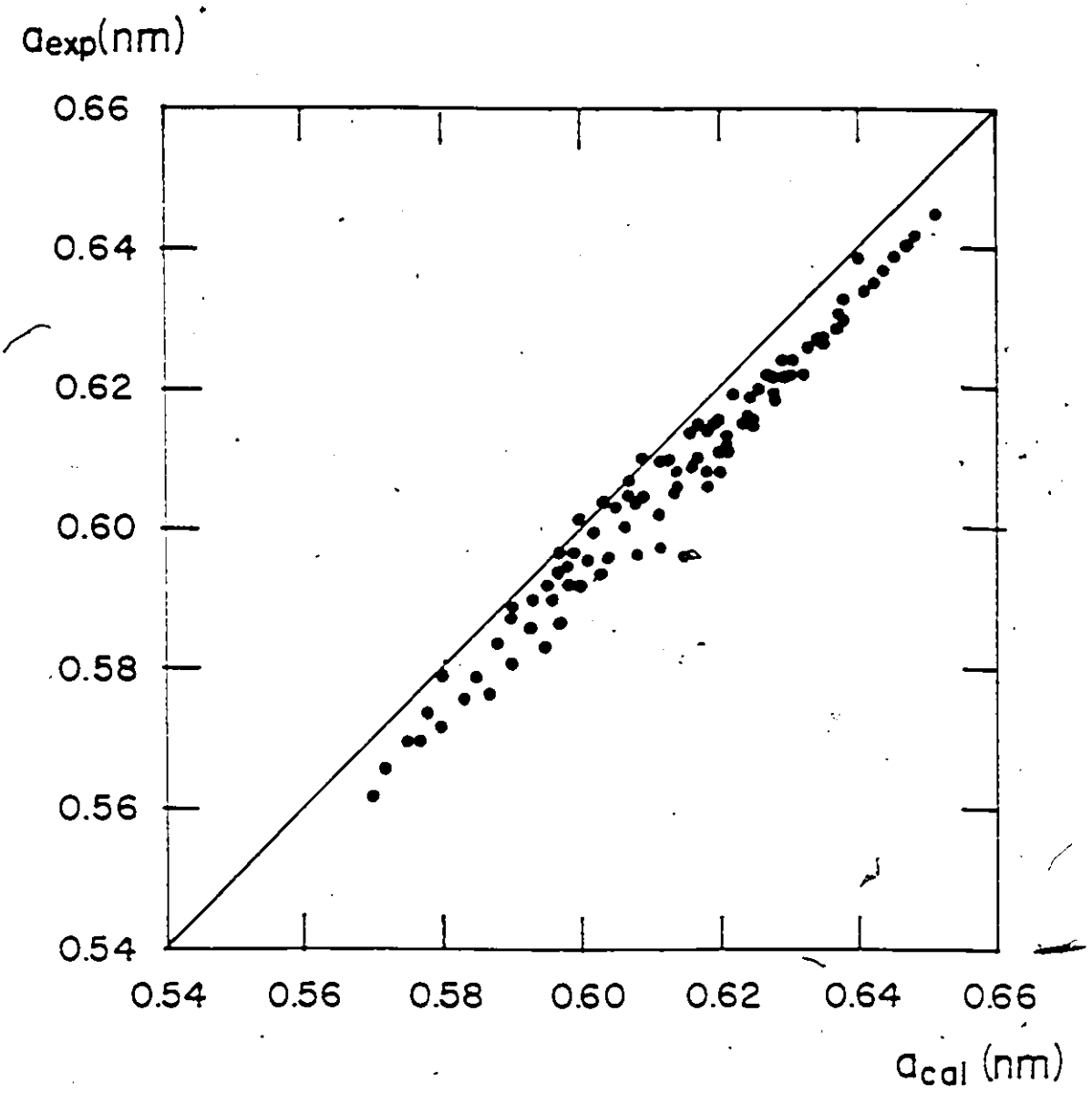

Fig. 2.22 $(Cu_{1-z}Ag_z)(Ga_{1-y}In_y)(Se_{1-z}Te_z)_2$ Plot of the measured lattice parameter a_{exp} against the value a_{cal} calculated from the CTB theory using the Pauling radii.

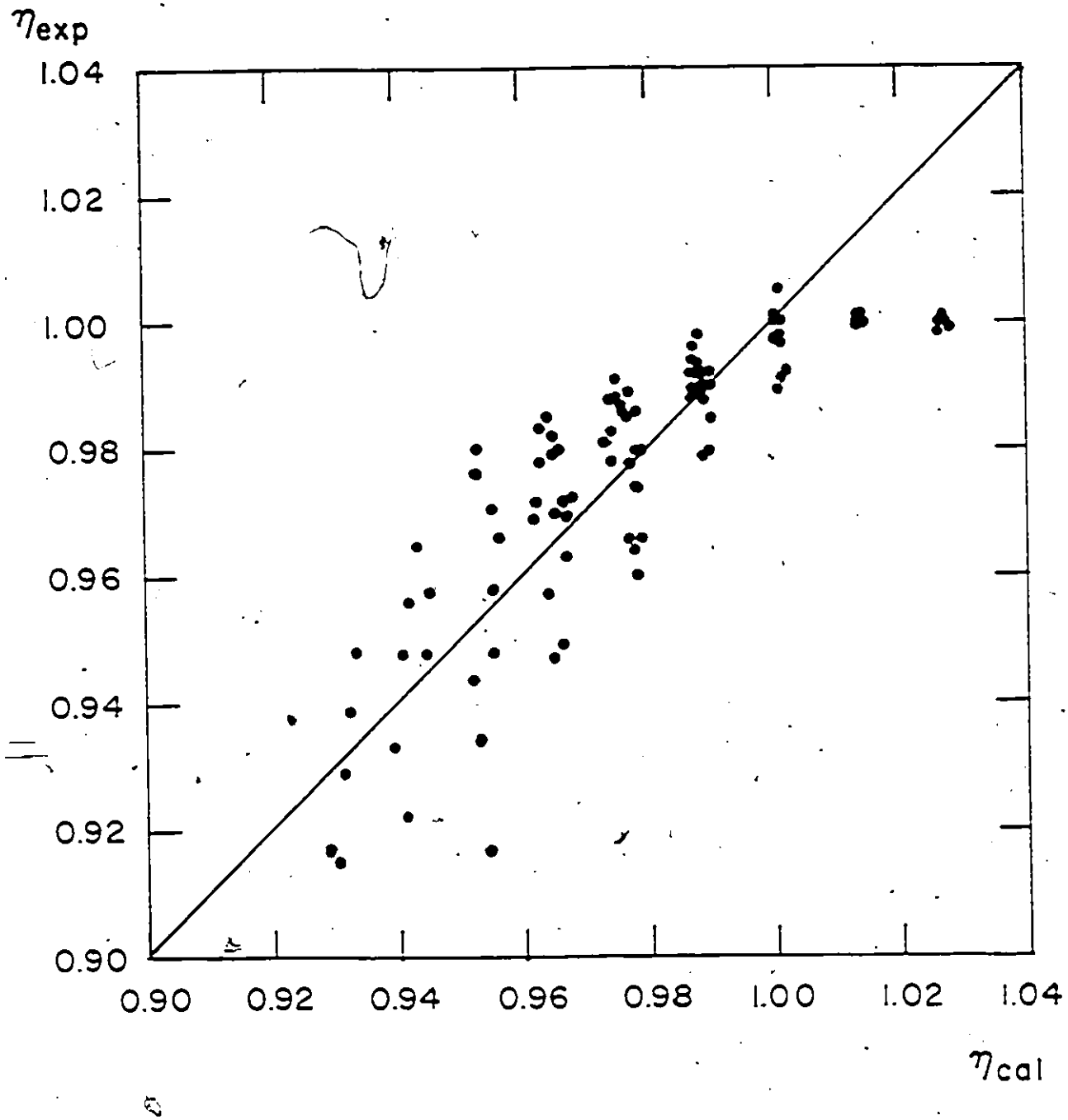

Fig. 2.23 $(Cu_{1-x}Ag_x)(Ga_{1-y}In_y)(Se_{1-z}Te_z)_2$ Plot of the measured tetragonal deformation η_{exp} against the value η_{cal} calculated from the CTB theory using the Pauling radii.

are available for u.

The correlation between the observed values and the calculated ones for these two parameters are shown in Figs. 2.21 - 2.23. It is seen that this analysis using Phillips radii gives reasonable agreement with the observed data for a. The predicted values of a using Pauling radii (Fig. 2.22) (σ = 0.007 nm) are larger than those for the Phillips radii (Fig. 2.21) and also than the observed values; the Shannon-Prewitt radii give the worst predicted values. The correlation between observed values and calculated values using Pauling radii for η shown in Fig. 2.23 is similar to those for ternary compounds [S4J1]. Jaffe and Zunger [S1J1] suggested that the CTB theory (Eq. 2-15) is not well suited for determining η the observed η values can be better predicted using the methods of Shaukat and Hussian [S5S1] discussed earlier. This will be done in the next section.

An attempt was made [S4A1] to correlate r with electronegativities of the constituent atoms using an empirically modified Weaire and Noolandi of the form

$$r = A'(X_A - X_B + qX_C)^2 \qquad (2-17)$$

to fit all of the experimental data. The parameter q and the proportional factor A' seem to be dependent to some extent on composition, but by assuming constant values for these quantities, a least-squares analysis applied to all of single phase results available gave mean values of $q = 0.105$ and $A' = 1.13$.

2.8 Tetragonal Distortion of Alloys Using Electronegativity Values

Defined through the density functional orbital radii.

The correlation between tetragonal distortion r and the difference in electronegativity ΔX_{C-H} between the $A-C$ and $B-C$ bonds were reported by Shaukat and Hussian [S5S1] The tetragonal distortion

occurs as a result of the difference in interactions parallel to the c-axis and those normal to the c-axis, i.e. difference between the $A-C-B$ interactions and the mean of the $A-C-A$ and $B-C-B$ interactions. This difference can be approximated by the difference between $A-C$ and $B-C$ interactions [73A1, 81B1]. The electronegativity values were defined through the density functional orbital radii of the elemental atom [80Z1]. They were derived from the ground-state screened atomic pseudopotential

$$V_{eff}^{(l)}(r) = V_{ps}^{(l)}(r) + \frac{l(l+1)}{r^2} + V_{ee}[n] + V_z[n] + V_{cr}[n] \qquad (2-18)$$

at its crossing point, i.e.,

$$V_{eff}^{(l)}(r_l) = 0 \qquad (2-19)$$

The values of r_l for the I-III-VI_2 compounds are listed in Table 2.11.

Table 2.11 Orbital radii r_l in atomic units for atoms taken from Ref.[80Z1]

atom	r_s	r_p	r_d
Cu	0.88	1.16	0.185
Ag	1.045	1.33	0.385
Ga	0.76	0.935	0.17
In	0.94	1.11	0.36
Se	0.615	0.67	0.15
Te	0.79	0.88	0.325

The hybridized atomic orbital (HAO) radii are defined for a σ-hybrid on the atom A by

$$r_\sigma(A) = r_p(A) + r_s(A) \quad . \qquad (2-20)$$

and for a π-hybrid on the atom A by

$$r_\pi(A) = r_p(A) - r_s(A) \quad . \qquad (2-21)$$

Mixtures of HAO radii for atoms A and B will form bond orbital (BO) radii :

$$r_\sigma(A,B) = r_\sigma(A) - r_\sigma(B) \quad . \qquad (2-22)$$

and

$$r_\pi(A,B) = r_\pi(A) + r_\pi(B) \quad . \qquad (2-23)$$

Taking only s- and p-orbital contributions into consideration, the bond electronegativity $\gamma(A,B)$ and hybridization $h(A,B)$ for a binary compound $A^N B^{8-N}$ are proportional to $| r_\sigma(A,B) |$ and $r_\pi(A,B)$, respectively. They were successfully used as the coordinates of St. John and Bloch diagram [74S1] to separate compounds of different coordination. Phillips [77P1], however, has pointed out that even in the case of nontransition elemental solids, these HAO radii can be used to separate the binary compounds into various structure groups only after d-orbital corrections. Now the definitions of the HAO radii can be extended for higher orbital corrections to

$$r_I(A) = r_\sigma(A) + dr_d(A) + \ldots \quad . \qquad (2-24)$$

$$r_{II}(A) = r_\pi(A) + dr_d(A) + \ldots \quad . \qquad (2-25)$$

where d represents the contribution of the d-orbital r_d. The bond electronegativity may be written as

$$\gamma(A,B) = r_I(A) - r_I(B) \quad . \qquad (2-26)$$

In ternary ABC_2 compounds the definition of $Y(A,B)$ becomes less trivial because of the presence of the two different types of bond. In order to define dimensionless bond electronegativity values $X(A,C)$ and $X(B,C)$, Shaukat and Singh [78S1] have redefined the HAO radii for atoms A, B and C as

$$r_I(A) = r_o(A) + dr_d(A) + \dots \quad , \tag{2-27}$$

$$r_I(B) = r_o(B) + dr_d(B) + \dots \quad , \tag{2-28}$$

and

$$r_I(C) = r_o(C) - 2dr_d(C) + \dots \quad , \tag{2-29}$$

in which the radius of the central C atom has been corrected in the opposite direction by double the amount of that used for the A and B atoms. Thus, the dimensionless bond electronegativity values for the $A-C$ and $B-C$ bonds in CH are written as

$$X(A,C) = \frac{r_I(A) - r_I(C)}{r_I(C)} \quad , \tag{2-30}$$

and

$$X(B,C) = \frac{r_I(B) - r_I(C)}{r_I(C)} \quad , \tag{2-31}$$

The difference in electronegativity between $A-C$ and $B-C$ bonds is then

$$\begin{aligned} \Delta X_{CH} &= X(A,C) - X(B,C) \\ &= \frac{r_I(A) - r_I(B)}{r_I(C)} \quad . \end{aligned} \tag{2-32}$$

Thus, ΔX_{CH} is the parameter which describes the different between $A-C$ and $B-C$ bonds in ternary CH compounds.

Using Eqs. (2-27) to (2-34) and the values of r_I listed in Table 2-11, ΔX_{CH} for ternary compounds at each corner of the representation cube can be calculated. The d- orbital correction was taken from

the values of $(1-G)$ in Table 4.6 for the ternary compounds as suggested in [S5S1]. In order to apply this result to the present alloy data for r, ΔX_{CH} for the alloys were defined as the weighted mean of the compound values, e.g., on the In- section $(Cu_{1-x}Ag_x)\,In\,(Se_{1-z}\,Te_z)_2$

$$\Delta X_{CH} = (1-z)[(1-x)\Delta X_{CH}(CuInSe_2) + x\Delta X_{CH}(AgInSe_2)] + z[(1-x)\Delta X_{CH}(CuInTe_2) + x\Delta X_{CH}(AgInTe_2)] \qquad (2-33)$$

In the work of Shaukat and Hussian [S5S1], fitting was made separately to the Cu- and Ag- compounds with the implication that variation in the III- or VI- atoms had less effect than that of Cu- and Ag- atoms. However, the present results in Figs. 2.24 and 2.25, the plots of the observed of r against ΔX_{CH} show that there is as much spread in the results of In- and Ga- sections, as there is for the Cu- and Ag- sections. Thus there is no justification for the equations presented separately for Cu- and Ag- sections. If a general equation,

$$r = r_0 + r_1\Delta X_{CH} + r_2(\Delta X_{CH})^2 \qquad (2-34)$$

is of use it must be applied to all points in the system. The best fit obtained for the alloys of all the sections is

$$r = -0.001 + 0.039(\Delta X_{CH}) + 0.530(\Delta X_{CH})^2 \qquad (2-35)$$

with a standard deviation of 0.015.

The observed values of r and calculated values of ΔX_{CH} are plotted and the fitted curve is also shown in Fig. 2.26. From inspection of graphs Figs. 2.23 and 2.26, it appears that this method gives a better correlation than that of the CTB theory but the analysis gives the same value of standard deviation in both cases.

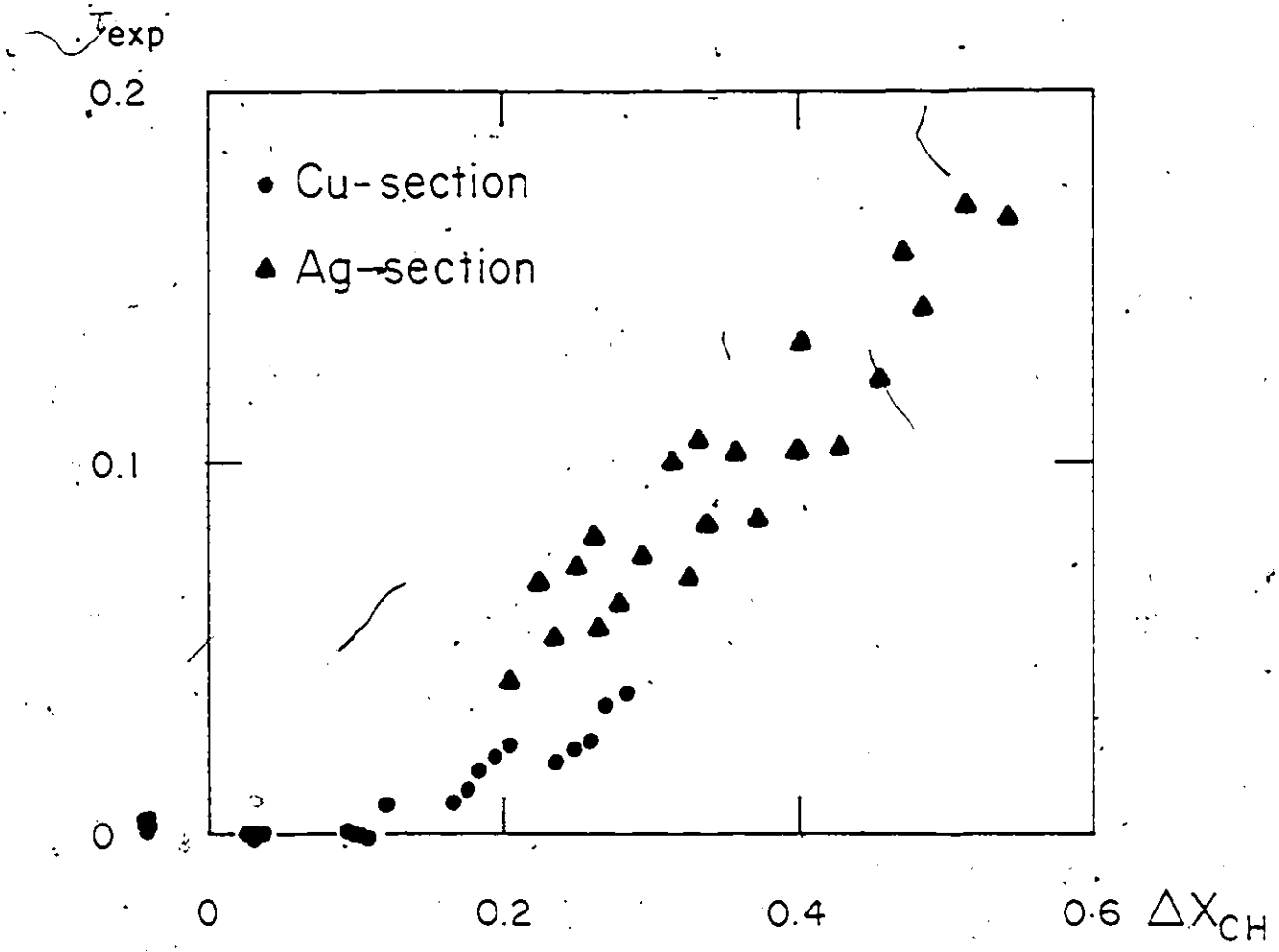

Fig. 2.24 $Cu\{Ga_{1-y}In_y\}(Se_{1-z}Te_z)_2$ and $Ag\{Ga_{1-y}In_y\}(Se_{1-z}Te_z)_2$ Plot of the measured tetragonal distortion τ_{exp} against the value of the difference in bond electronegativities ΔX_{CH} calculated from the method proposed by Shaukat and Hussian.

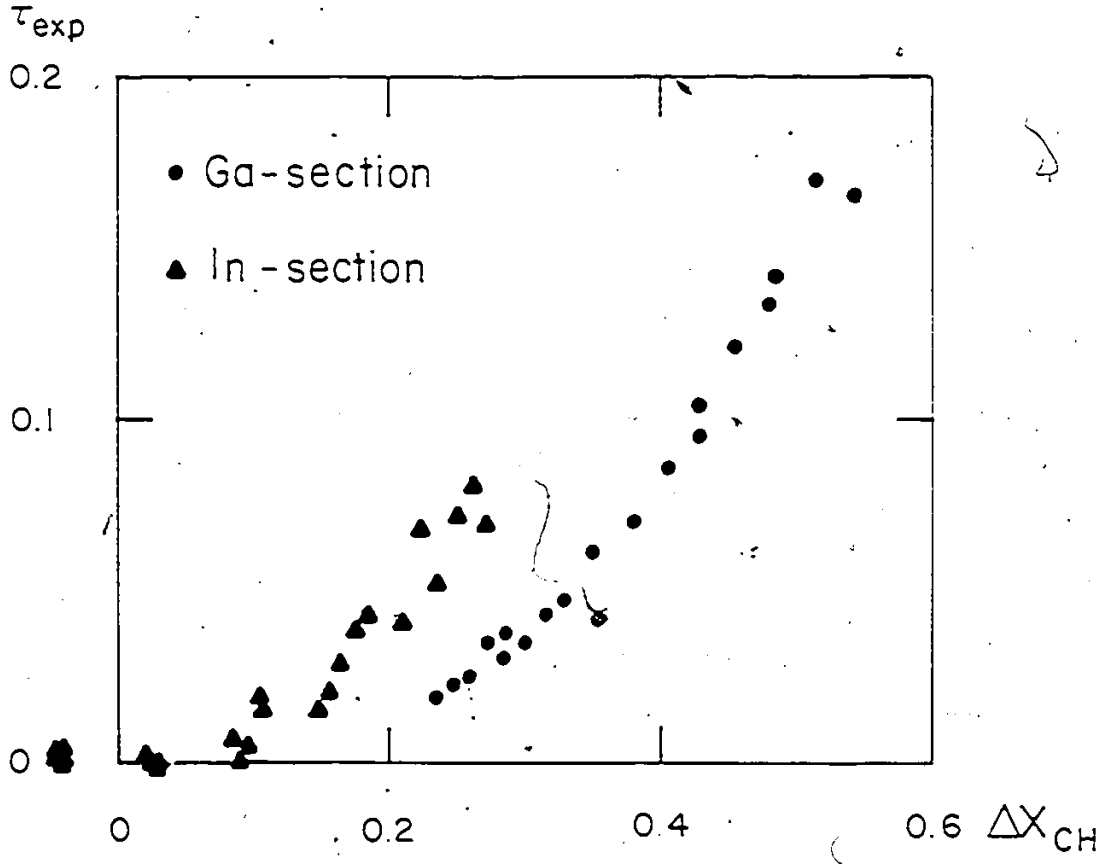

Fig. 2.25 $(Cu_{1-x}Ag_x)Ga(Se_{1-z}Te_z)_2$ and $(Cu_{1-x}Ag_x)In(Se_{1-z}Te_z)_2$ Plot of the measured tetragonal distortion τ_{exp} against the value of the difference in bond electronegativities ΔX_{CH} calculated from the method proposed by Shaukat and Hussian.

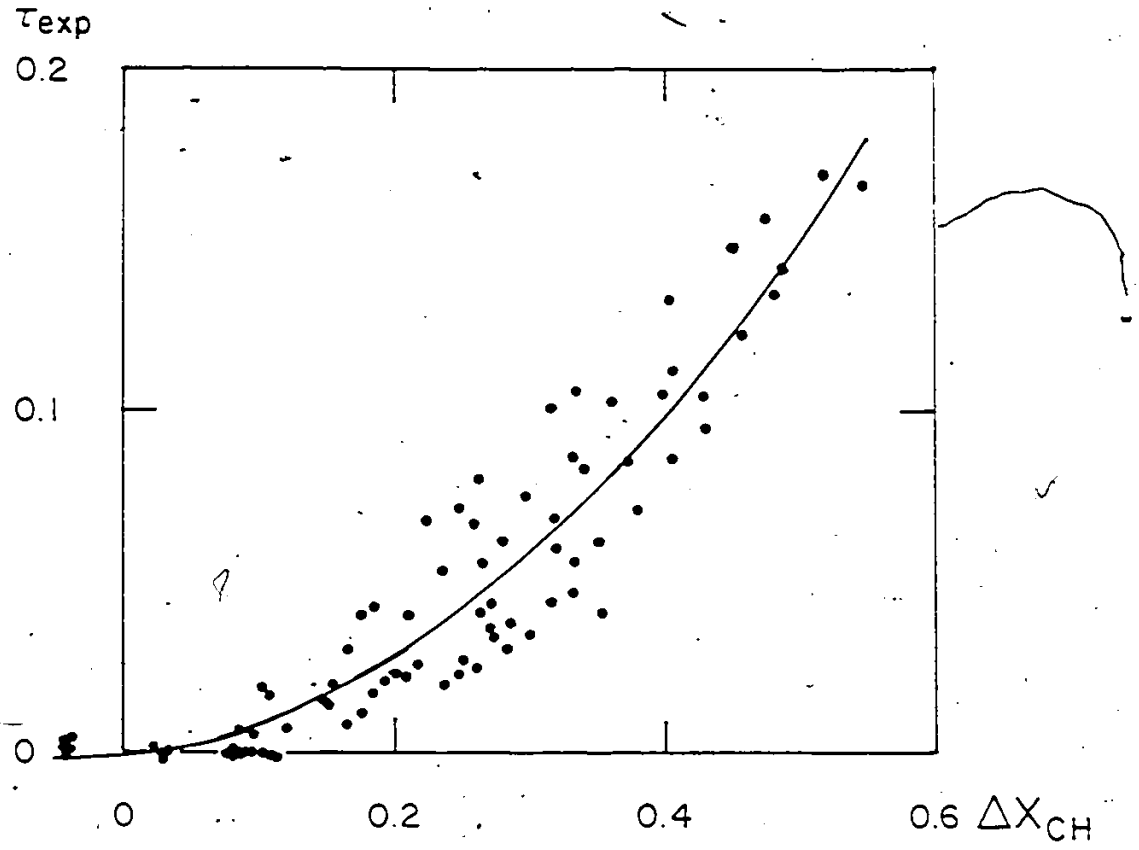

Fig. 2.26 $(Cu_{1-x}Ag_x)(Ga_{1-y}In_y)(Se_{1-z}Te_z)_2$ Plot of the measured tetragonal distortion τ_{exp} against the value of the difference in bond electronegativities ΔX_{CH} calculated from the method proposed by Shaukat and Hussian. The curve is a parabolic fit for τ_{exp} as a function of ΔX_{CH}.

2.9 Summary

The alloy system $(Cu_{1-x}Ag_x)(Ga_{1-y}In_y)(Se_{1-z}Te_z)_2$ was investigated and equilibrium conditions were determined throughout the complete range of composition. Polycrystalline samples of 125 different compositions with x,y, and z=0, 0.25, 0.50, 0.75 and 1.0 were prepared by a melt and anneal technique. Different annealing temperatures in the range 600−800°c were used depending upon the alloy composition and in some cases annealing times of up to 5 months needed to attain equilibrium conditions. Debye-Scherrer x-ray powder photographs were used to investigate the equilibrium conditions. It was found that single phase chalcopyrite structure was obtained for all compositions of the copper (x=0), indium (y=1) and tellurium (z=1) sections but that miscibility gaps occurred in the silver (x=1), gallium (y=0) and selenium (z=0) sections, and these miscibility gaps extended through the general alloy system inside the cube. Values of lattice parameters a and c were determined for all samples showing single phase condition and for each of the above sections the variaitons of a and c with composition were fitted to power series containing 9 parameters in the appropriate composition coordinates. Hence, contours of constant a and constant c were determined. From the parameters for each section, general series expressions for a and c in x, y, and z were developed and the necessary parameters were obtained by averaging over the corresponding parameters of all of the sections. The values determined from the general expression were then compared with the experimental values for the general alloys.

The CTB theory Eq. (2-15) was used to predict the lattice parameter a and the tetragonal deformation η. The radii of the anions and cations were taken as the weighted mean of the elemental values. The best correlation was obtained for lattice parameter a and tetragonal deformation η by using for the elemental radii the Phillips values and the Pauling values, respectively.

It was found that there was a good correlation between the values of tetragonal distortion r and the p electronegativity differences between the $A-C$ and $B-C$ bonds (ΔX_{CH}). The electronegativity values were defined in terms of the HAO radii of the elemental atoms using the density functional orbital radii of Zunger [S0Z1]. The d-orbital corrections to ΔX_{CH} were taken from $(1-\alpha)$, fractional d-character from the $p-d$ hybridization model in Chapter 4. These correlations for r are better than those of the CTB theory.

Chapter 3

Some Optical Properties of the $(Cu_{1-x}Ag_x)(Ga_{1-y}In_y)(Se_{1-z}Te_z)_2$ System

3.1 Overview

This chapter will be concerned with some optical properties of the alloy system. Optical absorption measurements have been used to determine values of optical energy gap at room temperature. This was done only for the Cu- and In- sections. Because of the problems of preparation of very thin samples for transmission measurement, it was not possible to obtain these energy gap values for some compostions even though the equilibrium conditions of those compositions had been obtained. Thus photoacoustic measurements in which powder samples can be used, were employed to give approximate optical energy gap values.

Constant E_g contours will be given in the last section, these being obtained by the same method as those for the lattice parameters in Section 2.6.

3.2 Optical Absorption Determination of Energy Gaps

3.2.1 Introduction

The fundamental absorption edge of semiconductors correspond to the threshold for electron transitions between the valence and conduction band. The absorption is very small for photon energies much

less than that of the energy gap and increases significantly for higher photon energies. The study of the fundamental absorption provides information about the electron states near the band extrema as well as a value for the energy gap.

In a I-III-VI_2 CH compound, the energy band structure is related to that of its II-VI ZB binary analog (see details in Chapter 4). The triple degeneracy of the p-like valence bands which are derived from the Γ_{15} level in the cubic structure is completely removed due to the simultaneous effects of the noncubic crystal-field and spin-orbit interactions. In addition to these effects, the uppermost valence bands of I-III-VI_2 compounds are influenced by the admixture of the noble-metal d levels [75S2] and as a result the valence bands are not simply related to those of II-VI binary analog. This problem will be studied in Chapter 4.

In the absence of spin-orbit interaction, the crystal-field interaction will split the triply degenerate Γ_{15} valence band into a non-degenerate Γ_4 and a doubly degenerate Γ_5 valence bands. The inclusion of the spin-orbit effects changes the symmetry of the Γ_1 conduction band to one of Γ_6, the Γ_4 valence band to one of Γ_7, and lifts the degeneracy of the Γ_5 valence band by splitting it into the valence bands of Γ_6 and Γ_7 symmetry.

The valence-to-conduction band transitions are conventionally labelled E_A,E_B and E_C in terms of increasing energy, and these transition together with the usual valence band ordering and the polarization selection rules are indicated in Fig. 4.3 (see page 110). Thus the fundamental absorption in this case would be expected to be the transition from the Γ_7 upper valence band to the Γ_6 conduction band.

The theory of optical absorption, and the transmission measurement will be briefly summarized in the next two sections. The experimental method will be appeared in Section 3.2.4. The last section of

this part will present the results and discussion of the experimental results.

3.2.2 Theory of Optical Absorption

A good review of the subject can be found in Volume 3 of Semiconductors and Semimetals [67J1]. Only a summary will be presented here.

The absorption coefficient determine the energy absorption in solid through which the light wave is travelling. It can be expressed as the energy absorbed per unit volume per unit time divided by the energy flux. From the quantum mechanical point of view it depends on the probability of an electron being promoted from the valence band to the conduction band. The shape of the absorption edge is determined by the nature of the optical transitions between the upper edge of the valence band and the lower edge of the conduction band. If both band extrema lie at the same point in the Brillouin zone, direct transitions (with the approximate conservation of the electron wave vector) are possible. These can be separated into "allowed" and "forbidden" transitions depending on whether the dipole optical matrix element which determines the transition probability exists or vanishes in the first approximation. At the Γ point of CH crystal , however, the transitions can be very weak if they are pseudo-direct [75S2, 81J1] because the optical matrix element is very small. When the band extrema lie at different $\vec{k}$ values, only indirect transitions with phonon participation are possible between them.

For simple parabolic bands, the absorption coefficient due to direct "allowed" transition has been shown [67J1] to satisfy the equation

$$(\alpha h\nu) = \frac{2ch}{n}\left(\frac{2\mu}{h^2}\right)^{\frac{3}{2}}|H_{cv}(o)|^2(h\nu - E_g)^{\frac{1}{2}} \quad .$$

or

$$(\alpha h\nu)^2 = A(h\nu - E_g) \quad . \qquad (3-1)$$

where μ is the reduced electron-hole mass, H_{cv} the optical matrix element between the valence band and conduction band states, $h\nu$ the photon energy, and E_g the fundamental gap. The corresponding result for direct "forbidden" transition is

$$(\alpha h\nu) = \frac{2ch}{n}\left(\frac{2\mu}{h^2}\right)^{\frac{3}{2}}\left|\frac{\partial}{\partial k}|H_{cv}(\bar{k})|\right|_{\bar{k}=0}(h\nu - E_g)^{\frac{3}{2}} \quad .$$

or

$$(\alpha h\nu)^{\frac{2}{3}} = A'(h\nu - E_g) \quad . \qquad (3-2)$$

However, for the indirect transition, the absorption coefficient is composed of two terms which describe the two possible processes, direct transition of the electron combined with absorption or emission of a phonon.

The absorption coefficient for indirect transition is expressed [78S2] as

$$\alpha_i = B\left[\frac{(h\nu - E_g + \hbar\omega_q)^2}{exp(\hbar\omega_q/k_BT) - 1} + \frac{(h\nu - E_g - \hbar\omega_q)^2}{1 - exp(-\hbar\omega_q/k_BT)}\right] \quad . \qquad (3-3)$$

where $\hbar\omega_q$ is the phonon energy.

In addition, the fundamental absorption could be affected by processes which depend upon departures from perfect periodicity that can occur in a real crystal at a finite temperature.

3.2.3 Transmission Measurement

The fundamental edge may be determined from transmission measurements by observing the change in absorption as a function of incident photon energy. In general, measurements are made at near normal incidence with both the transmitted and reflected intensities being recorded. However, as will be shown presently, the reflected portion of the incident radiation need not be considered here.

Consider a dielectric medium with a complex index of refraction given by $N = n + i\kappa$, where n is the refractive index and κ the extinction coefficient. At normal incidence radiation of intensity I_o, the transmitted and reflected intensities I_t and I_r are given by Greenway and Harbeke [GSG1] as

$$I_t = \frac{I_o(1-R)^2 e^{-\alpha d}(1+\kappa^2/n^2)}{1-R^2 e^{-2\alpha d}} \qquad (3-4)$$

and

$$I_r = \frac{I_o R(1-e^{-2\alpha d})}{1-R^2 e^{-2\alpha d}} \qquad (3-5)$$

where the reflectivity R and absorption coefficient α are expressed respectively as

$$R = \frac{(n-1)^2+\kappa^2}{(n+1)^2+\kappa^2} \qquad (3-6)$$

and

$$\alpha = \frac{4\pi\kappa}{\lambda} \qquad (3-7)$$

λ being the wavelength in vacuum. For energies near the absorption edge, κ is very much less than n. If in addition the sample thickness d is large enough to ensure that $R^2 e^{-2\alpha d}$ is much less than 1, Eq.(3-4) reduces to the simple form

$$\frac{I_t}{I_o} = (1-R)^2 e^{-\alpha d} \qquad (3-8)$$

Generally, the reflectivity varies slowly with photon energy, and the spectral variation of the transmission is principally due to the variation of the absorption coefficient. Thus the $(1-R)^2$ term may be treated as constant. Hence

$$\varsigma = \frac{1}{d}\ln(\frac{I_o}{I_t}) = \alpha + constant \quad . \qquad (3-9)$$

As can be seen from Eq. (3-9), the calculation of α from I_o/I_t ratio which neglects the reflection term will give values which are too large by a constant amount for a given sample.

In the experimental work the value of ς was determined as a function of photon energy $h\nu$. In order to determine the absorption coefficient α due to interband transitions, an appropriate background absorption must be subtracted from the measured values of ς before proceeding with any further analysis. This will be discussed in Section 3.2.5.

3.2.4 Experimental Method

The transmission measurements were made using the experimental set up shown in Fig. 3.1. The light from a 30W tungsten filament lightbulb was collected by a mirror and focused at the entrance slit of a Czerner-Turner scanning spectrometer. The light beam was chopped by a Rofin model 7500 light chopper positioned before the entrance slit. The monochromatic light from the exit slit of the spectrometer was refocussed by a mirror on to the sample which was mounted directly on a sample holder in front of a detector. The transmitted light was detected by either a Dumont-6911 photomultiplier or a biased PbS cell depending upon the energy range concerned. The signal from the detector was amplified by a PAR-213 preamplifier, the output of which was applied to a PAR-219 lock-in amplifier with a reference signal from the light chopper. The wavelength of the incident light was continuously varied and the output from

the lock-in amplifier traced on a strip chart recorder. In order to minimize the error in reading data from these charts, the sensitivities of the lock-in and the chart recorder were adjusted to maintain as close to full scale deflection as possible on the chart. This spectrum represents the transmitted I_t spectrum. The reference I_o spectrum was similarly obtained by removing the sample from the sample holder.

The sample was sliced from the ingot prepared in Section 2.3 to a thickness of 0.5 mm to 1 mm on a tungsten wire saw which used a mixture of oil and silicon carbide grit as the cutting slurry. The sliced sample was further polished using a polishing wheel. The sample was mounted on the end of a brass rod using molten paraffin wax. The rod was then held so that the sample was in contact with a rotating polishing disc. A slurry of water and 1 μm mesh alumina powder was used as the polishing agent. After a uniform smooth surface had been obtained, the sample was turned over and further polished down to a thickness of the order of 200 μm, or less if possible, to give samples for optical absorption measurements. When the sample had reached the desired thickness, the brass rod was immersed in warm acetone to remove the sample from the rod and the wax from the sample. However, since the samples were polycrystalline, they tended to crumble while being removed from the rod and hence very thin samples were not possible for a number of the alloys produced. As a result, in some cases, the background absorption was so high that no absorption edge could be observed and therefore for some compositions, although good lattice parameter data were obtained, no energy gap value could be determined.

The sample was next mounted on a blackened brass disc, the centre of which had been drilled out to as large an aperture as could be covered by the prepared slice, and placed in front of the detector. After the transmission measurements were made, the sample was removed and its thickness was measured using a micrometer capable of reading to within one micron.

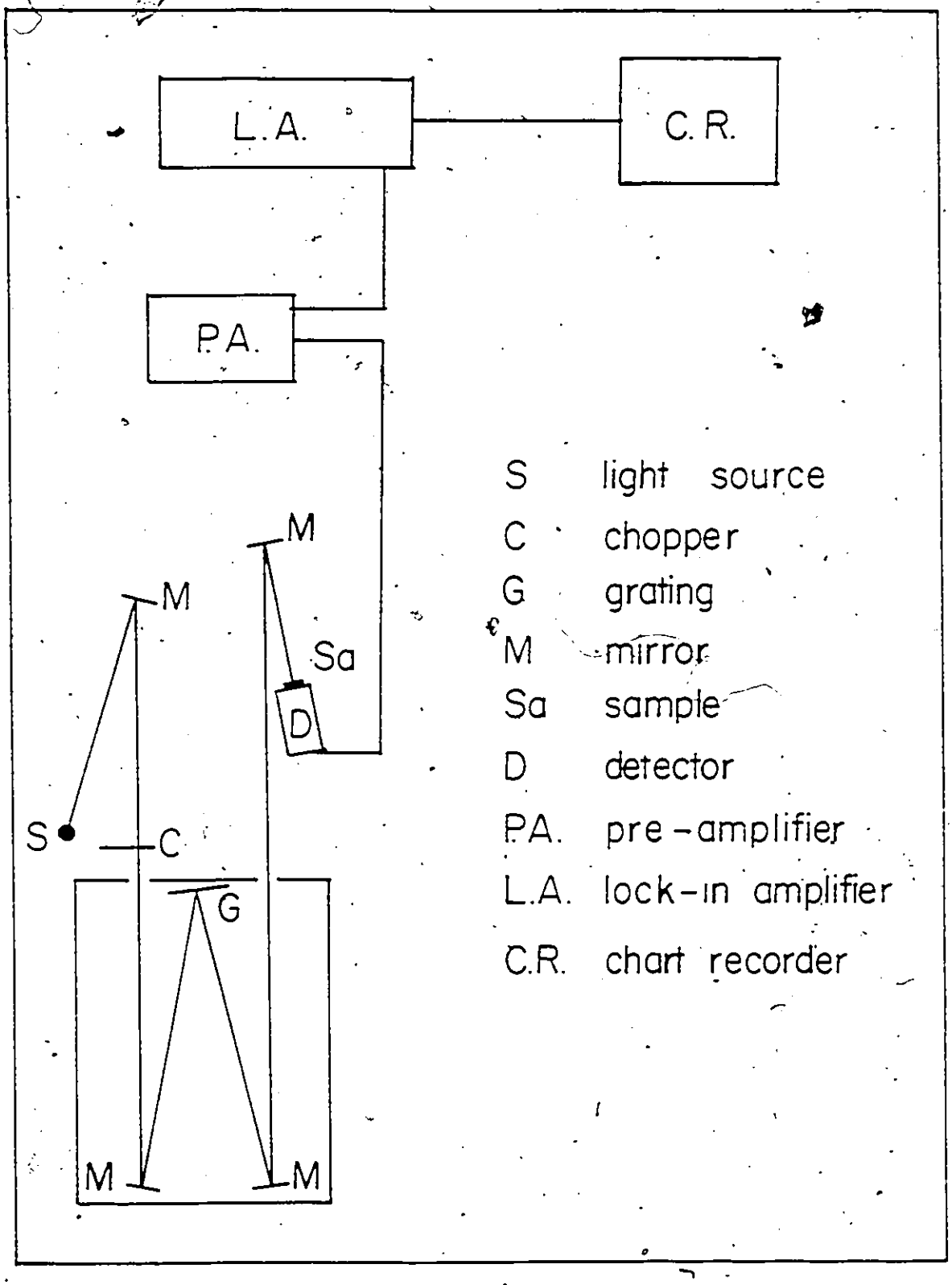

Fig. 3.1 Block diagram of optical absorption experimental arrangement.

3.2.5 Results and Discussion

Fig 3.2 - 3.4 show the typical resulting curves of $\varsigma = \frac{1}{d}\ln(\frac{I_o}{I_t})$ as a function of $h\nu$, the photon energy, for alloys of compositions 000075, 002550 and 005075 with sample thicknesses of 40.44 and 130 μm, respectively. The transmitted intensity was measured down to lower photon energies so as to ensure accurate determination of the background absorption. For the first two samples, straight line extraplation of the background absorption was made and is shown as the dashed lines in Figs. 3.2 and 3.3. But the background absorption for the alloy composition 005075 in Fig. 3.4 can be better fitted to a power law relation of the form $\varsigma = \varsigma_1(h\nu)^{-m}$ where ς_1 is the value of ς at 1 eV which was found to be 396 cm^{-1}, and m is equal to 1.4. This indicates the effect of free carrier scattering [S2G1].

These values of background absorption which included imperfection, free carrier effects, etc., were subtracted from the measured values of ς in order to give the absorption coefficient α due to interband absorptions. These are shown in Figs. 3.5 - 3.7. The absorption edges of these alloys are characterized by a steep variation of the absorption coefficient at high energies and a shallower portion at lower energies. The steep absorption coefficients extend to about 1500, 1100, and 500 cm^{-1} for the alloy compositions 000075, 002550, and 005075, respectively. The magnitude of these α values are comparable with those observed in CH semiconductors [73Y1, 79H1]. The highest values of α quoted in the literature are for $CuInSe_2$ [79H1]. That sample was a 0.11 μm thin film which had a direct band gap with α values, saturated above the band gap, of $2 - 5 \times 10^{-5}$ cm^{-1}. This saturation region of α has not been observed in the present work because very thin samples were not possible from polycrystalline crystals. The tail on the absorption edge at low absorption levels is similar to those observed in the fundamental absorption edge of CdTe [80D1] (binary analog of $AgInTe_2$) which has band extrema at the Γ-point.

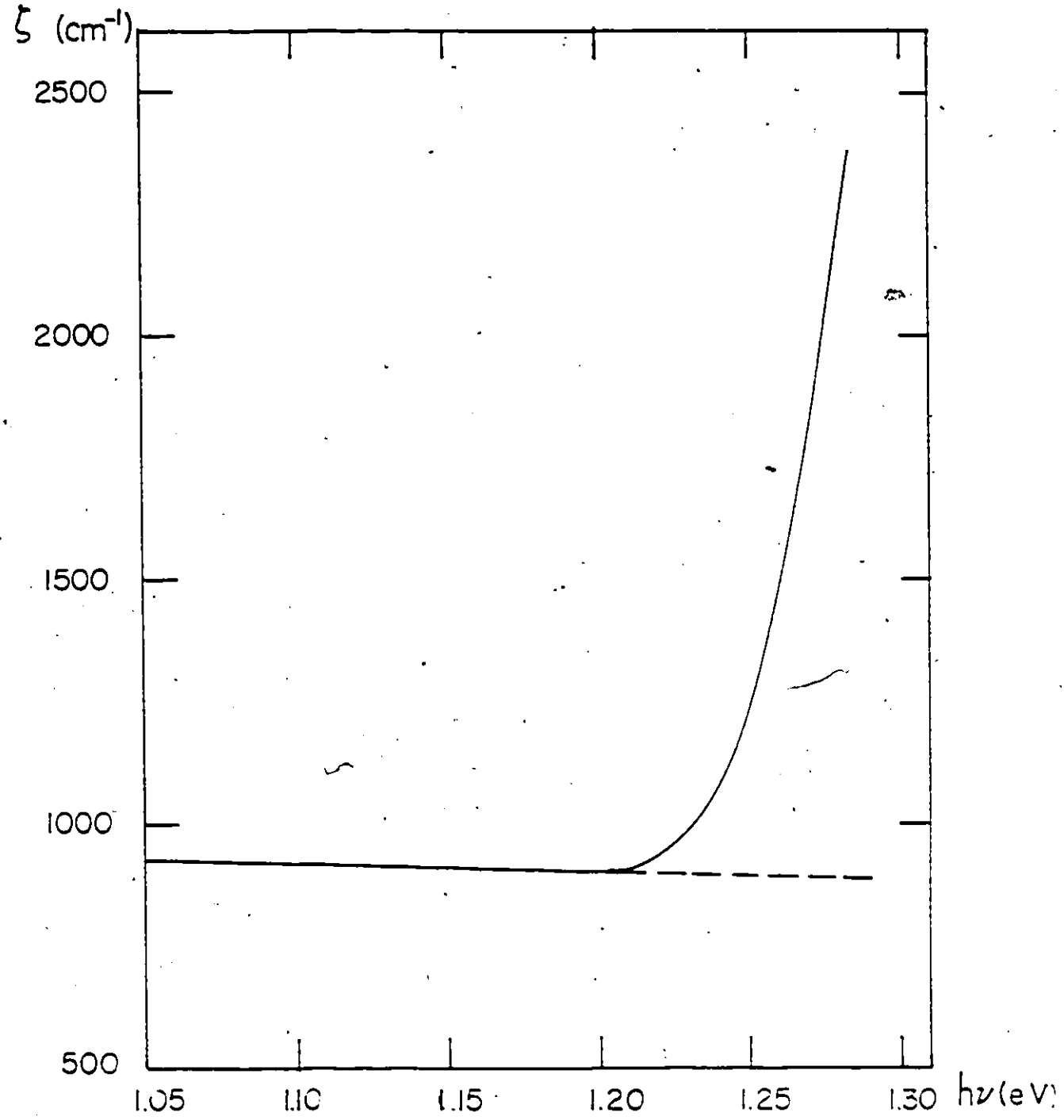

Fig. 3.2 $(Cu_{1-x}Ag_x)(Ga_{1-y}In_y)(Se_{1-z}Te_z)_2$ Variation of $\frac{1}{d}\ln(I_o/I_t)$ (i.e., ζ) with photon energy $h\nu$ for sample 000075. ($d = 40\mu m$). Full line experimental values. Dashed line extrapolation of background values.

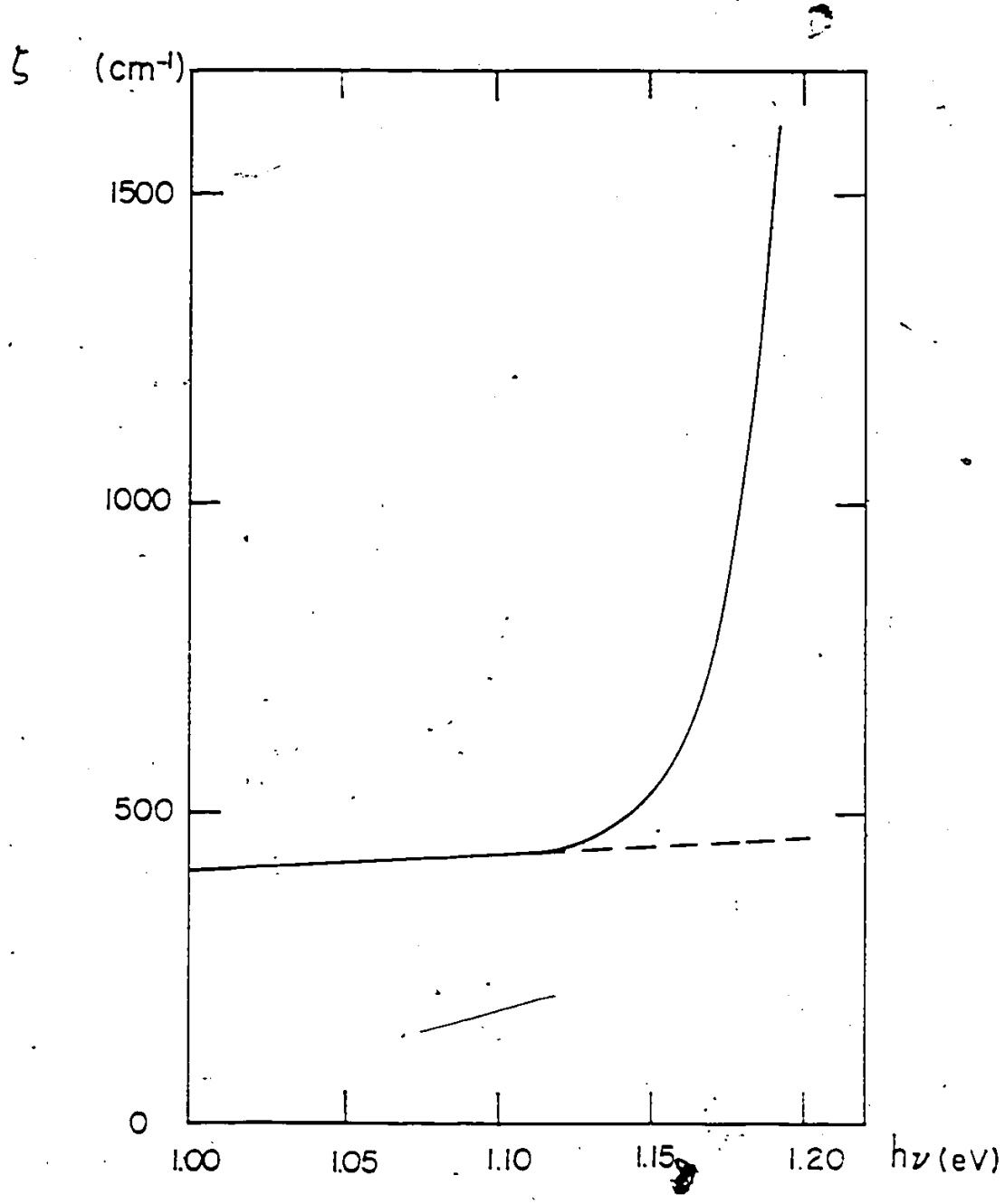

Fig. 3.3 $(Cu_{1-z}Ag_z)(Ga_{1-y}In_y)(Se_{1-x}Te_x)_2$ Variation of $\frac{1}{d}\ln(I_o/I_t)$ (i.e., ζ) with photon energy $h\nu$ for sample 002550. ($d = 44\mu m$). Full line experimental values. Dashed line extrapolation of background values.

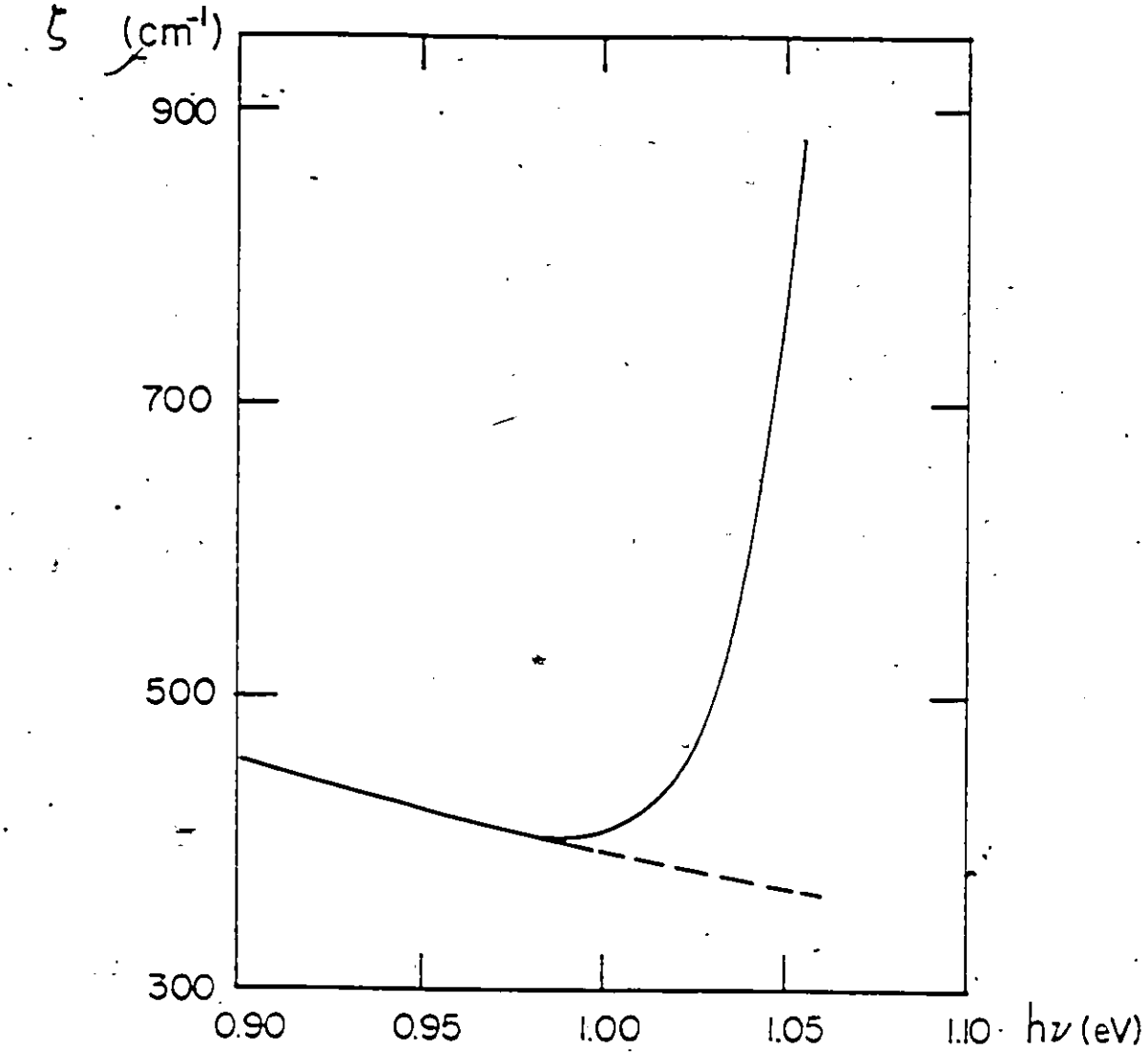

Fig. 3.4 $(Cu_{1-x}Ag_x)(Ga_{1-y}In_y)(Se_{1-z}Te_z)_2$ Variation of $\frac{1}{d}\ln(I_o/I_t)$ (i.e., ζ) with photon energy $h\nu$ for sample 005075. ($d = 130\mu m$). Full line-experimental values. Dashed line extrapolation of background values.

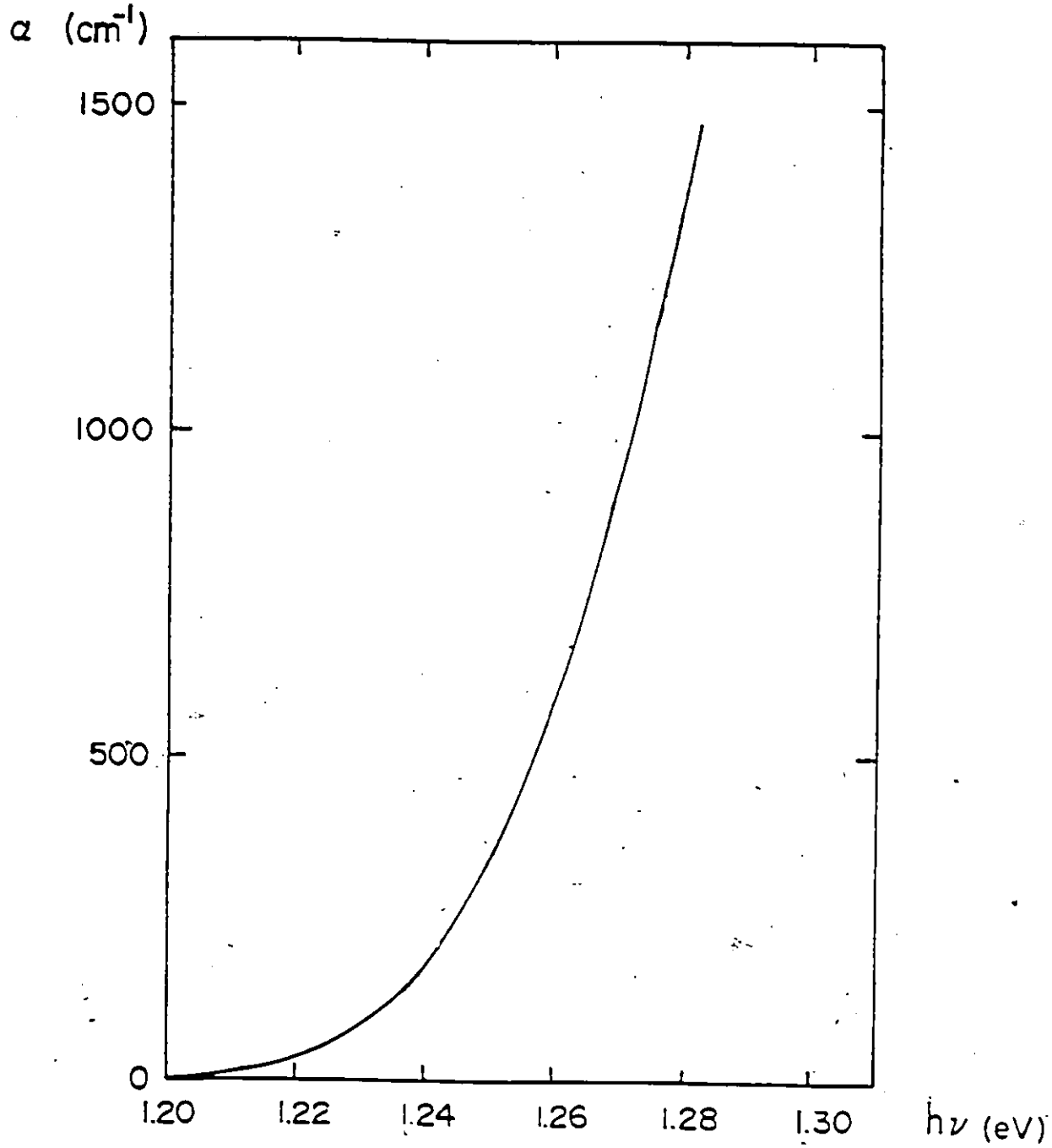

Fig. 3.5 $(Cu_{1-x}Ag_x)(Ga_{1-y}In_y)(Se_{1-z}Te_z)_2$ Variation of absorption coefficient α with photon energy $h\nu$ for sample 000075.

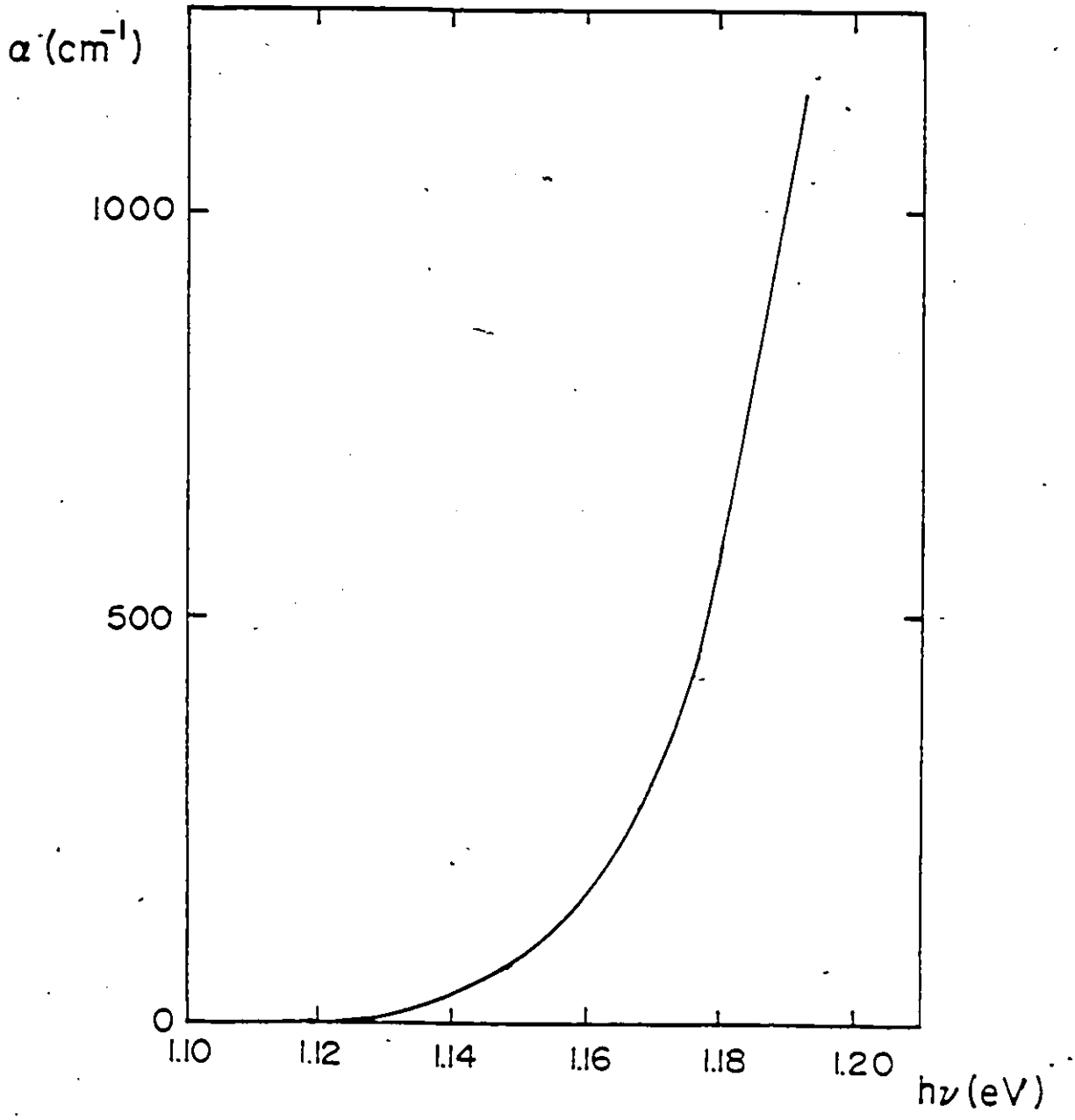

Fig. 3.6 $(Cu_{1-x}Ag_x)(Ga_{1-y}In_y)(Se_{1-z}Te_z)_2$ Variation of absorption coefficient α with photon energy $h\nu$ for sample 002550.

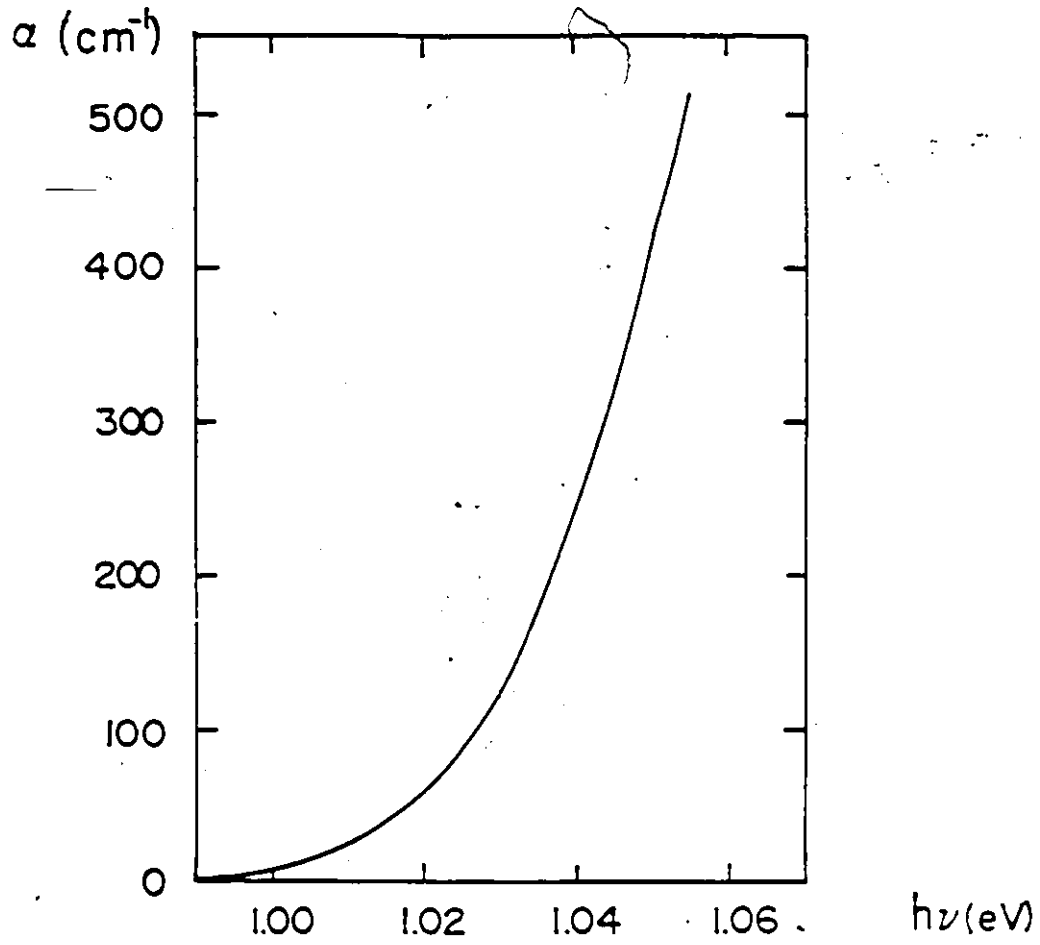

Fig. 3.7 $(Cu_{1-x}Ag_x)(Ga_{1-y}In_y)(Se_{1-z}Te_z)_2$ Variation of absorption coefficient α with photon energy $h\nu$ for sample 005075.

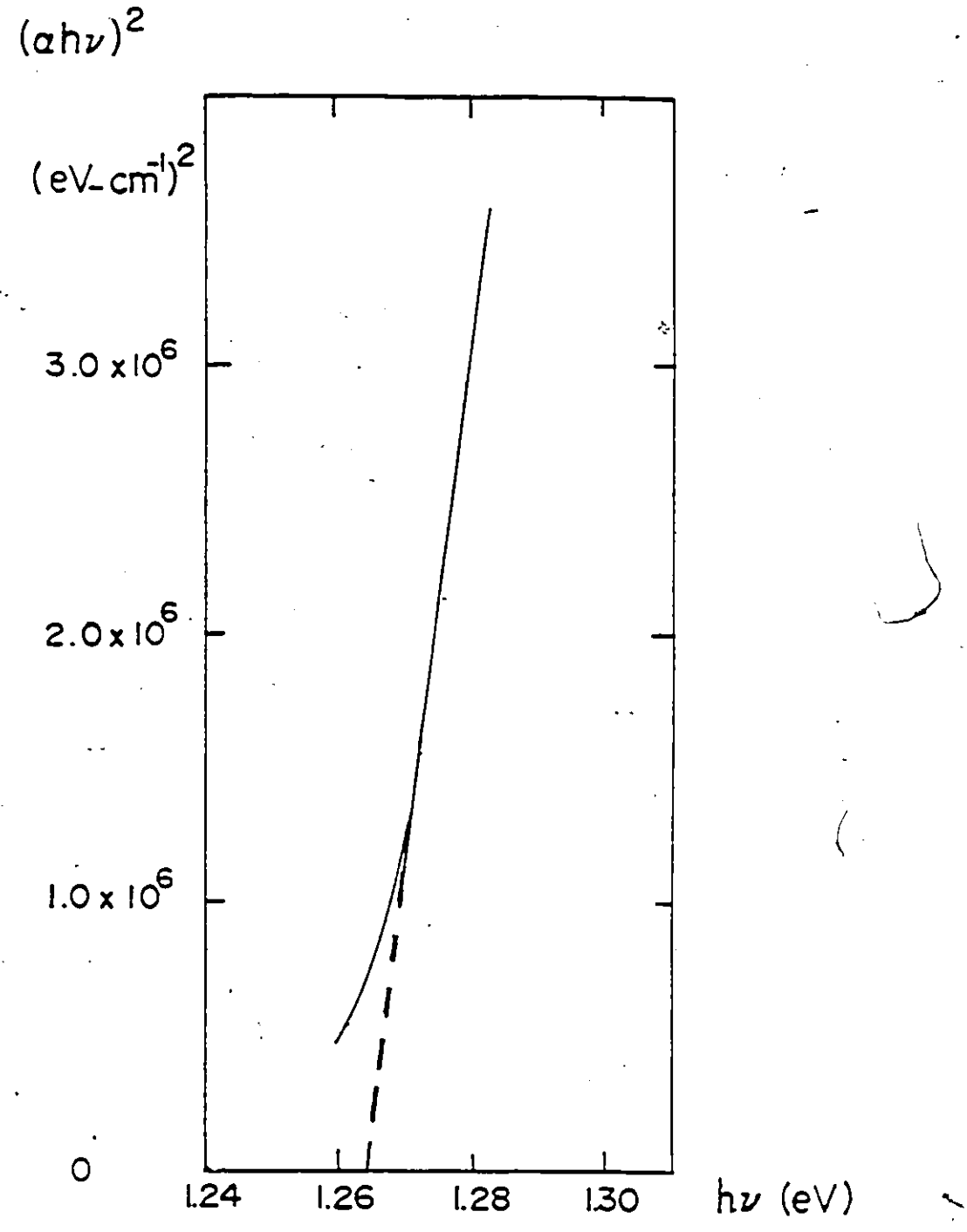

Fig. 3.8 $(Cu_{1-x}Ag_x)(Ga_{1-y}In_y)(Se_{1-z}Te_z)_2$ Variation of $(\alpha h\nu)^2$ with photon energy $h\nu$ for sample 000075 (Full line). A straight line extrapolation for energy gap E_g (dashed line).

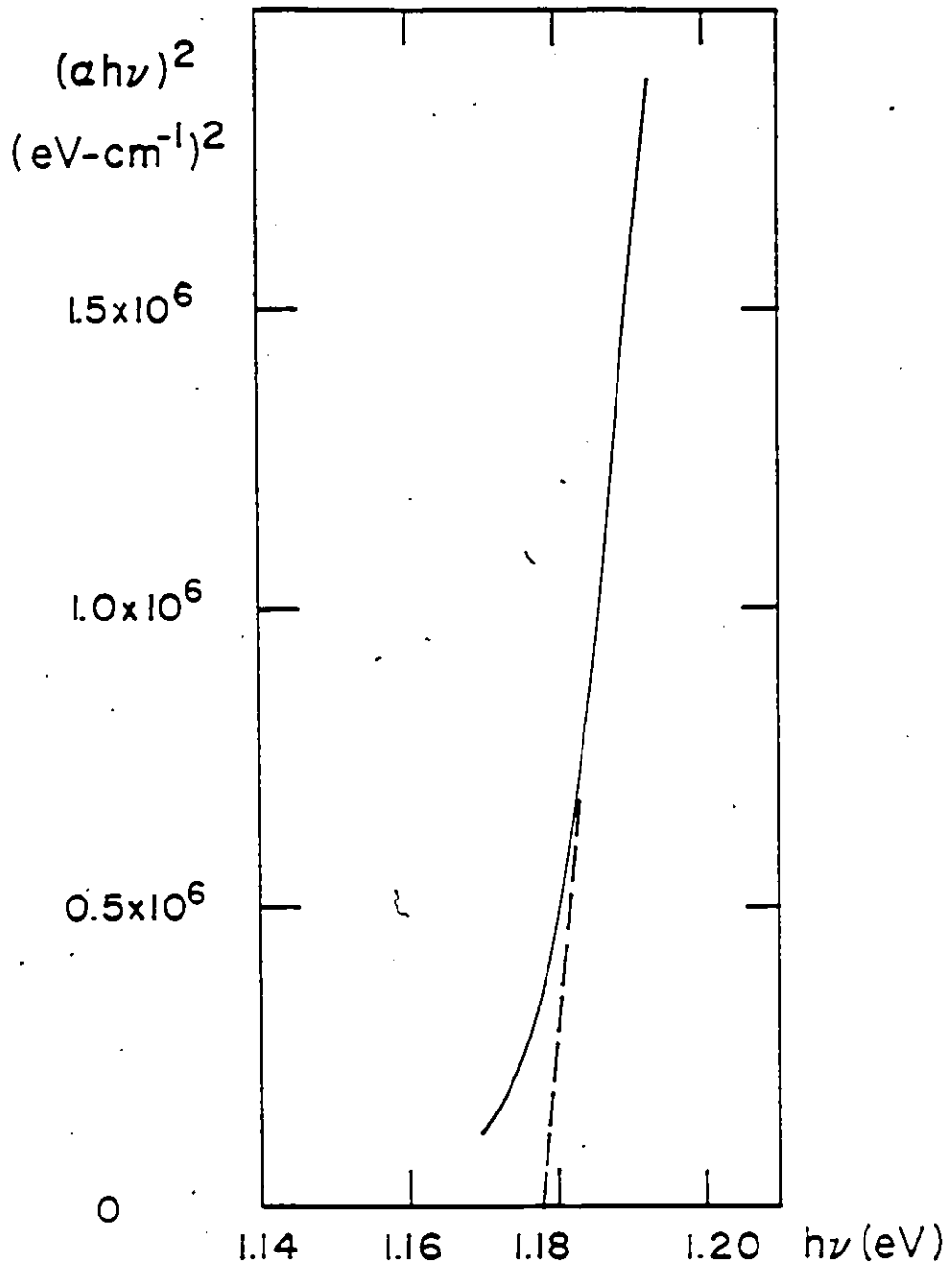

Fig. 3.9 $(Cu_{1-x}Ag_x)(Ga_{1-y}In_y)(Se_{1-z}Te_z)_2$ Variation of $(\alpha h\nu)^2$ with photon energy $h\nu$ for sample 002550 (Full line). A straight line extrapolation for energy gap E_g (dashed line).

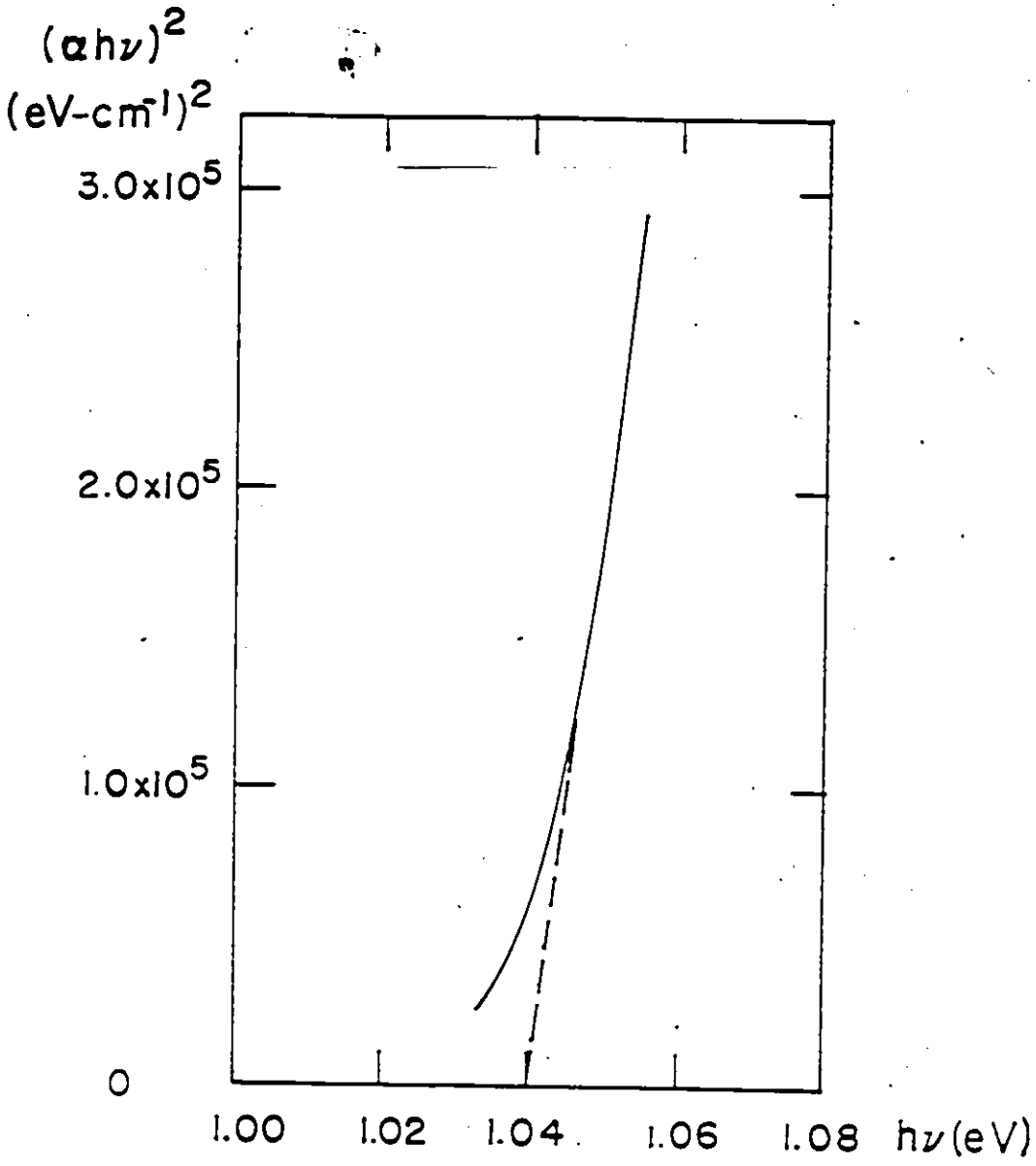

Fig. 3.10 $(Cu_{1-x}Ag_x)(Ga_{1-y}In_y)(Se_{1-z}Te_z)_2$ Variation of $(\alpha h\nu)^2$ with photon energy $h\nu$ for sample 005075 (Full line). A straight line extrapolation for energy gap E_g (dashed line).

Table 3.1 Energy gap values of the $Cu(Ga_{1-y}In_y)(Se_{1-z}Te_z)_2$ section. E_g denotes an absorption energy gap and E_p a photoacoustic energy gap.

Sample	E_g(eV)	E_p(eV)
000000	-	1.52
000025	1.395	1.42
000050	-	1.23
000075	1.264	1.30
000010	1.315	1.34
002500	1.384	1.37
002525	1.220	1.26
002550	1.178	1.18
002575	-	1.20
005000	1.229	1.21
005025	1.088	1.09
005050	1.044	1.06
005075	1.040	1.08
007500	1.106	1.06
007525	0.977	0.96
007550	0.926	0.96
007575	0.957	0.97
001000	0.954	0.94
001025	0.854	-
001050	0.845	-
001075	0.875	-
001010	0.945	0.90

Table 3.2 Energy gap values of the $(Cu_{1-x}Ag_x)In(Se_{1-z}Te_z)_2$ section. E_g denotes an absorption energy gap and E_p a photoacoustic energy gap.

Sample	E_g(eV)	E_p(eV)
251000	0.906	-
251025	0.859	-
251050	-	0.81
251075	0.870	-
251010	0.927	-
501000	1.032	-
501025	0.898	-
501050	0.845	-
501075	0.859	-
501010	0.916	-
751025	0.912	-
751050	0.893	-
751075	0.872	-
751010	0.930	-
101000	1.110	-
101025	1.040	-
101050	0.933	-
101010	0.938	0.91

This tail has also been observed in InSb [55R1]. Originally it was believed that in addition to the direct transition at the Γ-point, there were indirect transitions at energies a few hundreths of an electron volt lower [60D1, 6SL1]. However, Dumke [57D1] and Johnson [67J1] have analysed this type of absorption curve in terms of direct transitions only and have attributed the tail in the absorption curve to transitions involving the absorption of an optical phonon with momentum q very close to zero. This will affect the absorption curve only at lower portion energies below the direct energy gap. However, if such a phonon is emitted in an absorption, it will take place on the higher energies side of the direct energy gap, and will certainly be obscured by the much stronger absorption due to the direct transitions. In an alloy sample one might also expect some band tailing due to the random arrangement of the substituted atoms in the lattice, although this may be small.

In a I-III-VI_2 CH semiconductor which has band extrema at Γ point [75S2, 83J2], the optical dipole matrix element does not vanish. Thus direct transitions would be expected. In previous work, the absorption coefficient data for CH compounds and alloys have been fitted using the square law appropriate to a direct energy gap [77H2, 78N2, 82G1, 83M1]. Thus in the present work, the same form was used and graphs of $(\alpha h\nu)^2$ versus $h\nu$ were plotted and are shown in Figs. 3.8 - 3.10 for three typical alloy compositions. These graphs were found to give good straight lines and the intercepts were taken as the energy gap values. The direct energy gap values so obtained for the alloy compositions 000075, 002550, and 003075 were 1.264, 1.178, and 1.040 eV, respectively.

The optical absorption measurements were used to give values of optical energy gap E_g of alloys in the copper (x=0) and indium (y=1) sections. These energy gap values are reported in Table 3.1-3.2 but values for some compositions are not given because very thin samples could not be obtained, as

mentioned earlier. However, in some cases, the two-thirds law seemed to give a better fit and the energy gap values in those cases were lower than those of the corresponding direct gap analysis by as much as 20 meV. This is supported by Smith [78S2] that in some cases for which direct transitions have been observed the variation of α follows more nearly the two-thirds law, [see Eq.(3-2)], rather than the square law, [see Eq.(3-1)], indicated for direct allowed transitions.

For samples in other sections, optical energy gaps have not been determined as yet.

3.3 Photoacoustic Determination of Energy Gaps

3.3.1 Introduction

As shown in Section 3.2, optical absorption measurements have been used to determine the energy gaps of the alloys. However, in some cases, very thin samples could not be produced and hence no absorption edge could be observed. To overcome these difficulties, the photoacoustic spectroscopy (PAS) technique has also been used to measure energy gap values of these alloys. The principal advantage of PAS is that it enables one to obtain spectra similar to optical absorption spectra on any type of solid even when the material is highly opaque. The PAS technique can thus be used to study insulator, semiconductor, or even metals that cannot be readily studied by conventional absorption or reflection techniques. This includes substances that are in the form of powders, or are for some reason difficult to prepare for reflection studies [75R1].

In PAS of solids, the sample to be studied is placed inside a closed cell containing a gas such as air, and a sensitive microphone. The sample is then illuminated with chopped monochromatic light. The analog signal from the microphone is amplified and recorded as a function of the wavelength of the

incident light and the PA spectrum is obtained. The resulting spectrum must then be normalized to the power spectrum of the lamp to remove the structure of the light source. A typical result is shown in Fig. 3.15.

The PAS technique has previously been used to measure the direct energy gap of some II-VI semiconductor compounds [75R1] such as CdSe, CdS, and ZnS. They were all in powder form. The band edge, as measured by the positions of the knees in the normalized PA spectra for these compounds are 1.75, 2.40, and 3.70 eV, respectively. They agrees very well with the values recorded in Ref. [80M1].

In the present study, it was found that an empirical criterion of 50% between the knee and base values of the spectrum could be used to give a PA energy gap in reasonable agreement with that from optical absorption. However, for some alloys, the PA energy gap was higher than the optical absorption energy gap while for others it was lower. It is considered that the optical absorption values are more accurate and the PA energy gap should be used only to give approximate values of the energy gap when optical absorption values can not be obtained.

3.3.2 Theory of Photoacoustic Effect

The theory of PA effect in a solid was formulated by Rosencwaig and Gersho [76R1] (RG theory). It gives a simple physical description of the process and will be briefly described below. There were many workers refining the theory by treating more exactly the transport of the acoustic disturbance in the gas [76B1, 77A1] and by including the contribution to the PA signal due to the thermally induced vibrations of the solid [78M1]. These refinements, however, did not change the basic results of the RG theory for most experimental results [80R1].

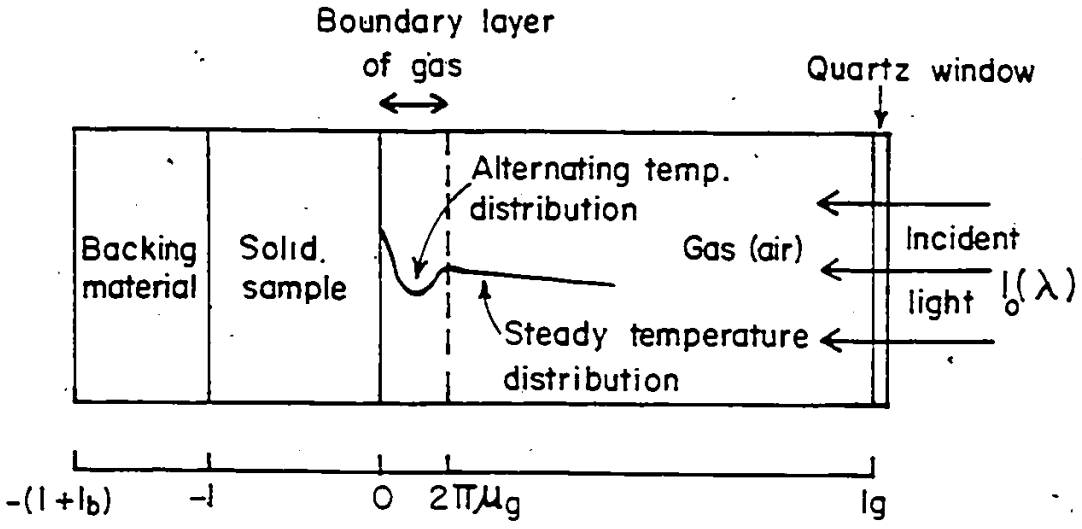

Fig. 3.11 Diagram of a simple photoacoustic (PA) cell. μ_g : thermal diffusion length of gas. l, l_b, and l_g : length of sample, backing, and gas column.

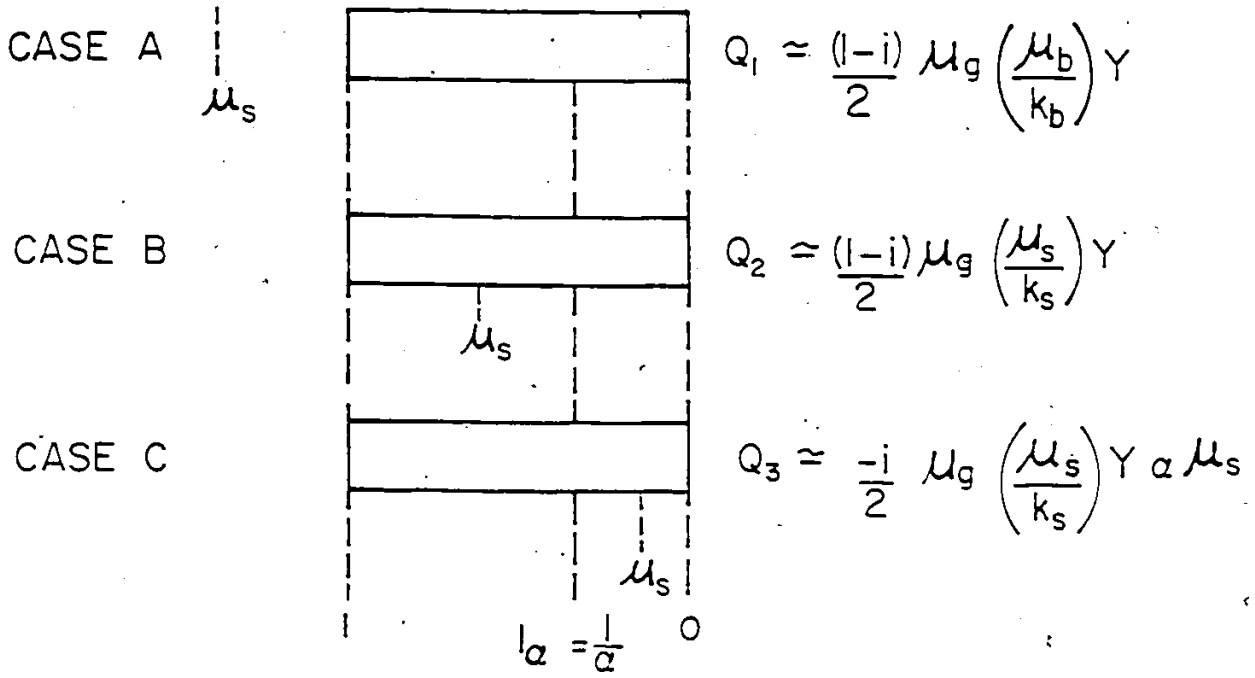

Fig. 3.12 Schematic representation of the special cases for the RG theory. μ_s, μ_g, and μ_b : thermal diffusion length of sample, gas, and backing. l and l_α : length of sample and optical absorption length. α : absorption coeffcient.

The RG theory is a one dimensional analysis of the production of a PA signal in a simple PA cell shown in Fig. 3.11. It shows that the primary source of the acoustic signal in the photoacoustic cell arises from the periodic heat flow from the solid to the surrounding gas as the solid is cyclically heated by the chopped light. Only a relative thin layer of air ($2\pi\mu_g \sim 1$ mm at 100 Hz) in the front of the surface of the solid responds thermally to the periodic heat flow from the solid. This boundary layer of air can then be regarded as a vibrating piston creating the acoustic signal detected in the cell. Since the magnitude of the signal is proportional to the amount of heat coming out from the solid absorber, there is a close correspondence between the magnitude of the acoustic signal and the amount of light absorbed by the solid. The analysis indicates that the magnitude and phase of the acoustic signal also depend on the thermal properties of the sample and the gas in the cell and the chopping frequency (ω). In spite of a rather complicated dependence, the PA spectrum turns out to correspond closely to the optical absorption spectrum of the sample provided that nonradiative recombination processes dominate in the dissipation of the absorbed light energy.

The pressure variation in the simple PA cell has been determined [70R1] to be

$$\delta P(t) = Qe^{i(\omega t - \frac{\pi}{2})} \qquad (3-10)$$

where Q is a pressure amplitude linearly related to the temperature on the surface of the sample. The expression for Q is fairly complicated involving not only the optical parameters of the sample but also thermal and geometrical parameters of sample, gas, and backing material. However, in the case of an optical absorption length l_α much less than the thickness l of the sample (i.e., $1/\alpha = l_\alpha \ll l$, α being the optical absorption coefficient of the sample), there are three useful approximations.

Case A Thermally thin solids, $\mu_s \gg l; \mu_g \gg l_a$

$$Q_1 \simeq \frac{(1-i)}{2}\mu_g \left(\frac{\mu_b}{k_b}\right) Y \quad . \tag{3-11}$$

where Y is a parameter depending on the ambient temperature and pressure, etc., and is proportional to the intensity of the incident light $I_o(\lambda)$. μ_s, μ_g, and μ_b are the thermal diffusion length of the sample, gas, and backing, respectively, and k_b thermal conductivity of the backing.

Case B Thermally thick solids, $\mu_s < l; \mu_g > l_a$

$$Q_2 \simeq \frac{(1-i)}{2}\mu_g \left(\frac{\mu_s}{k_s}\right) Y \quad . \tag{3-12}$$

Case C Thermally thick solids, $\mu_s \ll l; \mu_g < l_a$

$$Q_3 \simeq \frac{-i\mu_g}{2}\alpha\mu_s \left(\frac{\mu_s}{k_s}\right) Y \quad . \tag{3-13}$$

The schematic representations of these special cases are shown in Fig. 3.12

In Case A, the PA signal is quite strong and independent of α, but linearly proportional to $I_o(\lambda)$. The only term dependent on λ is the intensity $I_o(\lambda)$. The PA spectrum in this case is simply the spectrum of the light source. This would be the case for a very black absorber such as carbon black. This is verified by the existence of a one-to-one correspondence between the PA spectrum of the same light source, as seen by the PA cell, and that taken with a silicon diode power meter [73R3] which has a flat wavelength response in the wavelength region of $\lambda > 400$ nm.

Eq.(3-12) of Case B is analogous to Eq.(3-11), but the thermal parameters of the backing are now replaced by those of the solid.

Case C is very interesting and important. Even though a solid is optical opaque, it is not necessarily opaque photoacoustically and only the light absorbed within the first thermal diffusion length μ_s will

contribute to the acoustic signal. As long as $\alpha\mu_s < 1$, the PA signal is proportional to α although the optical thickness αl of the sample may be much greater than unity.

According to Eqs (3-11) (3-13) the PA spectrum of the sample is divided by the PA spectrum of carbon black in order to remove the structure of the spectrum of the light source, then the so-called normalized PA spectrum is obtained. As can be seen in Figs. 3.14 and 3.15, this spectrum corresponds closely to the optical absorption spectrum of the solid absorber.

3.3.3 Experimental Method

The experimental setup is shown in Fig. 3.13. The sample was crushed into fine powder and placed inside the PA cell shown in Fig. 3.13. The thickness of the sample was ~ 1 mm thick and the gas column in the cell was approximately ~ 5 mm long. The light source used was a 650 W quartziodine lamp and the light beam was focussed on to the entrance slit and chopped at a fixed frequency of 170 Hz at the exit slit of a CARL ZEISS spectrometer. The monochromatic light was refocussed on to the sample through the quartz window of the cell. The body of the cell was constructedof brushed stainless steel. The cell, acoustically resonant section, and the microphone were put into the acoustically isolated box. The PA signal was detected by a 1751 PA sensitive microphone via the resonance tube which was connected to the cell. The analog signal from the microphone was amplified by a PAR-213 preamplifier. A PAR-210 selective amplifier which was tuned to the chopping frequency was used to reduce noise signals at other than the chopping frequency. The signal from the selective amplifier was detected by a PAR-210 lock-in amplifier with a reference signal from the light chopper. Then the output from the lock-in amplifier was recorded by a digital multimeter as a function of wavelength of the incident light, and the PA spectrum

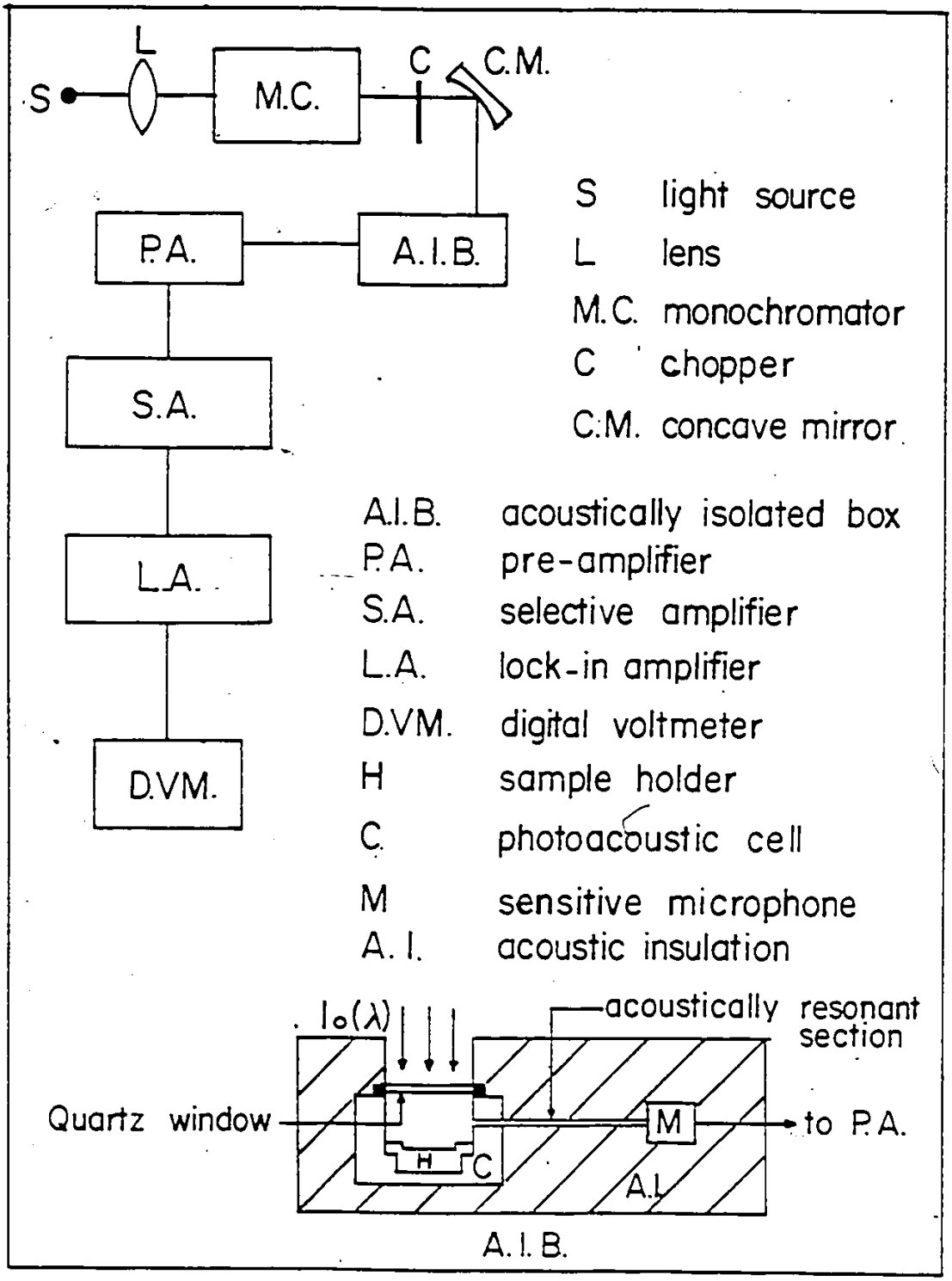

Fig. 3.13 Block diagram of P.A method experimental arrangement.

obtained. This spectrum then had to be normalized by dividing it by the PA spectrum of a carbon black sample to remove the structure of the light source.

3.3.4 Results and Discussion

Fig. 3.14 and Fig. 3.15 show the typical normalized PA spectrum of samples of compositions 005075, 002550, 000075, 101010, 107510, and 102575. From section 3.6, these spectra were found to correspond, qualititatively at least, to the optical absorption spectra of the samples. The slopes of these spectra are comparable with those for II-VI compounds [75R1] but they are very broad when compared with those of optical absorption (Figs. 3.5 - 3.7). So far there has not been a satisfactory theory to allow the energy gap to be determined from such a spectrum. The only experimental PA measurements are those of the II-VI semiconductor compounds mentioned earlier. In that case it was found that the band gap would be given by the energy of the knee of the normalized PA spectra.

In this work, from observation of such spectra for alloys with energy gap values known from Section 3.2.5 an empirical criterion of 50% between the knee and base value was found to be needed to give PA energy gaps of these alloys in reasonable agreement with those of optical absorption. The PA energy gaps of the alloys of compositions 005075, 002550, 000075, and 101010 would then be 1.08, 1.18, 1.30, and 0.91 eV, respectively, compared to the corresponding optical absorption energy gap values of 1.040, 1.178, 1.264, 0.938 eV, respectively. For some alloys the PA energy gap is higher than the energy gap from the optical absorption while for others it is lower. They, however, agree resonably well within the experimental error which is estimated to be ±50 meV for the PA measurement.

According to Eqs. (3-11) and (3-13) in Section 3.3.2, the relative PA signal for the sample is given

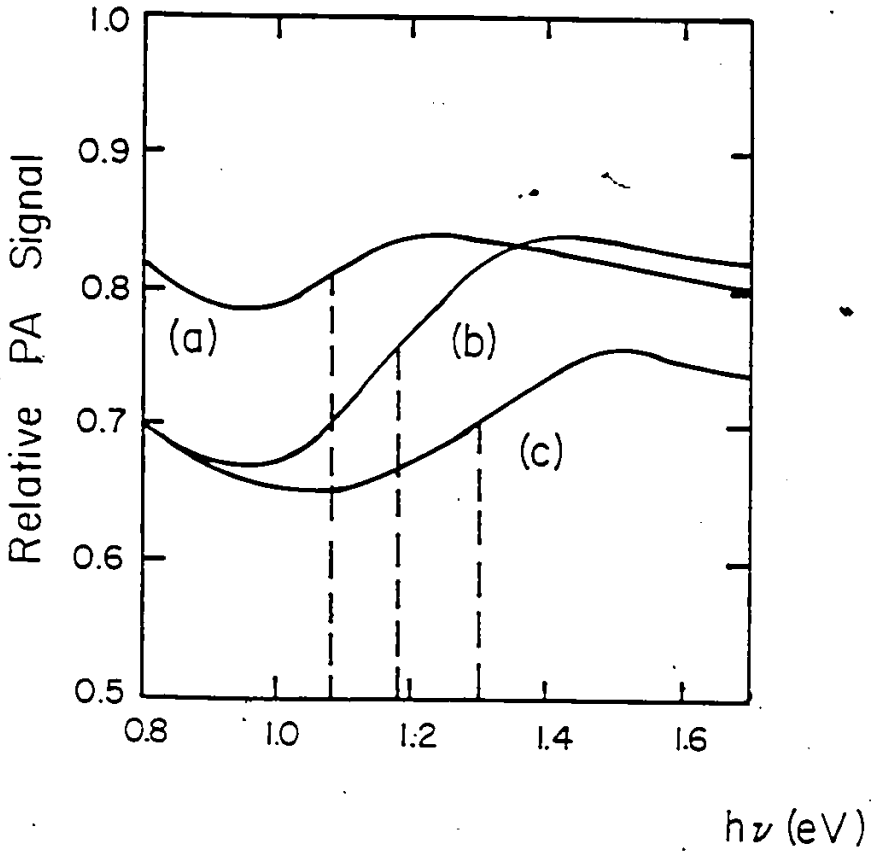

(a) 00 50 75

(b) 00 25 50

(c) 00 00 75

Fig. 3.14 Variation of relative PA signal with photon energy $h\nu$ (normalized PA spectrum) for samples (a)005075, (b)002550, and (c)000075.

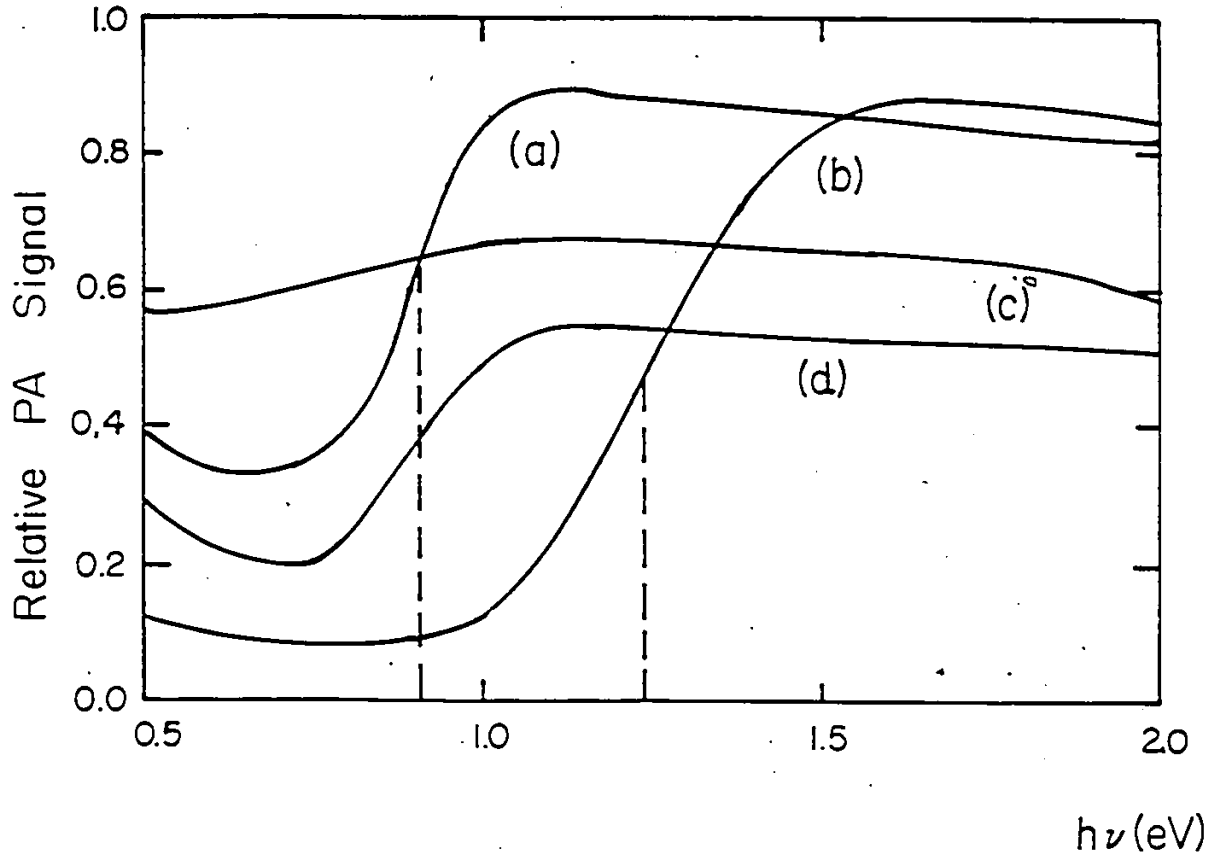

(a) 10 10 10

(b) 10 75 00

(c) 10 25 75

(d) 10 10 10 + Al_2O_3 (1:1)

Fig. 3.15 Variation of relative PA signal with photon energy $h\nu$ (normalized PA spectrum) for samples (a)101010, (b)107500, (c)102575, and (d)101010+Al_2O_3 (1:1).

Table 3.3 Energy gap values of the $(Cu_{1-x}Ag_x)(Ga_{1-y}In_y)(Se_{1-z}Te_z)_2$ system. E_p denotes a photoacoustic energy gap.

Sample	E_p(eV)
250000	1.55
250025	1.35
250050	1.25
250075	1.20
250010	1.18
252500	1.37
255010	1.12
257510	1.00
500075	1.20
500010	1.21
502500	1.09
750000	1.60
750050	1.35
750075	1.20
750010	1.15
752500	1.43
755010	1.10
757500	1.06
100000	1.78
100025	1.55
100075	1.25
100010	1.16
102510	1.13
107510	1.24

by

$$Q'(\lambda) \simeq \frac{-i}{(1-i)} \left(\frac{\mu_s k_b}{k_s \mu_b}\right) \mu_s \alpha(\lambda) \quad . \tag{3-14}$$

This indicates that the signal depends on the thermal properties of the sample and as long as $\alpha < (1/\mu_s)$ the signal is proportional to $\alpha\mu_s$. At high photon frequencies below $\nu_0 (h\nu_0 = E_g)$ there should be no interband absorption except from the background absorption and the condition $\alpha < (1/\mu_s)$ should be satisfied very well because of small value of α. At photon frequencies very near to the fundamental edge the value of α is getting so high that the condition $\alpha < (1/\mu_s)$ would not be satisfied. In this case the condition given in Case B should be applied to the PA signal of the sample. The relative PA signal would be expressed as

$$Q'' \simeq \left(\frac{\mu_s k_b}{k_s \mu_b}\right) \quad . \tag{3-15}$$

which gives a flat region of the spectrum above the fundamental edge. This interpretation implies that the position of the absorption edge should be very close to the knee of the absorption. However, for the ternary compound of this alloy system, the 70% criterion gave the better values for the PA energy gap compared to those of optical absorption but for the alloys the 50% was better.

It is found that the PA effect is very dependent on the nature of the surface involved. It works rather badly on bulk samples with high thermal conductivity because the surface layer loses heat readily to the bulk. The ideal sample consists of fine powder with poor thermal conductivity. Thus the surface is easily heated up and does not lose heat to its own bulk. Attempts were made to dilute the sample with Al_2O_3, a white powder, so as to effectively decrease the thermal conductivity of the sample and thereby decrease its thermal diffusion length μ_s. It did not improve the form of the spectrum but the position of the PA energy gap using the same empirical criterion remained the same. This is shown in Fig. 3.15(d) for the

compound of composition 101010.

Another problem with the PA method was that several of the normalized PA spectra were relatively flat and did not peak near the energy corresponding to the expected energy gap as shown in Fig. 3.15(c). It can be seen clearly that in this case, it is impossible to determine the energy gap value using the criterion discussed above since the spectrum never distincly peaks. This may be caused by inhomogeneity of the sample.

The available energy gap values are also listed in Tables 3.1-3.3 for the alloys being measured by the PA method. It is concluded that PAS is a fast method to obtain the value of an energy gap and does not need a special method of preparation of the surface of the sample. It is suitable for material which is very brittle such as these alloys. However, the optical absorption energy gap values are more accurate and the PA technique should be used only to give approximate values of energy gap .

3.4 Contours of Constant Energy Gap

It was found that the curves showing the variation of optical energy gap as a function of a composition variable for both the copper and indium sections are not linear. These are shown in Figs. 3.16 and 3.17. Within the limits of experimental error, they can be fitted to a parabolic form. This was done in the same fashion as for the lattice parameters values.

To produce constant energy gap contours, an equation similar to Eq.(2-12) was used to express E_g as a function of the composition variables appropriate to the section concerned. A least-squares method was used to give values of the nine coefficients for each section. These values are listed in Table 3.4. The resulting fitted curves of E_g as a function of z for constant y (Cu-face) and as a function of x for constant

z (In-face) are also shown in Figs. 3.16 and 3.17.

Using the data in Table 3.4, the constant E_g contours for the Cu- and the In- sections can be produced and they are shown in Figs. 3.18 and 3.19. On the Cu-section, the In-edge (y=1 on the Cu-face) has the lower energy gap values and reaches a minimum value at approximately z=0.50. On this face the maximum energy gap occurs at $CuGaSe_2$. On the In-section, there is a minimum energy gap at the compostion $x \simeq 0.30$ and $z \simeq 0.55$, and the maximum energy gap is for $AgInSe_2$. In this section, the energy gap does not vary as rapidly with composition as those of the Cu-section.

It was suggested [SIA1] in the case of the tellurium section that over most of the section the values of a and c could be used to determine the composition of any sample belonging to that face. For the copper and indium section, the a and c contours (see Fig. 2.19), intersect at much smaller angles and hence the values of a and c give only limited indication of composition. However, the a and E_g contours (see Figs. 3.18-3.19) are sufficiently different that values of a and E_g could be used to determine composition values.

As indicated in Section 3.3, the photoacoustic technique was used to give approximate values of energy gap. These values are fitted in the same way as the above, but the resulting contours are to some extent different from those obtained from optical absorption.

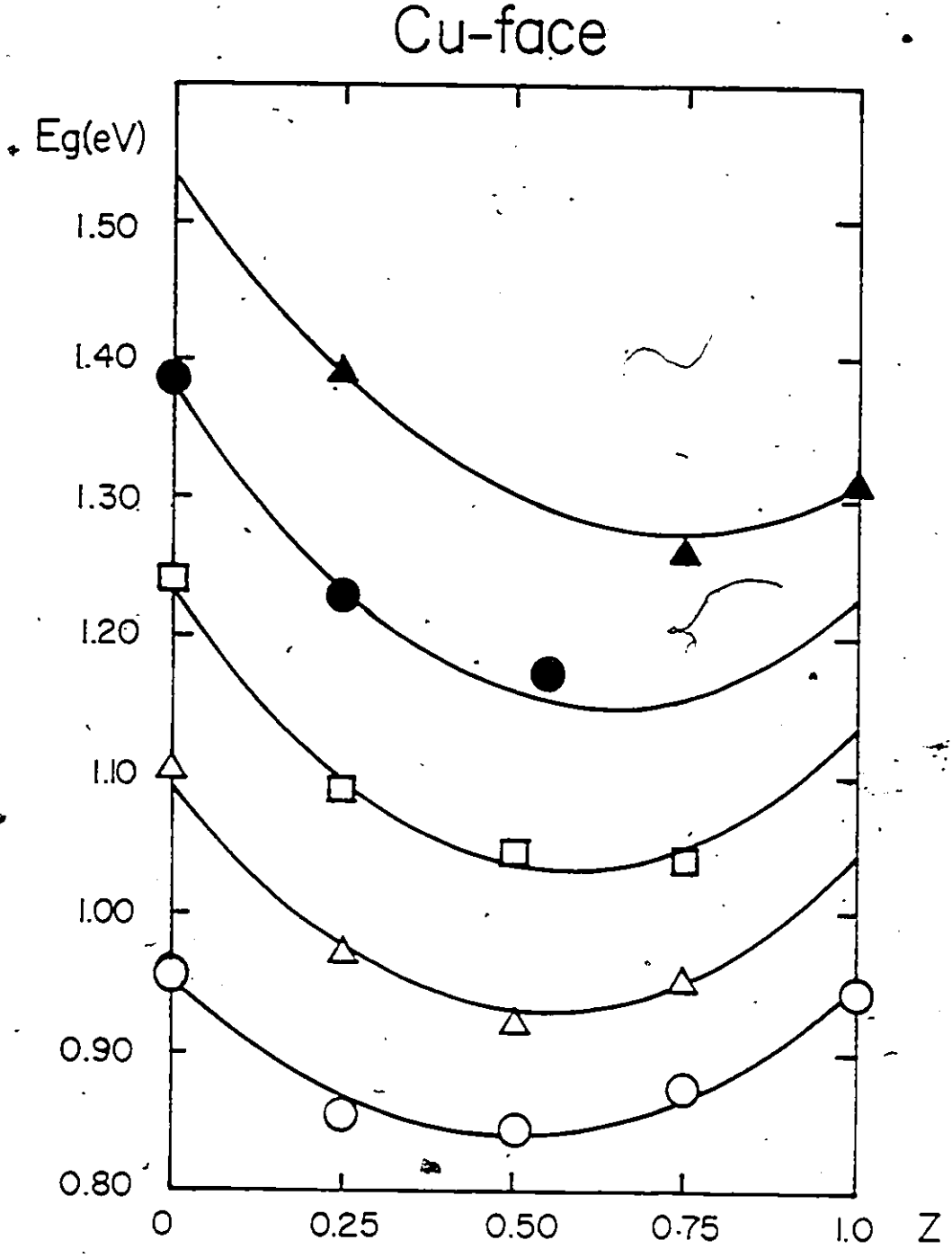

Fig. 3.16 $Cu(Ga_{1-y}In_y)(Se_{1-z}Te_z)_2$ Variation of optical absorption energy gap E_g with z for lines of constant y. ▲ : $y = 0$ ● : $y = 0.25$ □ : $y = 0.50$ △ : $y = 0.75$ ○ : $y = 1.0$

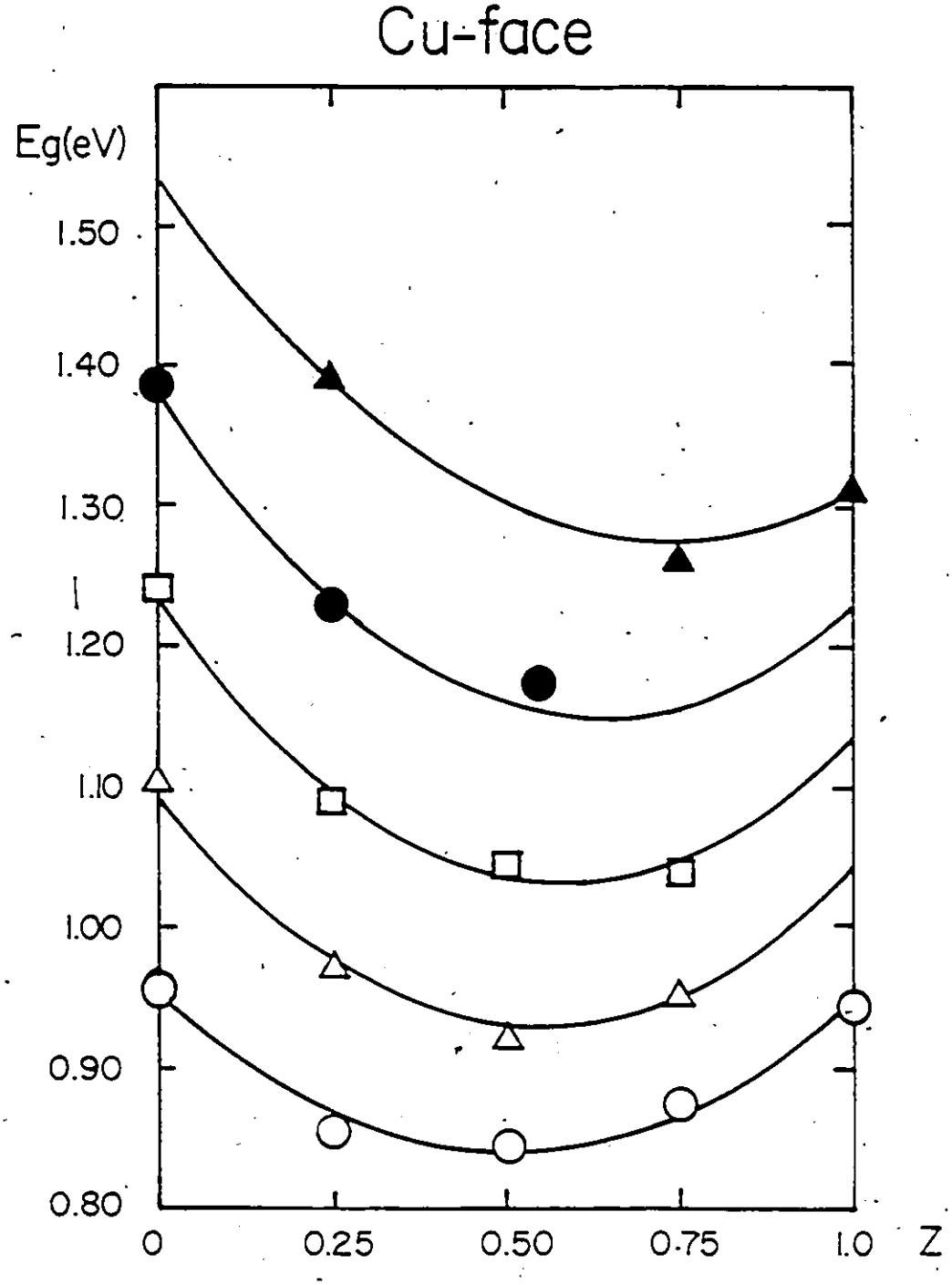

Fig. 3.16 $Cu(Ga_{1-y}In_y)(Se_{1-z}Te_z)_2$ Variation of optical absorption energy gap E_g with z for lines of constant y. ▲ : $y = 0$ ● : $y = 0.25$ □ : $y = 0.50$ △ : $y = 0.75$ ○ : $y = 1.0$

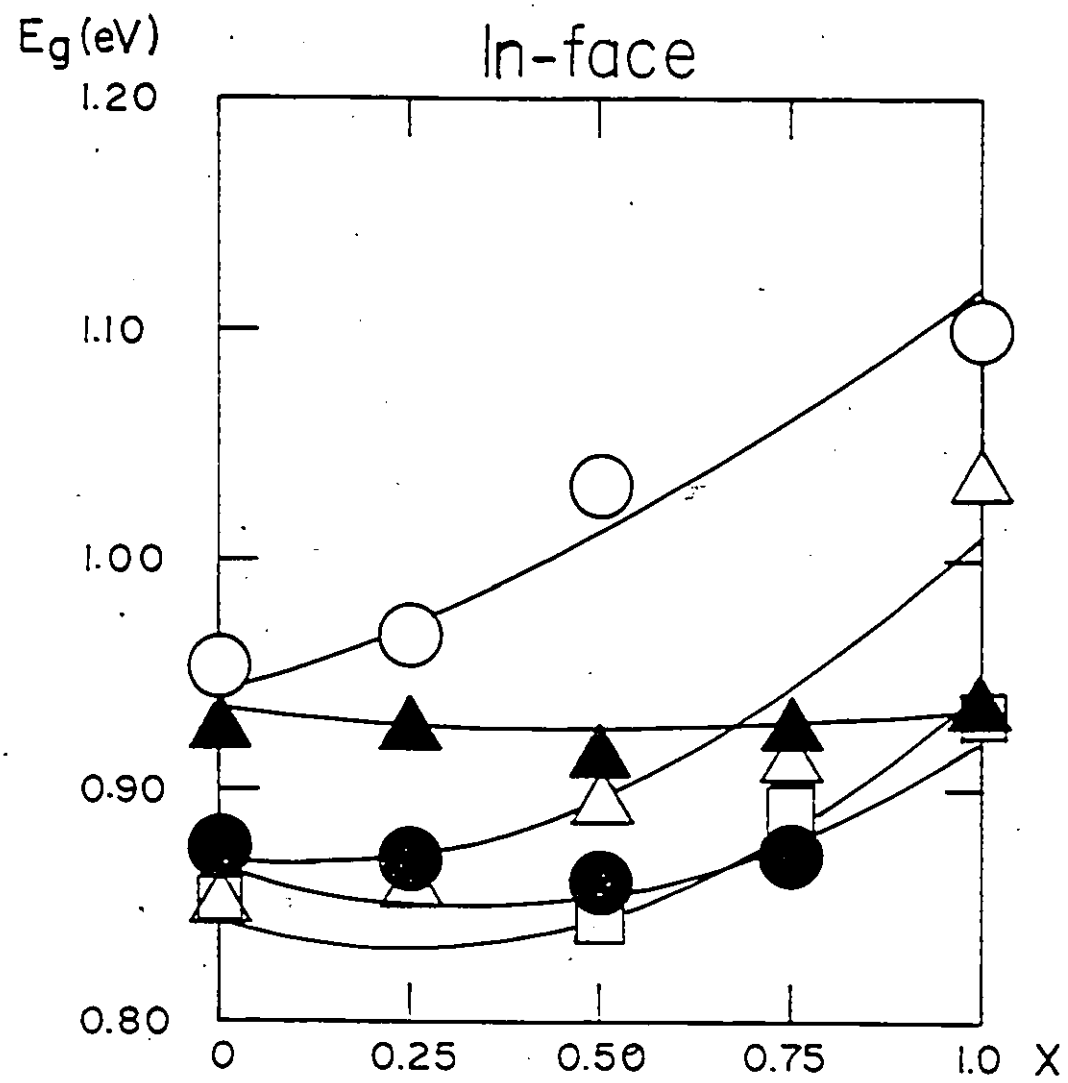

Fig. 3.17 $(Cu_{1-z}Ag_z)In(Se_{1-z}Te_z)_2$ Variation of optical absorption energy gap E_g with x for lines of constant z. ○ : $z = 0$ △ : $z = 0.25$ □ : $z = 0.50$ ● : $z = 0.75$ ▲ : $z = 1.0$

Table 3.4 Coefficients corresponding to Eq. (2-12) for the Cu- and In-section. The number of points used in the least squares fit and the standard deviation, σ, is also listed in each case.

	face	Cu	In
	number of points	19	22
	variable composition parameters (u,v)	(y,z)	(x,z)
E_s(eV)	α	1.538	0.943
	β	-0.608	0.104
	γ	-0.715	-0.386
	δ	0.023	0.071
	ε	0.487	0.379
	ζ	-0.253	-0.709
	η	0.519	0.594
	θ	0.533	0.569
	λ	0.008	0.013
	σ	0.008	0.013

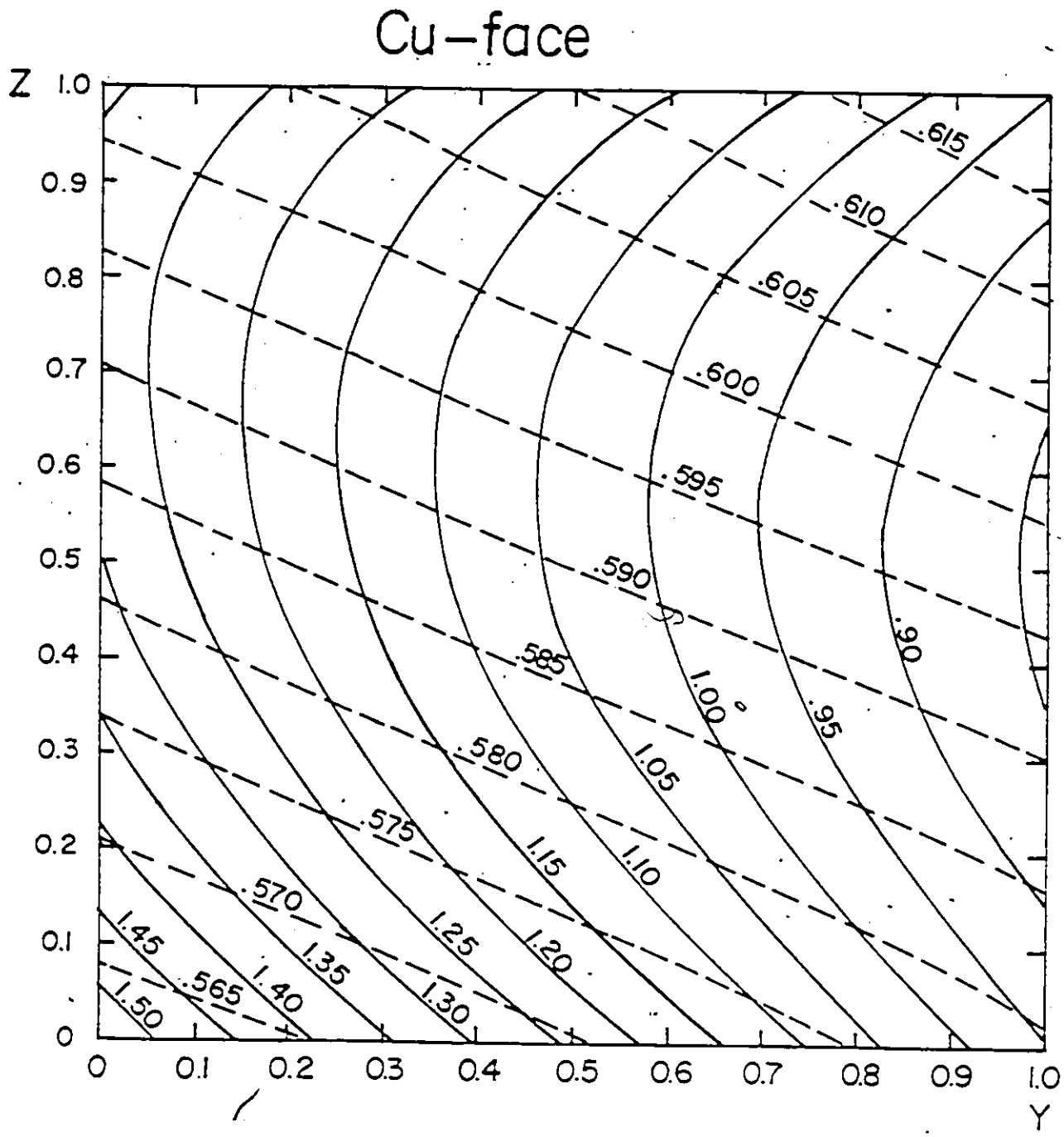

Fig. 3.18 $Cu(Ga_{1-y}In_y)(Se_{1-z}Te_z)_2$ Contours of constant optical absorption energy gap E_g and lattice parameter a. ——E_g (eV), - - - a(nm)

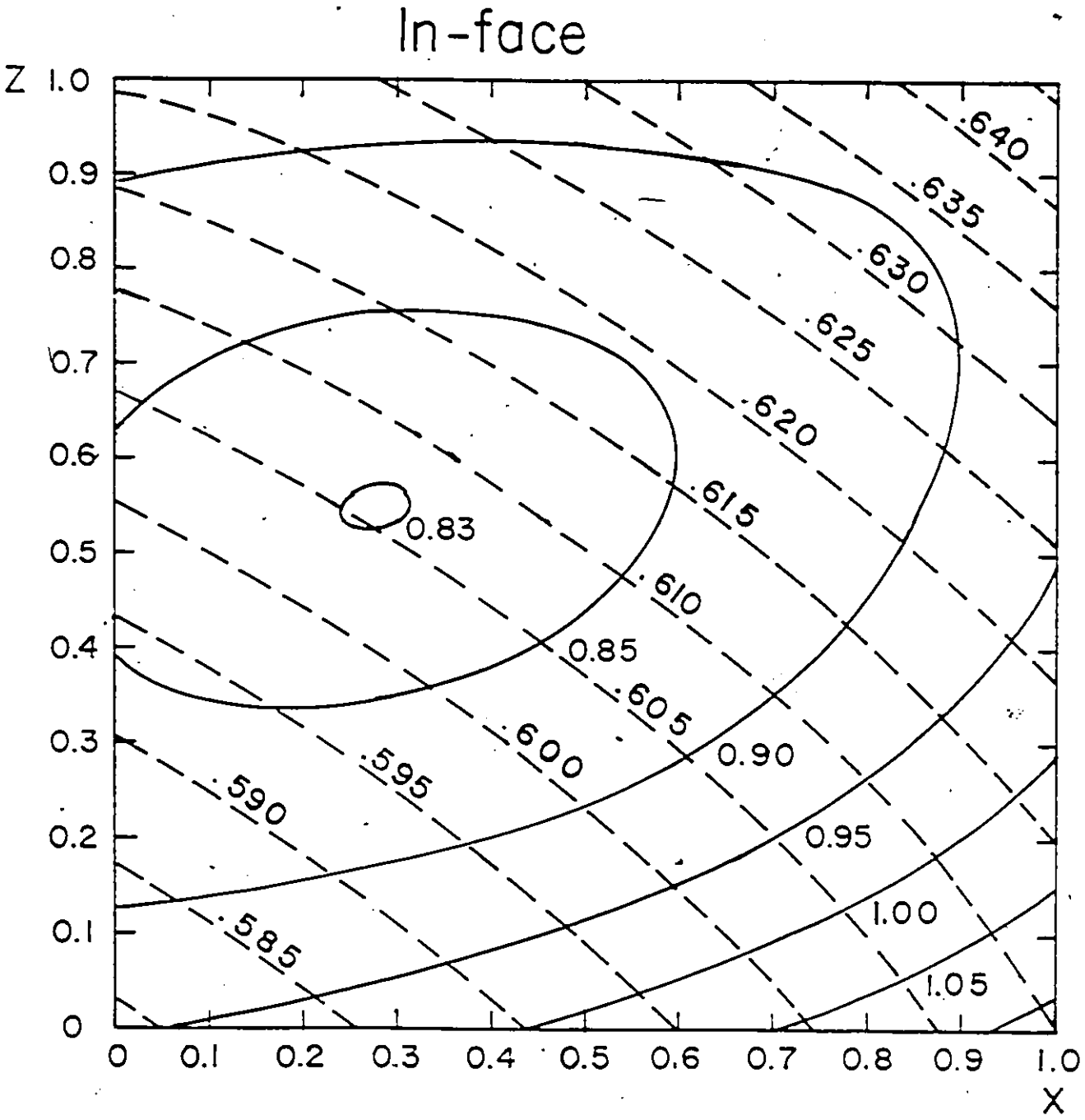

Fig. 3.19 $(Cu_{1-x}Ag_x)In(Se_{1-z}Te_z)_2$ Contours of constant optical absorption energy gap E_g and lattice parameter **a**. ——E_g (eV). - - - **a**(nm)

3.5 Summary

Optical energy gap values have been obtained for the alloys of the Cu- and In- sections. For some compositions, the absorption edges could not be observed because very thin samples for transmission measurement could not be produced and hence the background absorption was very high. When absorption curves were obtained in these alloys sections, they were characterized by a steep variation of absorption coefficient at higher energies and a shallower portion at lower energies. The tail of the absorption edge corresponding to the shallower portion of the absorption curve has been attributed to phonon boardening at lower photon energies similar to that observed in the binary analog CdTe [GOD1]. But the effect is smaller than in the binary analogs. The energy gaps for all of the ternary alloys were taken to be direct.

PA measurements also were used to give approximate values of energy gap. The criterion which was used to indicate the PA energy gap from the normalized PA spectrum was to take an energy at which the normalized signal was half way between the base and knee values. These values gave reasonable agreement with those from optical absorption measurements. This criterion was used because at present there is no satisfactory theory to allow the energy gap to be determined from the normalized PA spectrum.

The contours of constant E_g were determined and these contours together with the constant a contours in both the Cu- and the In- sections could be used to determine the composition of any sample belonging to that particular section.

Chapter 4

Effects of $p-d$ Hybridization on the Valence Band of I-III-VI_2 Chalcopyrite Semiconductors

4.1 Overview

This chapter is concerned with the energy band structure of I-III-VI_2 CH semiconductors, the simplest ternary analogs of II-VI ZB compounds. The energy band structure of a I-III-VI_2 compound is related to that of its ZB type binary analog in such a way that the p-like valence band derived from the Γ_5(ZB) in ZB structure is split into a Γ_7 and Γ_6 level and interacted with that of Γ_7 symmetry derived from the Γ_7(ZB) by the effect of the noncubic crystal-field interaction in CH structure. In addition, the uppermost valence bands of I-III-V_2 compounds are influenced by the admixture of the noble-metal (I) d levels and as a result there is a large reduction in the energy gap and in the spin-orbit splitting of the uppermost valence band as compared with the binary analogs. The presence of the noble-metal d levels in the valence band has been confirmed directly by the observation of electroreflectance structure due to transitions from the d levels themselves to the lowest conduction band minimum [75S2]. The energy band calculations which have not taken the noble-metal d levels into account have not provided an adequate description of the energy band structure of I-III-VI_2 CH semiconductors.

In this chapter, the studies of the energy band structure of I-III-VI_2 compounds will be reviewed

in the next section.In Section 4.3, a model is developed by adding the effects of $p-d$ hybridization and crystal-field to the Hamiltonian of the Kane model [57K1]. The model is then applied to the observed valence band splitting data of I-III-VI_2 compounds and the fractional d character in the valence bands can be determined. This also allows the deformation potentials of the p and d bands averaged over all of the compounds to be determined. These two quantities are very useful to the analysis of the variation of energy gaps with both composition and temperature for $CuGa(S_{1-x}Se_x)_2$ alloys. This will be done in the next chapter.

4.2 Energy Band Structure of I-III-VI_2 Compounds

As was shown earlier, the CH structure is superlattice of the cubic ZB structure and their crystal structures are closely related (see Chapter 2). The Brillouin zone (BZ) of the ZB structure is the well-known truncated octahedron shown in Fig. 4.1. The crystal structure of ternary CH compounds belongs to the space group D_{2d}^{12}. The primitive translation vectors are the translations of the body-centered tetragonal lattice which can be written as

$$\begin{aligned} \vec{a}_1 &= \frac{1}{2}(a, a, c) \quad , \\ \vec{a}_2 &= \frac{1}{2}(-a, a, c) \quad , \\ \vec{a}_3 &= \frac{1}{2}(a, -a, c) \quad , \end{aligned} \tag{4-1}$$

a and c being the lattice parameters. The primitive vectors in its reciprocal lattice are found to be

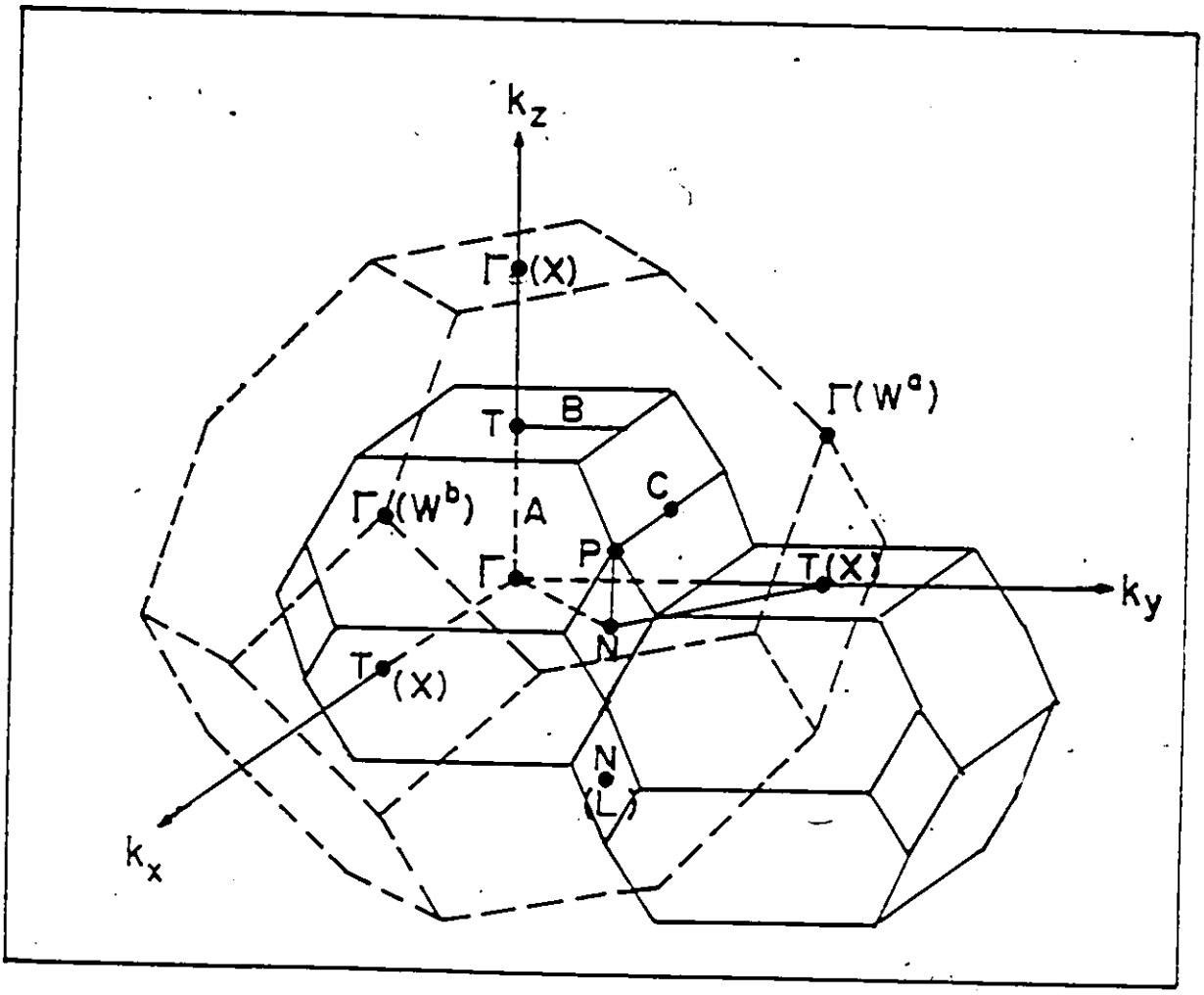

Fig. 4.1 Comparision of the Brillouin zones (BZs) of the zincblende (dashed line) and chalcopyrite lattices (solid line) with ideal $c/a = 2$. The zincblende points and lines are labeled with parentheses.

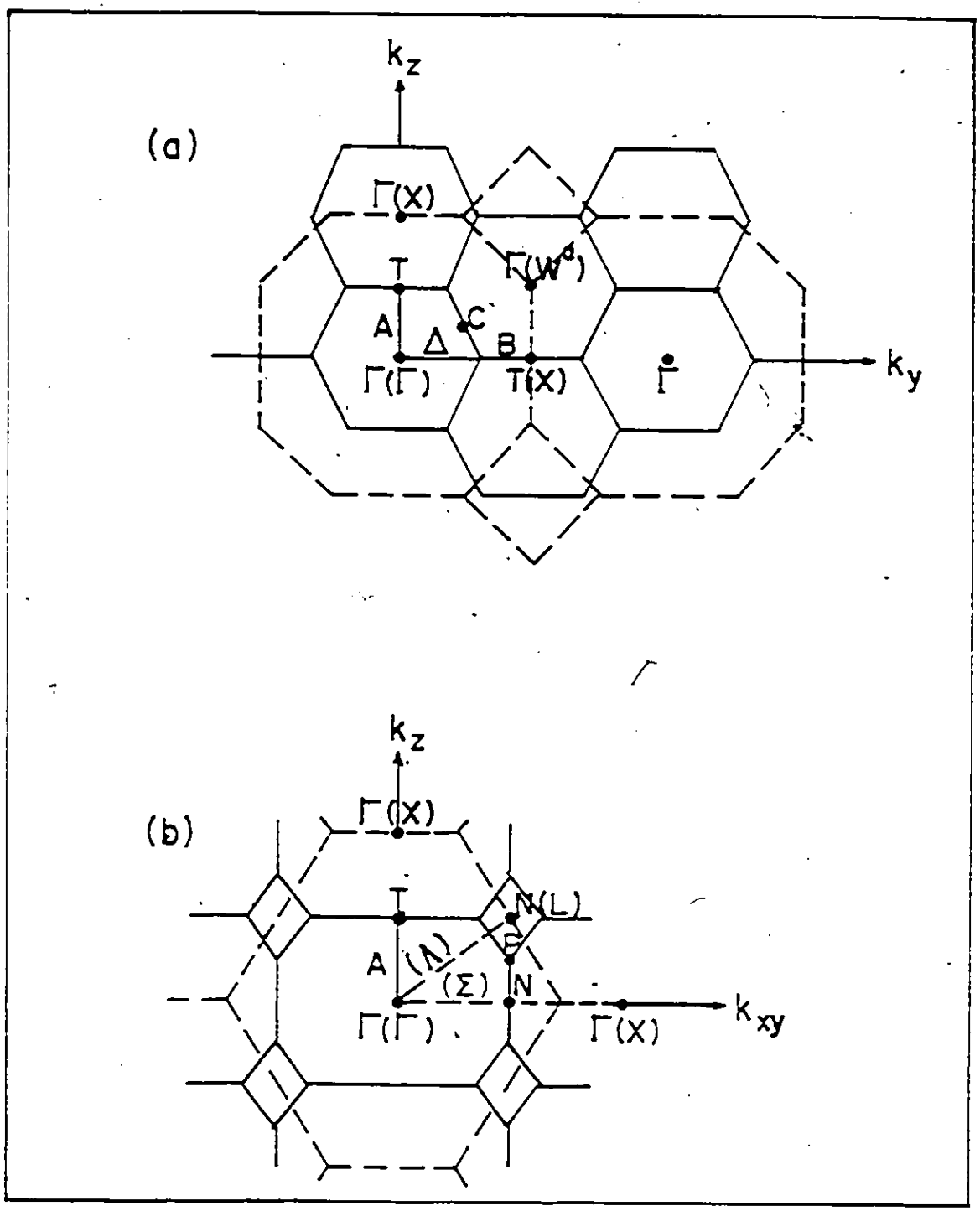

Fig. 4.2 Sections of two embeded BZs on (a) the $k_z - k_y$ plane and (a) the $k_z - k_{xy}$ plane. The zincblende points and lines are labeled with parentheses.

$$\vec{b}_1 = 2\pi(\frac{1}{a}, \frac{1}{a}, 0) \quad ,$$

$$\vec{b}_2 = 2\pi(0, \frac{1}{a}, \frac{1}{c}) \quad , \qquad (4-2)$$

$$\vec{b}_3 = 2\pi(\frac{1}{a}, 0, \frac{1}{c}) \quad .$$

Thus, the reciprocal translation vectors are expressed as

$$\begin{aligned} \vec{K} &= h\vec{b}_1 + k\vec{b}_2 + l\vec{b}_3 \\ &= \frac{2\pi}{a}\left[(h+l), (h+k), \frac{a}{c}(k+l)\right] \quad , \end{aligned} \qquad (4-3)$$

where h, k, and l are integers. Hence, the BZ can be constructed and is shown in Fig. 4.1 in comparision with the BZ of the ZB structure. The notation of Ref. [60C1] is used to label the CH symmetry points : $\Gamma(0,0,0)$, $T(0,0,\frac{2\pi}{c})$, $C(0,\frac{\pi}{a},\frac{\pi}{c})$, $N(\frac{\pi}{a},\frac{\pi}{a},0)$, $P(\frac{\pi}{a},\frac{\pi}{a},\frac{\pi}{c})$, and the symmetry line : $\Lambda(0,0,k_z)$, $\Delta(0,k_y,0)$, $B(0,k_y,\frac{2\pi}{c})$, etc.

With the approximation $c = 2a$, the unit cell of CH lattice is four times larger than that of ZB lattice, and the BZ of CH lattice is four times smaller. There will be a correspondence between symmetry points of the BZs of two structures. This can be seen in the sections of the two embedded BZs on the $k_x - k_y$ plane and the $k_z - k_{xy}$ plane as shown in Fig. 4.2. Some typical examples of the correspondence are [60C1, 63C1, 66K1] :

ZB		CH
$\Gamma(0,0,0), X(0,0,\frac{2\pi}{a}), W^a(0,\frac{2\pi}{a},\frac{\pi}{a}), W^b(\frac{2\pi}{a},0,\frac{\pi}{a})$	—	$\Gamma(0,0,0)$,
$L(\frac{\pi}{a},\frac{\pi}{a},\frac{\pi}{a}), \Sigma(\frac{\pi}{a},\frac{\pi}{a},0)$	—	$N(\frac{\pi}{a},\frac{\pi}{a},0)$,
$X(\frac{2\pi}{a},0,0), X(0,\frac{2\pi}{a},0), \Delta(0,0,\frac{\pi}{a})$	—	$T(0,0,\frac{\pi}{a})$.

(4-4)

The group theoretical studies of these two crystal structures have been made by Parmenter [55P1]

Table 4.1 Character table of the ZB structure at the Γ point. BSW : Ref.[36B1], D : Ref.[55D1]

Γ BSW	Γ D	E	$3C_4^2$	$8C_3$	$6IC_4$	$6IC_2$	Basis functions
Γ_1	Γ_1	1	1	1	1	1	$(x^2+y^2+z^2)$; xyz
Γ_2	Γ_2	1	1	1	-1	-1	$S_xS_yS_z$
Γ_{12}	Γ_3	2	2	-1	0	0	(x^2-y^2) . $(3z^2-r^2)$
Γ_{15}	Γ_4	3	-1	0	-1	1	x, y, z ; yz, zx, xy
Γ_{25}	Γ_5	3	-1	0	1	-1	S_x, S_y, S_z

Additional characters of the double group.

Γ	E	$\bar{E}$	$6C_4^2$	$8C_3$	$8C_3$	$6IC_4$	$6IC_4$	$12IC_2$
Γ_6	2	-2	0	1	-1	$\sqrt{2}$	$-\sqrt{2}$	0
Γ_7	2	-2	0	1	-1	$-\sqrt{2}$	$\sqrt{2}$	0
Γ_8	4	-4	0	-1	1	0	0	0

Spin-orbit splitting selection rules.

Γ_i	Γ_1	Γ_2	Γ_{12}	Γ_{15}	Γ_{25}
$\Gamma_i \times D_{\frac{1}{2}}$	Γ_6	Γ_7	Γ_8	$\Gamma_7+\Gamma_8$	$\Gamma_6+\Gamma_8$

Dipole transition selection rules.

Γ_i	Γ_1	Γ_2	Γ_{12}	Γ_{15}	Γ_{25}	Γ_6	Γ_7	Γ_8
$\Gamma_i \times \Gamma_{15}$	Γ_{15}	Γ_{25}	$\Gamma_{15}+\Gamma_{25}$	$\Gamma_1+\Gamma_{12}$ $+\Gamma_{15}$ $+\Gamma_{25}$	$\Gamma_2+\Gamma_{12}$ $+\Gamma_{15}$ $+\Gamma_{25}$	$\Gamma_7+\Gamma_8$	$\Gamma_6+\Gamma_8$	$\Gamma_6+\Gamma_7$ $+2\Gamma_8$

N.B. S_x, S_y, S_z mean a basis transforming like coordinates x, y, z except that they do not change sign under the inversion.

Table 4.2 Character table of the CH structure at the Γ point. [57K2, 64S1]

Γ	E	C_2	$2S_4$	$2C_2'$	$2\sigma_d$	Basis functions
Γ_1	1	1	1	1	1	$(3z^2 - r^2)$; $(x^2 + y^2)$
Γ_2	1	1	1	-1	-1	S_z
Γ_3	1	1	-1	1	-1	$(x^2 - y^2)$
$\Gamma_4(\parallel)$	1	1	-1	-1	1	z ; xy
$\Gamma_5(\perp)$	2	-2	0	0	0	x, y ; yz, zx ; S_x, S_y

Additional characters of the double group.

Γ	E	E	$2C_2$ $2C_2$	$2S_4$	$2S_4$	$2C_2'$ $2C_2'$	$2\sigma_d$ $2\sigma_d$
Γ_6	2	-2	0	$\sqrt{2}$	$-\sqrt{2}$	0	0
Γ_7	2	-2	0	$-\sqrt{2}$	$\sqrt{2}$	0	0

Spin-orbit splitting selection rules.

Γ_i	Γ_1	Γ_2	Γ_3	Γ_4	Γ_5
$\Gamma_i \times D_{\frac{1}{2}}$	Γ_6	Γ_6	Γ_7	Γ_7	$\Gamma_6 + \Gamma_7$

Dipole transition selection rules.

Γ_i	Γ_1	Γ_2	Γ_3	Γ_4	Γ_5	Γ_6	Γ_7
$\Gamma_i \times \Gamma_4(\parallel)$	Γ_4	Γ_3	Γ_2	Γ_1	Γ_5	Γ_7	Γ_6
$\Gamma_i \times \Gamma_5(\perp)$	Γ_5	Γ_5	Γ_5	Γ_5	$\Gamma_1 + \Gamma_2 + \Gamma_3 + \Gamma_4$	$\Gamma_6 + \Gamma_7$	$\Gamma_6 + \Gamma_7$

N.B. S_x, S_y, S_z mean a basis transforming like coordinates x, y, z except that they do not change sign under the inversion.

Table 4.3 Compatibility relations connecting the ZB and CH structures at the Γ point.

ZB	CH
Γ_1	Γ_1
Γ_{12}	$\Gamma_1+\Gamma_3$
Γ_{15}	$\Gamma_4+\Gamma_5$
Γ_{25}	$\Gamma_2+\Gamma_5$
Γ_6	Γ_6
Γ_7	Γ_7
Γ_8	$\Gamma_6+\Gamma_7$

and Dresselhauss [55D1] for the ZB structure and by Chaldyshev and Pokrovski [60C1] and Sandrock and Treusch [64S1] for the CH structure. Compatibility relations of the irrducible representations (IRs) of these two groups have been studied by Chaldyshev and Karavaev [63C1]. The present study will concern the energy band structure of the uppermost valence bands of I-III-VI_2 ternary CH compounds at $\bar{k} = \bar{o}$, the Γ point. Thus, character tables for the IRs of the ZB and CH structures at the Γ point are given in Table 4.1 and 4.2 and compatibility relations connecting the IRs of the two structures are also given in Table 4.3. These will provide information such as (i) the degeneracy of various energy bands in the vicinity of the Γ point, (ii) the symmetry of the wave functions, (iii) how the energy band splits when the spin-orbit interaction is inlcluded or when the symmetry of the crystal is reduced from T_d to D_{2d}, and (iv) the dipole-transition selection rules, etc.

Because of the correspondence between the crystal structures and the BZs of the CH and ZB compounds, the energy band structure of a ternary CH compound could be well approximated by a perturbation treatment on the well-established ZB energy band. The perturbation term is the noncubic potential caused by the noncubic aspects (see Section 2.2). If the perturbation term is neglected, the energy bands of the CH compound are those of its ZB binary analog but now they are folded back into the first BZ of the CH structure in order to allow for the reduced size of the BZ of the CH structure. These energy bands may then be used as a zero-order approximation (the unperturbed states) to the actual energy bands of the corresponding CH compound. The folding method and the symmetry properties of the perturbation terms have been studied by Miller et al [77M1, 81M1] and Karavaev and Poplavnoi [66K1]. It is found that the perturbation terms due to a cationic asymmetry and an anionic displacement transform according to both $\Gamma_1^a(0, \frac{2\pi}{a}, \frac{\pi}{a})$ and $\Gamma_1^b(\frac{2\pi}{a}, 0, \frac{\pi}{a})$ while those due to a tetragonal compression transform

as the $3z^2 - r^2$ component of Γ_{12} [66K1, 77M1, 81M1]. At the Γ point of the folded energy bands, the uppermost valence bands are a fourfold-degenerate Γ_8 and a doubly degenerate Γ_7 states and the lowest conduction band is a doubly degenerate Γ_6 state. The tetragonal compression is the largest contribution to the crystal-field splitting in I-III-VI_2 CH compounds. Although this effect is the first-order perturbation, the crystal-field splitting is small for the tetragonal compressions commonly observed in ternary CH compounds [75S2, 77M1, 81M1]. The folded states, which belong to X and W symmetries, appear above and below the Γ_6 and Γ_7, Γ_8 states and the interactions between the folded states and the Γ_6 and Γ_7, Γ_8 states are neglected in the quasi-cubic model [60H1, 71R1].

In this model, the uppermost valence-band states for CH compounds are considered to be derived from the Γ_7 and Γ_8 ZB valence-band states through the action of the perturbation due to the noncubic crystal-field potential. Using the information given in Tables 4.1-4.3, relationships between the valence-band splitting of ZB and CH structures due to these interactions can be established and are shown in Fig. 4.3. In the model, the crystal-field splitting, δ, is assumed to be given by splitting produced by a tetragonal uniaxial stress applied to a ZB crystal. The diagonalization of Hamiltonian matrix gives the energies of the Γ_7 levels relative to the Γ_6 level ($E_0 = 0$) in the valence band to be

$$E_{1,2} = -\frac{1}{2}(\Delta + \delta) \pm \frac{1}{2}\left[(\Delta + \delta)^2 - \frac{8}{3}\Delta\delta\right]^{1/2} \qquad (4-5)$$

It also yields wave functions from which the intensity ratios for different light polarizations can be calculated for a transition from a given Γ_7 valence-band to a Γ_6 conduction-band, viz.,

$$\frac{I_{\parallel}}{I_{\perp}}(\Gamma_7 \text{at} E_1 - \Gamma_6 \text{C.B.}) = (2 + \frac{3E_1}{\Delta})^2 \qquad (4-6)$$

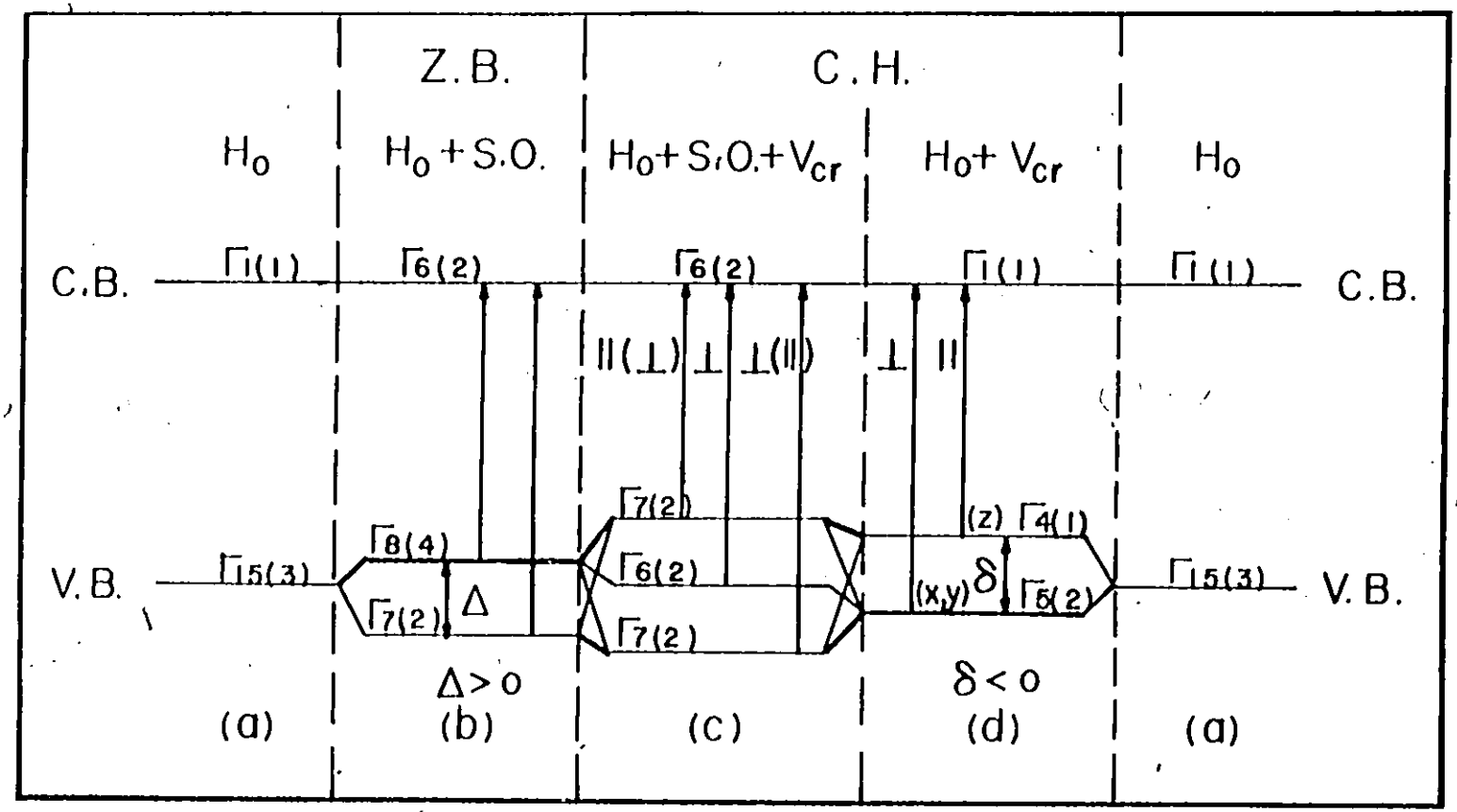

Fig. 4.3 Relationships between the valence band splittings in the zincblende and chalcopyrite lattices and between the irreducible representations of the bands at $\vec{k} = \vec{0}$, the Γ point. (b) shows the actual splitting found in ZB compounds, while (c) gives that found in the CH compounds. (a) and (d) show the relationship of these splittings to simpler cases where spin-orbit interaction and/or crystal-field interaction vanish (i.e., $\Delta = 0$ and /or $\delta = 0$).

where E_i is given by Eqs. (4-5). The spin-orbit splitting, Δ, the crystal-field splitting, δ, and the ratio of polarization-transitions can thus be determined from the observed valence-band splitting data using Eqs.(4-5) and (4-6).

Earlier studies [75S2] have shown that the structure of the uppermost valence bands in a II-IV-V_2 ternary CH compound is simply related to the energy bands of its III-V binary analog in good agreement with the quasicubic model. It has also been found that the energy gap values and spin-orbit splitting parameters are comparable to those of the binary analogs and the crystal-field splitting parameters are given in terms of tetragonal distortion by

$$\delta = \frac{3}{2} b \left(2 - \frac{c}{a}\right) \quad . \qquad (4-7)$$

where b is the deformation potential, estimated to be -1.2 eV [75S2] for all II-IV-V_2 compounds.

In the case of I-III-VI_2 ternary CH compounds, however, the observed energy gap values are between 0.4 and 2.4 eV lower and the spin-orbit splitting parameters are considerably smaller than those of II-VI binary analogs, as has been pointed out by Shay and Wernick [75S2], Miller et al [S1M1], and Jaffe and Zunger [84J1]. These effects have been attributed to the admixture of noble-metal *d* levels in the valence bands. Electroreflectance measurements have shown evidence of transitions between *d*−states of the Cu atoms and the conduction band in $CuInS_2$, $CuGaS_2$ [71T1], $CuInSe_2$ [72S1], and $CuGaSe_2$ [7ST1]. X-ray photoemission (XPS) and ultraviolet photoemission (UPS) studies have also reported the energies of the noble-metal *d* levels below the valence band edge in $CuAlS_2$ [73L1, 74K1, 77R1], $CuGaS_2$ [74K1, 77R1, S1D1], $CuInSe_2$ [77R1], $CuInS_2$ [74B1, 77R1], $AgGaS_2$ [73L1, 74K1, S1D1], and $AgInSe_2$ [77R1]. The small spin-orbit splitting parameters and the reduced energy gap values have been explained as due to

$p-d$ hybridization between the p bands and the noble-metal d levels. According to this interpretation, the observed spin-orbit splitting, Δ, of I-III-VI_2 compounds is written as [75S2, 77Y1, 77T1]

$$\Delta = \alpha_L \Delta_p + (1-\alpha_L)\Delta_d \quad , \tag{4-8}$$

where Δ_p is the positive spin-orbit splitting observed in the (p−like) binary analog, Δ_d the negative spin-orbit splitting of the noble-metal d levels, and α_L the fractional p-like character of the uppermost valence bands. This idea has been extended to the case of crystal-field splitting [79Y1, 82L1] where δ has been assumed to be

$$\delta = \alpha_L \delta_p + (1-\alpha_L)\delta_d \quad . \tag{4-9}$$

δ_p and δ_d being the crystal-field splittings associated with the p−like and d−like valence bands, respectively. The strong $p-d$ hybridization of the valence bands has been directly determined from x-ray photoemission studies [73L1, 74K1, 77R1]. The compounds containing Cu show a stronger $p-d$ hybridization than the Ag compounds. This is in agreement with α_L derived from the optical measurement data using Eq.(4-8).

Tell and Bridenbaugh [75T1] have qualitatively demonstrated the observed reduction in energy gap values and in spin-orbit splitting of $CuGaS_2$ and $CuGaSe_2$ compounds using the $p-d$ hybridization model with two adjustable parameters, the energy separation and interaction between the p and d bands. In this model it has been assumed that the Γ_{15} levels of the p and d bands in the absence of $p-d$ hybridization would be mid way between the corresponding Γ_8 and Γ_7 levels. This, however, is not the case [57K1]. In addition, the effect of the crystal field has not been taken into account. According to the results of

Tell and Bridenbaugh, to explain the effect of negative spin-orbit splitting in $CuGaS_2$, the unperturbed d−like Γ_{15} level must lie above the unperturbed p−like Γ_{15} level. This is contrary to the experimental results [71T1] which have observed transitions from the d levels to the lowest conduction-band minimum. These discrepancies will be discussed further in Section 4.3.

The electronic structure of I-III-VI_2 compounds has been calculated by Poplavnoi et al [71P1, 76P1] using the empirical pseudopotential method [65C1]. These calculations for several Cu compounds has neglected the noble-metal d levels and has been unable to predict the observed valence band splittings. The first energy band calculation, which has taken the d levels into account, for $CuGaS_2$ and $CuAlS_2$ has been made by Oguchi et al [80O1] using the self-consistent numerical linear combination of atomic orbitals [77Z1]. The results indicate an admixture state of Cu($3d$) and S($3p$) orbitals at the top of the valence bands.

Bendt and Zunger [82B1] recently calculated the electronic structure of $CuInSe_2$ using the potential-variation mixed-basis (PVMB) approach which avoids pseudopotential approximations and solves the all-electron problem self-consistently. The Cu $3d$ states are present at $\sim$ 2 - 3 eV below the band edge in good agreement with the results of XPS [77R1].

The PVMB approach has been used by Jaffe and Zunger [83J2] to study the chemical trends in the electronic structure of $CuAlS_2$, $CuGaS_2$, $CuInS_2$, $CuAlSe_2$, $CuGaSe_2$ and $CuInSe_2$. It has been found that in an energy range of appproximately 18 eV below the valence band maximum (VBM), there are four distinct valence-band regions, separated by three heteropolar gaps (see Fig. 4.4). Firstly, there is an upper valence band made up predominantly from the Cu($3d$)-chalcogen ($3p$ or $4p$) bond. The local density of states indicates that the Cu d character reaches its maximum at 3 - 4 eV below the VBM.

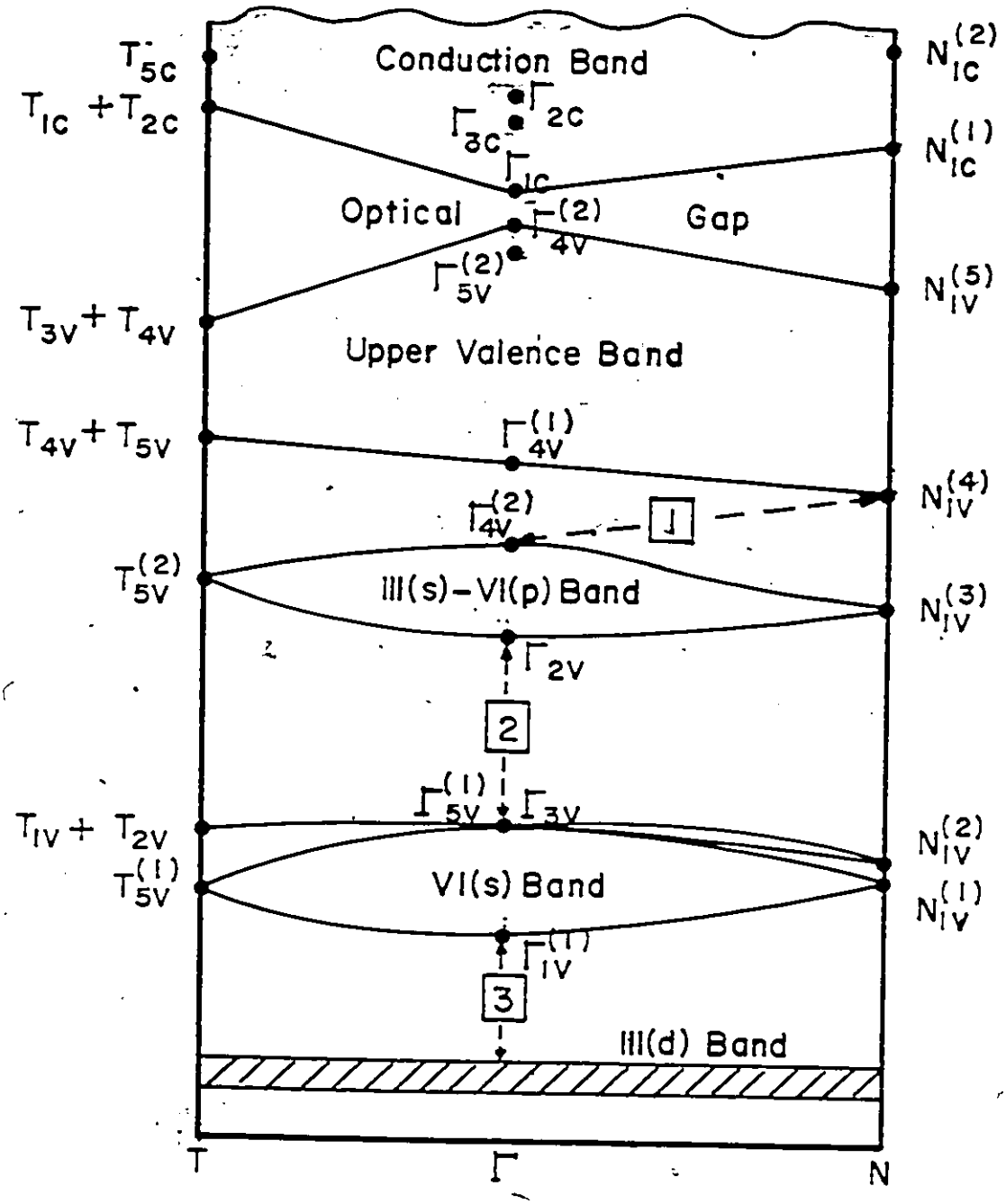

Fig. 4.4 Schematic band diagram for I-III-VI_2 chalcopyrite compounds showing the major subbands (after Jaffe and Zunger [83J2]). Boxed numbers indicate the three heteropolar gaps.

Below this are a valence band labelled the III-VI band, which represents the weak bond between the III(s) and VI(p) atoms, e.g., the Ga($4s$) - S($3p$) bond in $CuGaS_2$, the VI(s) band contributed from the chalcogen s electrons, and in the case of Ga and In compounds, a narrow III(d) band comes progressively lower in energy. The calculated density of states of the six Cu compounds are in good agreement with the available data from XPS and UPS results [73L1, 74K1, 74B1, 77R1, 81D1]. At the conduction band minimum (CBM) Γ_{1c} consists predominantly of excited anion s orbitals and Cu $4s$ orbitals. The calculated electronic charge densities of the VBM and CBM of $CuAlS_2$ and $CuGaS_2$ show a significant overlaps between the two states on the same (anion) sublattice and to a lesser extent on the Cu site.

Finally, Neuman et al [84N1] have calculated the valence band density of states of all Ga and In compounds of the form Cu III VI_2 on an atomic orbital basis with the noble-metal d levels explicitly included. The agreement between the theoretical results and experimental results from XPS and UPS is good for $CuGaTe_2$ and also $CuInVI_2$ compounds excepts for the particular case of the In($5s$) - VI(p) bonding states. Larger discrepencies are found for $CuGaS_2$ and $CuGaSe_2$.

It is seen that in order to provide an adequate description of the energy band structure of I-III-VI_2 CH compounds, the noble-metal d levels must be taken into account. In the next section, a model is developed to study the effect of $p - d$ hybridization on the uppermost valence bands of I-III-VI_2 CH semiconductors.

4.3 Theory of the Effects of $p-d$ Hybridization on the Valence Band of I-III-VI_2 Chalcopyrite Semiconductors.

Here, a model [S4Y1] is proposed which takes into account the $p-d$ hybridization effect on the uppermost valence bands of I-III-VI_2 CH compounds, considering the Γ point only. This study extends the $p-d$ hybridization approach of Tell and Bridenbaugh [75T1]. For convenience, it is assumed that the $p-$like valence bands lie above the $d-$like ones, although a similar analysis could be carried out without this assumption. In a cubic (tetrahedral) field, the fivefold-degenerate d levels split into a threefold-degenerate $\Gamma_{15}(d)$ and a twofold-degenerate $\Gamma_{12}(d)$ set, and the $\Gamma_{15}(d)$ levels lie at higher energy than the $\Gamma_{12}(d)$ [67S1, 83T1] (see also Fig. 8 and text in page 189 of [84J1]). The d level $\Gamma_{15}(d)$ has the same symmetry as the p level $\Gamma_{15}(p)$, so that these will interact with each other. Since the d level $\Gamma_{12}(d)$ has the wrong symmetry to interact with the $\Gamma_{15}(p)$, it can be neglected. Thus, only the p band $\Gamma_{15}(p)$ and the d band $\Gamma_{15}(d)$ will be considered.

There are two important parameters in this model, viz., the energy separation E between p and d levels and the interaction matrix element M due to the $p-d$ hybridization interaction between these levels. Starting from a quasicubic crystal with spin-orbit interaction, the wave functions of the diagonalized spin-orbit interaction are used as basis functions. The $p-d$ hybridization interaction is applied and levels of the same symmetry will mix and repel each other, the magnitude of the interaction depending on the energy separation and the strength of the interaction potential. The interaction is responsible for both the reduction ΔE_g in the energy gap compared with the value for the corresponding binary compound (i.e., the band-gap anomaly [84J1]) and for the reduced or negative spin-orbit splitting of the ternary CH compounds. Here the effect of anion displacement is neglected and the crystal field is taken to be due

only to tetragonal compression of the CH. In order to see the effect of this field on the uppermost valence bands, the first three mixed levels, which have Γ_8 and Γ_7 symmetry, are then perturbed further; and they split into three separate levels with Γ_7, Γ_6, and Γ_7 symmetry, repsectively. All of the energy eigenvalues and wave functions, including the coefficient of d–like character, can then be determined exactly. The two parameters E, M, and the band-gap anomaly ΔE_g play an important role in the theory. Three special cases will be considered, viz., the cases when there is no $p-d$ hybridization and/or crystal field, and the one when the strength of the interaction potential is very weak.

4.3.1 Theoretical Development

The Hamiltonian for cubic crystals with spin-orbit interaction is of the form

$$H = \frac{p^2}{2m} + V_0 + \frac{\hbar}{4m^2c^2}(\vec{\nabla}V_0 \times \vec{p}) \cdot \vec{\sigma} \quad . \qquad (4-10)$$

where $\vec{p}$ is the momentum operator and $\vec{\sigma}$ is the spin operator. The term V_0 is the cubic potential of the crystal.

The basis functions in the diagonalized spin-orbit Hamiltonian at the Γ-point can be written as follows [57K1] :

For the conduction band,

$$o_c^a(\Gamma_6) = |iS\ \downarrow\rangle \quad ,$$
$$o_c^a(\Gamma_6) = |iS\ \uparrow\rangle \quad , \qquad (4-11)$$

these are degenerate wave functions.

For the p band,

$$o^{o}_{p1}(\Gamma_8) = (\tfrac{1}{3})^{1/2}\left|\frac{X - iY}{\sqrt{2}}\uparrow\right\rangle + (\tfrac{2}{3})^{1/2}|Z\downarrow\rangle \quad ,$$

$$o^{o}_{p0}(\Gamma_8) = \left|\frac{X + iY}{\sqrt{2}}\uparrow\right\rangle \quad , \qquad (4-12)$$

$$o^{o}_{p2}(\Gamma_7) = (\tfrac{2}{3})^{1/2}\,|\,\frac{X - iY}{\sqrt{2}}\uparrow\rangle - (\tfrac{1}{3})^{1/2}\,|\,Z\downarrow\rangle \quad ;$$

$$o^{a}_{p1}(\Gamma_8) = (\tfrac{1}{3})^{1/2}\left|-\frac{X + iY}{\sqrt{2}}\downarrow\right\rangle + (\tfrac{2}{3})^{1/2}|Z\uparrow\rangle \quad .$$

$$o^{a}_{p0}(\Gamma_8) = \left|\frac{X - iY}{\sqrt{2}}\downarrow\right\rangle \quad , \qquad (4-13)$$

$$o^{a}_{p2}(\Gamma_7) = (\tfrac{2}{3})^{1/2}\,|\,-\frac{X + iY}{\sqrt{2}}\downarrow\rangle - (\tfrac{1}{3})^{1/2}\,|\,Z\uparrow\rangle \quad .$$

The first three functions are degenerate, respectively with the last three.

For the d band ,

$$o^{o}_{d1}(\Gamma_8) = (\tfrac{1}{3})^{1/2}\left|\frac{YZ - iZX}{\sqrt{2}}\uparrow\right\rangle + (\tfrac{2}{3})^{1/2}|XY\downarrow\rangle \quad .$$

$$o^{o}_{d0}(\Gamma_8) = \left|\frac{YZ + iZX}{\sqrt{2}}\uparrow\right\rangle \quad , \qquad (4-14)$$

$$o^{o}_{d2}(\Gamma_7) = (\tfrac{2}{3})^{1/2}\,|\,\frac{YZ - iZX}{\sqrt{2}}\uparrow\rangle - (\tfrac{1}{3})^{1/2}\,|\,XY\downarrow\rangle \quad ;$$

$$o^{a}_{d1}(\Gamma_8) = (\tfrac{1}{3})^{1/2}\left|-\frac{YZ + iZX}{\sqrt{2}}\downarrow\right\rangle + (\tfrac{2}{3})^{1/2}|XY\uparrow\rangle \quad .$$

$$o^{a}_{d0}(\Gamma_8) = \left|\frac{YZ - iZX}{\sqrt{2}}\downarrow\right\rangle \quad , \qquad (4-15)$$

$$o^{a}_{d2}(\Gamma_7) = (\tfrac{2}{3})^{1/2}\,|\,-\frac{YZ + iZX}{\sqrt{2}}\downarrow\rangle - (\tfrac{1}{3})^{1/2}\,|\,XY\uparrow\rangle \quad .$$

The first three of these functions are again degenerate, respectively, with the last three.

These are the wave functions which form a set of orthonormalized states for the conduction band and the noninteracting p and d bands. The resulting energy configuration which has taken into account the negative spin-orbit splitting of the d band [65S1, 67S1, 69C1] is shown in Fig. 4.5 under the headings H_0 and H_0 + S.O. Here, E_s, E_p and E_d are the eigenvalues of H_0 and the spin-orbit splitting of the p and d bands, respectively, are defined by

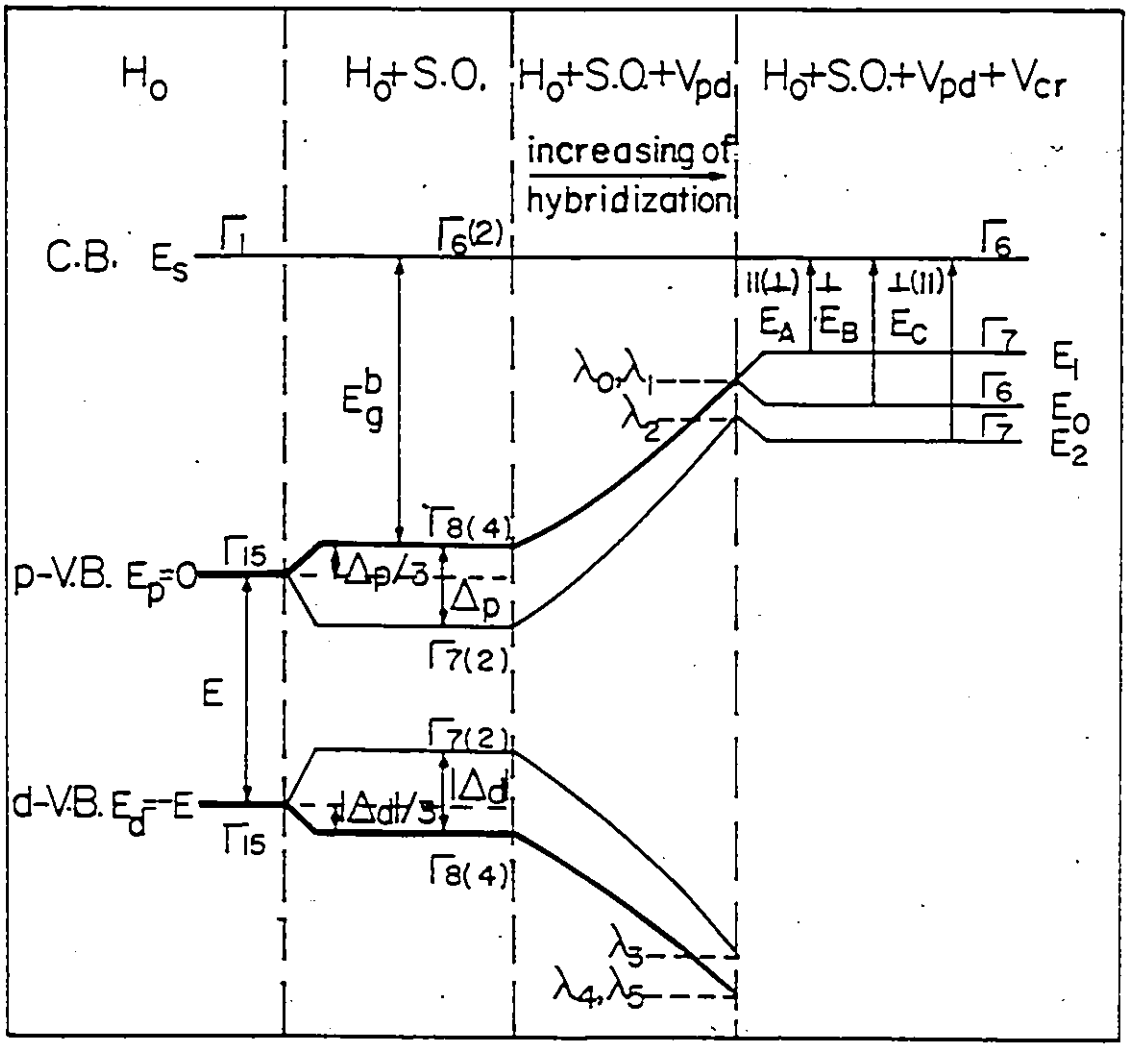

Fig. 4.5 Sketch of the energy-band configuration at the Γ point showing the variations in the *p* and *d* bands as spin-orbit interaction, $p-d$ hybridization, and crystal-field interaction are successively applied.

$$\Delta_p = \frac{3\hbar i}{4m^2c^2}\left\langle X\left|\frac{\partial V_0}{\partial x}p_y - \frac{\partial V_0}{\partial y}p_x\right|Y\right\rangle \quad (4-16)$$

and

$$\Delta_d = \frac{3\hbar i}{4m^2c^2}\left\langle YZ\left|\frac{\partial V_0}{\partial x}p_y - \frac{\partial V_0}{\partial y}p_x\right|ZX\right\rangle \quad (4-17)$$

In the presence of a hybridization interation potential V_{pd}, the interaction matrix between the p and d bands can be written as

$$\begin{bmatrix} V_{pd} & 0 \\ 0 & V_{pd} \end{bmatrix} \quad (4-18)$$

The basis wave functions used in this representation are as follows: $o^{\alpha}_{p1}(\Gamma_8)$, $o^{\alpha}_{d1}(\Gamma_8)$, $o^{\alpha}_{p0}(\Gamma_8)$, $o^{\alpha}_{d0}(\Gamma_8)$, $o^{\alpha}_{p2}(\Gamma_7)$, $o^{\alpha}_{d2}(\Gamma_7)$, $o^{\beta}_{p1}(\Gamma_8)$, $o^{\beta}_{d1}(\Gamma_8)$, $o^{\beta}_{p0}(\Gamma_8)$, $o^{\beta}_{d0}(\Gamma_8)$, $o^{\beta}_{p2}(\Gamma_7)$, and $o^{\beta}_{d2}(\Gamma_7)$. The first six functions are degenerate with the last six, repectively. The matrix elements of the hybridization interaction potential V_{pd} can be written in the form

$$\begin{aligned} \langle o^{\alpha}_{pi}(\Gamma_m)|V_{pd}|o^{\beta}_{dj}(\Gamma_n)\rangle &= M\delta_{ij}\delta_{\alpha\beta}\delta_{mn} \\ \langle o^{\alpha}_{pi}(\Gamma_m)|V_{pd}|o^{\beta}_{pj}(\Gamma_n)\rangle &= 0 \\ \langle o^{\alpha}_{di}(\Gamma_m)|V_{pd}|o^{\beta}_{dj}(\Gamma_n)\rangle &= 0 \end{aligned} \quad (4-19)$$

where M is the interaction between these levels and δ_{ij} is a Kronecker δ function. The full matrix representation of the submatrix V_{pd} then becomes

$$V_{pd} = \begin{bmatrix} \Delta_p/3 & M & 0 & 0 & 0 & 0 \\ M & -E-|\Delta_d|/3 & 0 & 0 & 0 & 0 \\ 0 & 0 & \Delta_p/3 & M & 0 & 0 \\ 0 & 0 & M & -E-|\Delta_d|/3 & 0 & 0 \\ 0 & 0 & 0 & 0 & -\frac{2}{3}\Delta_p & M \\ 0 & 0 & 0 & 0 & M & -E+\frac{2}{3}|\Delta_d| \end{bmatrix} \quad (4-20)$$

The resulting energy eigenvalues are

$$\lambda_0 = \lambda_1 = \frac{1}{2}\left[\frac{\Delta_p}{3} - E - \frac{|\Delta_d|}{3}\right] + \frac{1}{2}\left[\left(\frac{\Delta_p}{3} + E + \frac{|\Delta_d|}{3}\right)^2 + 4M^2\right]^{1/2}$$

$$\lambda_2 = \frac{1}{2}\left[-\frac{2}{3}\Delta_p - E + \frac{2}{3}|\Delta_d|\right] + \frac{1}{2}\left[\left(-\frac{2}{3}\Delta_p + E - \frac{2}{3}|\Delta_d|\right)^2 + 4M^2\right]^{1/2} \quad (4-21)$$

$$\lambda_3 = \frac{1}{2}\left[-\frac{2}{3}\Delta_p - E + \frac{2}{3}|\Delta_d|\right] - \frac{1}{2}\left[\left(-\frac{2}{3}\Delta_p + E - \frac{2}{3}|\Delta_d|\right)^2 + 4M^2\right]^{1/2}$$

$$\lambda_4 = \lambda_5 = \frac{1}{2}\left[\frac{\Delta_p}{3} - E - \frac{|\Delta_d|}{3}\right] - \frac{1}{2}\left[\left(\frac{\Delta_p}{3} + E + \frac{|\Delta_d|}{3}\right)^2 + 4M^2\right]^{1/2} \quad (4-22)$$

and the corresponding eigenfunctions are as follows :

for λ_0,

$$\Phi_0^{\alpha}(\Gamma_8) = a_0 o_{p0}^{\alpha}(\Gamma_8) + b_0 o_{d0}^{\alpha}(\Gamma_8)$$

$$\Phi_0^{\beta}(\Gamma_8) = a_0 o_{p0}^{\beta}(\Gamma_8) + b_0 o_{d0}^{\beta}(\Gamma_8) \quad (4-23)$$

for λ_1,

$$\Phi_1^{\alpha}(\Gamma_8) = a_1 o_{p1}^{\alpha}(\Gamma_8) + b_1 o_{d1}^{\alpha}(\Gamma_8)$$

$$\Phi_1^{\beta}(\Gamma_8) = a_1 o_{p1}^{\beta}(\Gamma_8) + b_1 o_{d1}^{\beta}(\Gamma_8) \quad (4-24)$$

for λ_2,

$$\Phi_2^{\alpha}(\Gamma_7) = a_2 o_{p2}^{\alpha}(\Gamma_7) + b_2 o_{d2}^{\alpha}(\Gamma_7)$$

$$\Phi_2^{\beta}(\Gamma_7) = a_2 o_{p2}^{\beta}(\Gamma_7) + b_2 o_{d2}^{\beta}(\Gamma_7) \quad (4-25)$$

for λ_3,

$$\Phi_3^{\alpha}(\Gamma_7) = a_3 o_{p2}^{\alpha}(\Gamma_7) + b_3 o_{d2}^{\alpha}(\Gamma_7)$$

$$\Phi_3^{\beta}(\Gamma_7) = a_3 o_{p2}^{\beta}(\Gamma_7) + b_3 o_{d2}^{\beta}(\Gamma_7) \quad (4-26)$$

for λ_4,

$$\Phi_4^{\alpha}(\Gamma_8) = a_4 o_{p0}^{\alpha}(\Gamma_8) + b_4 o_{d0}^{\alpha}(\Gamma_8) \quad ,$$

$$\Phi_4^{\beta}(\Gamma_8) = a_4 o_{p0}^{\beta}(\Gamma_8) + b_4 o_{d0}^{\beta}(\Gamma_8) \quad , \tag{4-27}$$

for λ_5,

$$\Phi_5^{\alpha}(\Gamma_8) = a_5 o_{p1}^{\alpha}(\Gamma_8) + b_5 o_{d1}^{\alpha}(\Gamma_8) \quad ,$$

$$\Phi_5^{\beta}(\Gamma_8) = a_5 o_{p1}^{\beta}(\Gamma_8) + b_5 o_{d1}^{\beta}(\Gamma_8) \quad . \tag{4-28}$$

The a_i and b_i coefficients can be evaluated. Writing $\gamma_i = a_i^2$, then

$$\gamma_0 = \gamma_1 = a_1^2 = 1 - b_1^2 = 1/\left[1 + M^2/\left(\lambda_1 + E + \frac{|\Delta_d|}{3}\right)^2\right] \quad . \tag{4-29}$$

$$\gamma_2 = a_2^2 = 1 - b_2^2 = 1/[1 + M^2/(\lambda_2 + E - \tfrac{2}{3}|\Delta_d|)^2] \quad . \tag{4-30}$$

$$\gamma_3 = a_3^2 = 1 - b_3^2 = 1 - 1/[1 + M^2/(\lambda_3 + \tfrac{2}{3}\Delta_p)^2] \quad . \tag{4-31}$$

$$\gamma_4 = \gamma_5 = a_5^2 = 1 - b_5^2 = 1 - 1/\left[1 + M^2/\left(\lambda_5 - \frac{\Delta_p}{3}\right)^2\right] \quad . \tag{4-32}$$

Next, it is necessary to include the crystal-field interaction due to the noncubic potential arising from the tetragonal lattice compression along the chalcopyrite z axis, this being the largest contribution to the crystal-field splitting of the valence bands. In order to find the splitting of the uppermost valence bands, only the first three levels are considered. Using the wave-function equations (4-23)-(4-25) as basis function, the interaction matrix for the crystal-field interaction, V_{cr}, can be written as

$$\begin{bmatrix} V_{cr} & 0 \\ 0 & V_{cr} \end{bmatrix} \qquad (4-33)$$

where

$$V_{cr} = \begin{bmatrix} \lambda_1 - \gamma_1 \frac{\delta_p}{3} - \gamma_1' \frac{\delta_d}{3} & (2\gamma_1\gamma_2)^{1/2}\frac{\delta_p}{3} + [2\gamma_1'\gamma_2']^{1/2}\frac{\delta_d}{3} & 0 \\ (2\gamma_1\gamma_2)^{1/2}\frac{\delta_p}{3} + [2\gamma_1'\gamma_2']^{1/2}\frac{\delta_d}{3} & \lambda_2 & 0 \\ 0 & 0 & \lambda_0 + \gamma_0\frac{\delta_p}{3} + \gamma_0'\frac{\delta_d}{3} \end{bmatrix}$$

$$\gamma_0' = 1 - \gamma_0$$

$$\gamma_1' = 1 - \gamma_1$$

and

$$\gamma_2' = 1 - \gamma_2 \qquad (4-34)$$

The quantities δ_p and δ_d are the crystal-field-splitting parameters of the p and d bands, respectively. They are defined [74K2] by

$$< X \mid V_{cr} \mid X >=< Y \mid V_{cr} \mid Y >= \frac{\delta_p}{3} \qquad (4-35)$$

$$< Z \mid V_{cr} \mid Z >= -\frac{2}{3}\delta_p \qquad (4-36)$$

and, similarly,

$$< YZ \mid V_{cr} \mid YZ >=< ZX \mid V_{cr} \mid ZX >= \frac{\delta_d}{3} \qquad (4-37)$$

$$< XY \mid V_{cr} \mid XY >= -\frac{2}{3}\delta_d \qquad (4-38)$$

It is to be noted that the static shift [74K2] due to the crystal field has already been taken into account. However, the crossterm matrix element due to the crystal field has been neglected in the present model.

To determine the level splitting at the BZ center, the matrix in Eq. (4-33) must be diagonalized. The valence band then splits into three doubly degenerate levels, which are

$$E_0(\Gamma_6) = \lambda_0 + \gamma_0 \frac{\delta_p}{3} + (1-\gamma_0)\frac{\delta_d}{3} \quad . \tag{4-39}$$

$$E_{1,2}(\Gamma_7) = \frac{1}{2}\left[\lambda_1 + \lambda_2 - \gamma_1 \frac{\delta_p}{3} - (1-\gamma_1)\frac{\delta_d}{3}\right] \pm \frac{1}{2}\left[\left(\lambda_1 - \lambda_2 - \gamma_1 \frac{\delta_p}{3} - (1-\gamma_1)\frac{\delta_d}{3}\right)^2 + \frac{8}{9}\{(\gamma_1\gamma_2)^{1/2}\delta_p + [(1-\gamma_1)(1-\gamma_2)]^{1/2}\delta_d\}^2\right]^{1/2} \quad . \tag{4-40}$$

The resulting energy configuration and the polarization-transitions are shown in Fig. 4.5 under the heading $H_0 + S.O. + V_{pd} + V_{cr}$. In order to estimate a value for the band-gap anomaly ΔE_g, it is assumed that the Γ_8 level of the unperturbed p bands (see Fig. 4.5) in this analysis is the same as the top level in the valence band of the equivalent binary compound. In that case, ΔE_g then takes the value

$$\Delta E_g = E_g^b - E_A = E_1 - \Delta_p/3 \quad . \tag{4-41}$$

where E_A and E_g^b are the band gaps of the ternary CH compound and the equivalent binary compound, respectively.

The wave functions corresponding to Eqs. (4-39) and (4-40) are

$$\Psi_1^v(\Gamma_7) = c_1\Phi_1^v(\Gamma_8) + d_1\Phi_2^v(\Gamma_7) = c_1a_1o_{p1}^v(\Gamma_8) + d_1a_2o_{p2}^v(\Gamma_7) + c_1b_1o_{d1}^v(\Gamma_8) + d_1b_2o_{d2}^v(\Gamma_7) \quad . \tag{4-42}$$

$$\Psi_1^v(\Gamma_7) = c_1a_1o_{p1}^v(\Gamma_8) + d_1a_2o_{p2}^v(\Gamma_7) + c_1b_1o_{d1}^v(\Gamma_8) + d_1b_2o_{d2}^v(\Gamma_7) \quad . \tag{4-43}$$

$$\Psi_0^v(\Gamma_6) = \Phi_3^v(\Gamma_8) = a_0o_{p0}^v(\Gamma_8) + b_0o_{d0}^v(\Gamma_8) \quad . \tag{4-44}$$

$$\Psi_0^{\beta}(\Gamma_6) = \Phi_0^{\beta}(\Gamma_6) = a_0 o_{p0}^{\beta}(\Gamma_6) + b_0 o_{d0}^{\beta}(\Gamma_6) \quad . \tag{4-45}$$

and

$$\Psi_2^{\alpha}(\Gamma_7) = c_2 \Phi_1^{\alpha}(\Gamma_6) + d_2 \Phi_2^{\alpha}(\Gamma_7) = c_2 a_1 o_{p1}^{\alpha}(\Gamma_6) + d_2 a_2 o_{p2}^{\alpha}(\Gamma_7) + c_2 b_1 o_{d1}^{\alpha}(\Gamma_6) + d_2 b_2 o_{d2}^{\alpha}(\Gamma_7) \quad . \tag{4-46}$$

$$\Psi_2^{\beta}(\Gamma_7) = c_2 a_1 o_{p1}^{\beta}(\Gamma_6) + d_2 a_2 o_{p2}^{\beta}(\Gamma_7) + c_2 b_1 o_{d1}^{\beta}(\Gamma_6) + d_2 b_2 o_{d2}^{\beta}(\Gamma_7) \quad . \tag{4-47}$$

Using these levels, the fractional p—like character of the uppermost valence bands are found to be

$$\alpha_1 = c_1^2 a_1^2 + d_1^2 a_1^2 = c_1^2 \gamma_1 + d_1^2 \gamma_2 \quad . \tag{4-48}$$

$$\alpha_0 = a_0^2 = \gamma_0 \quad . \tag{4-49}$$

$$\alpha_2 = c_2^2 a_1^2 + d_2^2 a_2^2 = c_2^2 \gamma_1 + d_2^2 \gamma_2 \quad . \tag{4-50}$$

where

$$c_1^2 = 1 \Big/ \left[1 + \left((2\gamma_1\gamma_2)^{1/2} \frac{\delta_p}{3} + [2(1-\gamma_1)(1-\gamma_2)]^{1/2} \frac{\delta_d}{3} \right)^2 \Big/ (E_1 - \lambda_2)^2 \right] \quad . \tag{4-51}$$

$$d_2^2 = 1 \Big/ \left[1 + \left((2\gamma_1\gamma_2)^{1/2} \frac{\delta_p}{3} + [2(1-\gamma_1)(1-\gamma_2)]^{1/2} \frac{\delta_d}{3} \right)^2 \Big/ \left(E_2 - \lambda_1 + \gamma_1 \frac{\delta_p}{3} + (1-\gamma_1) \frac{\delta_d}{3} \right)^2 \right] \quad . \tag{4-52}$$

$$c_1^2 + d_1^2 = 1 \quad . \tag{4-53}$$

$$c_2^2 + d_2^2 = 1 \quad . \tag{4-54}$$

Using Eqs. (4-11), (4-42), (4-43), (4-46) and (4-47), the polarization-intensity ratios for transitions from a given Γ_7 valence band (at energy E_1 or E_2) to a Γ_6 conduction band are determined to be

$$\frac{I_{\parallel}}{I_{\perp}}(\Gamma_7 \text{ at } E_i - \Gamma_6) = \left[\frac{2c_i a_1 - \sqrt{2} d_i a_2}{c_i a_1 + \sqrt{2} d_i a_2} \right]^2 \quad . \tag{4-55}$$

where i refers to 1 and 2. The light is polarized, respectively, parallel or perpendicular to the CH z-axis. In the derivation of Eq. (4-55), a matrix element of the type $< S \mid P_z \mid XY >$ has been neglected since according to the tight binding approximation, the value of the matrix element is proportional to a dipole optical matrix element between the atomic s- and d- orbitals which is not allowed for the atomic case. Thus, the value of $< S \mid P_z \mid XY >$ is very small compared to that of $< S \mid P_z \mid Z >$ [85S2]. Thus, from the above analysis, the energy separations of the valence bands are given by Eqs. (4-39) and (4-40) and the fractional p and d characters of the valence are determined by Eqs. (4-48) to (4-50). Equations (4-39) and (4-40) can be used to analyze the experimental data available for various chalcopyrite materials and give values for the various material parameters. This will be done in Sec. 4.3.3. Before this analysis, however, it is instructive to show that the present model will reduce to the previously proposed models under the appropriate limits.

4.3.2 Limiting Cases

Three previous models are considered and it is shown that each is a special case of the present model and can be derived from it.

A. Tell and Bridenbaugh model

In the Tell and Bridenbaugh analysis, there is no noncubic crystal field and, in the absence of $p-d$ hybridization, the Γ_{15} levels of the p and d bands are assumed to be midway between their Γ_8 and Γ_7 levels. For the present model, if δ_p and δ_d are made zero, the E_1, E_0, and E_2 levels, Eqs.(4-39) and (4-40), reduce to a doubly degenerate Γ_8 level at the energy $\lambda_1 = \lambda_0$, and to a Γ_7 level at the energy λ_2, i.e.,

$$E_1 = \lambda_1 = E_0 = \lambda_0(\Gamma_8), \quad E_2 = \lambda_2(\Gamma_7) \quad . \tag{4-56}$$

From Eqs. (4-48) to (4-50), it is seen that the fractional p-like characters then become

$$\alpha_1 = \gamma_1 = \alpha_0 = \gamma_0, \quad \alpha_2 = \gamma_2 \quad . \tag{4-57}$$

The energy-gap anomaly ΔE_g [from Eq. (4-41)] becomes

$$\Delta E_g = E_1 - \frac{\Delta_p}{3} = \lambda_1 - \frac{\Delta_p}{3} \quad . \tag{4-58}$$

Equations (4-56) to (4-58) are the same as those of Tell and Bridenbaugh, except for the different choice of the energy of the Γ_{15} levels mentioned above.

B. Kildal's model

In this case a noncubic crystal field is assmed, i.e., $\delta_p \neq 0$ and $\delta_2 \neq 0$, but there is no $p-d$ hybridization, i.e., $M = 0$. Thus, in the present analysis, if the d-like character is ignored, then only the p-like character remains and the various parameters take the values

$$\gamma_0 = \gamma_1 = \gamma_2 = 1, \quad \alpha_1 = \alpha_0 = \alpha_2 = 1$$

and (4-59)

$$\lambda_1 = \lambda_0 = \frac{\Delta_p}{3}, \quad \lambda_2 = -\frac{2}{3}\Delta_p \quad .$$

The energies of the Γ_7 and Γ_6 levels can then be expressed as follows : For Γ_6,

$$E_0 = \frac{\Delta_p + \delta_p}{3} \quad . \tag{4-60}$$

and For Γ_7,

$$E_{1,2} = -\frac{1}{6}(\Delta_p + \delta_p) \pm \frac{1}{2}\left[\left(\Delta_p - \frac{\delta_p}{3}\right)^2 + \frac{8}{9}\delta_p^2\right]^{1/2}$$
$$= -\frac{1}{6}(\Delta_p + \delta_p) \pm \frac{1}{2}\left[(\Delta_p + \delta_p)^2 - \frac{8}{3}\Delta_p\delta_p\right]^{1/2} \qquad (4-61)$$

This is identical to Kildal's final result except for the different choice of the energy zero (i.e., $E_p + \frac{\Delta_p+\delta_p}{3} = 0$). Furthermore, it is to be noted that Kane's form can be obtained by neglecting the crystal field completely, i.e., by setting $\delta_p = 0$.

C. Linear hybridization limit

This is the form used by various workers [75S2, 77Y1, 79Y1, 77T1, 82L1]. Essentially, it assumes that the parameters Δ and δ in Eq. (4-5) can each be written as a linear sum of the p and d contribtions, i.e.,

$$\Delta = \alpha_L\Delta_p - (1-\alpha_L)|\Delta_d|$$
$$and \qquad (4-62)$$
$$\delta = \alpha_L\delta_p + (1-\alpha_L)\delta_d$$

In the present model, this case is represented by the conditions $M/E < 1$ and $E > \Delta_p$ and $|\Delta_d|$. The energy eigenvalues λ_1 and λ_2 can then be rewritten, using a Taylor expansion, as

$$\lambda_1 = \frac{1}{2}\left[\frac{\Delta_p}{3} - E - \frac{|\Delta_d|}{3}\right] + \frac{1}{2}\left[\frac{\Delta_p}{3} + E + \frac{|\Delta_d|}{3}\right]\left[1 + \frac{4M^2}{(E + \Delta_p/3 + |\Delta_d|/3)^2}\right]^{1/2} \qquad (4-63)$$
$$\simeq \frac{\Delta_p}{3} + \frac{M^2}{E[1 + (\Delta_p + |\Delta_d|)/3E]}$$

Expanding further,

$$\lambda_1 \simeq \frac{M^2}{E} + \frac{\Delta_p}{3}\left[1 - \frac{M^2}{E^2}\right] - \frac{M^2}{E^2}\frac{|\Delta_d|}{3} \qquad (4-64)$$

The first term on the right-hand side represents the shift due to the hybridization and will be the same for all three bands. Hence, it will disappear when the differences $E_1 - E_0$, etc. are calculated. However, it will be an important term in the expression for the band-gap anomaly ΔE_g. Similarly,

$$\lambda_2 \simeq \frac{M^2}{E} - \frac{2\Delta_p}{3}\left[1 - \frac{M^2}{E^2}\right] + \frac{2}{3}\frac{M^2}{E^2}|\Delta_d| \quad . \tag{4-65}$$

Thus,

$$\lambda_1 + \lambda_2 = \frac{2M^2}{E} - \frac{\Delta_p}{3}\left[1 - \frac{M^2}{E^2}\right] + \frac{1}{3}\frac{M^2}{E^2}|\Delta_d| \quad . \tag{4-66}$$

Similarly,

$$\lambda_1 - \lambda_2 = \Delta_p\left[1 - \frac{M^2}{E^2}\right] - |\Delta_d|\frac{M^2}{E^2} \quad . \tag{4-67}$$

From Eqs. (4-29) and (4-30),

$$\gamma_1 = \gamma_0 = \gamma_1 = \alpha_L \simeq \left[1 - \frac{M^2}{E^2}\right] \quad . \tag{4-68}$$

Thus,

$$\lambda_1 + \lambda_2 = \frac{2M^2}{E} - \frac{1}{3}[\alpha_L\Delta_p - (1-\alpha_L)|\Delta_d|]$$

$$\text{and} \qquad \Bigg\} \tag{4-69}$$

$$\lambda_1 - \lambda_2 = \alpha_L\Delta_p - (1-\alpha_L)|\Delta_d| \quad .$$

From Eq. (4-39),

$$E_0 = \lambda_0 + \gamma_0\delta_p/3 + (1-\gamma_0)\delta_d/3 \quad ,$$

so that, in the linear hybridization limit,

$$E_1 \simeq \frac{M^2}{E} + \frac{1}{3}[\alpha_L\Delta_p - (1-\alpha_L)|\Delta_d|] - \frac{1}{3}[\alpha_L\delta_p + (1-\alpha_L)\delta_d] \quad . \tag{4-70}$$

Similarly, from Eq. (4-40),

$$E_{1,2} = \frac{1}{2}\left[\lambda_1 + \lambda_2 - \gamma_1\frac{\delta_p}{3} \quad (1-\gamma_1)\frac{\delta_d}{3}\right]$$

$$\pm \frac{1}{2}\left[\left(\lambda_1 - \lambda_2 - \gamma_1\frac{\delta_p}{3} - (1-\gamma_1)\frac{\delta_d}{3}\right)^2 + \frac{8}{9}\{(\gamma_1\gamma_2)^{1/2}\delta_p + [(1-\gamma_1)(1-\gamma_2)]^{1/2}\delta_d\}^2\right]^{1/2}$$

which, in the limit, gives

$$E_{1,2} \simeq \frac{M^2}{E} - \frac{1}{6}[\alpha_L\Delta_p - (1-\alpha_L)|\Delta_d| + \alpha_L\delta_p + (1-\alpha_L)\delta_d]$$

$$\pm \frac{1}{2}(\{[\alpha_L\Delta_p \quad (1-\alpha_L)|\Delta_d|] - \frac{1}{3}[\alpha_L\delta_p + (1-\alpha_L)\delta_d]\}^2 + \frac{8}{9}[\alpha_L\delta_p + (1-\alpha_L)\delta_d|^2)^{1/2} \quad (4-71)$$

The band-gap anomaly ΔE_g now becomes

$$\Delta E_g = E_1 - \frac{\Delta_p}{3} \simeq \frac{M^2}{E} - \frac{\Delta_p}{3} - \frac{1}{6}[\alpha_L\Delta_p - (1-\alpha_L)|\Delta_d| + \alpha_L\delta_p + (1-\alpha_L)\delta_d]$$

$$\pm \frac{1}{2}(\{[\alpha_L\Delta_p - (1-\alpha_L)|\Delta_d|] - \frac{1}{3}[\alpha_L\delta_p + (1-\alpha_L)\delta_d]\}^2 \quad (4-72)$$

$$+ \frac{8}{9}[\alpha_L\delta_p + (1-\alpha_L)\delta_d|^2)^{1/2}$$

In Eqs. (4-60) and (4-61), from the Kildal model, it can be assumed that Δ_p and δ_p are the total spin-orbit and crystal-field contributions, i.e., Δ_p is replaced by Δ and δ_p by δ. If, in that modified form, Δ and δ are substituted from Eq. (4-62), the resulting equations are identical with Eqs. (4-70) and (4-71) above. Thus, Eqs. (4-70) to (4-71) include the linear form assumed in previous work [75S2, 77Y1, 79Y1, 77T1, 82L1].

4.3.3 Numerical Analysis and Results

In order to apply the present model to analyze the behavior of various I-III-VI_2 compounds, it is first necessary to review what experimental data are available for the analysis. For many of the I-III-VI_2 compounds, three valence-band—conduction-band transitions E_A, E_B, and E_C have been determined at room temperature and are listed in Table 4.4. The lattice-parameters values have been determined for all of the compounds, so that the ratio c/a is known and is also given in Table 4.4.

Table 4.4 Input parameters.

Code letter	Ternary compound	Energy gaps (eV) E_A	E_B	E_C	Δ_p (eV)	c/a	Binary analog[a]	Band-gap anomaly ΔE_g (eV)
A	$CuAlS_2$	3.49[b]	3.62[b]	3.62[b]	0.09	1.96[b]	$Mg_{0.5}Zn_{0.5}S$	2.41[a]
B	$CuGaS_2$	2.43[b]	2.55[b]	2.55[b]	0.12	1.96[b]	ZnS	1.37[a]
C	$CuInS_2$	1.53[b]	1.53[b]	1.53[b]	0.16	2.00[b]	$Zn_{0.5}Cd_{0.5}S$	1.04[a]
D	$CuAlSe_2$	2.72[c]	2.86[c]	3.01[c]	0.32	1.95[b]	$Mg_{0.5}Zn_{0.5}Se$	1.47[a]
E	$CuGaSe_2$	1.68[b]	1.75[b]	1.96[b]	0.35	1.96[b]	$ZnSe$	1.00[a]
F	$CuInSe_2$	1.04[b]	1.04[b]	1.27[b]	0.39	2.00[b]	$Zn_{0.5}Cd_{0.5}Se$	1.29[a]
G	$CuAlTe_2$	2.06[d]			0.91	1.97[b]	$Mg_{0.5}Zn_{0.5}Te$	1.44[a]
H	$CuGaTe_2$	1.24[c]	1.27[c]	1.85[d]	0.94	1.98[b]	$ZnTe$	1.32[f]
I	$CuInTe_2$	1.06[c]	1.06[c]	1.67[c]	0.98	2.00[b]	$Zn_{0.5}Cd_{0.5}Te$	1.12[f]
J	$AgAlS_2$	3.13[d]			0.10	1.772[g]	$Mg_{0.5}Cd_{0.5}S$	
K	$AgGaS_2$	2.73[b]	3.01[b]	3.01[b]	0.13	1.79[b]	$Zn_{0.5}Cd_{0.5}S$	0.44[a]
L	$AgInS_2$	1.87[b]	2.02[b]	2.02[b]	0.17	1.92[b]	CdS	0.66[a]
M	$AgAlSe_2$	2.55[d]			0.33	1.793[g]	$Mg_{0.5}Cd_{0.5}Se$	
N	$AgGaSe_2$	1.82[b]	2.03[b]	2.29[b]	0.354	1.82[b]	$Zn_{0.5}Cd_{0.5}Se$	0.55[a]
O	$AgInSe_2$	1.24[b]	1.33[b]	1.60[b]	0.40	1.92[b]	$CdSe$	0.61[a]
P	$AgAlTe_2$	2.27[f]	2.38[f]		0.92	1.88[b]	$Mg_{0.5}Cd_{0.5}Te$	1.03[f]
Q	$AgGaTe_2$	1.32[f]	1.43[f]	2.23[f]	0.95	1.90[b]	$Zn_{0.5}Cd_{0.5}Te$	0.86[f]
R	$AgInTe_2$	0.90[f]			0.99	1.96[b]	$CdTe$	0.84[f]

[a] Reference [84J1].
[b] Reference [75S2].
[c] Reference [72B1].
[d] Reference [71H1].
[e] Reference [77T1].
[f] Reference [81M1].
[g] Reference [74S2].
[h] Reference [75S2].
[i] Reference [79P1].

Table 4.5 Atomic p spin-orbit splitting of elements used in the analysis (in eV).

Δ_p(Cu)=0.031[a]	Δ_p(Ga)=0.12[b]	Δ_p(S)=0.077[c]
	Δ_p(Al)=0.016[b]	Δ_p(Se)=0.286[c]
Δ_p(Ag)=0.114[a]	Δ_p(In)=0.27[b]	Δ_p(Te)=0.8335[c]

[a] Reference [63Y1].

[b] Reference [62B1].

[c] Reference [71P1].

However, if only these data were assumed known, there would be too many unknown parameters in the analysis. The band-gap anomaly ΔE_g can be estimated by comparing the value of E_A with the value of the corresponding binary analog, and these values of ΔE_g are listed in Table 4.4. Finally, values of the spin-orbit-splitting parameters Δ_p and Δ_d can be estimated from the atomic values [62B1, 71P1]. Thus, Δ_p can be written in the form

$$\Delta_p = G_p\left(\frac{1}{16}\Delta_{pI} + \frac{3}{16}\Delta_{pIII} + \frac{12}{16}\Delta_{pVI}\right) \quad , \qquad (4-73)$$

where Δ_{pI}, etc., are the atomic p spin-orbit splittings of the elements and G_P is an enhancement factor for the solid. For both zinc-blende [62B1] and chalcopyrite [71P1] structures, G_p has been taken to be 29/20. The values of Δ_{pI},etc. used in the analysis have been taken from various sources and are listed in Table 4.5. For Δ_d, only the effects of the copper or silver d elctrons are considered since the other d levels are much too deep to contribute [83J2]. Thus Δ_d is assumed to be given by

$$\Delta_d = G_d\Delta_{dI} \quad . \qquad (4-74)$$

Since, as indicated above, the d triplet acts like the p levels, it is assumed that G_d also has the value 29/20. Taking Δ_{dCu} as -0.15 eV and Δ_{dAg} as -0.33 eV [69C1], this gives Δ_d values of -0.22 eV for the copper compounds and -0.48 eV for the silver compounds.

The final requirement in this collection of input data is to obtain the crystal-field p splitting δ_p from the tetragonal distortion $(2 - c/a)$. As indicated in Section 4.2, the relation can be written in the form

$$\delta_p = \frac{3}{2}b_p(2 \quad c/a) \quad . \qquad (4-75)$$

where b_p is the deformation potential associated with the p bands. Because of the interaction with the d bands, no explicit value for b_p has been determined for the I-III-VI_2 compounds. However, for the II-IV-V_2 compounds, where no $p-d$ hybridization occurs, the mean value of b_p for the various compounds is found to be -1.2 eV [75S2]. Thus this value was used initially for b_p in the present work. However, as is shown below, a different value was needed in the final analysis.

With the above parameters taken as known, the number of unknown in the analysis is reduced to three, viz., E, M, and δ_d, and thus Eqs. (4-39) - (4-41) can be solved to determine values for these parameters. From these values of E, M, and δ_d, values can be determined for E_1, E_0, E_2, α_1, α_0 and α_2 from Eqs. (4-39), (4-40), and (4-48) - (4-54). The differences between the E_1, E_0, and E_2 values should, of course, be the same as the differences between the E_A, E_B, and E_C input values, but the separate values will be different by a constant quantity since the energy zero in the present analysis was chosen to be at the $\Gamma_{15}(p)$ level of the initial quasicubic crystal, as is shown in Fig. 4.5. The values of α_1, α_0 and α_2 show the relative amount of p character in the three separate valence bands. In each case the variation from one band to another is quite small, but it is of interest for purposes of comparison to have $\bar{\alpha}$ as a mean value, i.e., $\bar{\alpha} = \frac{1}{3}(\alpha_1 + \alpha_0 + \alpha_2)$.

When the above calculations were made using the value of $b_p = -1.2$ eV, it was found that the values obtained for the various parameters listed above appeared to be in satisfactory agreement from one compound to another, except in the case of δ_d. On the assumption that δ_d satisfies the same form as δ_p with regard to the tetragonal distortion, i.e.,

$$\delta_d = \frac{3}{2} b_d (2 - c/a) \qquad (4-70)$$

it was possible to obtain values of b_d for all compounds considered. These were found to vary condiserably, with values from -5.8 to +4.7 eV. Since it had further been assumed that, as in the case of b_p, b_d should have the same value for all of those compounds, the above result was taken to indicate that the value assumed for b_p was incorrect. The complete analysis was therefore repeated a number of times using values of b_p lying in the range -0.5 to -1.8 eV and the values obtained for b_d compared in each case. Figure 4.6 shows the values of b_d obtained for each compound for values of b_p in the range -0.5 to -1.3 eV. It is apparent that the spread in b_d values appears smallest for b_p in the vicinity of -0.8 eV. For each value of b_p, a mean value of b_d and a standard deviation σ were calculated. Figure 4.7 shows the variation of σ with b_p. It is seen that the minimum in σ occurs at $b_p = -0.8$ eV, at which point the mean value of b_d is -3.9 eV and $\sigma = 1.5$ eV. In view of these results, it is suggested that for all of the I-III-VI_2 compounds and alloys, appropriate values for the deformation potentials are $b_p = (-0.8 \pm 0.2)$ eV and $b_d = (-3.9 \pm 1.5)$ eV.

Unlike b_d, the other parameters determined by the analysis were found to be relatively insensitive to variations in b_p except for the values of E in the cases of $AgGaS_2$ and $AgGaSe_2$ which have larger values of tetragonal distortion. In these cases, a variation of b_p from resulting in changes in the values of E are ~ 0.5 eV for $AgGaS_2$ and ~ 1 eV for $AgGaSe_2$. Thus, in the final calculations the method described above was used with a value of $b_p = -0.8$ eV. The resulting values of the parameters $E, M, E_1, E_0, E_2, \alpha_1, \alpha_0, \alpha_2$, and $\bar{\alpha}$ are listed in Tables 4.6 and 4.7. Also given in Table 4.6 for purposes of comparison are values of $(1 - \alpha_L)$ given from the linear hybridization model and of $(1 - \alpha)$ from the self-consistent energy-band calculation by Jaffe and Zunger [S4J1].

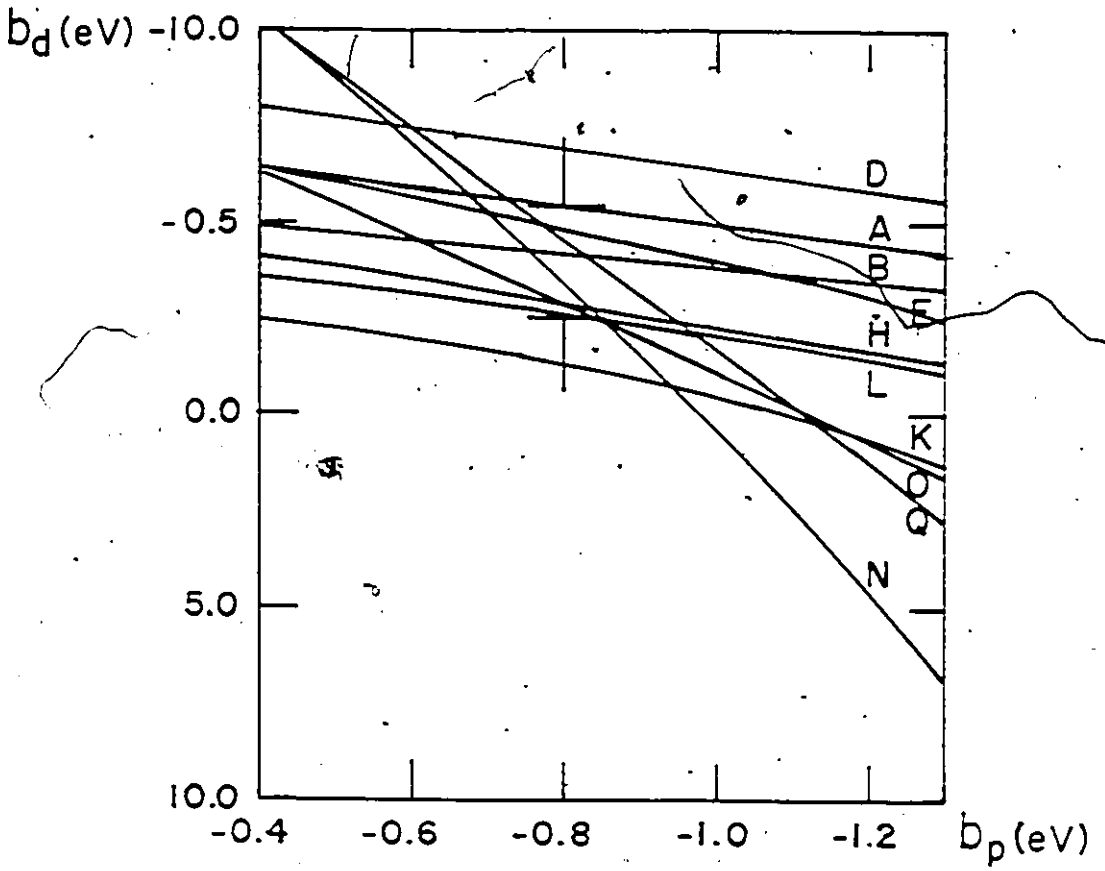

Fig. 4.6 Values of the deformation potential b_d obtained in present analysis for given values of the deformation potential b_p. For meaning of code letter see Table 4.4. $\frac{\perp}{\top}$ denotes the mean $b_d \pm \sigma$ at $b_p = -0.8$ eV

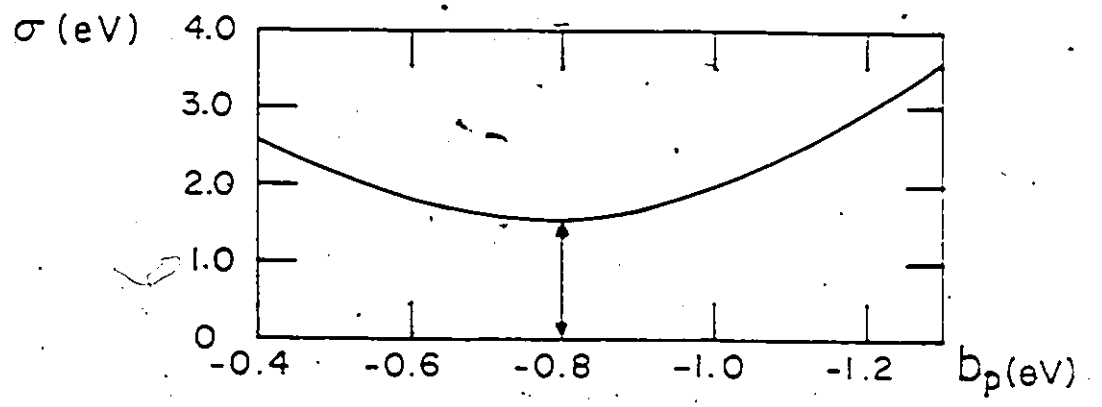

Fig. 4.7 Variation of standard deviation σ for b_d (averaged over 13 compounds) for given values of b_p.

Table 4.6 Parameters determined from the analysis.

Ternary compound	M (eV)	E (eV)	M/E	$1-\bar{\alpha}$	$\Delta E_g/E$	$1-\alpha_1$	$1-\alpha^a$	$1-\alpha_L$
$CuAlS_2$	3.000	3.340	1.096	0.293	0.722	0.293	0.352	0.290
$CuGaS_2$	1.794	1.096	1.637	0.354	1.250	0.355	0.315	0.353
$CuInS_2$	2.015	0.708	2.846	0.413	2.316	0.398	0.240	0.421
$CuAlSe_2$	2.396	2.588	0.926	0.263	0.568	0.254	0.275	0.264
$CuGaSe_2$	2.006	3.037	0.661	0.199	0.329	0.188	0.251	0.203
$CuInSe_2$	2.294	2.585	0.887	0.255	0.499	0.240	0.220	0.262
$CuAlTe_2$								
$CuGaTe_2$	2.275	2.271	1.002	0.280	0.581	0.248		0.293
$CuInTe_2$	1.935	1.822	1.062	0.291	0.615	0.251		0.308
$AgAlS_2$								
$AgGaS_2$	0.588	0.918	0.641	0.204	0.479	0.205		0.213
$AgInS_2$	1.047	1.100	0.878	0.257	0.553	0.260		0.262
$AgAlSe_2$								
$AgGaSe_2$	1.711	0.979	0.245	0.051	0.072	0.049		0.052
$AgInSe_2$	1.701	4.314	0.394	0.109	0.141	0.099		0.112
$AgAlTe_2$								
$AgGaTe_2$	2.081	1.756	0.202	0.069	0.081	0.064		0.071
$AgInTe_2$								

[Reference [343]]

Table 4.7 Parameters determined from the analysis.

Ternary compound	E_1 (eV)	E_0 (eV)	E_2 (eV)	α_1	α_0	α_2	$\bar{\alpha}$
$CuAlS_2$	2.44	2.31	2.31	0.707	0.713	0.702	0.707
$CuGaS_2$	1.41	1.29	1.29	0.645	0.660	0.632	0.646
$CuInS_2$	1.09	1.09	1.09	0.602	0.602	0.556	0.587
$CuAlSe_2$	1.57	1.43	1.28	0.746	0.750	0.715	0.737
$CuGaSe_2$	1.12	1.05	0.84	0.812	0.813	0.777	0.801
$CuInSe_2$	1.42	1.42	1.19	0.760	0.760	0.715	0.745
$CuAlTe_2$							
$CuGaTe_2$	1.03	1.00	1.02	0.752	0.752	0.656	0.720
$CuInTe_2$	1.45	1.45	0.84	0.749	0.749	0.628	0.709
$AgAlS_2$							
$AgGaS_2$	0.483	0.203	0.203	0.795	0.845	0.749	0.796
$AgInS_2$	0.717	0.567	0.567	0.740	0.799	0.710	0.743
$AgAlSe_2$							
$AgGaSe_2$	0.618	0.418	0.158	0.951	0.952	0.942	0.949
$AgInSe_2$	0.743	0.653	0.383	0.901	0.902	0.870	0.891
$AgAlTe_2$							
$AgGaTe_2$	1.17	1.06	0.26	0.937	0.937	0.921	0.931
$AgInTe_2$							

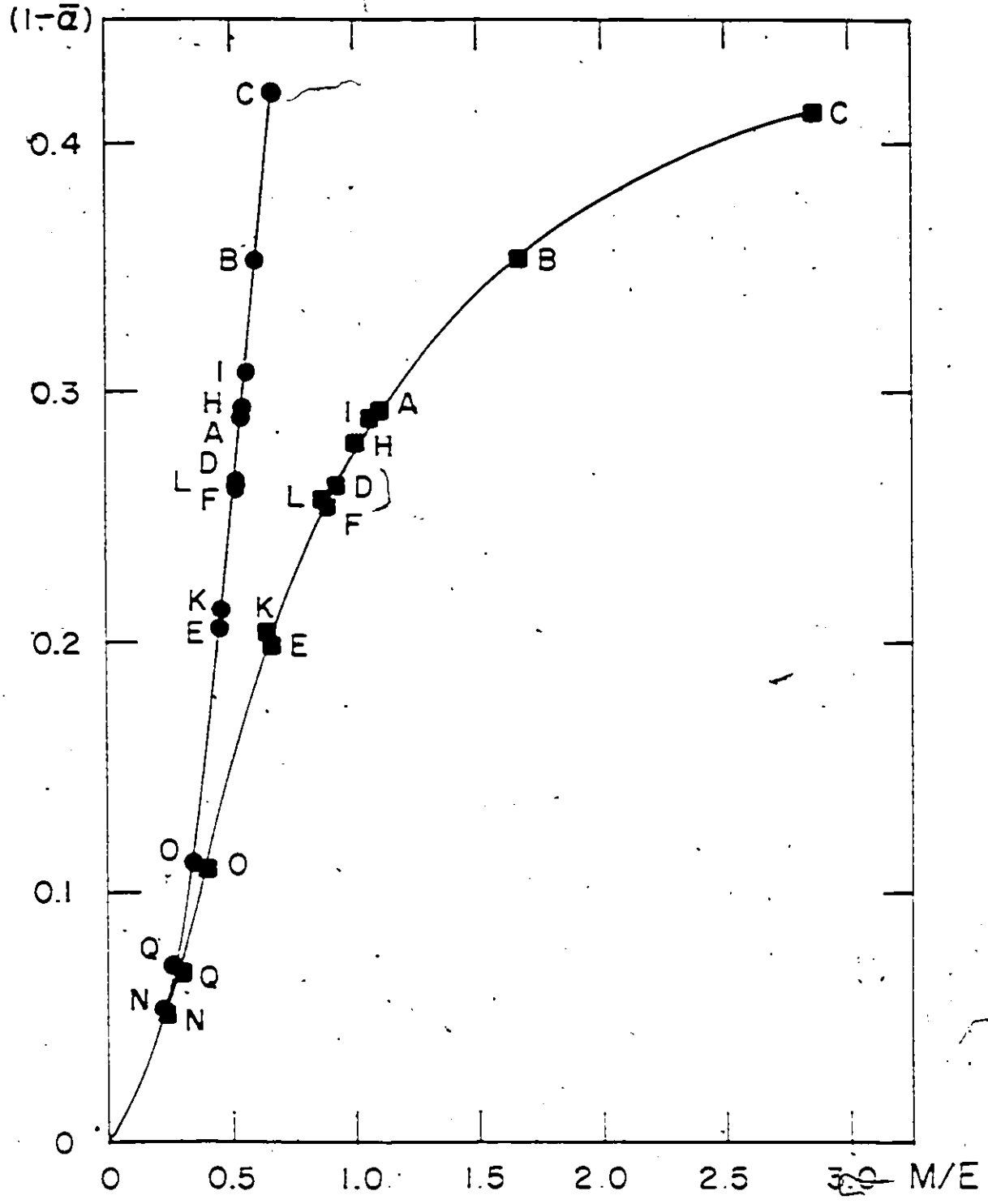

Fig. 4.8 Variation of mean value of fractional d character of valence band $(1-\bar{a})$ with M/E. ■ : present model. ● : linear hybridization approximation. For meaning of code letter see Table 4.4

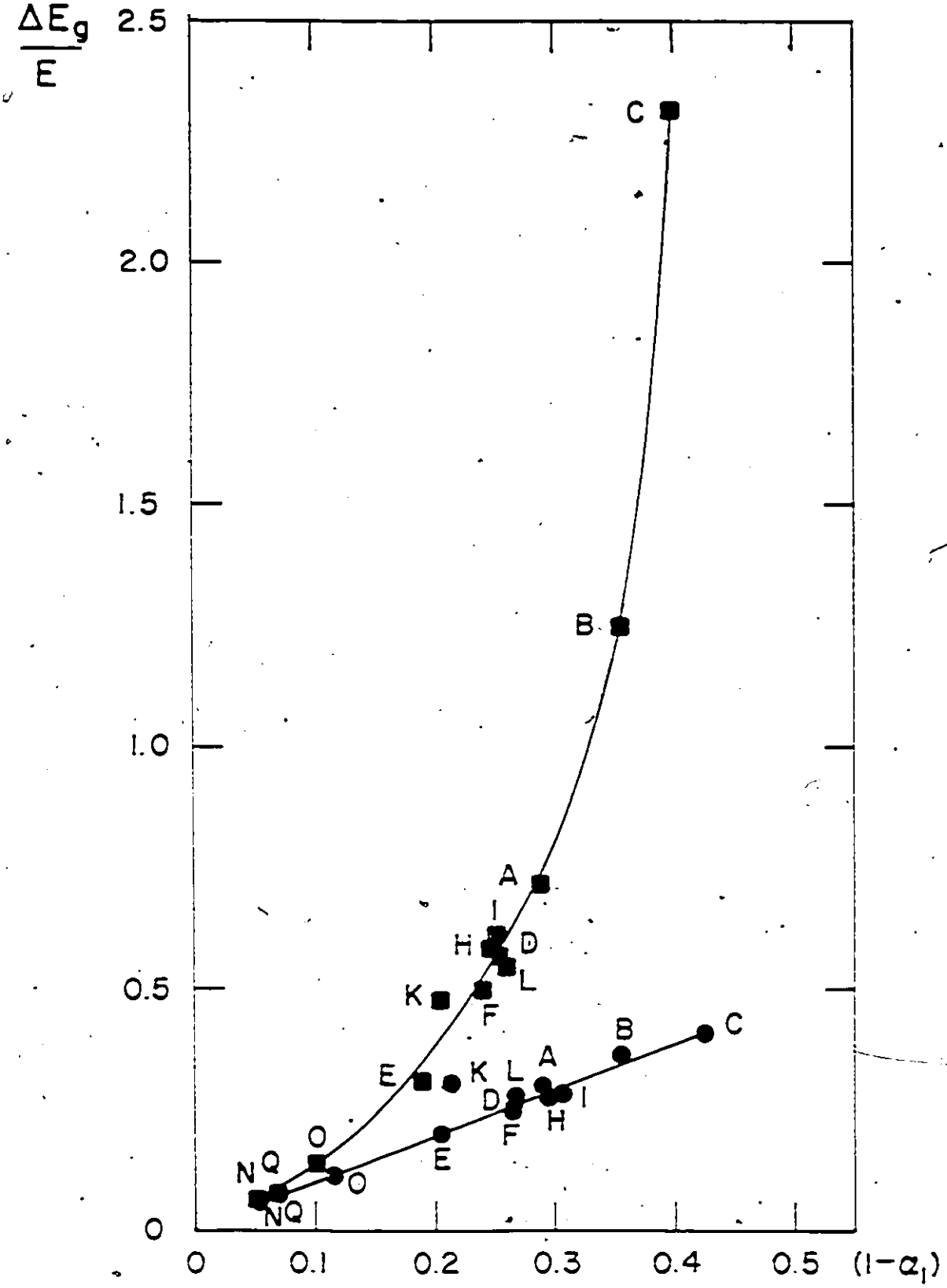

Fig. 4.9 Variation of $\Delta E_g/E$ with fractional d character of top valence band $(1-\alpha_1)$. ■ : present model, ● : linear hybridization approximation. For meaning of code letter see Table 4.4

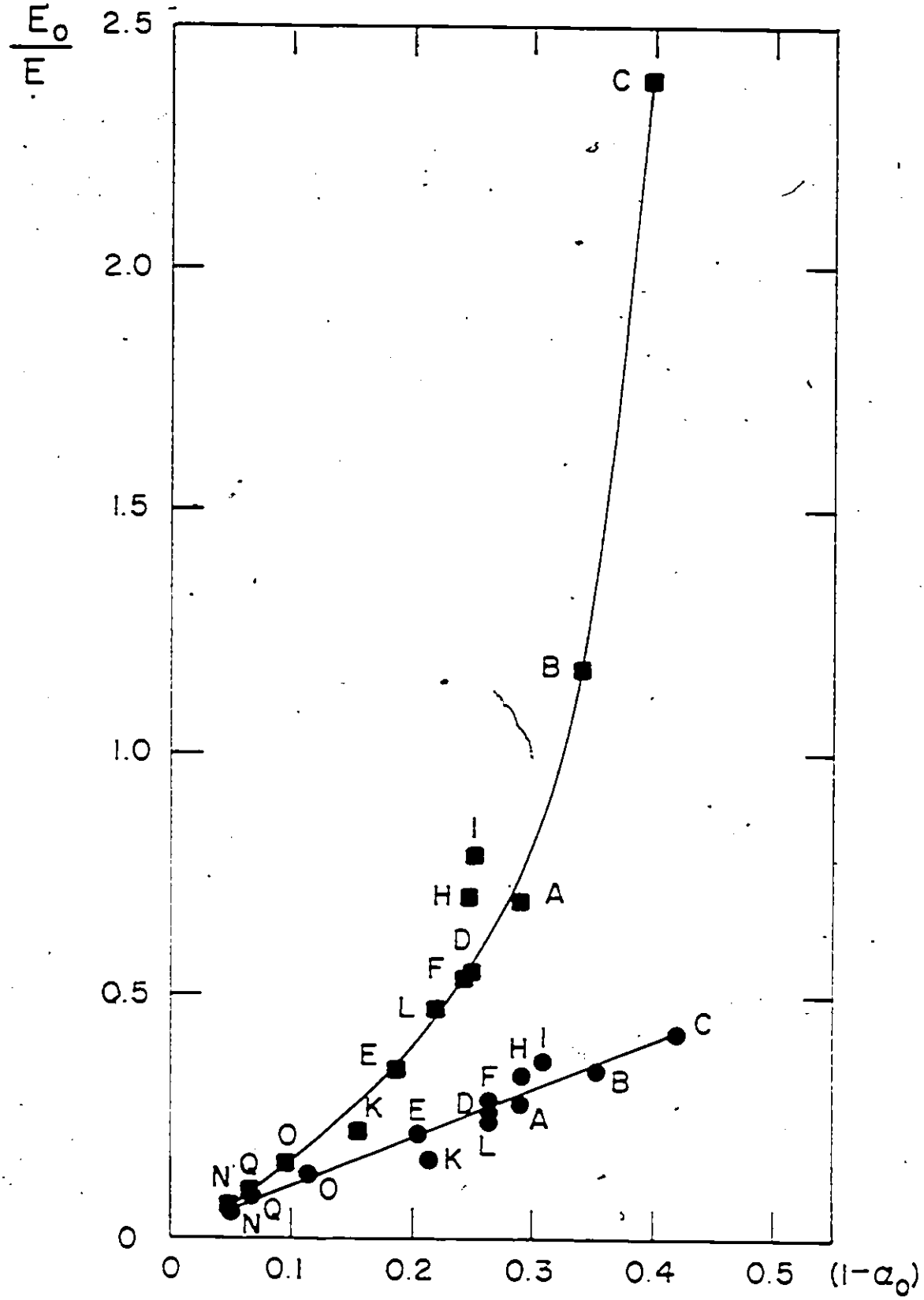

Fig. 4.10 Variation of E_0/E with fractional d character $(1-\alpha_0)$. ■ : present model. ● : linear hybridization approximation. For meaning of code letter see Table 4.4

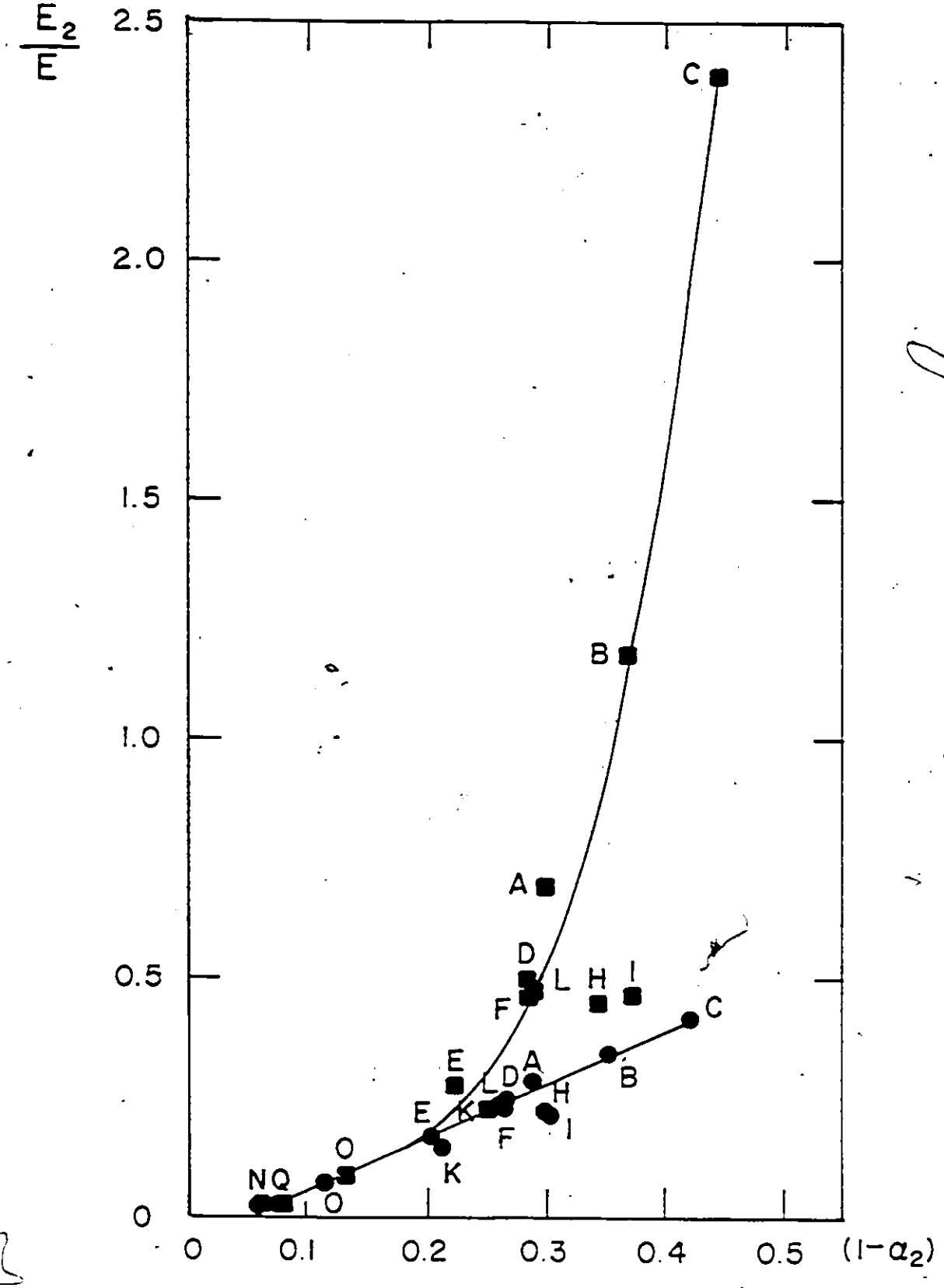

Fig. 4.11 Variation of E_2/E with fractional d character $(1-\alpha_2)$. ■ : present model, ● : linear hybridization approximation. For meaning of code letter see Table 4.4

The ratios M/E and $\Delta E_2/E$ are dimensionless and indicate the general character of the model. These ratios are given in Table 4.6. Figure 4.8 shows the values of $1-\bar{\alpha}$, i.e., the mean fraction of d character in the three bands, plotted against M/E while Fig. 4.9 gives the values of $\Delta E_2/E$ plotted against $1-\alpha_1$, the fraction of d character in the top valence band. It is seen that the values for the different compounds lie on smooth curves which appear to be characteristic of the structure. In Fig. 4.8 and 4.9, values determined from the linear hybridization model are also given for comparison. These curves will be discussed further below.

Also, the variation of the reduced energy values E_1/E, E_0/E, and E_2/E should depend, respectively, on the values of α_1, α_0 and α_2. In Fig. 4.10 and 4.11 the variations of E_0/E with $1-\alpha_0$ and E_2/E with $1-\alpha_2$ are given, and the variation of E_1/E with $1-\alpha_1$ is very similar to that of $\Delta E_2/E$ in Fig. 4.9

Finally, the polarization-intensity ratios for the transitions from the Γ_7 valence-band to the Γ_6 conduction-band are determined using Eq. (4-55) and these are compared with the available intensity data from Ref. [75S2] in Table 4.8. It is seen that the calculated values are in good agreement with the observed ones.

4.3.4 Discussion

The aim of the work has been to produce a theoretical model describing the effect of $p-d$ hybridization in the valence band of a I-III-IV_2 ternary CH compound. From the considerations in Section 4.2, the uppermost valence bands of the ternary CH compound can be derived from the Γ_7 and Γ_8 levels of its ZB binary analog with the crystal-field interaction included (quasicubic model). Since the presence of the noble-metal d levels bring about the $p-d$ hybridization effect, it is necessary to include the d levels in the

Table 4.8 Comparison of experimental results and theoretical predictions of the model for the polarization intensity ratios.

Ternary Compound	$I_\parallel / I_\perp$			
	A(V_1 —C.B.)		B(V_2 —C.B.)	
	Expt.	Theory	Expt.	Theory
$CuGaSe_2$	~10	8.5	-	0.5
$AgGaSe_2$	~16	15.5	-	0.3
$AgInSe_2$	~7.5	8.5	~0.5	0.5

analysis. Thus the starting point of the model is the Kane model at $\vec{k} = \vec{o}$ with the d levels lying below the p levels. This is confirmed by the experimental results [71T1, 72S1, 7ST1]. In a cubic (tetrahedral) field, the d—levels split into a threefold-degenerate $\Gamma_{15}(d)(YZ, ZX, XY)$ level and a twofold-degenerate $\Gamma_{12}(d)(3Z^2 - R^2, X^2 - Y^2)$ level. The energy band calculations by Song [67S1] indicate that for the Cu-d levels in CuCl crystal which has the cubic ZB structure the Γ_{15} level lies above the Γ_{12} level at approximately 0.5 eV. In the presense of spin-orbit interaction, the $\Gamma_{15}(d)$ state splits further into $\Gamma_8(\Gamma_{15})$ and $\Gamma_7(\Gamma_{15})$ states and the $\Gamma_{12}(d)$ state becomes a $\Gamma_8(\Gamma_{12})$ state. The interaction between the $\Gamma_8(\Gamma_{15})$ and the $\Gamma_8(\Gamma_{12})$ states has been neglected in the present model. Since the basis functions of the d band derived from the $\Gamma_{15}(d)$ level have the same symmetry as those of the p band, hence their matrix representations in the spin-orbit interaction have the same form. Thus when $p - d$ hybridization is applied, the p and d bands mix and repel each other. This might be expected since the simplest tight binding approximation, the self-consistent energy-band calculation [63J2], and also x-ray-photoemission studies [73L1, 74K1, 77R1, 84N1] show that the p—like valence band lies on the VI-atom while the

d−like valence band lies on the I-atom, the I- and VI- atoms being nearest neighbors, i.e., overlapping of their wave functions. In the present analysis, the magnitude of this mixing and repulsion can be calculated exactly. After this, the crystal-field interaction due to the tetragonal lattice comparison along the CH z-axis is introduced and the energy expressions for the uppermost valence band are obtained. The order of perturbations used here, which is different from that used by Kildal, was chosen to simplify the mathematics. Since each step is carried out exactly, the order of application should not affect the final result. In order to reduce the number of unknown parameters in the analysis, however, the off-diagonal matrix elements due to crystal field interaction between the p and d bands have been neglected, i.e., it has been assumed that

$$(X \mid V_{cr} \mid YZ) = (Y \mid V_{cr} \mid ZX) = (Z \mid V_{cr} \mid XY) = 0 \quad .$$

These matrix elements appear only in the non-zero matrix elements of Eq. (4-34). Since M and E are used as adjustable parameters, this means that the effect of the neglected interband-interaction will be taken up in the values determined for M and E.

In order to use the model to analyze the experimental data for various compounds, in addition to the measured values of E_A, E_B, and E_C, and of $(2 - c/a)$, it necessary to know Δ_p and Δ_s, which here are calculated from atomic spin-orbit values, and also ΔE_y, the band gap anomaly. The latter can be determined for most of the compounds considered by subtracting the value of E_A from the energy-gap value of the equivalent binary compound, either real, e.g., ZnS, etc., or a pseudocompound, e.g., $Mg_{x}Zn_{1-x}S$, etc. This involves a further assumption in the theoretical analysis that ΔE_y can be equated to the energy separation of the $\Gamma_1(\Gamma_7)$ and $\Gamma_5(p)$ level in Fig. 4.5, an assumption made previously by

Tell and Bridenbaugh [75T1] and Jaffe and Zunger [84J1].

In the case of atomic spin-orbit values for the d level, it is found that $\Delta_{dI} = \frac{5}{2}\zeta_d$, where ζ_d is the Condon-Shortley one-electron parameter [65S1]. However, if the interaction from $(3z^2 - r^2)$ and $(x^2 - y^2)$ orbitals is neglected, i.e., only the yz, zx, and xy orbitals are considered, then $\Delta_{dI} = \frac{3}{2}\zeta_d$ which is $\frac{3}{5}$ of the above value. This corresponds, in the present analysis, to neglecting the interaction between the $\Gamma_8(\Gamma_{12})$ and $\Gamma_8(\Gamma_{15})$ levels [65S1, 67S1] as discussed above. The value of ζ_d for Ag-atom is -0.22 eV [71M1]. The value of -0.55 eV [63Y1] originally used for Δ_{dAg} in the analysis in Ref. [84Y1], thus corresponds to the case where the $3z^2 - r^2$ and $x^2 - y^2$ orbitals are taken into accoount. However the present analysis has been carried out using the value $\Delta_d Ag = -0.33$ eV., which is equal to $\frac{3}{2}\zeta_d$ and is the value quoted by Cordona [69C1]. When the results of the present analysis are compared with those given in Ref. [84Y1], it is found for the Ag compounds that the reduction in Δ_{dAg} results in increase in the values of the d-like character in the valence bands and also decreases the value of b_d from -4.3 ± 1.5 eV to -3.9 ± 1.5 eV. However, the general conclusions drawn are the same for the two cases.

The analysis then enables the mean values of the deformation potentials b_p and b_d to be determined over the range of compounds considered. This is an important point for analysis of further material since, now, the extra parameter assumed known can be b_d rather than ΔE_p. This analysis can be extended to the temperature variation of the energy gaps of a number of the compounds, and also to the variation of energy gaps with both composition and temperature for a number of alloys of the compounds. In none of these cases will the value of ΔE_p be available: thus acceptable values of the deformation potentials are essential.

As indicated above, M/E and $\Delta E_p/E$ are dimensionless quantities, where the former determines

the fractional d character in the valence band $(1-\bar{\alpha})$ and the latter is determined by the fractional d character $(1-\alpha_1)$ in the top valence band. Hence Figs. 4.8 and 4.9 show plots of $(1-\bar{\alpha})$ versus M/E and $\Delta E_g/E$ versus $(1-\alpha_1)$ for all compound considered. In addition Figs. 4.10 and 4.11 show plots of E_0/E and E_2/E versus the relevant fractional d character. In each, all points lie on a single smooth curve indicating that M/E and $\Delta E_g/E$ are characteristic of the structure. Also plotted in the figures are the values determined from the linear hybridization approximation. These graphs clearly indicate that for fractional d characters approximately larger than 7.5%, the linear model breaks down. Thus for the case of $(1-\bar{\alpha})$ versus M/E, the linear model indicates that values of $(1-\bar{\alpha})$ greater than 0.5 could be obtained with relative small values of M/E, even in the case when an initial postulate was that the p levels were higher than the d levels. However, the present model indicates that $(1-\bar{\alpha})$ is limited to approximately 0.5, whatever values of M/E are considered. Similarly, in the case of $\Delta E_g/E$ versus $(1-\alpha_1)$, the linear model indicates a maximum value for $\Delta E_g/E$ of approximatley 1, even with values of $(1-\alpha_L)$ up to 1, while the present model allows very much larger values of $\Delta E_g/E$, although $(1-\alpha_1)$ is limited to a maximum of approximately 0.5. This comment is similar to that made by Jaffe and Zunger [84J1] concerning the plot of ΔE_g versus $(1-\alpha_L)$ by Shay and Kasper [72S1]. The latter plot was assumed to give a linear variation and fitted fairly well for low ΔE_g values with the straight line extrapolated through the known ΔE_g and hybridization values for the well understood ZB compounds CuCl [65S1, 67S1]. However, in the case of $CuAlS_2$, the value of ΔE_g of 2.4 eV would then indicate a value for $(1-\alpha_L)$ of 0.77, very different from the value of 0.35 determined from the spin-orbit splitting data (using Eq. (4-62)). In addition, it is found that the values of $(1-\alpha_1)$, or, in the linear hybridization limit, $(1-\alpha_L)$ do not show a linear variation with ΔE_g, as indicated by Shay and Kapper [72S1], but

show appreciably scattering even when ΔE_g is corrected by subtracting ΔE_g^S so as to leave only the contribution from ΔE_g^d. These two parameters, ΔE_g^S and Δ_g^d, will be discussed further below.

In Table 4.7 values of $(1-\bar{a})$ from the present model are given together with values of $(1-\alpha)$ from Jaffe and Zunger [84J1] and $(1-\alpha_L)$ from the linear hybridization limit. The values show appreciable differences in some cases, and this could be due to the method of analysis. Thus, in the self-consistent energy-band calculations of Jaffe and Zunger, spin-orbit interaction was neglected, while in the present calculations the crystal-field effect due to an anionic displacement was neglected. The values of $(1-\alpha_L)$ here are slightly different from those of the Shay and Wernick results [75S2] because the values of Δ_g used in the latter case were taken from the binary analogs and not from the atomic values, as in the present work.

The theory of the band-gap anomaly in ABC_2 CH semiconductors of Jaffe and Zunger [84J1] indicates that the band-gap anomaly in Cu CH compounds is controlled by (i) the $p-d$ hybridization ΔE_g^d and (ii) the structural effect due to an anionic displacement $\Delta E_g^s \simeq (\frac{1}{4}-u)\frac{\partial \varepsilon}{\partial u}$, where u is the anion displacement and $\frac{\partial \varepsilon}{\partial u}$, the structural derivative, is the change in energy-gap values with anion displacement. Hence $\Delta E_g = \Delta E_g^d + \Delta E_g^s$. Thus if the value of u was set to its ideal ZB value, $u = 0.25$, and $p-d$ interaction were assumed neglected the energy gap value of ternary CH compound would be almost the same as that of its binary analog. Jaffe and Zunger found that the valence-band states drop in energy with increasing u while the conduction-band states rise with u giving large $\frac{\partial \varepsilon}{\partial u}$ values of ~ 18-22 eV while the crystal field splitting remains almost the same. However, the changes in u partially control the $p-d$ hybridization since, with decreasing u, an VI anion moves closer to a noble-metal group I cation, thereby increasing the $p-d$ hybridization and consequently decreasing the band gap. Hence, an analysis assuming ΔE_g

arises solely from the $p-d$ hybridization would overestimate or underestimate values of fractional d−like character, depending on the sign of $\Delta E_g'$. Therefore, complete analysis given in Section 4.4.3 was redone using $\Delta E_g^d = \Delta E_g - \Delta E_g'$, assuming the value of $\frac{\partial \epsilon}{\partial u} = 20$ eV, and using the values of u in Ref. [84J1]. The resulting plots of M/E versus $(1-\bar{\alpha})$ and $\Delta E_g^d/E$ versus $(1-\alpha_1)$ are shown in Figs. 4.12 and 4.13, respectively. It was found that both M and E increase when $\Delta E_g^d > \Delta E_g$, i.e., when $\Delta E_g' < 0$ or $u > 0.25$ and decrease when $\Delta E_g^d < \Delta E_g$ (i.e., $u < 0.25$). But the changes in the values of M/E, $\Delta E_g^d/E$ and fractional d−like characters are very small even for the larger value of $\Delta E_g'$. For example, in the case of $AgGaS_2$ which has the value of $\Delta E_g' = -0.82$ eV, i.e., $\Delta E_g^d = 1.26$ eV, $(1-\bar{\alpha})$ increases from 0.204 to 0.210 and M/E increases from 0.641 to 0.698. In the case of $CuInSe_2$ when $\Delta E_g' = 0.5$ eV, i.e., $\Delta E_g^d = 0.79$ eV, $(1-\bar{\alpha})$ decreases from 0.255 to 0.252 and M/E also decreases from 0.887 to 0.866. The resulting curves, however, are very similar to those in Figs. 4.8 and 4.9 supporting the suggestion that M/E and $\Delta E_g/E$ are characteristic of the structure. In this case, the values of b_p and b_d were redetermined by the same method as before. The values found are the same, i.e., $b_p = (-0.8 \pm 0.2)$ eV and $b_d = (-3.0 \pm 1.5)$ eV. These values seem to be insensitive to the value of ΔE_g, as may be expected since the results of Jaffe and Zunger [84J1] show that the crystal-field splitting is almost constant when u is varied from the equilibrium position to the ideal ZB position ($u = 0.25$).

For the I-III-VI_2 CH compounds, the experimental evidence indicates that the three valence bands have Γ_7 Γ_6 Γ_7 symmetry in order of energy values. However, Tell and Bridenbaugh [75T1] have taken their experimental results to indicate that the $CuGaS_2$ valence band ordering would be Γ_7 Γ_7 Γ_6 (negative spin-orbit splitting). In this case they found it necessary to postulate in their model that initially d levels lay above the p levels. For all of the sulfides, Δ_p, the p spin-orbit splitting, is small (see Table 4.4).

and, as is seen from Fig. 4.5, the effect of $p-d$ hybridization further reduces this Γ_8 Γ_7 difference, and hence the $E_0 - E_2$ difference, after the effect of the crystal field is included. There is no limit, in this case, to this reduction, and $\Gamma_8 - \Gamma_7$ (and hence $E_0 - E_2$) could become zero or even change sign, depending upon the amount of hybridization occuring (and the strength of the crystal field interaction). Thus the Γ_7 Γ_7 Γ_6 order suggested by Tell and Bridenbaugh for $CuGaS_2$ could occur, even when in the starting quasicubic structure the d levels are well below the p levels. This is demonstrated in Fig. 4.14 for the result of $CuGaS_2$ in the present analysis. It is seen that the ordering of Γ_8 and Γ_7 states is inverted due to the interaction of $p-d$ hybridization. When the crystal-field interaction is included and the off-diagonal elements in Eq. (4-34) are neglected, the Γ_7 level remains Γ_7 at the same energy while the Γ_8 level splits into a Γ_7 and a Γ_6 level, the energy of the Γ_7 being increased by an amount $[-\gamma_1 \frac{\delta_x}{3} - (1-\gamma_1)\frac{\delta_z}{3}] = 0.039$ eV and that of the Γ_6 decreasing by $[\gamma_0 \frac{\delta_x}{3} + (1-\gamma_0)\frac{\delta_z}{3}] = -0.039$ eV. When the off-diagonal elements are included, the Γ_7 levels will interact and repel each other, hence obtaining energies of $E_1 = 1.410$ eV and $E_2 = 1.290$ eV. There is no interaction between the Γ_6 and Γ_7 levels hence the Γ_6 level is not affected and has energy E_0. Thus, the Γ_7 Γ_7 Γ_6 ordering of the valence band could be possible depending on the strength of the $p-d$ hybridization and crystal-field interaction discussed above. This is the picture of the uppermost valence band of all the sulphides.

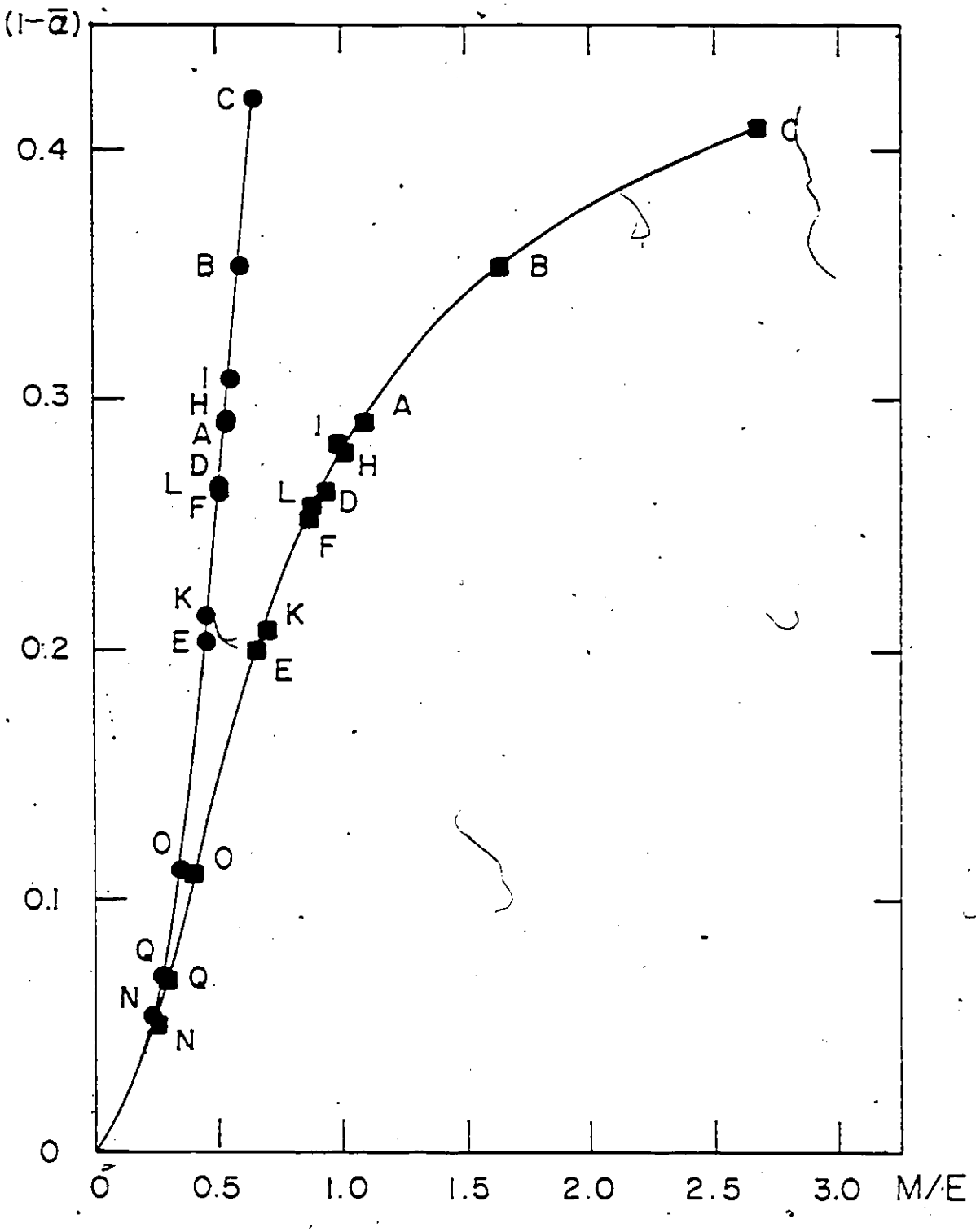

Fig. 4.12 Variation of mean value of fractional d character of valence band$(1-\bar{a})$ with M/E (the analysis being corrected for the band-gap anomaly due to the structural effect). ■ : present model. ● : linear hybridization approximation. For meaning of code letter see Table 4.4

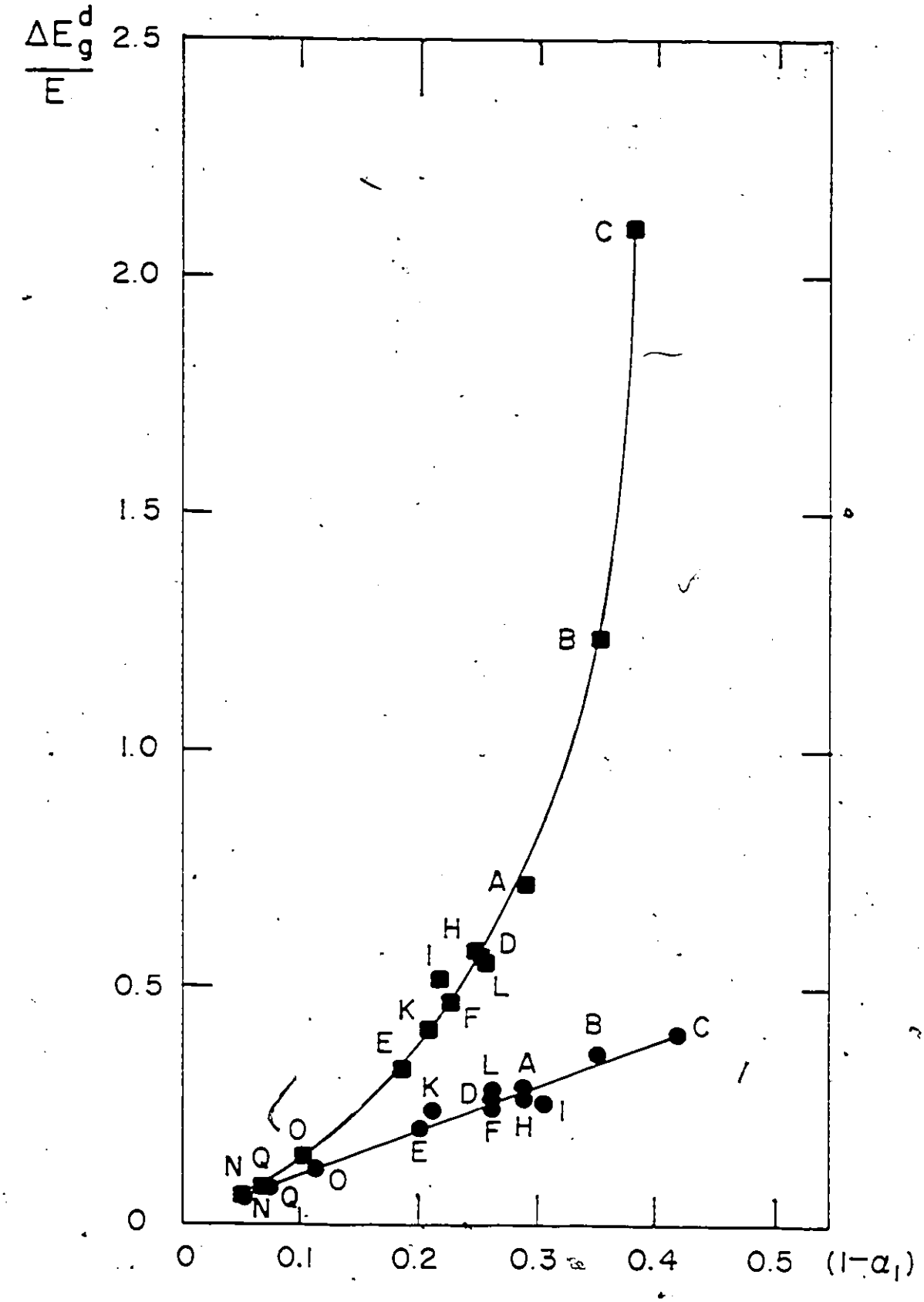

Fig. 4.13 Variation of $\Delta E_g^d/E$ with fractional d character of valence band $(1-\alpha_1)$ (the analysis being corrected for the band-gap anomaly due to the structural effect). ■ : present model. ● : linear hybridization approximation. For meaning of code letter see Table 4.4

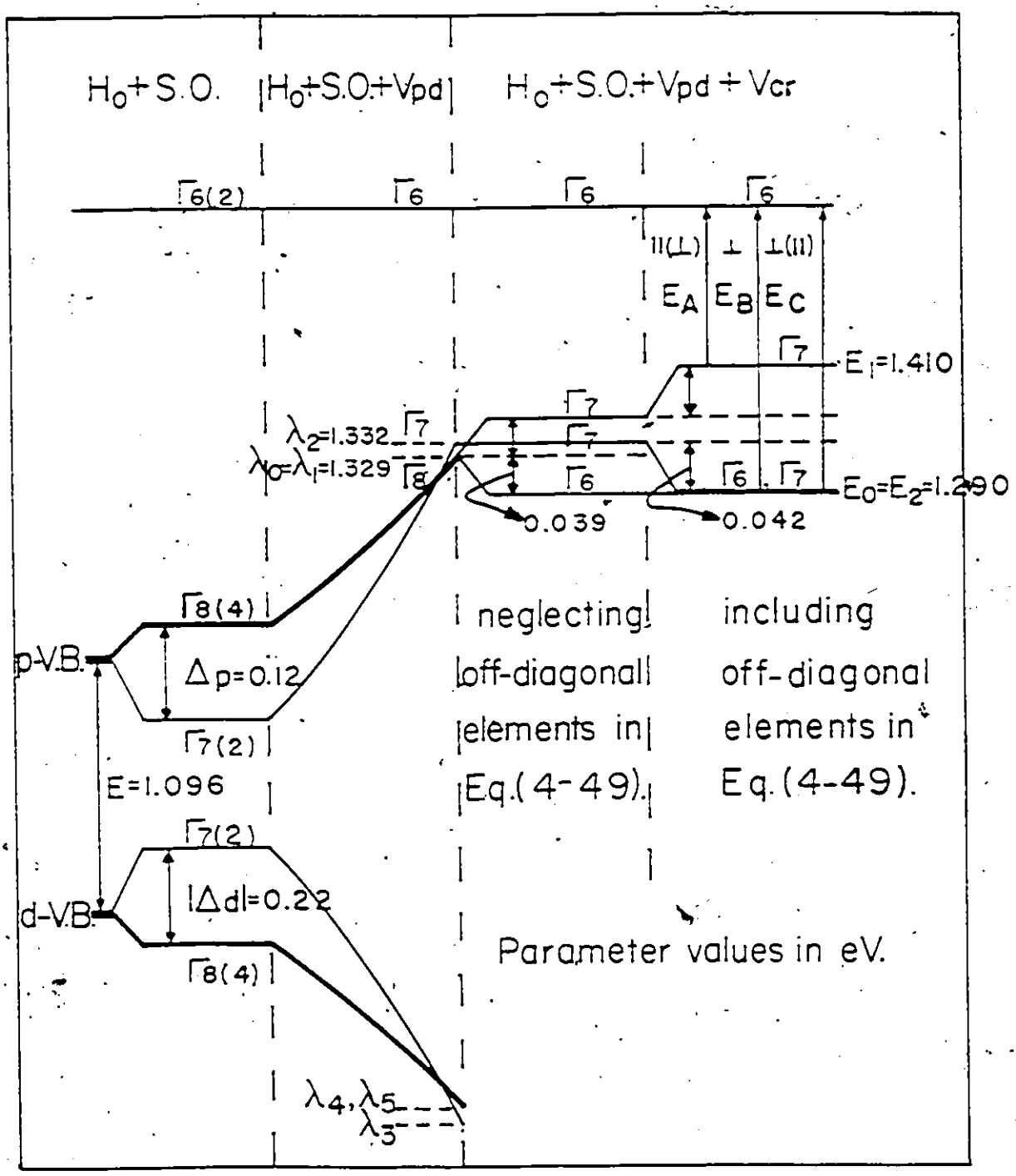

Fig. 4.14 Sketch of the energy-band configuration of $CuGaS_2$ at the Γ point showing the possibility of small or negative value of spin-orbit splitting ($\Gamma_7, \Gamma_6, \Gamma_6$ orderding).

4.4 Summary

A model was developed by adding the effects of $p-d$ hybridization and crystal field to the Hamiltonian of Kane model. It has been used to study the electronic structure of the uppermost valence bands at the Γ point of the I-III-VI_2 CH compounds. There are two important parameters in the model, the energy separation E between the p and d levels and the interaction matrix element M due to the hybridization between these levels. It is shown that three previous models (Tell and Bridenbaugh, Kildal, and the linear hybridization model) can be derived as special cases of the present model. The model gives a clear picture of how the $p-d$ hybridization and the crystal field affect the uppermost valence bands of I-III-VI_2 compounds. This model has been used to analyze the available data on some 13 ternary CH compounds and the values of E, M, and fractional d character have been determined. It is shown that the dimensionless parameters M/E and $\Delta E_2/E$ show a smooth variation with the appropriate fractional d character of the valence band and appear to be characteristic of the structure. The analysis also enables the deformation potentials b_2 and b_4, averaged over all of the compounds to be determined and these are found to be $b_2 = (-0.8 \pm 0.2)$ eV and $b_4 = (-3.0 \pm 1.5)$ eV. The polarization-intensity ratios for the Γ_7 valence-band to the Γ_6 conduction-band transition have also been derived in terms of the coefficients of the wave function for the valence bands. The calculated values obtained are in good agreement with the observed data. Finally, the model can explain more clearly the valence band splitting of the sulphides which have small positive or even negative spin-orbit splitting (i.e., Γ_7 Γ_7 Γ_6 ordering).

Chapter 5

Temperature Variation of the Valence-Band Splittings of the System $CuGa(S_{1-x}Se_x)_2$

5.1 Overview

This chapter will be concerned with temperature variation of the valence-band splittings of the system $CuGa(S_{1-x}Se_x)_2$ as well as of some CH compounds. There has been some controversy over the explanation in terms of the quasicubic model of the temperature variation of these splittings [75S1, 79Y1, 82L1]. This will be discussed in the next section. In the present program of work, wavelength modulated reflectance measurements [85Q1] were made on the single crystal samples to determine the variation of the values of E_A, E_B and E_C with composition and temperature for the alloy system $CuGa(S_{1-x}Se_x)_2$. The model developed in Chapter 4 has been used to interpret these data in terms of the temperature dependences of the $p-d$ hybridization interaction and the crytal-field interaction, the latter being determined by the temperature variation of the tetragonal distortion. The averaged values of the deformation potential b_p and b_d obtained in Chapter 4 were used in the analysis. The calculation of M/E was found to be sensitive to these values. Thus allowance was made in the analysis for the errors in these values of b_p and b_d (see Chapter 4) as well as the experimental errors of E_A, E_B and E_C. This gave the range of probable values of M/E and $(1 - \alpha_t)$ as a function of temperature. The results indicate

that the $p-d$ interaction decreases with the increasing temperature for the ternary compounds and alloys but increases with increasing temperature for the quaternary compound.

5.2 Introduction

As was shown in Chapter 4, the valence-band structures of the I-III-VI_2 CH compounds are influenced by the admixture of the noble-metal d levels and as a result there is a large reduction in the energy gap and in the spin-orbit splitting of the uppermost valence-band as compared with the binary analogs. Studies of temperature dependence of the fundamental energy gap have indicated that the compounds of group IV, III-V, II-VI and II-IV-V_2 of the same isoelectronic sequence have nearly the same temperature coefficient value (dE_g/dT) [75C2, 78N2, 79H1]. The temperature dependence of the energy gap is caused by thermal electron energy shifts. There are three contributions to the energy shifts, viz., the thermal expansion (dilation) effect, and the electron-phonon interaction effects (i.e., self energy and Debye-Waller effects) [74B2, 76A1]. The temperature coefficient values of these compounds are negative and are of the order of 10^{-4} eV/K. In the case of I-III-VI_2 compounds, however, the temperature coefficient values are two or three times smaller than those of II-VI binary analogs or even, in some of Ag-compounds, have positive values in the lower temperature region (< 100 K) [73S2, 73Y1, 75S1]. Because of the $p-d$ hybridization effect, the results of the energy band calculation on the Cu compounds [83J2] show that the VBM — CBM transition has an intraatomic component which could be larger than the analogous interatomic transition in the II-VI binary analogs. This suggests that the effect of lattice thermal expansion on the temperature dependence of the optical energy gap will be smaller in CH compounds than in the binary compounds [83J2]. This is consistent with the lower temperature

coefficients of the band gap in ternary CH compounds. The $p-d$ hybridization effects of the uppermost valence bands have been used to explain this tendency to lower temperature coefficients of the fundamental gap in the I-III-VI_2 compounds to their II-VI analogs. The values of temperature coefficient anomaly $[\Delta(dE_g/dT) = |\,(dE_g/dT)_{I-III-VI_2} - (dE_g/dT)_{II-VI}\,|]$ have appeared to increase with rising d-like character in the valence band [78N2, 79H1]. It seems to be evident that the $p-d$ hybridization effect plays an important role in the interpretation of the temperature dependence of the energy gap values as well as the valence-band splittings.

There has been considerable study of the temperature dependence of the valence-band splittings in $AgGaSe_2$ and $AgGaTe_2$ [75S1], in $CuGaS_2$ [79Y1], and in $CuGaSnSe_4$, a quaternary analog of $CuGaSe_2$ [82L1]. From these data, the temperature dependence of the spin-orbit and crystal-field splittings has been determined using Eq. (4-5) of the quasicubic model. The linear hybridization of spin-orbit splitting, Eq.(4-8), has been applied to the observed temperature dependence of spin-orbit splitting to give a temperature dependence of the d-like character $(1-\alpha_L)$. For the crystal-field splitting which can be expressed as in Eq.(4-7), if the deformation potential b is assumed to be temperature independent, then one would expect the crystal-field splitting in I-III-VI_2 CH compounds to increase with temperature due to the increase in tetragonal distortion, which is observed experimentally [77I1, 79Y1, 82B1, 83L1]. However, if the observed variation with temperature of the valence band splitting is analyzed using Eq. (4-5), the resulting values determined for the crystal-field splitting are found to decrease with temperature [75S1, 79Y1, 82L1].

Yamamoto et al [79Y1] modified the expression for the crystal-field splitting to the linear hybridization form of Eq.(4-9). They were able to explain the observed temperature dependence of crystal-field

splitting of $CuGaS_2$ which slightly decreases with temperature. In the case of $CuGaSnSe_4$, Lopez-Rivera et al [82L1] also used this modification and assumed a linear variation of the tetragonal distortion with temperature T, viz.,

$$\frac{3}{2}(2-c/a)_T = \frac{3}{2}(2-c/a)_{300} + \beta(T-300) \quad . \tag{5-1}$$

where β is assumed constant independent of T. The values of the spin-orbit splitting parameters Δ_p and Δ_d (in Eq. (4-8)) were estimated from the atomic values for the elements (see Eqs. (4-73) and (4-74)) and b_p was taken as -1.0 eV. Hence values of α_L as a function of temperature were determined from Eq. (4-8). A least squares fit of the values of δ to Eqs. (4-9), (4-75), (4-76), and (5-1) was made using b_d and β as adjustable parameters. It was found that a reasonable fit could be obtained, but with a negative value of β of -6.6×10^{-5} K^{-1}. However, later measurements of c/a as a function of temperature by x-ray diffraction techniques [83L1] gave a value of β of $+2.53 \times 10^{-5}$ K^{-1}.

This contradiction has also been shown by Quintero [85Q1] in the case of $CuGa(S_{1-x}Se_x)_2$ and by the present author in the case of $AgGaSe_2$ and $AgGaTe_2$ [75S1]. Thus using the quasicubic model, it is not possible to explain the temperature dependence of the crystal-field. If one wished to modify Eq.(4-9) in order to fit the observed data of crystal-field splitting, firstly, one might allow the deformation potentials to be temperature dependence, or, secondly, one might replace α_L by an adjustable parameter, α_L', different from α_L in the spin-orbit splitting, Eq.(4-8). These changes, however, would be ad hoc and empirical. It is also shown in Section 4.3.2 C that in the linear hybridization limit there is only one value of α_L in the expressions for both Δ and δ. The theory of the $p-d$ hybridization effect developed in Chapter 4 indicates that the crystal-field interaction and the spin-orbit interaction between $p-$ and

$d-$bands are non-linear and the theory allows each band to have a different value of $d-$like character. Thus this theory will be used below to interpret the values of temperature dependence of the valence-band splitting for the system $CuGa(S_{1-x}Se_x)_2$ and also for the compounds $AgGaSe_2$, $AgGaTe_2$, and $CuGaSnSe_4$.

5.3 Analysis and Results

The single crystal samples of the system $CuGa(S_{1-x}Se_x)_2$ with $x = 0$, 0.25, 0.5, 0.65, 0.75 and 1.0 were grown by the method of static iodine vapor transport (CVD method), details of the method being given in Chapter III of Ref.[S5Q1]. Small pieces of the samples were powdered and lattice parameter data obtained from x-ray powder photographs. Wavelength modulated reflection (WMR) measurements were made on the samples to give values of energy gaps E_A, E_B and E_C in the temperature range 10-300 K [S5Q1]. The Γ_7, Γ_7 ordering of the valence bands (see Fig.4.5) was determined by using polarized light in the WMR measurements. Thus the values of E_A, E_B and E_C as a function of composition, x, and temperature, T, were obtained.

The values of E_A, E_B and E_C as a function of temperature for $AgCuSe_2$ and $AgGaTe_2$ were taken from Ref.[75S1] and those for $CuGaSnSe_4$ from Ref.[S2L1].

In the analysis, the values of Δ_p for the ternary compounds are given in Table 4.4 and that for $CuGaSnSe_4$ was calculated in the same way as Eq.(4-73) and found to be 0.44 eV. In the case of the alloys, the atomic p spin-orbit splittings of the anions, $\Delta_{p\ VI}$, were taken as the weighted mean of the S and Se atomic p spin-orbit splittings. Δ_d values of -0.22 eV were used for the Cu-compounds and -alloys and of -0.48 eV for the Ag-compounds. The crystal-field p and d splittings, δ_p and δ_d, were taken as

shown in Eqs. (4-75) and (4-76), respectively. The average values of the deformation potentials $b_p = -0.8$ eV and $b_d = -3.9$ eV obtained in Section 4.3.2 were used in the analysis. The temperature variation of the tetragonal distortion was assumed to be linear, Eq. (5-1). The values of temperature coefficient β were taken from the experimental data of x-ray powder photographs, i.e., 2.80×10^{-5} K^{-1} for $CuGaS_2$ [79Y1], 2.32×10^{-5} K^{-1} for $CuGaSe_2$ [83L1], 2.53×10^{-5} K^{-1} for $CuGaSnSe_4$ [83L1], 13.65×10^{-5} K^{-1} for $AgGaSe_2$ [77I1] and 6.56×10^{-5} K^{-1} for $AgGaTe_2$ [82B1]. Since the temperature coefficient of the tetragonal distortion is linearly proportional to the value of the tetragonal distortion (see Eq.(2-7)) [82B1] and the alloys of the system $CuGa(S_{1-x}Se_x)_2$ show a linear variation of lattice parameters and of tetragonal distortion with composition [73R2, 85Q1], then the values of β for the alloys were taken as a linear extrapolation between those of $CuGaS_2$ and $CuGaSe_2$.

The experimental value of $E_B - E_A$ and $E_C - E_B$ give values of $E_1 - E_0$ and $E_0 - E_2$ given by Eqs. (4-39) and (4-40). The only unknown in these equations were then M and E and a computer program was used to determine the values of these parameters at each composition and each temperature. The analysis was found to be sensitive to the values of b_p and b_d used, so that in a few cases no real solution could be found for M and E. It was therefore decided to use the range of values quoted previously, i.e., $b_p = -0.8 \pm 0.2$ eV and $b_d = -3.9 \pm 1.5$ eV. In addition a range of experimental error of ± 4 meV was applied to the values of E_A, E_B, and E_C. With these values a range of probable values of M/E was determined for each sample at each temperature. From these values of M/E, values of fractional d-like character $(1 - \alpha_i)$ for the different valence bands could be calculated, this giving the range of probable values of $(1 - \alpha_i)$.

Fig. 5.1 shows a typical example of temperature variation of the range of probable values of $(1 - \alpha_i)$.

$(1-\alpha_0)$ and $(1-\alpha_2)$, the $d-$like character for each band, of $CuGa(S_{0.75}Se_{0.25})_2$. Small variation of $(1-\alpha_1)$ with temperature can be seen although the ranges of probable values tend to be large. It is more convenient to show the temperature variation of $(1-\bar{\alpha})$, the mean value of $(1-\alpha_i)$, for each sample in order to indicate values of $d-$like character averaged over the three valence bands. Thus the range of probable values of $(1-\bar{\alpha})$ as well as M/E as a function of temperature are shown for each sample in Fig. 5.2 to 5.10. In the figures showing the temperature variation of M/E, straight lines have been drawn fitted to the mid-point values of M/E. For the alloy $CuGa(S_{1-z}Se_z)_2$ except $z=0$, the slope lay in the range -1.6×10^{-4} K^{-1} to -7.3×10^{-4} K^{-1} but show no systematic variation with z. The corresponding values for the slopes are $+7.4\times10^{-4}$ K^{-1}, -5.2×10^{-4} K^{-1} and -4.0×10^{-4} K^{-1} for $CuGaS_2$, $AgGaSe_2$ and $AgGaTe_2$, respectively, and $+5.1\times10^{-4}$ K^{-1} for $CuGaSnSe_4$. This indicates that the relative change in the strength of $p-d$ hybridization with temperature, i.e., $\frac{1}{M/E}\left|\frac{d(M/E)}{dT}\right|$, is of the order of $10^{-3}-10^{-4}$ K^{-1}.

Fig. 5.11 to 5.14 show the variations of E/M as a function of composition z at fixed temperatures of 0, 20, 77 and 150 K, respectively. At $T=0$ K, the data are taken from the extrapolated values of the fitted lines of M/E in Figs. 5.2 to 5.7 and the line shown in Fig. 5.11 is a straight line fit to the E/M versus z data. The values in Figs. 5.11 to 5.14 indicate that at the chosen temperatures, the variation of E/M as a function of composition is practically linear. This result was observed at all other temperatures investigated.

The variations of $(1-\bar{\alpha})$ are shown as a function of composition z at fixed temperatures of 20 and 77 K in Figs. 5.15. It is seen that the $d-$like character varies non-linearly with composition, the total variation between $z=0$ and $z=1$ being in the range 37% to 20%.

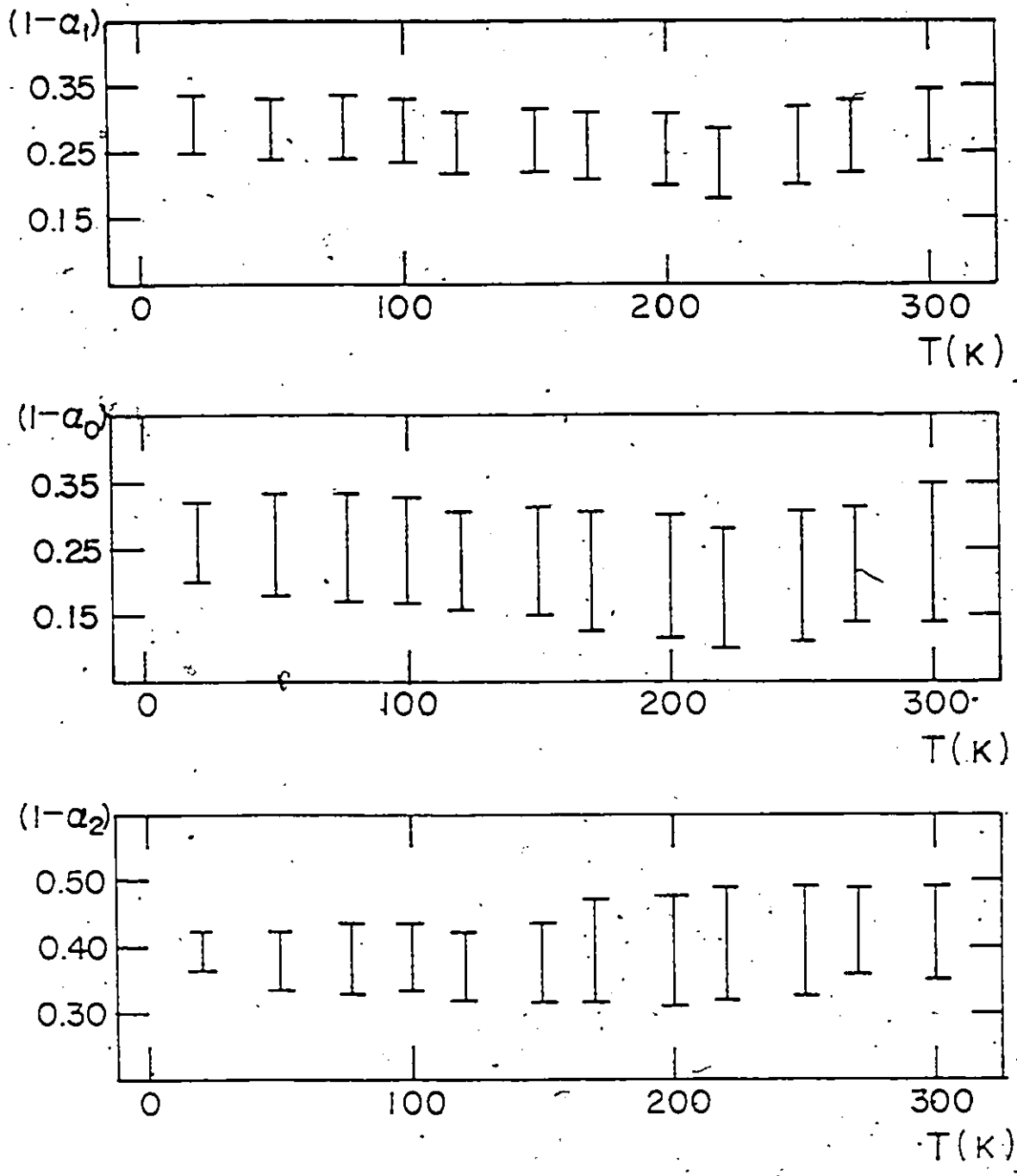

Fig. 5.1 $CuGa(S_{1-z}Se_z)_2$ Temperature variation of the range of probable values of $(1-\alpha_1)$, $(1-\alpha_0)$ and $(1-\alpha_2)$, the fractional *d* character for each band, of sample z=0.25.

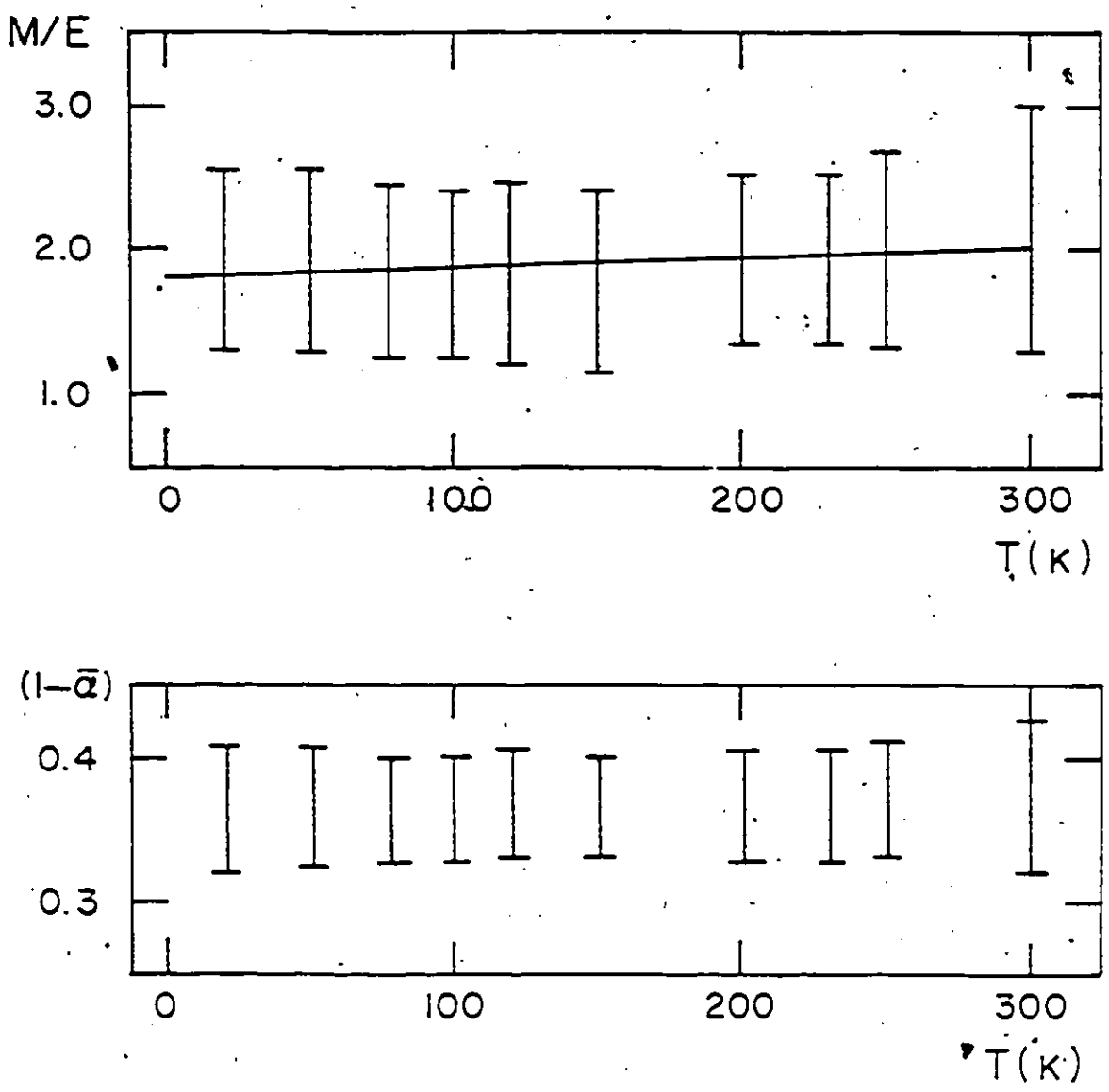

Fig. 5.2 $CuGa(S_{1-z}Se_z)_2$ Variations of the range of probable values of M/E and of $(1-\bar{\alpha})$ with temperature for sample z=0. The straight line is a linear fit for the mid-point values of M/E as a function of temperature.

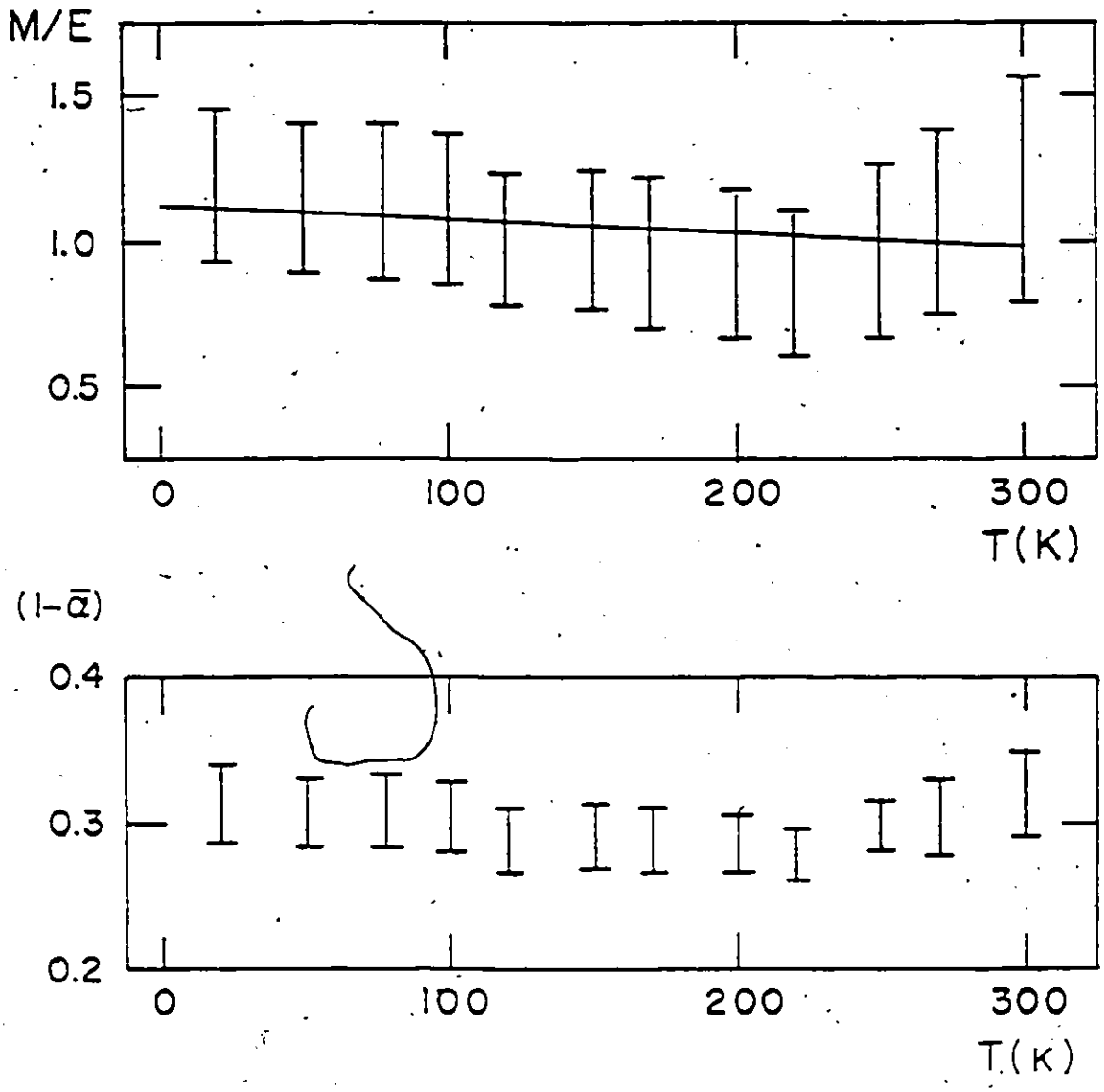

Fig. 5.3 $CuGa(S_{1-z}Se_z)_2$ Variations of the range of probable values of M/E and of $(1-\bar{\alpha})$ with temperature for sample z=0.25. The straight line is a linear fit for the mid-point values of M/E as a function of temperature.

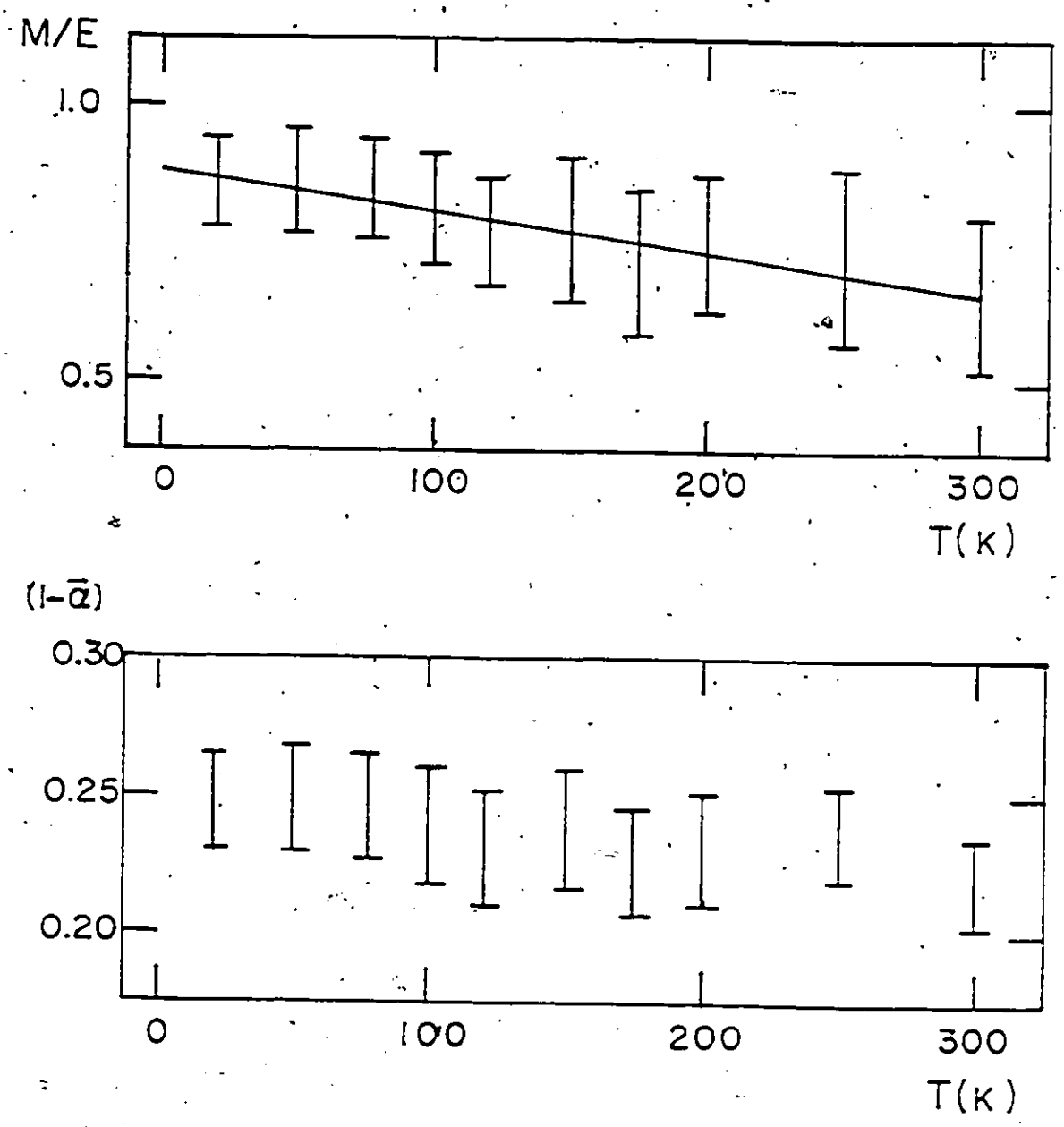

Fig. 5.4 $CuGa(S_{1-z}Se_z)_2$ Variations of the range of probable values of M/E and of $(1-\bar{\alpha})$ with temperature for sample z=0.50. The straight line is a linear fit for the mid-point values of M/E as a function of temperature.

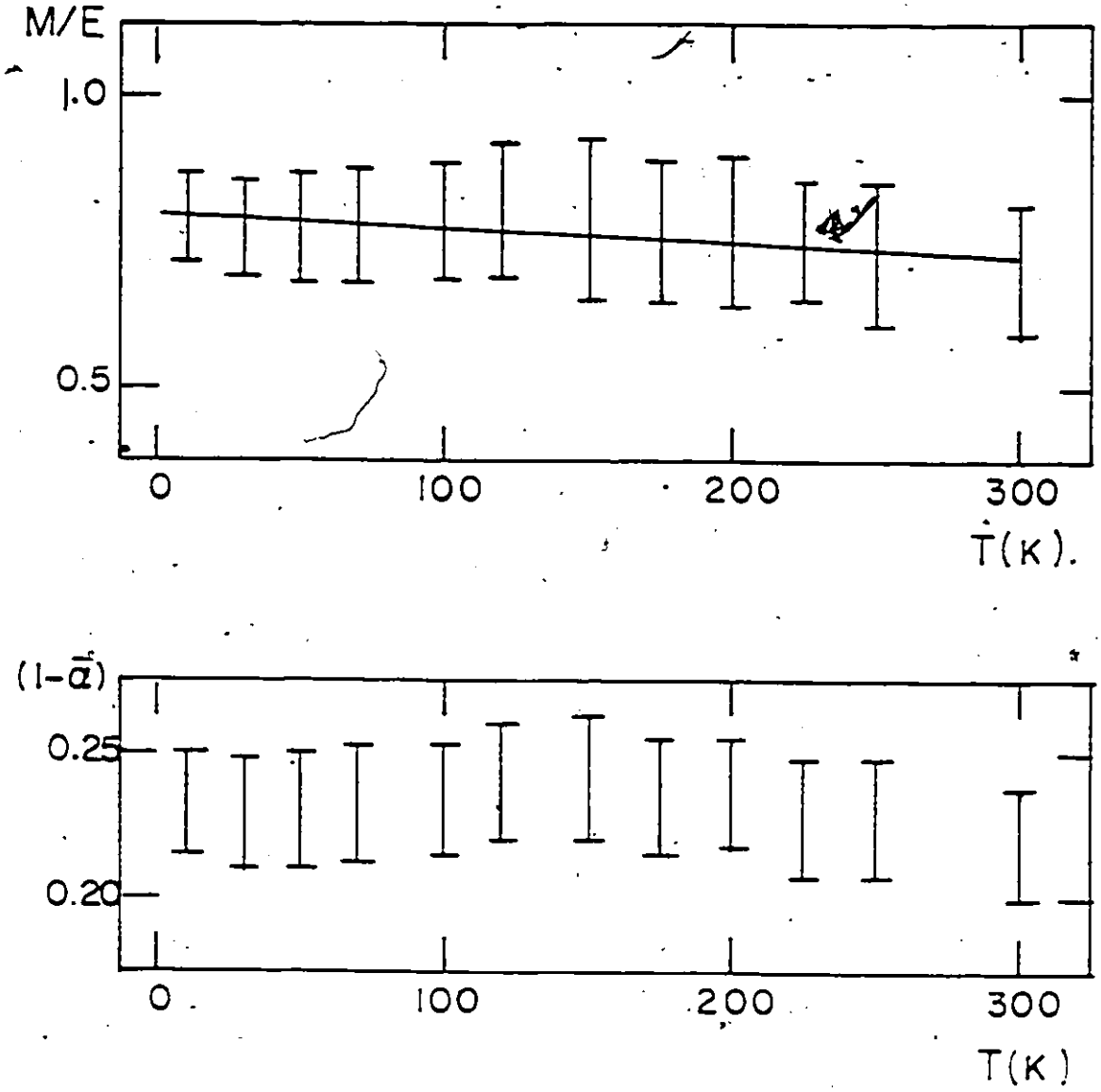

Fig. 5.5 $CuGa(S_{1-z}Se_z)_2$ Variations of the range of probable values of M/E and of $(1-\alpha)$ with temperature for sample z=0.65. The straight line is a linear fit for the mid-point values of M/E as a function of temperature.

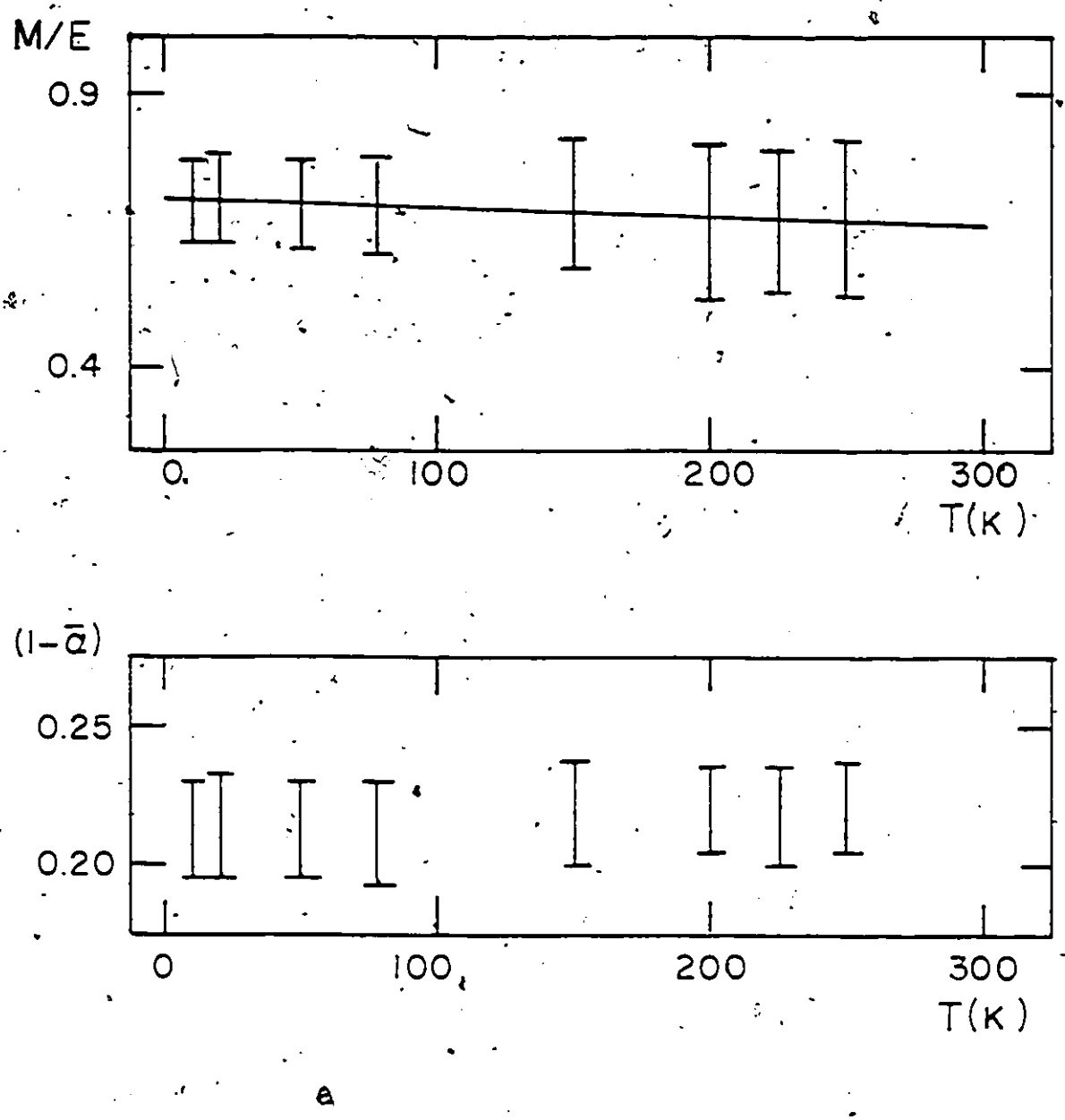

Fig. 5.6 $CuGa(S_{1-z}Se_z)_2$ Variations of the range of probable values of M/E and of $(1-\bar{\alpha})$ with temperature for sample z=0.75. The straight line is a linear fit for the mid-point values of M/E as a function of temperature.

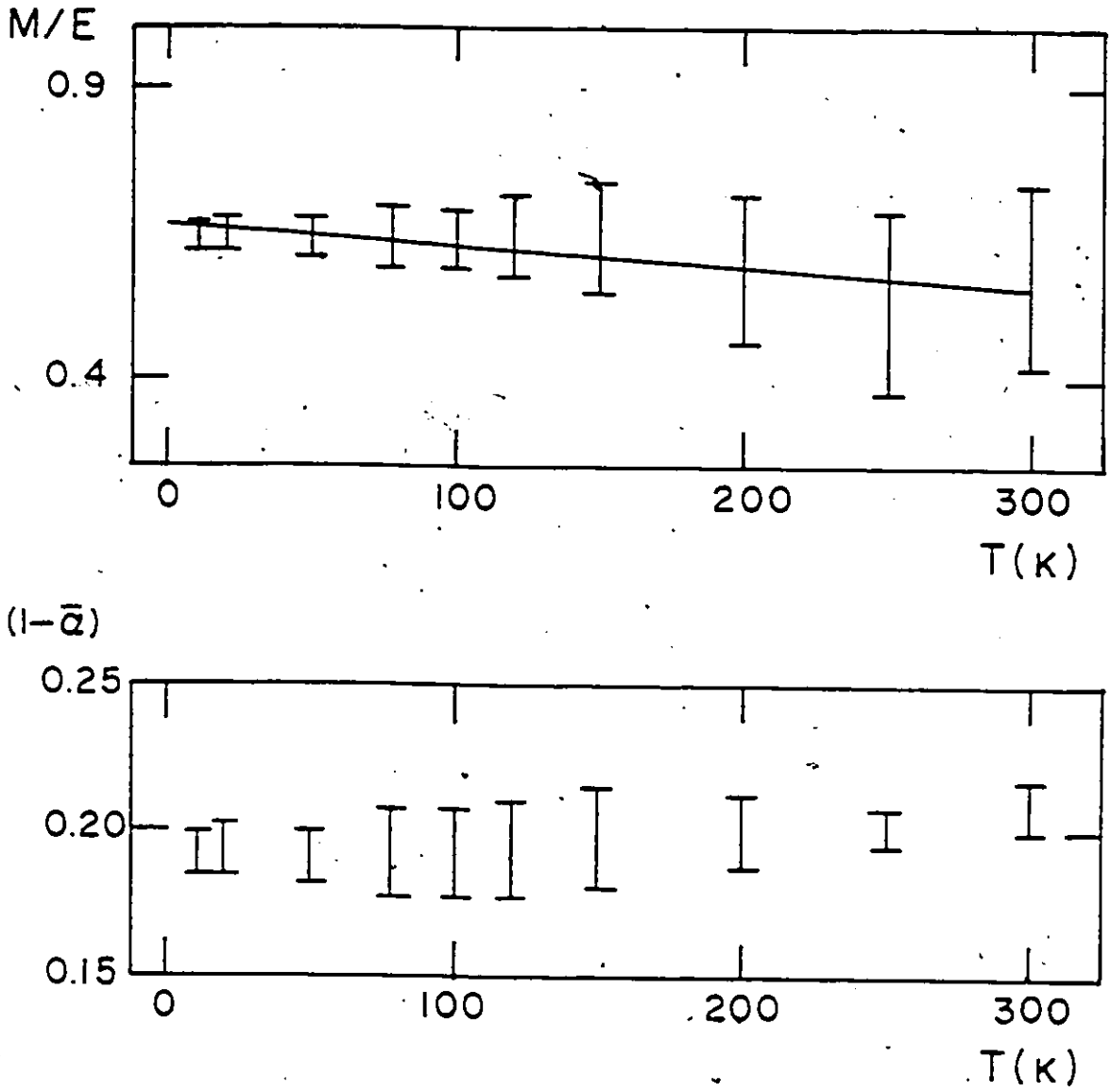

Fig. 5.7 $CuGa(S_{1-z}Se_z)_2$ Variations of the range of probable values of M/E and of $(1-\bar{\alpha})$ with temperature for sample z=1.0. The straight line is a linear fit for the mid-point values of M/E as a function of temperature.

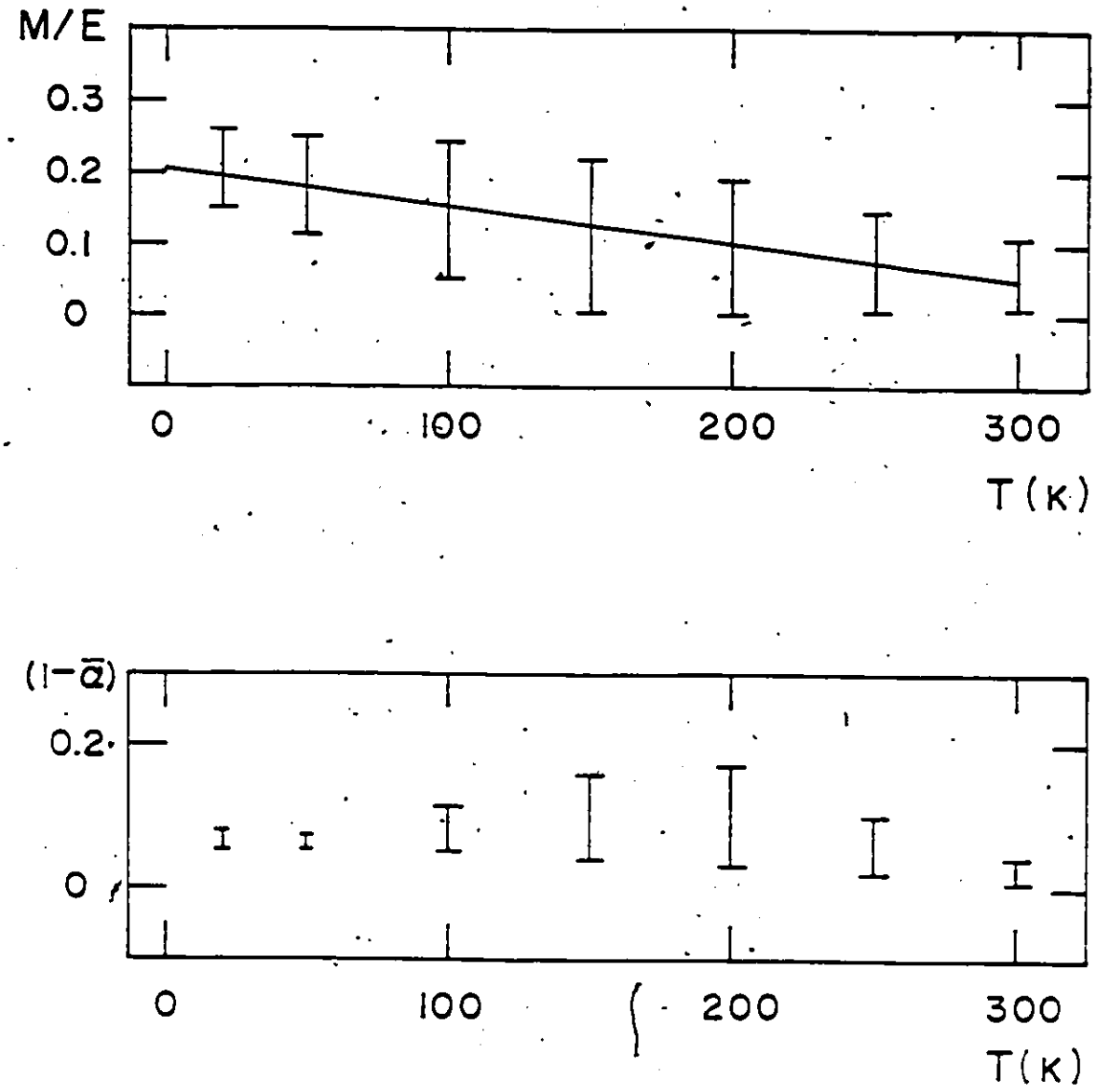

Fig. 5.8 Variations of the range of probable values of M/E and of $(1-\bar{\alpha})$ with temperature for $AgGaSe_2$.

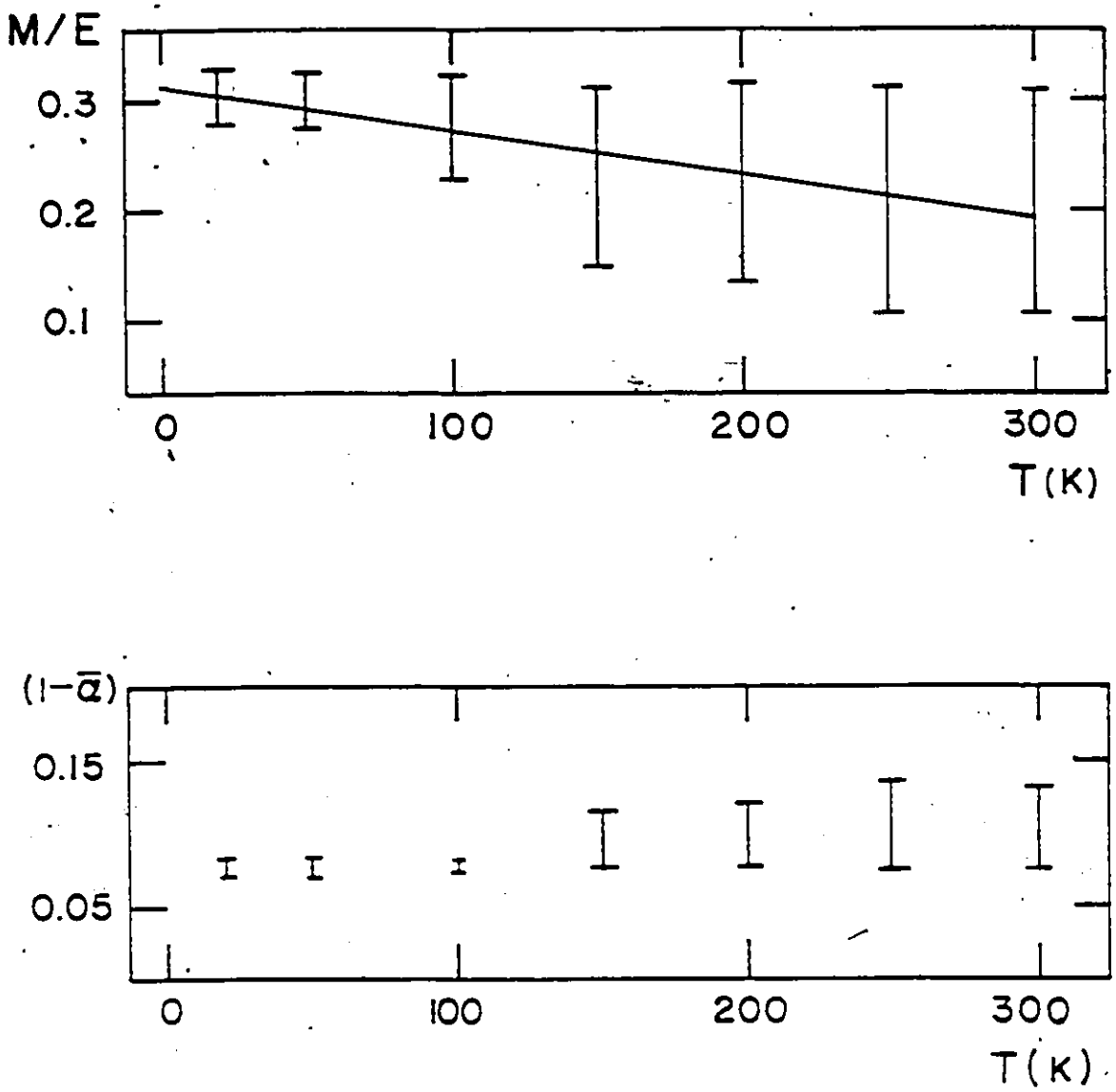

Fig. 5.9 Variations of the range of probable values of M/E and of $(1-\bar{\alpha})$ with temperature for $AgGaTe_2$.

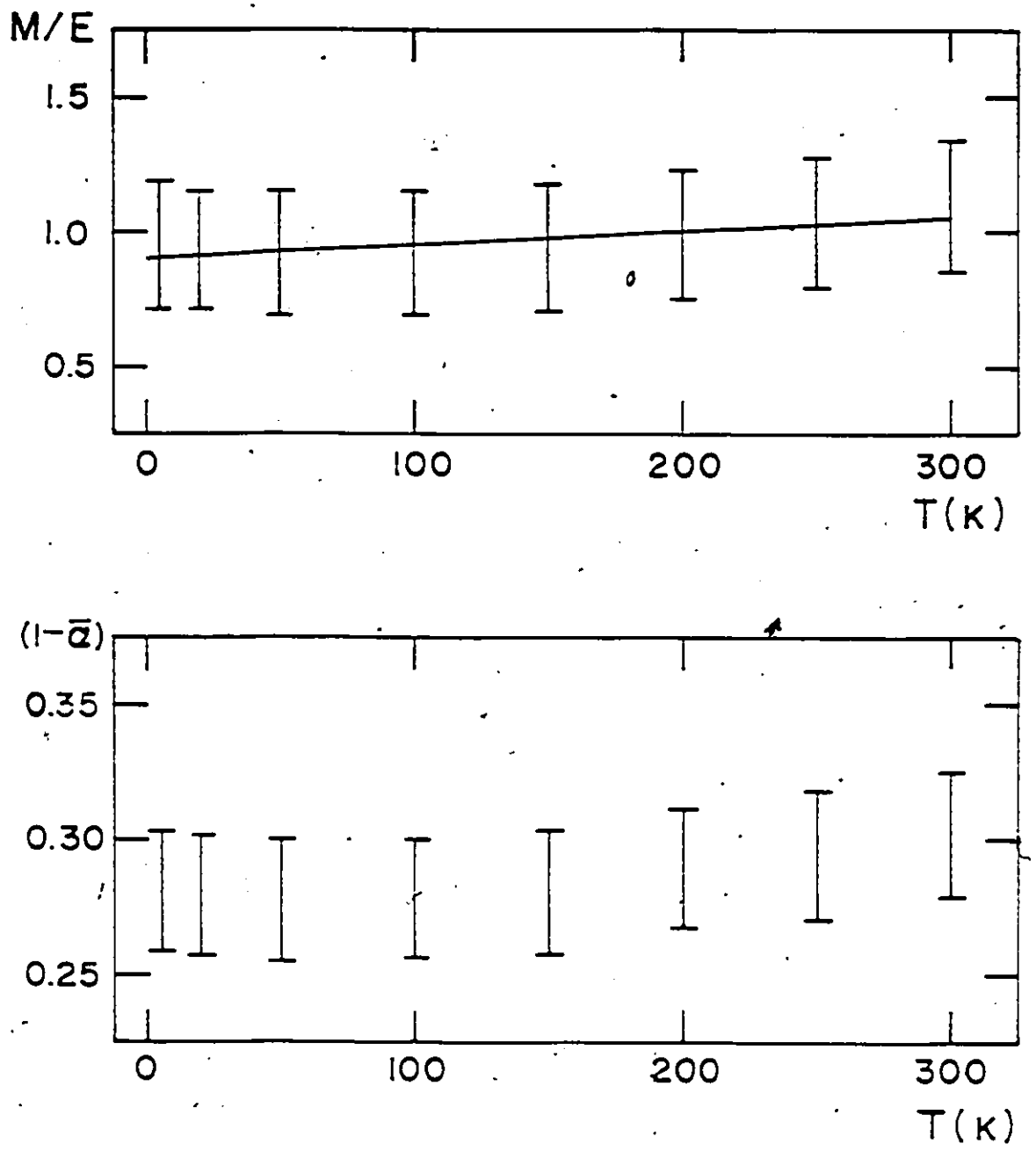

Fig. 5.10 Variations of the range of probable values of M/E and of $(1-\bar{\alpha})$ with temperature for $CuGaSnSe_4$.

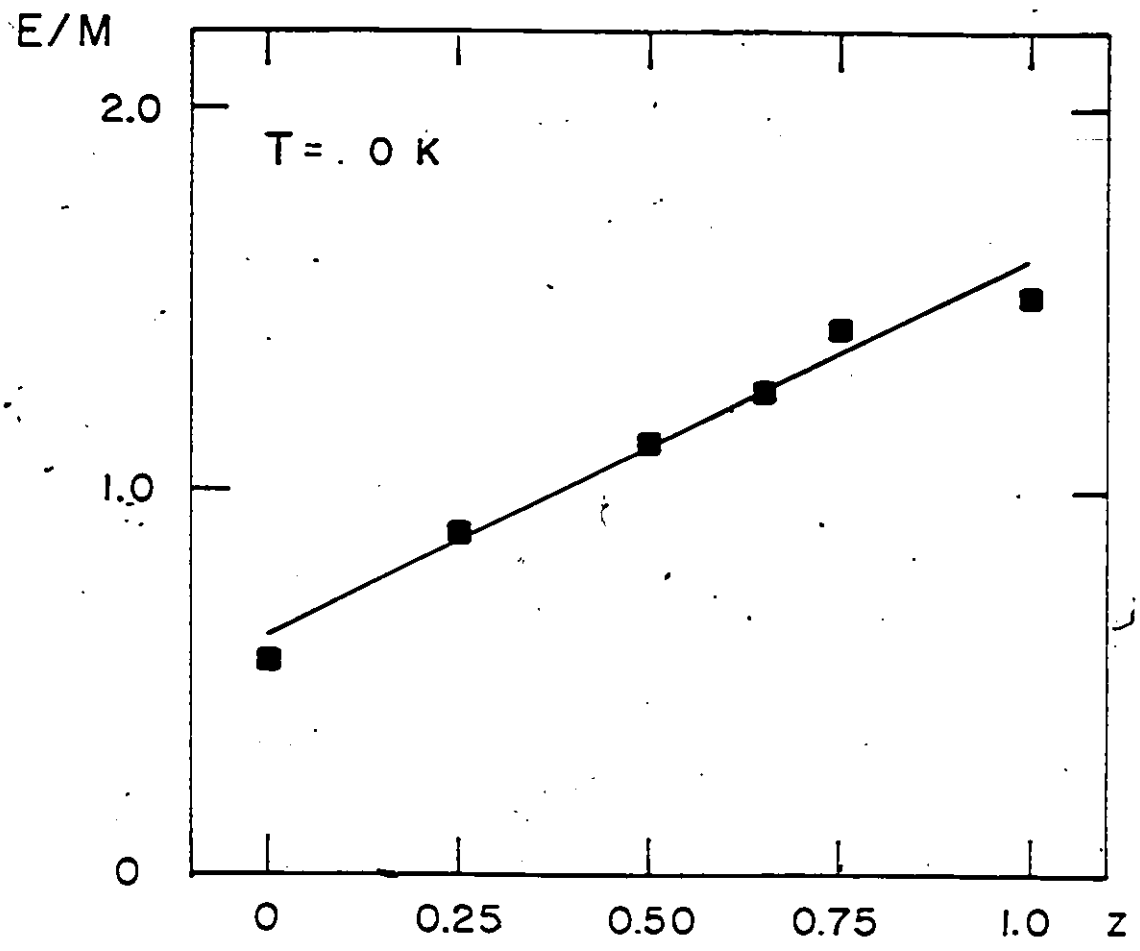

Fig. 5.11 $CuGa(S_{1-z}Se_z)_2$ Variation of the range of probable values of E/M with z at fixed temperature T = 0 K. (data taken from the fitted lines of the mid-point values of M/E as a function of temperature for each sample).

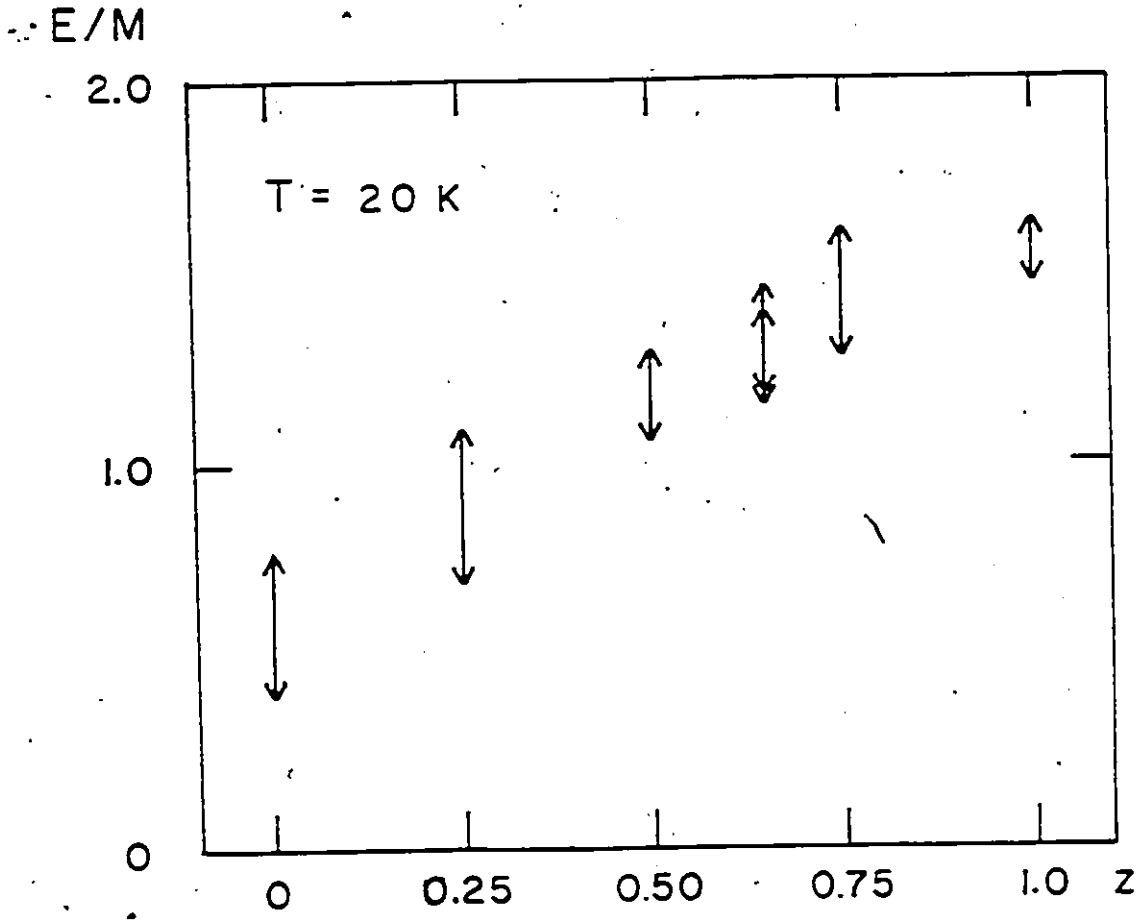

Fig. 5.12 $CuGa(S_{1-z}Se_z)_2$ Variation of the range of probable values of E/M with z at fixed temperature T = 20 K.

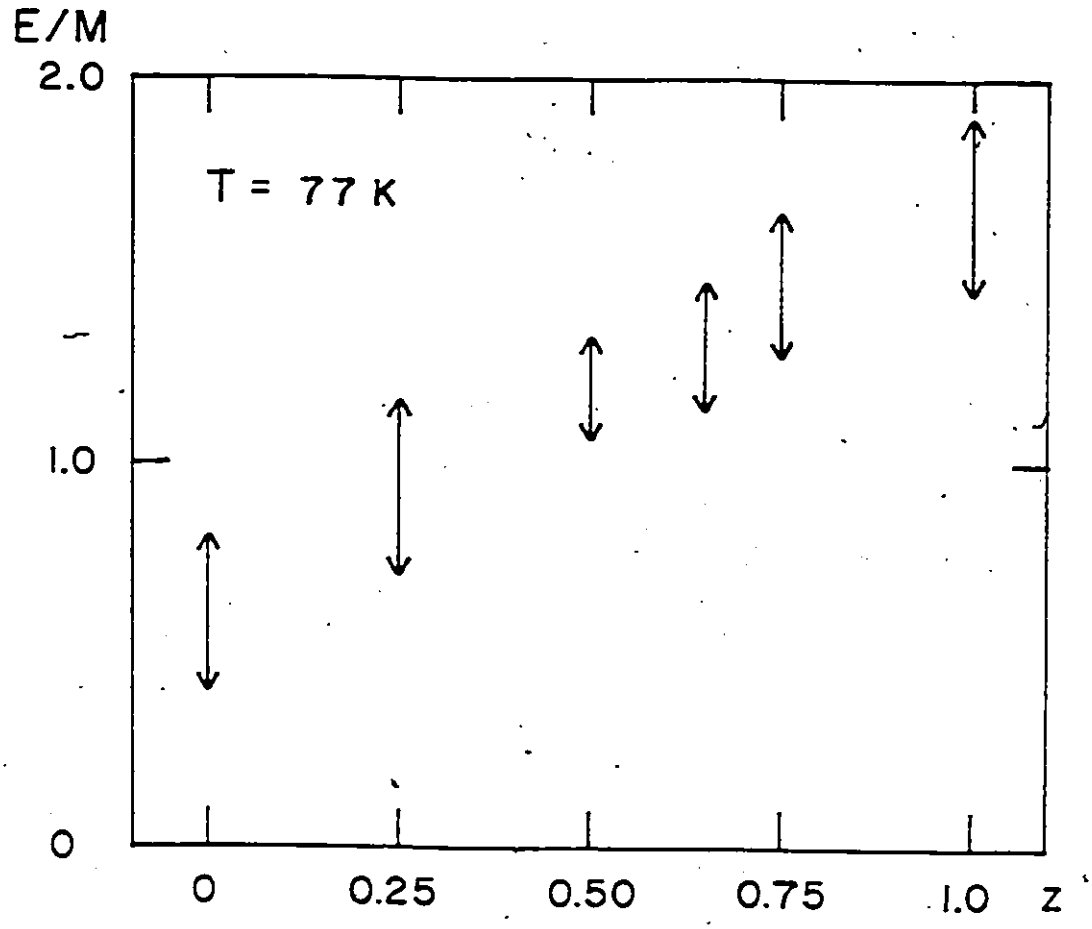

Fig. 5.13 $CuGa(S_{1-z}Se_z)_2$ Variation of the range of probable values of E/M with z at fixed temperature T = 77 K.

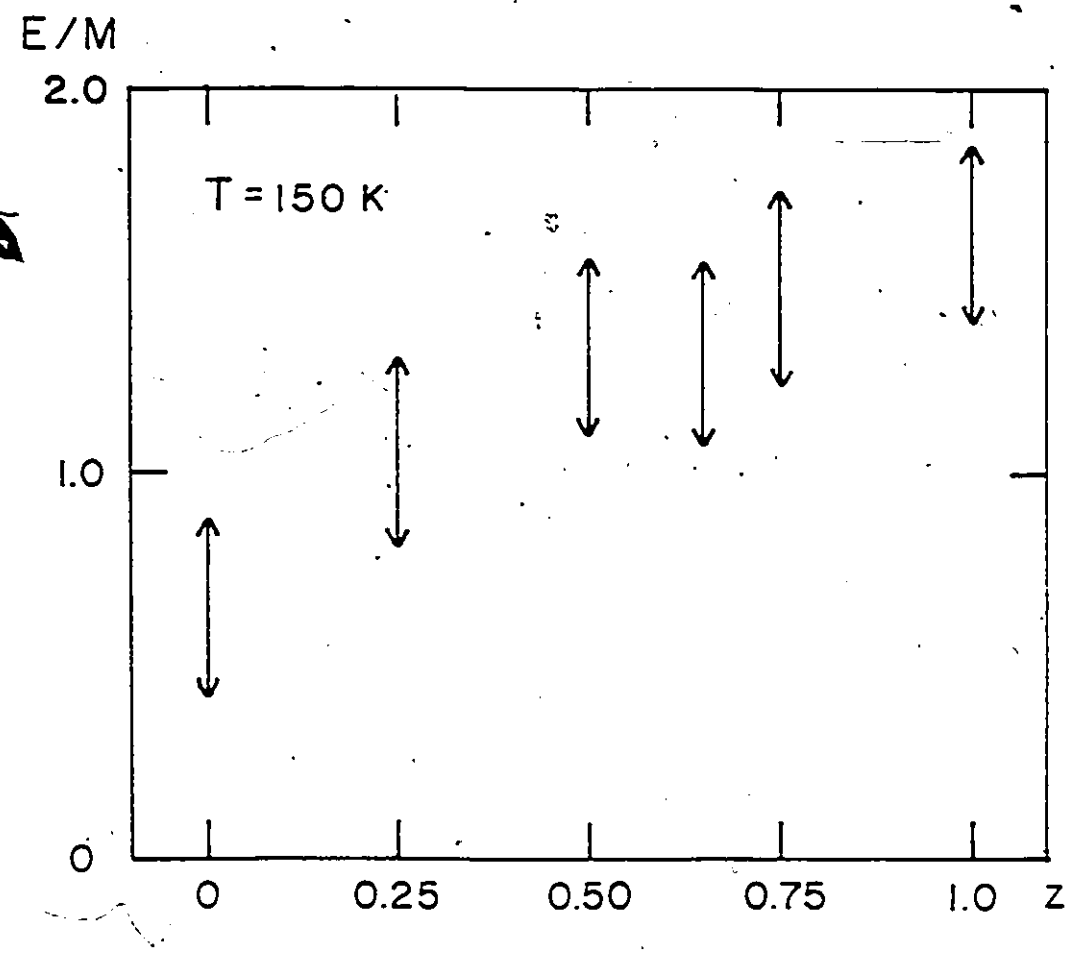

Fig. 5.14 $CuGa(S_{1-z}Se_z)_2$ Variation of the range of probable values of E/M with z at fixed temperature T = 150 K.

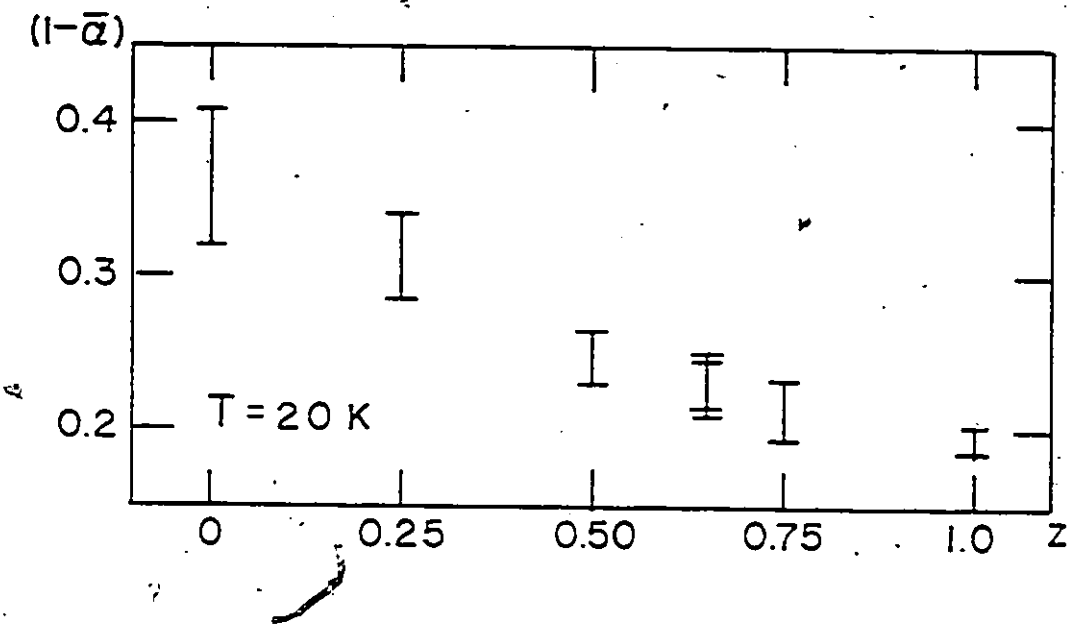

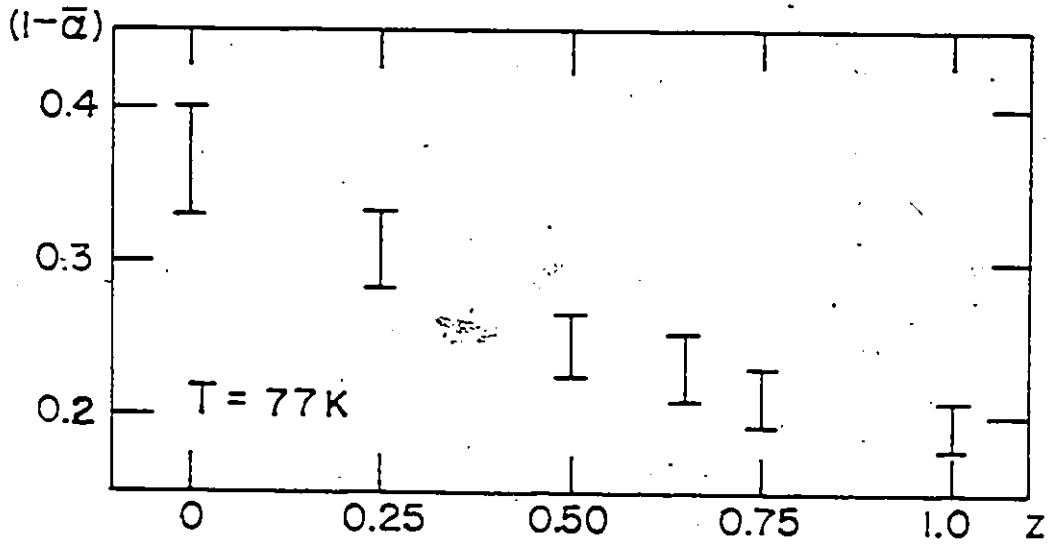

Fig. 5.15 $CuGa(S_{1-z}Se_z)_2$ Variation of the range of probable values of $(1-\bar{\alpha})$ with z at fixed temperature T = 20 K and 77 K.

5.4 Discussion

In this analysis it was assumed that the temperature variation of the valence-band splittings is due to both the temperature dependence of the $p-d$ hybridization effect and the temperature dependence of the crystal-field interaction, the lattice being determined by the temperature variation of the tetragonal distortion. As was mentioned earlier, the uncertainties in the values of the deformation potential b_p and b_d as well as in the energy gap values were introduced into the analysis. As a result, a range of probable error in the values of the $d-$like character and the strength of the $p-d$ hybridization M/E is obtained. For the alloys $CuGa(S_{1-z}Se_z)_2$, the average probable error of M/E varies from 1.30 at $z=0$ to 0.15 at $z=1$. The sulphur-rich alloys (i.e. z close to zero) show larger probable error because of the larger values of M/E. The Ag-compounds have smaller probable error values for M/E, while the corresponding value for $CuGaSnSe_4$ is 0.50. The relative probable error, however, is smaller for the alloys but larger for the Ag-compounds.

Earlier studies [79Y1, 82B1] showed that the I-III-VI_2 compounds having a positive value of β show a positive temperature coefficient of the u parameter. This indicates that the anions gradually move away from the I cation and come relatively closer to the III cation as the temperature is increased. Thus the overlap between anion $p-$orbital and the noble-metal(I) $d-$orbital will decrease as the temperature is increased and consequently, the interaction matrix element M between p and d levels decreases with increasing temperature. If the energy separation E is assumed to be constant, then the strength of the $p-d$ hybridization will decrease as the temperature is increased. This would explain the results of the temperature variation of M/E which show M/E to decrease with increasing temperature except for the case of $CuGaS_2$. In this case, however, the value of M/E with temperature has a large uncertainty which

masks the values of that slope. This behavior may not apply for the quanternary compound $CuGaSnSe_4$ because the structure has been shown to be $(Cu\square)(GaSn)Se_4$, i.e., half of the I sublattice sites are vacant [S1G1]. Thus it could have a different form of temperature variation. Bhar and Samanta [82B1] have shown that for the I-III-VI_2 compounds the temperature coefficient β is linearly proportional to the temperature coefficient of the u parameters, this latter determines the change in overlap between the noble-metal d orbitals and the anion p orbitals. Thus a relation between β and the variation of M/E with temperature might be expected. This, however, could not be obtained in the present analysis because the variation of M/E temperature was smaller than the uncertainties in the M/E values.

It was indicated above that the variation of E/M as a function of composition is practically linear (see Figs. 5.11 to 5.14). The approximate values of E/M for $CuGaS_2$ and $CuGaSe_2$ are 0.6 and 1.6 respectively. In Chapter 4, it was shown that the strength of the $p-d$ hybridization depends inversely on the energy separation E between the Cu d levels and the anion p levels. The values of E are approximately 1 and 3 eV for $CuGaS_2$ and $CuGaSe_2$, respectively (Table 4.4). This difference is consistent with the atomic energy level values for Cu d orbitals, S and Se p orbitals [74C1, 71M1]. The value of M is approximately 2 eV for both $CuGaS_2$ and $CuGaSe_2$. Thus in the case of sulphur-rich materials (i.e. $\bar{x}$ close to 0) E will be relatively small, M/E relatively large and hence the $p-d$ interaction will be stronger and the d-like character in the valence band will be greater. This explains the variation of E/M with composition shown in Figs. 5.11 to 5.14 and the variation of $(1-\bar{a})$ with composition for the present alloys shown in Fig. 5.15.

5.5 Summary

The temperature variation data of the valence-band splittings were obtained by WMR measurements made on the single crystal samples of the system $CuGa(S_{1-z}Se_z)_2$. The corresponding data for $AgGaSe_2$ and $AgGaTe_2$ were taken from Ref.[75S1] and for $CuGaSnSe_4$ from [82L1]. The model developed in Chapter 4 was used to analyse these data in terms of d–like characters and the strength of $p-d$ hybridization. The average values of the deformation potentials b_p and b_d as well as their errors were used in the analysis. The range of probable values for M/E and α_i were calculated for a given sample at a fixed temperature. Thus the variation of M/E and $(1-\alpha_i)$ as a function of temperature were obtained for each sample. The temperature variation of M/E of the ternary compounds and alloys decrease with increasing temperature except for the case of $CuGaS_2$ which has a large uncertainty in M/E values. The results indicate that the $p-d$ hybridization interaction decreases with increasing temperature. The x-ray studies indicate that the anions are moving away from the I cation and coming relatively closer to the III cation thereby reducing the $p-d$ interaction as the temperature is increased which is consistent with the above results. The variation of M/E increases with temperature in the case of $(Cu\square)(GaSn)Se_4$ which could have a different form of temperature variation due to the vacancy in the I sublattice sites.

The relation between the temperature coefficient β and the temperature variation of M/E could not be obtained because the variation of M/E with temperature was smaller than the uncertainties in the M/E values. For the alloys, the variation of E/M as a function of composition is practically linear, with E/M having approximate values of 0.6 at z=0 and 1.6 at z=1.0. The variation of $(1-\alpha)$ with composition, however, is nonlinear. This indicates that the $p-d$ interaction is stronger for the sulphur-rich materials (i.e., z close to 0) than those for the selenium-rich materials (z close to 1).

REFERENCES

1920-1959

[20B1] W.L. Bragg, Phil. Mag. 40, 169 (1920).

[36B1] L.P. Bouckaert, R. Smoluchowski, and E. Wigner, Phys. Rev. 50, 58 (1936).

[55D1] G. Dresselhaus, Phys. Rev. 100, 580 (1955).

[55P1] R.H. Parmenter, Phys. Rev. 100, 573 (1955).

[55R1] V. Roberts and J.E. Quarrington, J. Electron. 1, 152 (1955).

[57D1] W.P. Dumke, Phys. Rev. 108, 1419 (1957).

[57K1] E.O. Kane, J. Phys. Chem. Solids. 1, 249 (1957).

[57K2] G.F. Koster, in *Solid State Physics*, edited by F. Seitz and D. Turnbull (Academic, New York, 1957), Vol.5, p.1.

1960-1964

[60C1] V.A. Chaldyshev and V.N. Pokrovskii, Izv. Vyssh. Ucheb. Zaved. Fizika 2, 173 (1960).

[60D1] P.W. Davis and T.S. Shilliday, Phys. Rev. 118, 1020 (1960).

[60H1] J.J. Hopfield, J. Phys. Chem. Solids 15, 97 (1960).

[62B1] R. Braunstein and E.O. Kane, J. Phys. Chem. Solids 23, 1423 (1962).

[63C1] V.A. Chaldyshev and G.F. Karavaev, Izv. Vyssh. Ucheb. Zaved. Fizika 5, 103 (1963).

[63Y1] Y. Yafet, in *Solid State Physics*, edited by F. Seitz and D. Turnbull (Academic Press, New York, 1963), Vol.14, p.1.

[64S1] R. Sandrock and J. Treusch, Z. Naturforschg. 19a, 844 (1964).

1965-1969

[65C1] M.L. Cohen and T.K. Bergstresser, Phys. Rev. 141, 799 (1965).

[65S1] K. Shindo, A. Morita, and H. Kamimura, J. Phys. Soc. Japan 20, 2054 (1965).

[66K1] G.F. Karavaev and A.S. Poplanoi, Fizika Tverd. Tela 8, 2143 (1966) [Soviet Phys. Solid State 8, 1704 (1967).]

[67J1] E.J. Johnson, in *Semiconductors and Semimetals*, edited by R.K. Willardson and A.C. Beer (Academic Press, New York, 1967), Vol.3, p.153.

[67P1] L. Pauling, *The Nature of the Chemical Bond* (Cornell University Press, Ithaca, New York, 1967).

[67S1] K.S. Song, J. Physique (Paris) 28, 195 (1967).

[68G1] D.L. Greenaway and G. Harbeke, *Optical Properties and Band Structure of Semiconductors* (Pergamon Press, Oxford, 1968), p.9.

[68L1] D. Long, *Energy Bands in Semiconductors* (Interscience Publishers, New YOrk, 1968), p.120.

[69C1] M. Cordona, *Modulation Spectroscopy in Solid State Physics*, edited by H. Ehrenreich, F.Seitz, and D.Turnbull (Academic, New York, 1969), Suppl. 11, p.167.

1970-1974

[70P1] J.C. Phillips, Rev. Mod. Phys. 42, 317 (1970).

[71A1] S.C. Abrahams and J.L. Bernstein, J. Chem. Phys. 55, 796 (1971).

[71H1] W.N. Honeyman and K.H. Wilkinson, J. Phys. D 4, 1182 (1971).

[71M1] C.E. Moore, *Atomic Energy Levels*, Nat. Stand. Ref. Data Ser., National Bureau of Standards (U.S.) 35 (Washington D.C., 1971), Vol.I, p.181, Vol.II, p.111 and 150, Vol.III, p.48.

[71P1] A.S. Poplavnoi and Yu. I. Polygalov, Izv. Akad. Nauk SSSR, Neorg. Mater. 7, 1706 (1971) and 7,

1711 (1971) [Inorg. Mater. (USSR) 7, 1527 (1971) and 7, 1531 (1971)].

[71R1] J.E. Rowe and J.L. Shay, Phys. Rev. B 3, 451 (1971).

[71T1] B. Tell, J.L. Shay, and H.M. Kasper, Phys. Rev. B 4, 2463 (1971).

[72S1] J.L. Shay and H.M. Kasper, Phys. Rev. Lett. 29, 1162 (1972).

[72Y1] N. Yamamoto and T. Miyauchi, Jpn. J. Appl. Phys. 11, 1383 (1972).

[73A1] S.C. Abrahams and J.L. Bernstein, J. Chem. Phys. 59, 5415 (1973).

[73B1] M. Bettini, Solid State Commun, 13, 599 (1973).

[73L1] M.J. Luciano and C.J. Vesely, Appl. Phys. Lett. 23, 60 (1973) and 23, 453 (1973).

[73R1] M. Robbins, J.C. Phillips, and V.G. Lambrecht, Jr., J. Phys. Chem. Solids 34, 1205 (1973).

[73R2] M. Robbins and V.G. Lambrecht, Jr., J. Solid State Chem. 6, 402 (1973).

[73R3] A. Rosencwaig, Opt. Commun. 7, 305 (1973).

[73S1] G. Simons and A.N. Bloch, Phys. Rev. B 7, 2754 (1973).

[73S2] J.L. Shay, B. Tell, H.M. Kasper, and L.M. Schiavone, Phys. Rev. B 7, 4485 (1973).

[73Y1] P.W. Yu, W.J. Anderson, and Y.S. Park, Solid State Commun. 13, 1883 (1973).

[74A1] S.C. Abrahams and J.L. Bernstein, J.Chem. Phys. 61, 1140 (1974).

[74B1] W. Braun, A. Goldmann, and M. Cordona, Phys. Rev. B 10, 5069 (1974).

[74B2] K. Baumann, Phys. Stat. Sol. (b) 63, K71 (1974).

[74C1] E. Clementi and C. Roetti, At. Data Nucl. Data Tables 14, 177 (1974).

[74K1] S. Kono and M. Okusawa, J. Phys. Soc. Japan 37, 1301 (1974).

[74K2] H. Kildal, Phys. Rev. B 10, 5082 (1974).

[74M1] R.L. Moon, G.A. Antypas, and L.W. James, J. Electron. Mater. 3, 365 (1974).

[74N1] J. Noolandi, Phys. Rev. B 10, 2490 (1974).

[74P1] J.C. Phillips, J. Phys. Chem. Solids 35, 1205 (1974).

[74S1] J. St. John and A.N. Bloch, Phys. Rev. Lett. 33, 1095 (1974).

[74S2] H.W. Spiess, V. Haeberln, G. Brandt, A. Rauber, and J. Schneider, Phys. Stat. Sol. B 62, 183 (1974).

[74W1] S. Wagner, J.L. Shay, P. Migliorato, and H.M. Kasper, Appl. Phys. Lett. 25, 434 (1974).

1975-1979

[75C1] Deuxieme Conference International sur les Composés Semiconductors Ternaries, Strasbourg, 1975 [J. Physique Coll. 36, C3 (1975)].

[75C2] J. Camassel and D. Auvergne, Phys. Rev. B 12, 3258 (1975).

[75R1] A. Rosencwaig, Analytical Chem. 47, 592A (1975).

[75S1] B. Sermage, F. Barthe-Lefin, and A.C. Papadopoulo-Scherle, J. Physique Coll. 36, C3-137 (1975).

[75S2] J.L. Shay and J.H. Wernick, *Ternary Chalcopyrite Semiconductors : Growth, Electronic Properties, and Applications* (Pergamon, Oxford, 1975).

[75T1] B. Tell and P.M. Bridenbaugh, Phys. Rev. B 12, 3330 (1975).

[75W1] D. Weaire and J. Noolandi, J. Physique Coll. 36, C3-27 (1975).

[76A1] P.B. Allen and V. Heine, J. Phys. C 9, 2305 (1976).

[76B1] H.S. Bennett and R.A. Forman, Appl. Opt. 15, 2405 (1976).

[76C1] J.J. Coleman, N. Holonyak, Jr., J.J. Ladourse, and P.D. Wright, J. Appl. Phys. 47, 2015 (1976).

[76P1] A.S. Poplanoi, Yu.I. Polygalov, and A.M. Ratner, Izv. Vyssh. Ucheb. Zaved. Fizika 6, 7 (1976) [Soviet Phys. J. 19, 689 (1976)].

[76R1] A. Rosencwaig and A. Gersho, J. Appl. Phys. 47, 64 (1976).

[77A1] L.C. Aamodt, J.C. Murphy, and J.G. Parker, J. Appl. Phys. 48, 927 (1977).

[77H1] *Ternary Compounds, 1977*, edited by G.D. Holah (IOP Conference Series No. 35) (Institute of Physics, London, 1977).

[77H2] W. Hörig, H. Neumann, H.J. Höbler, and G. Kühn, Phys. Stat. Sol. (b) 80, K21 (1977).

[77I1] G.W. Iseler, J. Cryst. Growth 41, 146 (1977).

[77M1] A. Mackinnon, A. Mirror, and G. Ross, in *Ternary Compounds, 1977*, edited by G.D. Holah (IOP Conference Series No. 35) (Institute of Physics, London, 1977), p.171.

[77P1] J.C. Phillips, *Festkörperprobleme XVII* (Advn. Solid State Physics) (Pergamon-Vieweg, Frankfurt, 1977).

[77R1] J.C. Rife, R.N. Dexter, P.M. Bridenbaugh, and B.W. Veal, Phys. Rev. B 16, 4491 (1977).

[77T1] M.J. Thwaites, R.D. Tomlinson, and M.J. Hamshire, in *Ternary Compounds, 1977*, edited by G.D. Holah (IOP Conference Series No. 35) (Institute of Physics, London, 1977), p.227.

[77Y1] N. Yamamoto, H. Horinaka, K. Okada, and T. Miyauchi, Jpn. J. Appl. Phys. 16, 1817 (1977).

[77Z1] A. Zunger and A.J. Freeman, Phys. Rev. B 15, 4716 (1977).

[78C1] J.R. Chelikowsky and J.C. Phillips, Phys. Rev. B 17, 2453 (1978).

[78H1] W. Hörig, H. Neumann, H. Sobotta, B. Schumann, and G. Kühn, Thin Solid Films 48, 67 (1978).

[78M1] F.A. McDonald and G.C. Wetsel Jr., J. Appl. Phys. 49, 2213 (1978).

[78N1] R.E. Nahory, M.A. Pollack, and J.C. Dewinter, Appl. Phys. Lett. 33, 659 (1978).

[78N2] H. Neumann, W. Hörig, and E. Reccius, Solid State Commun. 27, 449 (1978).

[78S1] A. Shankat and R.D. Singh, J. Phys. Chem. Solids 39, 1269 (1978).

[78S2] R.A. Smith, *Semiconductors*, second edition (Cambridge University Press, Cambridge, 1979), Section 10.5.

[78T1] M.J. Thwaites, R.D. Tomlinson, and M.J. Hamshire, Solid State Commun. **27**, 727 (1978).

[79C1] G.H. Chapman, J. Shewchun, J.J. Loferski, B.K. Garside, and R. Beaulieu, Appl. Phys. Lett. **34**, 735 (1979).

[79H1] W. Hörig, H. Neumann, E. Reccius, H. Weinert, G. Kühn, and B. Schumann, Phys. Stat. Sol. (a) **51**, 57 (1979).

[79P1] B. R. Pamplin, T. Kiyosawa, and K. Matsumoto, Prog. Cryst. Growth Charact. **1**, 331 (1979).

[79S1] J. Shewchun, J.J. Loeferski and R. Beaulieu, G.H. Chapman, and B.K. Garside, J. Appl. Phys. **50**, 6978 (1979).

[79Y1] N. Yamamoto, H. Horinaka, and T. Miyauchi, Jpn. J. Appl. Phys. **18**, 255 (1979).

1980-1985

[80B1] H.G. Brühl and H. Neumann, Solid State Com. **34**, 225 (1980).

[80C1] Proceedings of the Fourth International Conference on Ternary and Multinary Compounds, Tokyo, Japan, 1980 [Jpn. J. Appl. Phys. **19**, Suppl. 19-3 (1980)].

[80M1] G.A. Thomas and V.B. Timofeev, in *Handbook on Semiconductors : Optical Properties of Solids*, edited by M. Balkanski (North-Holland, Amsterdam, 1980), Vol.2, p.48.

[80O1] T. Oguchi, T. Hamajima, T. Kambara, and K.I. Gondaira, Jpn. J. Appl. Phys. **19**, Suppl. 19-3, 107 (1980).

[80R1] A. Rosencwaig, in *Photoacoustic and Photoacoustics Spectroscopy in Chemical Analysis : A Series of Monographs on Analytical Chemistry and its Applications*, edited by P.J. Elving and J.D.

Winefordner (John Wiley & Sons, New York, 1980), Vol.57.

[80T1] H. Takenoshita, T. Nakan, and I. Nakao, Jpn. J. Appl. Phys. 19, Suppl. 19-3, 33 (1980).

[80Z1] Alex Zunger, Phys. Rev. B 22, 5839 (1980).

[81A1] J.E. Avon, J.C. Woolley, A. Asbjornsen, S. Chatraphorn, K. Ratanathammapan, and K. Yoodee, J. Appl. Phys. 52, 6423 (1981).

[81B1] J.J.M. Binsma, L.T. Giling, and J. Bloem, Phys. Stat. Sol. (a) 63, 595 (1981).

[81D1] E.P. Domashevskaya, L.N. Marshakova, V.A. Terekhov, A.N. Lukin, Ya.A. Ugai, V.I. Nefedov, and Ya.V. Salyn, Phys. Stat. Sol. (b) 106, 429 (1981).

[81G1] R.G. Goodchild, O.H. Hughes, J.C. Woolley, Phys. Stat. Sol. 68, 239 (1981).

[81M1] A. Miller, A. Mackinnon, and D. Weaire, in *Solid State Physics*, edited by H. Ehrenreich, F. Seitz, and D. Turnbull (Academic, New York, 1981), Vol.36, p.119.

[81S1] R.D. Shannon, Review in *Structure and Bonding in Crystals*, edited by M. O'Keefe and A. Navrotsky (Academic Press, New York, 1981), Vol.II, p.53.

[82B1] G.C. Bhar and L.K. Samanta, Phys. Rev. 26, 2275 (1982).

[82B2] P. Bendt and Alex Zunger, Phys. Rev. 26, 3114 (1982).

[82C1] Proceedings of the Fifth International Conference on Ternary and Multinary Compounds, Cagliari, Italy, 1982 [Nouvo Cimento, Vol.2D, No.6 (1983)].

[82D1] E.R. DeGil, Phys. Stat. Sol. (a) 70, 519 (1982).

[82G1] R.G. Goodchild, O.H. Hughes, S.A. Lopez-Rivera, and J.C. Woolley, Can. J. Phys. 60, 1096 (1982).

[82L1] S.A. Lopez-Rivera, R.G. Goodchild, O.H. Hughes, J.C. Woolley, and B.R. Pamplin, Can. J. Phys. 60, 10 (1982).

[S3J1] J.E. Jaffe and Alex Zunger, Phys. Rev. 27, 5176 (1983).

[S3J2] J.E. Jaffe and Alex Zunger, Phys. Rev. 28, 5822 (1983).

[S3L1] S.A. Lopez-Rivera, B.R. Pamplin, and J.C. Woolley, Nuovo Cimento 2D, 1728 (1983).

[S3M1] L. Martinez, S.A. Lopaz-Rivera, and V. Sagredo, Nuovo Cimento 2D, 1687 (1983).

[S3T1] M. Turowski, A. Kisiel, and R.D. Tomlinson, Nuovo Cimento 2D, 2064 (1983).

[S4A1] J.E. Avon, M. Sc. Thesis (1984), University of Ottawa.

[S4C1] Proceedings of the Sixth International Conference on Ternary and Multinary Compounds, Caragus, Venezuela, 1984 [To be published.]

[S4J1] J.E. Jaffe and Alex Zunger, Phys. Rev. B 29, 1882 (1984).

[S4J2] J.E. Jaffe and Alex Zunger, Phys. Rev. B 30, 741 (1984).

[S4N1] H. Neumann, D.W. Bullett, H. Sommer, R.D. Tomlinson, and W. John, Phys. Stat. Sol. (b) 121, 641 (1984).

[S4Q1] M. Quintero and J.C. Woolley, J. Appl. Phys. 55, 2825 (1984).

[S4Y1] K. Yoodee, J.C. Woolley, and V. Sa-yakanit, Phys. Rev. B 10, 5904 (1984).

[S5C1] S. Chatraphorn, T. Panmatarite, S. Pramatus, A. Prichavudhi, R. Kritayakirana, J. Berananda, V. Sa-yakanit, and J.C. Woolley, to be appeared in J. Appl. Phys., February (1985).

[S5Q1] M. Quintero, Ph. D. Thesis (1985), University of Ottawa.

[S5S1] A. Shanker and K. Hussain, J. Phys. Chem. Solids 46, 61 (1985).

[S5S2] K.S. Song, private communication.